A Characterisation of Matrix-assisted Laser Desorption Ionisation

Colin Thomas Joseph Scott

Department of Physics and Astronomy

University of Glasgow

Presented as a thesis for the degree of Doctor of Philosophy in the University of Glasgow

To Wendy

I wandered lonely as a cloud
That floats on high o'er vales and hills,
When all at once I saw a crowd,
A host of golden daffodils,
Beside the lake, beneath the trees
Fluttering and dancing in the breeze.

Continuous as the stars that shine
And twinkle on the milky way,
They stretched in never-ending line
Along the margin of the bay;
Ten thousand saw I at a glance
Tossing their heads in sprightly dance

The waves beside them danced, but they
Out-did the sparkling waves in glee:
A poet could not but be gay
In such jocund company!
I gazed - and gazed - but little thought
What wealth the show to me had brought:

For oft, when on my couch I lie
In vacant or in pensive mood,
They flash upon that inward eye
Which is the bliss of solitude;
And then my heart with pleasure fills,
And dances with the daffodils

William Wordsworth

Summary

Matrix-assisted Laser Desorption Ionisation (MALDI) is a laser based technique which can produce intact high mass ions from labile molecules initially in the solid state. The technique is now widely used in analytical chemistry and biochemistry but the underlying mechanisms remain poorly understood. The aim of the work undertaken by the author was to carry out a characterisation of MALDI and ultimately develop the technique to the stage where it could be used routinely as an ion source for photofragmentation studies.

The thesis begins with an introduction to biomolecular mass analysis and the mass spectrometric techniques leading up to the discovery of MALDI. A rationale is given for the work described in later Chapters, followed by a brief history of the discovery of MALDI. The fundamentals of the technique are then described, including i) the expected role of matrix, ii) sample preparation, iii) observed physical characteristics and iv) a variety of the useful matrices identified to date.

Chapter 3 is concerned with the theory used throughout the thesis. The first section of Chapter 3 describes the theory of time-of-flight (TOF) mass spectrometric techniques. Factors affecting the resolution of TOF mass spectrometers are discussed, and a detailed derivation of the mass resolution of an ideal reflectron TOF mass spectrometer is given in Appendix A. The second section of Chapter 3 desribes laser/solid interactions. The initial deposition of the laser pulse within the matrix solid is described, followed by a detailed critical analysis of the three main mechanisms discussed in the literature by which material ejection may be occuring. The section closes with a description of the homogeneous bottleneck model, proposed to explain the apparent lack of analyte fragmentation, and a phenominological model for MALDI based solely on the assumption of a fluence threshold. The third section of Chapter 3 deals with hydrodynamic modelling which is used in an attempt to characterise the ablation process via application of the models to the particle velocity distributions observed in the ablation plume. Possible ionisation mechanisms are also discussed briefly.

The apparatus used by the author in the course of the work is described in Chapter 3. For ease of description the equipment is seperated into four distinct areas; the mass spectrometer, the lasers used in the experiments, the optical appartus used to control and manipulate the laser light, and the data aquisition and electronic control systems. The samples and sample preparation techniques employed throughout the work are also described.

The experimental results obtained by the author are detailed in Chapters 4, 5, 6 & 7. The author was solely responsible for carrying out the bulk of this work. Typical characteristics of MALDI are detailed in Chapter 4. In addition, the ablated neutral post-ablation ionisation (PAI) signal dependence on ablation laser fluence is modelled using the theory detailed in Chapter 2. Investigations into the effect of molar ratio on the ion yield and the presence of acidic cluster ion species are also described in this Chapter. Chapter 5 is concerned with experiments carried out using the PAI technique in order to probe the MALDI plume. The particle distributions observed in the expanded plume are modelled using hydrodynamic theory. The production of enhanced quasimolecular ion signals using PAI in the dense proto-plume are described for the first time. The discovery of atomic hydrogen in the MALDI ablation plume with mean velocities an order of magnitude greater than that of the matrix parent and fragment species is described in Chapter 6. A large enhancement was observed in the abundance of neutral atomic hydrogen as the ablation laser fluence was increased to values greater than the ion production threshold fluence. Chapter 7 describes the initial results obtained using MALDI as an ion source for ion photofragmentation studies. A discussion of the work and conclusions relating to possible ablation mechanisms are given in Chapter 8.

Acknowledgments

The preparation of this thesis was a long and arduous road. Many people helped me along the way, both during the experimental work and while writing up. I would like to thank the following in particular;

My supervisor and group leader Dr Kenneth Ledingham, for help and advice, an endless supply of enthusiasm and for helping me find the road.

Dr Ravi Singhal for help and advice on some theoretical aspects of the work.

Dr Ian Borthwick for initial guidance on the operation of the laboratory.

Dr Rong-er Zheng for friendship and table tennis lessons.

Dr Wei-Jie Jia for assistance with some of the experiments.

Dr Alastair Clark, Dr Archie Marshall, Dr Joseph Sander, Dr Chris McLean, Dr Costas Kosmidis, Robert Deas, Hamdi Kilic and Wei-Xian Peng for interesting discussions, their friendly banter and general good humour.

Robert Maxwell and Tom McCanny for technical support and assistance.

All the technical staff from the electronic and mechanical workshop who put things together and on occasion stopped them from seizing up altogether.

Miss C McIntyre for secretarial help.

SERC for a studentship.

My family, friends, and most of all Wendy without whom all this would be nothing.

Publications List

Borthwick I S, Ledingham K W D, **Scott C T J** and Singhal R P, (1992)
Laser ablation as a sample atomisation technique for resonant ionisation mass spectrometry
Resonance Ionisation Spectroscopy 1992, Inst. Phys. Conf. Series, 128 pp 279-282

Borthwick I S, **Scott C T J**, Ledingham K W D and Singhal R, (1993)
Velocity distributions of aluminium atoms ablated from aluminium metal
Laser ablation: Mechanisms and applications-II, 1993, AIP conference proceedings 288, pp 414-420

Scott C T J, Kosmidis C, Jia W J, Ledingham K W D
and Singhal R P, (1994)
Formation of atomic hydrogen in matrix-assisted laser desorption ionisation
Rap. Comm. Mass Spectrom., 8 pp 829-832

Zheng R, Campbell M, Ledingham K W D, Jia W, **Scott C T J** and Singhal R P, (1994)
The characterisation of laser ablation of bulk super-conducting material using post ablation ionisation of the neutrals
Resonance ionisation spectroscopy 1994, AIP conference proceedings 329, pp 353-356

Scott C T J, Kosmidis C, Jia W J, Ledingham K W D
and Singhal R P, (1994)
Investigations of desorbed species from matrix materials used in MALDI
Resonance ionisation spectroscopy 1994, AIP conference proceedings 329, pp 64-67

Jia W J, Ledingham K W D, **Scott C T J**, Kosmidis C
and Singhal R P, (1995)
A tandem reflectron time-of-flight mass spectrometer for the investigation of laser photofragmentation of molecular ions
Rap. Comm. Mass Spectrom., 9 pp 761-766

Jia W J, Ledingham K W D, **Scott C T J**, Kosmidis C
and Singhal R P, (1996)
Photofragmentation studies of biomolecular ions of amino acids using a tandem reflectron time-of-flight mass spectrometer
Rap. Comm. Mass Spectrom., 10 pp 1597-1604

Jia W J, Kosmidis C, Ledingham K W D, **Scott C T J**,
and Singhal R P, (1996)
Laser mass-spectrometry of biological molecular ions produced by matrix-assisted laser-desorption ionisation (MALDI)
App. Surf. Sci., 106 pp 108-113

Zheng R, Campbell M, Ledingham K W D, Jia W, **Scott C T J**
and Singhal R P, (1997)
Diagnostic study of laser ablated $YBa_2Cu_3O_y$ plumes
Spectrochimica Acta B - At. Spectr., 52 pp 339-352

Contents

Tables & Figures

List of Tables

List of Figures

Chapter One

Introduction

1.1 Introduction to Biomolecular Mass Analysis

The analysis of biologically important molecules using Mass Spectrometry (MS) has seen a rapid expansion during the past twenty years. This development has mainly been driven by the requirement of researchers in various fields, such as protein analysis in analytical chemistry or biochemistry, for an accurate and sensitive method to determine both molecular mass and structural information from large complex molecules.

Mass analysis of these types of molecules has been traditionally done by separation methods based on particle mobility, such as chromatography and gel electrophoresis or ultra centrifugation (Vertes 1993b, Kaufmann 1995). Although these techniques can cover the mass range from 1,000 to 5,000,000 amu, they usually require considerable sample preparation and lengthy analysis times with mass accuracies typically limited to no better than 5 or 10% (Chait 1992).

Mass spectrometric methods of analysis require the production of gas phase molecular ions of the compound to be analysed. Until recently this has proven to be a major limitation to the attainable mass range. Biomolecules are typically polar and massive, and therefore extremely non-volatile. They also tend to be thermally labile or unstable, leading to decomposition of the molecule when subjected to thermal heating. For example, as an ion source for mass spectrometry, laser ablation of a pure material is limited to small biomolecules below 1000 (Beavis 1992b) to 1500 Da (Karas 1990).

These problems were solved partially in the 1970's with the discovery of various soft ionisation techniques (such as chemical ionisation, field desorption and secondary ion mass spectrometry) which increased the

accessible mass range, although the upper limit was still limited to a relative molecular mass (M_r) of approximately 10,000 amu (Vertes 1993b).

During the 1980's the development of four techniques occurred which surpassed this limit; Plasma Desorption Mass Spectrometry (PDMS) (MacFarlane 1976), Fast Atom Bombardment (FAB) (Barber 1981), Electrospray Ionisation (ESI) (Fenn 1989) and Matrix Assisted Laser Desorption Ionisation (MALDI) (Karas 1988). Of these four, ESI and MALDI have emerged as the dominant techniques. In terms of their application as biomolecular research tools, there is no clear favourite between the two, although each technique has advantages over the other. ESI offers the advantage of increased mass resolution, while MALDI is well suited towards the analysis of mixtures (Favretto 1994). The techniques are complementary rather than competitive. The record for the largest functional biomolecular ion detected lies with MALDI at a mass limit of M_r = 272,500 Da (Karas 1990) compared to M_r = 133,000 for ESI (Fenn 1989).

When the performance of typical gel electrophoresis (sodium dodecyl sulphate polyacrylamide gel electrophoresis (SDS-PAGE)) is compared with that of MALDI, it is immediately apparent that with respect to mass resolving power, accuracy and precision of mass determination, MALDI is far superior (2 to 4 orders of magnitude better (Kaufmann 1995)). The sensitivities attainable with each technique are comparable at present. It is only with respect to the mass limit, that electrophoresis achieves better results (up to 5 MDa). The limit to the mass range in MALDI is probably set by the poor detection efficiency at large masses of the generation of ion detectors currently used in mass spectrometry, rather than by the ion generation process itself. Advances in detection technology should rapidly close the gap between the mass limits of MALDI, and electrophoresis or ultra centrifugation.

1.2 Motivation For This Research

Although the practical aspects of MALDI are well known, the underlying physical principles governing the mechanisms of volatilisation and

ionisation are still uncertain. One of the more obvious questions which is yet to be answered satisfactorily, is how laser ablation, a highly energetic process, can result in the ejection of large, thermally labile molecules into the gas phase, with apparently little or no fragmentation. The bulk of research performed into MALDI to date has focused on the search for new applications rather than on the basic understanding of the processes involved.

The purpose of the research program carried out by the author was twofold. In the first instance, since MALDI had not previously been performed in the research group at Glasgow, a thorough investigation into the process was undertaken in order to build a core of knowledge. This work included a study of different sample preparation techniques, ablation laser power dependencies, and the characteristics of the ejected material plume produced by laser ablation using techniques already well established in the Laser Ionisation Studies (LIS) group at Glasgow (Towrie 1990, McCombes 1991, Borthwick 1992). It was hoped that this work, which is detailed in Chapters 4 to 6, would provide a better understanding of the processes involved in MALDI.

For some years now, there has been considerable interest amongst the scientific community in novel techniques which can be used for structural analysis, or can provide sequence specific information on biologically important molecules, without the use of wet chemistry. Most direct sequencing of biological molecules (peptides, proteins, oligonucloetides & DNA etc.) is still done by some form of derivitisation technique, such as Edman degradation, followed by identification of the residue by high performance liquid chromatography (HPLC), or electrophoresis (Fitzgerald 1996). This is a lengthy process, which currently takes one to two hours to identify only 500 base pairs, using capillary electrophoresis. Although this is a considerable improvement over the situation a few years ago, where a maximum of approximately 50 base pairs could be identified in one day (Chait 1993), this is still slow when for example, compared to the number of nucleotide base pairs in the human genome (3×10^9).

MALDI is the newest addition to the range of mass spectrometric techniques (Biemann 1987) from which sequence specific information can be obtained, the appeal of which is that samples can be analysed in seconds, rather than hours or days. Sequence specific information using MALDI has been obtained up to now using either chemical degradation followed by standard MALDI analysis (Chait 1993, Fitzgerald 1993b, Pappin 1993), or through analysis of the molecular fragmentation products, produced following MALDI (Kaufmann 1993, Kaufmann 1994, Patterson 1994, Lee 1995).

The initial work by the author on characterisation of MALDI laid the groundwork for the development of tandem time-of-flight mass spectrometry (TOF/TOF) of labile organic molecules, using MALDI as the ion source. A second pulsed laser was to be used at the turn around point of the reflectron mass spectrometer to allow photofragmentation of selected molecular ions. The overall aim of the work was to develop the technique to the stage where it could be used routinely, to allow future investigations into whether a) sequence specific information can be obtained, and b) selectivity of the bond cleavage site is possible, using tuneable lasers. Initial results of the work on TOF/TOF and prospects for future research are described in Chapter 8.

1.3 Brief History of MALDI

As mentioned previously, until the advent of MALDI, laser mass analysis of biomolecules was limited to compounds of less than approximately 1000 to 1500 amu. The problem was essentially how to produce intact gas phase ions from organic molecules which have negligible vapour pressure regardless of temperature. The breakthrough with MALDI came almost entirely due to the novel method of sample preparation.

Work by Karas and Hillenkamp (Karas 1985) on UV laser ablation of small organic molecules showed that the optimum conditions for "soft" ablation were obtained if the molecule showed strong resonant absorption at the ablation laser wavelength. This led the group to analyse mixtures of strongly absorbing compounds with poor absorbers, in the hope that

absorption of the laser light by the strong absorber would lead to ablation of a volume of material containing both species, with an enhanced molecular ion yield of the non absorbing molecules. This was found to be the case and the first reference to the term "Matrix-Assisted" Laser Desorption was made (Karas 1985), the "matrix" being the strongly absorbing host molecule.

The full potential of MALDI was not realised until it was discovered that one particular matrix, nicotinic acid (Karas 1988), had special properties for large peptides and proteins. Almost simultaneously, an alternative technique for producing gas phase ions of large proteins was developed by Tanaka (Tanaka 1988), who used a metal powder/glycerol matrix. The metal powder provided the coupling between the UV laser light and the glycerol, which is transparent at the wavelength used (266 nm).

The sample preparation method of Karas and Hillenkamp soon became the method of choice after it became apparent that it provided far superior sensitivity (a factor of 10^3 or greater) compared to the method outlined by Tanaka (Beavis 1992b). Many reviews of the initial discovery, progression and fundamentals of the technique have been published in the literature (Karas 1990, Karas 1991, Vertes 1991, Beavis 1992b). MALDI has progressed rapidly since its beginnings in the late eighties and is now a standard analytical technique in biotechnology and biomolecular analysis (Kaufmann 1995, Stults 1995, Burlingame 1996, Mann 1996).

1.4 Fundamentals of MALDI

MALDI is essentially a very simple technique, both in principle and practice. Two solutions are made up with compatible solvents; one a strong solution of a small organic molecule (the matrix), the other a weak solution of the biomolecule of interest (the analyte). Small amounts of the two solutions are then mixed together, and an aliquot of the resulting solution is deposited onto a sample mount and dried. When the sample has fully dried, a crystalline deposit is left on the sample mount, the exact form of which depends on the matrix used. The sample mount is transferred to a mass spectrometer, and a pulsed laser, usually

ultraviolet (UV), is then focused onto these crystals. Above a certain ablation laser fluence threshold, ions of both the matrix and analyte are ejected into the gas phase from where they can be analysed (Fig.1.1).

The rest of this section gives a more detailed description of;

i) the role of the matrix,
ii) sample preparation,
iii) general characteristics of the technique, and
iv) useful matrices.

1.4.1 Role of The Matrix

It is generally accepted that the matrix is responsible for, or involved in, at least three fundamental and separate processes (Hillenkamp 1991, Karas 1991, Levis 1994).

i) The matrix acts as a solid state solvent for the analyte molecules, which are actually somehow incorporated into the lattice structure of the matrix crystals. Experiments have been performed which conclusively demonstrate this (Strupat 1991, Beavis 1993, Karas 1993) and which also found that the molar ratio of analyte to matrix in the sample crystals was the same as that in the original solution. In addition, studies of persistent contaminants found in extracts from plant leaves showed that DHB and the cinnamic acid derivatives strongly bind to the protein fractions, which is exactly the property required by a good matrix material if analyte molecules are to be successfully incorporated into the matrix crystals (Beavis 1993).

Since the analyte molecules are relatively dilute in the liquid sample solution, they are completely separated (or solvated) within the matrix crystals (Fig.1.1a). It is generally believed that this level of mixing is essential for a successful matrix/analyte combination (Strupat 1991), although it has been suggested that this may not strictly be necessary (Doktycz 1991) for smaller analyte molecules. The solvation of analyte molecules within matrix crystals has the added benefit that a certain

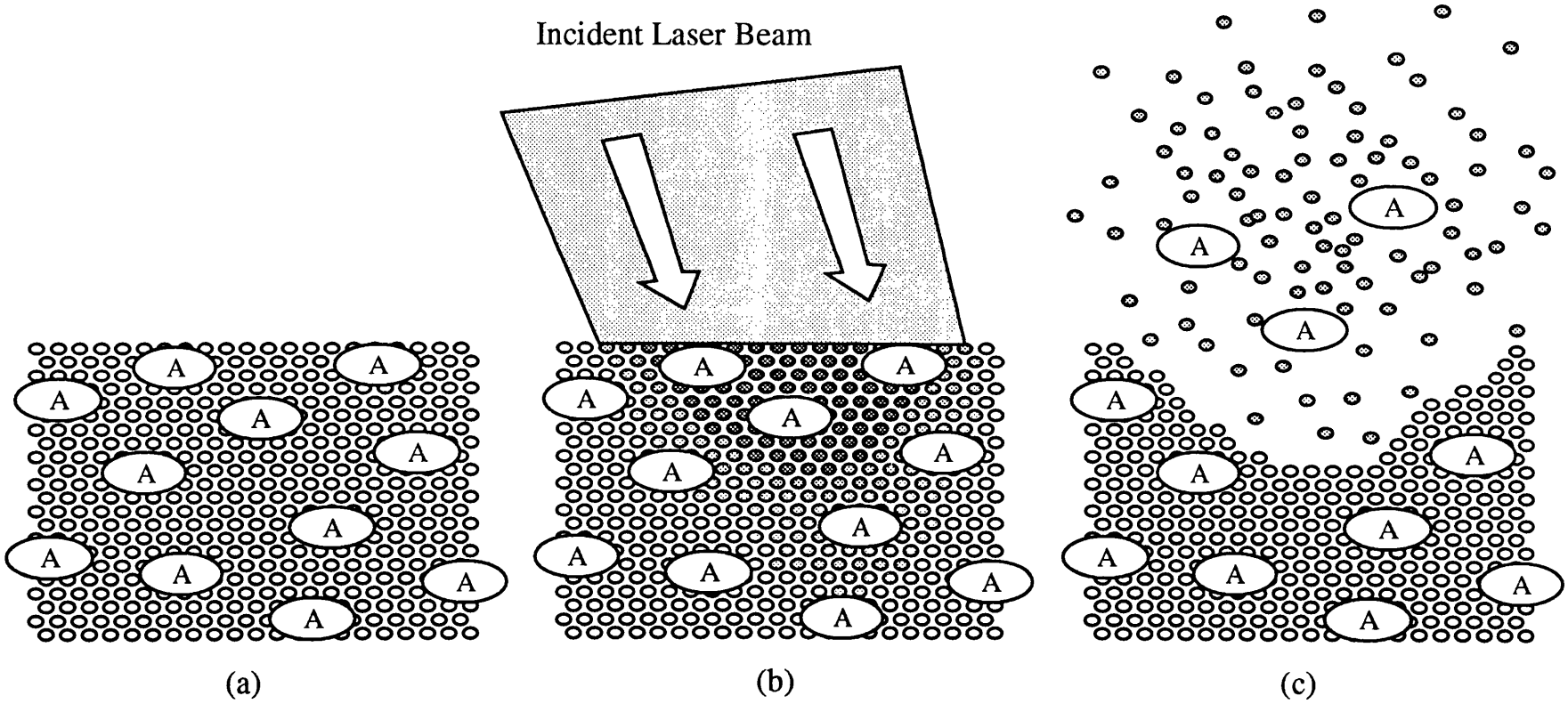

Fig.1.1 (a) The Analyte molecules A are incorporated into the matrix crystal lattice and completely solvated by the matrix molecules. (b) Resonant absorption of an incident laser beam by the matrix molecules, with minimal absorption by the analyte. (c) Ablation of a volume of the sample resulting in ejection of excited matrix species and intact, relatively cold analyte molecules. NB This diagram does not imply that ablation occurs after the cessation of the laser beam, but is merely depicted this way for clarity of presentation.

degree of sample purification occurs, as typical contaminants are excluded, and are left as a residue outwith the crystals.

ii) The matrix is responsible for coupling the laser energy into the solid state. The matrix molecule should show strong absorption at the wavelength of the ablation laser, while the analyte should ideally have poor absorption at this wavelength to keep the internal energy of analyte molecules to a minimum (Fig.1.1b). Absorption at ablation fluences above the threshold fluence for ablation in a good matrix material (strong absorber), is thought to still follow the Beer-Lambert law (Eqn.2.8) resulting in controllable energy deposition. In a poor absorber the energy deposition process above the threshold fluence for ablation is highly non-linear and difficult to control (Kaufmann 1995). Energy transfer to matrix molecules occurs via resonant absorption of the laser light, either through coupling with electronic states in the case of UV MALDI, or through ro-vibrational states for IR MALDI. Most of the UV matrices have the UV absorbing chromophore in the form of a cyclic pi structure, but this is not essential and matrices without this structure can still produce strong protein ion signals (Beavis 1989a)

iii) The most contentious issue in the discussion of the mechanisms involved in MALDI, is the role that the matrix plays in the analyte ion formation process. It is generally believed that the matrix must play an active role in ion formation, but suggestions as to what this role is have ranged from photoionisation or photochemistry (Ehring 1992), to proton transfer reactions from radical matrix species (Gimon 1992), to the ejection of pre-formed ions from the solid, following chemical reactions in solution during sample preparation (Zhu 1995). Ionisation processes are discussed in more detail in Chapter 2, section 2.4.

1.4.2 Sample Preparation

Samples can be prepared and analysed in a few minutes, in marked contrast to the lengthy preparation and analysis required for chromatography or electrophoresis (Chait 1992). Most solid phase

matrices are prepared according to a recipe which is based on the following typical method.

A solution of the chosen matrix is prepared in a suitable solvent or solvent mixture at a concentration of typically 10-50mMl^{-1} (Beavis 1989b). A solution of the compound of interest (the analyte) is also made using the same, or a similar solvent mixture to a concentration of typically 1 to 10μMl^{-1}. The concentration of this will vary depending on the solubility and the quantity of the compounds used in the analysis. Typical solvent mixtures tend to be water based since the majority of compounds analysed are biomolecules. The solubility of protein samples can be enhanced by adding small amounts of trifluoroacetic acid (TFA). Small volumes of these solutions are combined to achieve the required molar ratio of matrix to analyte (M/A) in the final sample solution. The optimum M/A ratio varies depending on matrix and analyte used, but is typically between 1:1000 and 1:10000 (Kaufmann 1995, Karas 1991). Although molar ratio will be used throughout this thesis, the relative concentration between matrix and analyte is sometimes given in terms of a mass ratio (Karas 1991) since this gives an immediate indication of the relative volumes occupied by the matrix and analyte in the final sample crystals.

In the standard dried droplet MALDI sample preparation, a small drop of the sample solution is applied to a flat metal sample stub and introduced to a stream of warm air or compressed nitrogen, or left in the ambient atmosphere in order to evaporate the solvent. This leaves the sample in the form of a deposit on the stub, consisting of matrix crystals containing embedded analyte molecules, and a residue of impurities from the original sample solution and some analyte molecules. The majority of matrices crystallise from the rim of the drop of sample solution, the crystal needles growing towards the centre of the preparation (Strupat 1991), although sinapinic and nicotinic acid form small crystallites evenly distributed over the full area of the sample drop (Doktycz 1991, Beavis 1993). All matrix sample deposits are heterogeneous when viewed through an optical microscope.

It is generally observed that the presence of organic or inorganic contaminants in the initial sample solution does not interfere with

MALDI, provided that matrix crystal growth is not impaired (Hillenkamp 1991, Strupat 1991). This means that typical salts and buffers used in biochemical procedures do not have to be removed from the sample solution prior to analysis, and also makes MALDI an ideal choice for the analysis of complex or crude biological mixtures (Mock 1992). However, some compounds have been found to inhibit MALDI the most potent of which is sodium azide, frequently used in biological samples as a preservative. This compound does not inhibit matrix crystallisation, but is thought instead to interfere with the analyte ionisation process.

Considerable effort has gone into developing novel sample preparation techniques in order to; a) improve shot to shot reproducibility and more quantitative analyses by producing more homogeneous samples (Vorm 1994a & b, Gusev 1995, Perera 1995), b) increase tolerance to contaminants (Mock 1992, Bai 1994, Xiang 1994), c) couple MALDI with liquid chromatography using liquid matrices such as 3-NBA (Murray 1993), and d) couple MALDI with standard separation techniques such as SDS-PAGE, through the direct desorption of biomolecules from transfer membranes (Kaufmann 1995, Blackledge 1995)

The production of more homogeneous samples will undoubtedly offer both improved reproducibility and quantitivity, but may not always be beneficial depending on the analysis required (Kaufmann 1995). One of the qualities of a good matrix is that it isolates analyte molecules within the matrix crystal lattice, and separates them from sample contaminants. The production of relatively homogeneous samples will mean that contaminants, matrix and analyte are present in the same area of irradiated sample, and may lead to problems with adduct formation or reductions in sensitivity. This is discussed in more detail in Chapter 4.

1.4.3 General Characteristics of The Technique

MALDI is characterised by a highly non-linear behaviour of the laser induced ion signal (Fig.1.2) as a function of ablation fluence (the total deposited energy density on the surface, usually expressed in $mJcm^{-2}$).

As mentioned previously, a threshold type behaviour is apparent in both the ion and neutral production from the sample. No ions are produced below a particular value of the ablation laser fluence. Above this fluence value ion production increases rapidly, reaching a plateau which slowly rises or falls depending on the type of ion. A similar behaviour is observed with neutral production from the sample (Huth-Fehre 1991, Dreisewerd 1995) although this occurs at a lower fluence value, and the rise in ion yield above threshold is not as steep. This type of behaviour is observed for both positive and negative ions, and both solid and liquid matrices (Yau 1993). Initially it was thought that the threshold occurred at a particular laser irradiance (the incident power density on the surface, usually expressed in Wcm^{-2}), but experiments with femtosecond pulses have swung the argument in favour of a fluence threshold (Demirev 1992, Beavis 1992c).

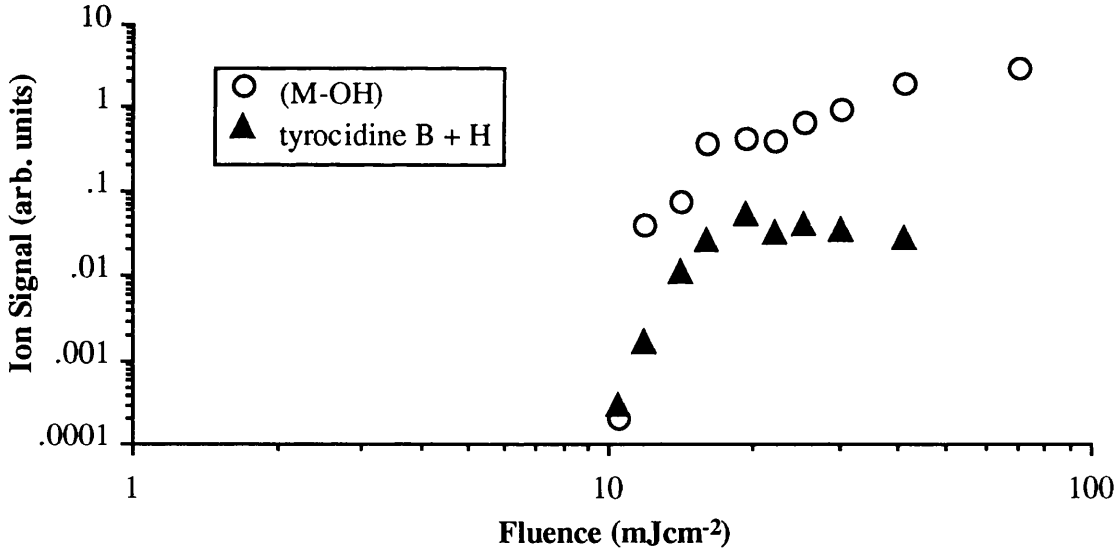

Fig.1.2 Typical MALDI fluence dependence obtained by the author (see Chapter 4). Vacuum dried sample of tyrothricin in DHB ablated with 300 ps nitrogen laser. M represents the matrix parent molecular ion.

The strongest ion signals are usually obtained from the crystals which form at the edge of the sample drop, but this is matrix dependent and nicotinic and sinapinic acid give good ion signals from the full area of the sample. A typical MALDI mass spectrum is shown in Fig.1.3. Matrix specific ions are confined to the low mass regions of the spectrum and

usually consist of the monomer, dimer or quasi-molecular ions (monomer ion minus; -OH, $-OH_2$, $-CO_2$ or $-CO_2H$). It is thought that analyte fragmentation is minimised partly by the use of relatively short pulse duration lasers in ablation, which results in a short timescale for energy transfer from the matrix to the analyte. Analyte ions typically show no fragmentation originating from cleavage of covalent bonds in the biomolecular backbone, at least not in standard linear and reflectron TOF mass spectrometric analyses, although a small fraction of the analyte ion signal may appear in the form of fragment ions due to the loss of small molecules such as H_2O or NH_3. However, more complicated reflectron TOF analysis techniques show that considerable fragmentation of analyte ions is apparent on a timescale 100's of microseconds to milliseconds, due to the low unimolecular decomposition rates for molecules with a large number of degrees of freedom (Fountain 1994). This is known as postsource decay (PSD) since the majority of fragmentation occurs in the field free region of the spectrometer (Spengler 1991, Spengler 1992, Kaufmann 1994) and typically results in somewhat decreased mass resolution due to 'tailing' on the low mass side of the analyte ion peak, although this is only significant for relatively large molecules.

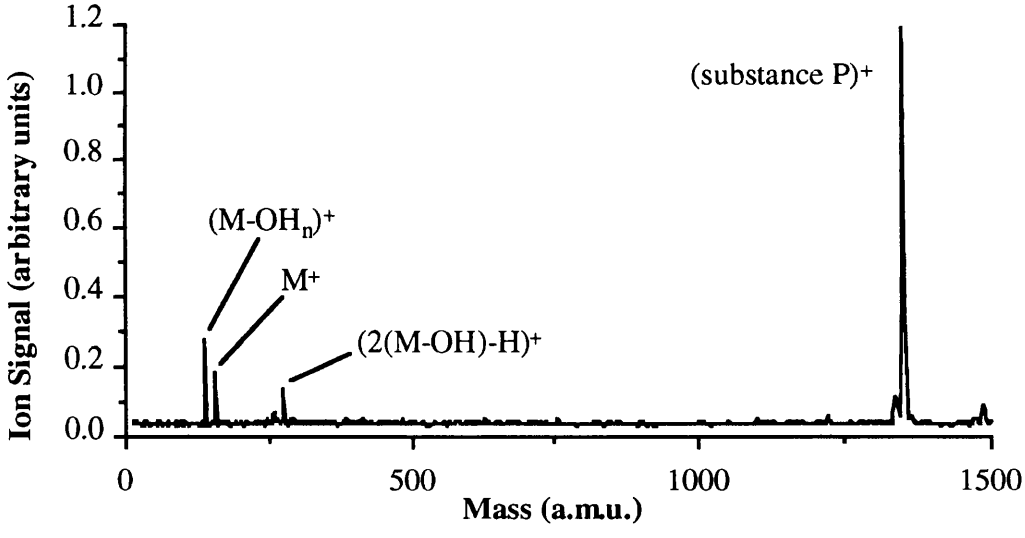

Fig.1.3 MALDI mass spectrum of substance P in DHB (M/A = 440). Sum of 200 shots with a 300 ps nitrogen laser from the crystals formed around a standard sample preparation. M represents the matrix parent molecular ion (mass 154 Da).

The main analyte ion signal appears in either the protonated (peptides and proteins), cationated (oligosaccharides) or deprotonated form (oligonucleotides), or as a matrix adduct depending on both the chosen matrix and the type of biomolecule under investigation (Karas 1990). The analyte ions formed are predominantly singly charged (M_A^+), although multiply charged ions M_A^{n+} and cluster ions nM_A^+ are also apparent in mass spectra, with ion signal intensities decreasing as a function of n.

The spectrum shown in Fig.1.3 is of the low mass peptide substance P (mass of the protonated monoisotopic molecular ion 1347.7 amu.) prepared in the matrix DHB at a molar ratio of M/A = 450 (see Chapter 4). It is immediately obvious that despite the large molar excess of the matrix, the protonated analyte ion peak is an order of magnitude larger than the matrix related ion peaks. In fact it has been shown for most matrices that by judicious choice of the sample molar ratio and the irradiating fluence, the low mass matrix peaks can be virtually eliminated (Dominic Chan 1991, Beavis 1992a, Juhasz 1993b).

The sensitivities which can be achieved using MALDI are comparable and in some cases better than that achievable using chromatography or electrophoresis, although this is very compound dependent. Useful ion signals are easily and routinely achieved with a total sample loading of a few picomoles of analyte, only a small fraction of which is used in the analysis. To the authors knowledge the highest sensitivity reported using MALDI (Jespersen 1994) is that of a single shot detection limit of 250 zeptomole in the analysis of a sample containing a total of 2.5 attomole of human bradykinin. In other words the total number of analyte molecules contained in the ablated sample volume at the detection limit was approximately 1.5×10^5.

The highest resolution spectra are obtained at laser fluences just above the threshold fluence for ion production, with a rapid decrease in resolution occurring as the laser fluence is increased significantly above threshold (Perera 1994). It has been suggested that this may be due to charge shielding effects in the higher density plume, or to an increase in the temporal or energy distributions of the initial ion packet (see Chapter 2).

Although mass resolutions in MALDI spectra of up to 12000 have been reported for small peptides (approximately 1000 amu), these have been achieved using ion traps or fourier transform mass spectrometry (Doroshenko 1993). The achievable mass resolution to date using TOF instrumentation and standard techniques has been disappointing. Although typical mass resolutions of 500 for linear instruments and 2000 for reflectrons can be obtained in the mass range below 10000 amu (Kaufmann 1995), the resolution is degraded for masses greater than 20000 amu due to effects in the ion formation process. However, new delayed ion extraction techniques are now resulting in significantly improved resolution and mass accuracy (Colby 1994, Vestal 1995, Stults 1995).

1.4.4 Useful Matrices

Although a large number of different materials have been tested to investigate their suitability as matrices for MALDI (Ehring 1992, Beavis 1992b, Fitzgerald 1993a), only a small number of compounds have been found to be practically useful. This is perhaps not surprising when it is considered that a successful matrix must satisfy not only the requirements listed in Section.1.4.1, but also must have the ability to co-dissolve with the analyte in a common solvent, should not be too volatile, and should not be chemically reactive with the analyte. A chronological list of matrix discovery since 1988 and the types of analyte investigated with each matrix is given in table.1.1. The information in this table is not exhaustive, and due to the still expanding interest into MALDI and the wealth of related publications, it is inevitable that some matrices have not been included. However, the main matrices in use today are included in the table, the most important and heavily used of which are (Vertes 1993b, Perera 1994, Juhasz 1993a):

Solid phase

i) The cinnamic acid derivatives (sinapinic, ferulic and caffeic)
ii) DHB
iii) 4-HCCA

Principle Author	Year	Common Name	Chemical Name	Analyte Suitability
Karas	1988	Nicotinic Acid	3-pyridinecarboxylic Acid	Peptides and proteins.
Beavis	1989a	Vanillic Acid	4-hydroxy-3-methoxybenzoic Acid	Peptides and proteins.
		Pyrazinoic Acid	2-pyrazinecarboxylic Acid	
		Thymine		
		Thiourea		
Beavis	1989b	Sinapinic Acid	3,5-dimethoxy-4-hydroxycinnamic Acid	Peptides, proteins and oligosaccharides.
		Ferulic Acid	4-hydroxy-3-methoxycinnamic Acid	Peptides and proteins.
		Caffeic Acid	3,4-dihydroxycinnamic Acid	Peptides and proteins.
Overberg[1]	1990	Malic Acid		Proteins.
		Malonic Acid		
		Succinic Acid		
		Urea		
		Glycerol[2]		
			Triethanolamine[2]	
		Lactic Acid[2]		
Strupat	1991	Gentisic Acid (DHB)	2,5-dihydroxybenzoic Acid	Peptides, proteins, synthetic polymers, glycolipids, oligosaccharides (linear and nonlinear), glycoconjugates[4].
Strobel	1991	3-NBA[2]	3-nitrobenzyl Alcohol	Peptides and proteins.
Zhao	1991			
Gimon	1992		4-nitroaniline	Peptides.
			2,4-dinitroaniline	
			α-naphthylamine	Small peptides.
Beavis	1992a	α-CHCA or 4HCCA[3]	α-cyano-4-hydroxy-*trans*-cinnamic Acid	Low mass peptides & glycopeptides[5]

Table 1.1 Discovery of MALDI matrices since 1988. This list is not meant to be exhaustive. It is merely an indication of the range of matrices available and the types of biomolecule which have been investigated since the discovery of MALDI.

Tang	1992	Rhodamine B		Proteins and small oligonucloetides (to 15 bases).
		Rhodamine 6G		Proteins and small oligonucloetides (to 11 bases).
Bahr	1992		Nitrophenyloctylether[2]	Synthetic polymers (polystyrene).
Fitzgerald	1993a		2-amino-4-methyl-5-nitropyridine[6]	Oligonucleotides (to 20 bases)
			2-amino-5-nitropyridine[6]	Peptides
Juhasz	1993a	HABA	2-(4-hydroxyphenylazo)-benzoic Acid	Peptides, proteins, glycoproteins, glycolipids and synthetic polymers[7]
Juhasz	1993b		9-nitroanthracene	Oligoferrocenes.
		Dithranol		
		Quinizarin		
Danis	1993	IAA	trans-3-indoleacrylic Acid	Synthetic polymers.
Kuang Jen Wu	1993	3-HPA	3-hydroxypicolinic Acid	Peptides, proteins and large oligonucleotides (to 67 bases).
Perera	1994	Coumarin 2, 47, 120 & 152		Proteins, fullerenes, synthetic polymers and oligonucleotides.
Tang	1994	Picolinic Acid	2-pyridinecarboxylic Acid	Large oligonucleotides (to 190 bases).
Taranenko	1994	3-APA	3-aminopicolinic Acid	Proteins and large oligonucleotides (to 246 bases).
George	1994	PCC	4-phenyl-α-cyanocinnamic Acid	Polycyclic aromatic hydrocarbons (PAH), and PAH modified DNA bases.
		BCC	4-benzyloxy-α-cyanocinnamic Acid	PAH modified DNA bases.
Harvey	1994		1,4-dihydroxynapthalene-2-carboxylic Acid	Oligo- and polysaccharides (NB DHB performed better than this matrix in a comparison study).
Metzger	1994		3-aminoquinoline	Polysaccharides and proteins (this matrix performed better than DHB for certain oligosaccharides).
Lecchi	1995		6-aza-a-thiothymine	Oligonucleotides.

(1) Infrared MALDI. Many existing UV MALDI matrices were also succesful.
(2) Liquid matrices.
(3) In a study of low molecular weight compounds, 4-HCCA generally proved more versatile than DHB (Lidgard 1995).
(4) See also Ehring 1992, Danis 1993, Karas 1993, Perera 1994 and Montaudo 1994a.
(5) High degree of multiple protonation. Up to charge state 9+ observed (Beavis 1992).
(6) Basic matrices for acid labile molecules.
(7) See also Montaudo 1994 and Danis 1993.

iv) HABA & 3-HPA

Liquid phase

v) 3-NBA

vi) Glycerol (IR ablation)

The structure and molecular mass of these matrices is shown in Fig.1.4.

Many papers have been published containing statements on the relative merits of one matrix compound over another. These should only be used as a rough indication of the applicability of a matrix for a particular analyte, as the data underlying these statements is usually not obtained under very rigorous or standardised conditions, and often only reflects the particular sample preparation methods used by the researcher. Some general characteristics of the more commonly used matrices are now discussed.

Despite the fact that nicotinic acid was the first successful matrix compound identified, and that a number of other matrix compounds have since been discovered, nicotinic acid is still in use today for very large molecules (M_r > 100 kDa) (Kaufmann 1995). However, nicotinic acid has a number of drawbacks as follows: A significant fraction of the analyte ion signal can be present as a matrix adduct (Beavis 1989a). This is a considerable problem for high masses where the resolution of the spectrometer is insufficient to separate the two peaks, resulting in reduced mass accuracy; Due to the absorption spectrum of nicotinic acid, ablation must be performed at relatively short wavelength UV (typically 266 nm) which is resonant with electronic absorption bands in most biomolecules, and will lead to an increased analyte internal energy and probability of fragmentation; If even small quantities of most typical contaminants found in biological solutions are present in the initial sample solution, then useful mass spectra cannot be obtained using nicotinic acid as the matrix (Beavis 1993).

DHB and the cinnamic acid derivatives were a marked improvement on nicotinic acid. These matrices produce far less adduct ions, exhibit less analyte selectivity than nicotinic acid (Beavis 1989b, Hillenkamp 1991), a

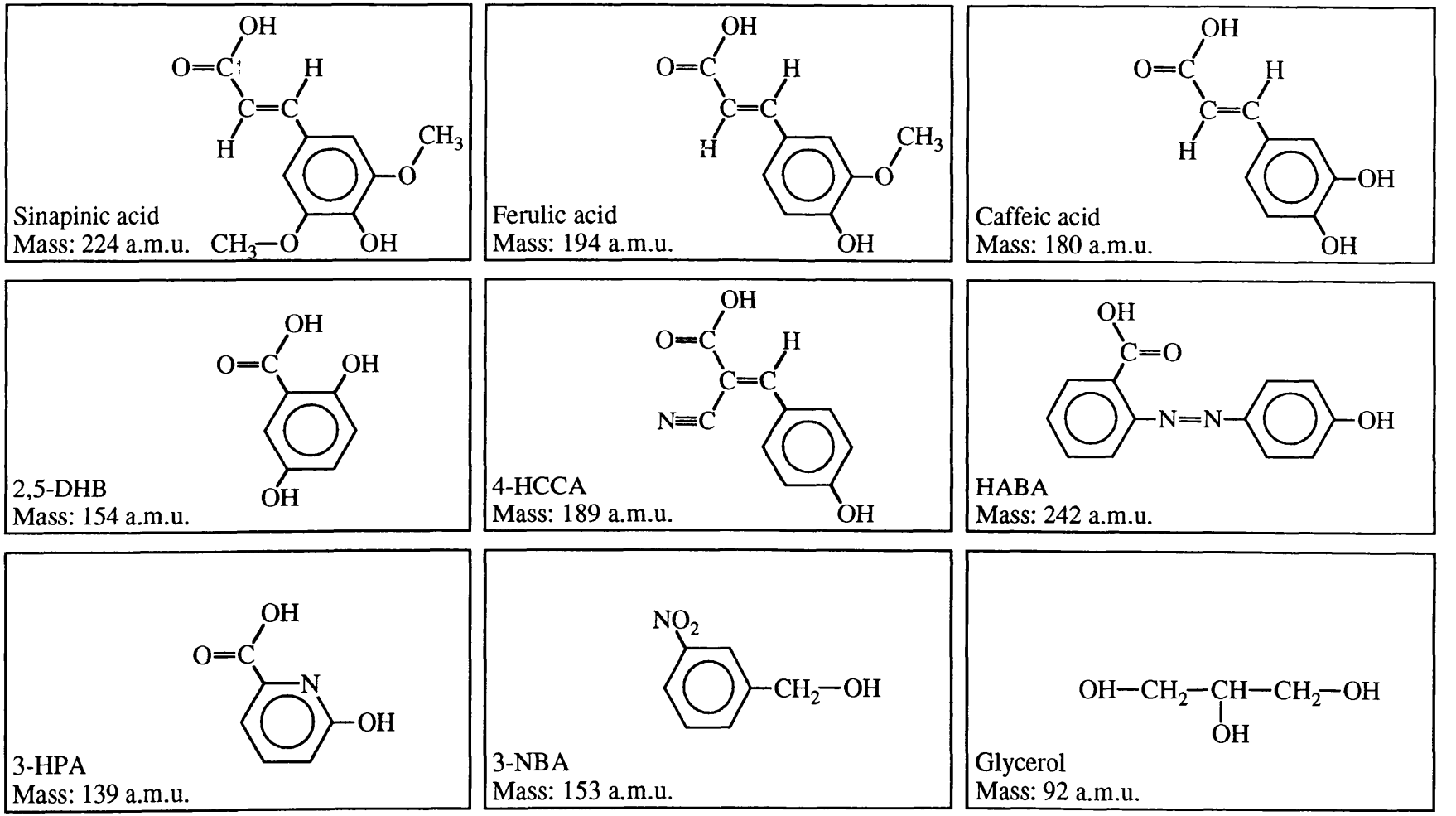

Fig.1.4 Structure and molecular masses of the most commonly used matrix compounds.

problem in the attempt to obtain quantitative analysis, and can be used at longer wavelengths (i.e. 355 and 337 nm) where most analytes have negligible absorption. The ability to ablate at 337 nm made the technique of MALDI much more accessible due the widespread availability of relatively cheap nitrogen lasers. DHB tends to be used for proteins below 20 kDa with sinapinic acid used for larger proteins, since DHB shows a poor signal to noise ratio for larger molecules (Karas 1993).

A number of matrices have been developed to cater for classes of biomolecule such as synthetic polymers (Danis 1993, Montaudo 1994) and nucleic acids which have proven difficult to analyse using conventional matrices. Nucleic acids are not amenable to analysis with standard matrices since the majority developed to date are acidic, while nucleic acids are acid sensitive. Several basic matrices have been developed which extend the utility of MALDI to acid sensitive species (Fitzgerald 1993a).

The main motivation behind the development of useful liquid phase MALDI matrices stems from the interest in improving the interface between liquid and gas phase separation techniques such as Liquid Chromatography / Mass Spectrometry (LC/MS). Several real time continuous flow sample introduction systems have been developed (Murray 1993, Kaufmann 1995). However, although liquid phase matrices offer some advantages over solid in terms of superior shot-to-shot reproducibility and ion signal stability, they also show significantly reduced resolution and sensitivity (Juhasz 1993a).

Some work has been carried out using two-component matrices or co-matrices, where, in an attempt to optimise each aspect of the matrix role, a number of different compounds are mixed together to form the matrix (Cornett 1992a, Karas 1993, Taranenko 1995). The work of Karas et al (Karas 1993) involved mixing other benzoic acid derivatives with DHB, and resulted in enhanced spectra and an increased mass range over that normally accessible using DHB alone. It is thought that the lattice energy of the composite crystal is reduced from that of a pure DHB crystal due to reduced hydrogen bonding (with suitable choice of additive).

The exact qualities that determine whether a material will make a good matrix are still obscure. It is well known that closely related compounds such as 2,4-dihydroxybenzoic acid and 2,5-dihydroxybenzoic acid, 3-hydroxycinnamic acid and 4-hydroxycinnamic acid, or 3-pyridinecarboxylic acid and 4-pyridinecarboxylic acid have very different matrix characteristics although their solubilities, absorption characteristics and chemical properties are similar (Beavis 1989a, Beavis 1992b, Perera 1994). This may well be related to either the ability of a compound to incorporate analyte molecules within its crystal lattice, or the role the matrix molecules are required to play in the analyte ionisation process.

Chapter Two

Theory

2.1 Mass Spectrometry

A variety of different types of mass spectrometry (MS) have been used in conjunction with MALDI; quadrupole MS (Doroshenko 1993, Jonscher 1993), Fourier Transform MS (McIver 1994, Solouki 1994), linear & reflectron TOF-MS (Karas 1991, Cornish 1993, Beavis 1989a, Scott 1994) and also a number of hybrid instruments combining different techniques (Fountain 1994, Lee 1995). However, since pulsed lasers induce the ionisation event in MALDI, TOF instruments are ideally suited as they allow acquisition of a complete mass spectrum from each laser shot and are by far the most common type of mass spectrometer used. The other techniques mentioned above require some instrumental parameter to be scanned in order to build up a complete mass spectrum, and tend to be more complex and costly than TOF-MS. For this reason TOF-MS was used exclusively by the author and is described in detail in the following sections.

2.1.1 Time of Flight Mass Spectrometry

This type of mass spectrometry operates on the following simple principle; a packet of ions, with differing mass to charge ratios (m/z) but with equal energies, when projected into a region of uniform electric potential will separate according to their m/z ratios. Since the types of ion sources used in mass spectrometry predominantly produce singly charged ions (z is unity) the separation of ions is essentially by mass alone.

A linear time-of-flight (TOF) mass spectrometer in its simplest form is shown in Fig.2.1. The source region of the spectrometer consists of a backing plate and an extraction grid. A potential (U) is applied to the backing plate creating a static electric field across the source region.

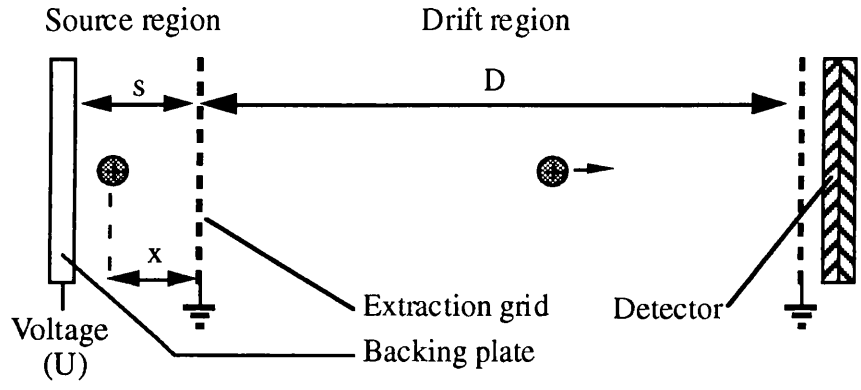

Fig.2.1 Schematic diagram of a linear time-of-flight (TOF) mass spectrometer.

Ions created in the source region at a distance x from the extraction grid are accelerated into the drift region with velocity

$$v = \left[\frac{2qU}{m}\right]^{\frac{1}{2}}\left[\frac{x}{s}\right]^{\frac{1}{2}} \qquad \text{Eqn.2.1}$$

where m = ion mass and q = ion charge. The ions then travel along the drift region and, assuming a drift length D much larger than the ion source dimension s, arrive at the ion detector after a time of approximately:

$$t = D\left[\frac{2qU}{m}\right]^{-\frac{1}{2}}\left[\frac{s}{x}\right]^{\frac{1}{2}} \qquad \text{Eqn.2.2}$$

The mass of each ion can easily be calculated by rearranging Eqn.2.2. In practice however, the masses of ions are not calculated in this way. The mass spectrometer is calibrated by measuring the flight times of at least two known masses and, assuming singly charged ions, determining the constants a and b in the empirical equation:

$$\sqrt{m} = at + b \qquad \text{Eqn.2.3}$$

Each mass spectrum is calibrated internally in this manner, since the ion flight times are not completely constant due to variations in source conditions. It should be noted that in MALDI the initial energies of

desorbed species tend to be somewhat mass dependant, the velocity of the desorbed analyte species being comparable to that of the matrix (Dominic Chan 1994, Beavis 1991). In a linear TOF this will lead to under-estimation of the analyte mass if lighter species (either matrix molecules or an added calibrant molecule) are used to provide mass calibration for the spectrum. In a reflectron instrument, as used by the author, this effect will not be as significant due to energy focusing (see section 2.1.3).

2.1.2 Mass Resolution

Not all of the ions within each separated packet (same m/z) arrive at the detector at the same time, but are spread out over a time interval Δt (usually the Full Width at Half Maximum (FWHM) of the ion signal pulse height) around the arrival time t. The temporal resolution of the system is defined as $t/\Delta t$. An important parameter in any mass spectrometer is the mass resolution. This determines the upper limit of the mass range over which two ions differing in mass by a single mass unit can be resolved as distinct ion peaks. The relation between the mass and temporal resolution of a TOF mass spectrometer is obtained by differentiating Eqn.2.2 and rearranging to give:

$$\frac{m}{\Delta m} = \frac{1}{2}\frac{t}{\Delta t} \qquad \text{Eqn.2.4}$$

The achievable mass resolution in a TOF mass spectrometer is limited by instrument design and by the parameters of the ion packet produced in the source region. In the ablation work performed by the author the limitations on mass resolution are caused by the source parameters, the effects of which are far in excess of any instrument design limitations of the detector, mass spectrometer and signal recording technology. The most important ion source parameters affecting resolution are;

i) The time interval for ion formation.
ii) The spatial extent of ion formation.
iii) The initial energy spread of ions.
iv) Space charge effects.

v) Metastable fragmentation.

Of the five parameters listed, only the first three will be discussed in this section. The ablation powers used by the author were well below those required to generate a high charge density in the ablated plume of material (Vertes 1993b), and consequently space charge effects are not expected to contribute significantly to the overall resolution.

The temporal distribution of ions (parameter one) is usually due to the finite duration of the ionisation pulse. This adds a constant time interval (Δt) to the width of the ion signals. If temporal distribution is the limiting factor in the overall mass resolution, then the mass resolution will increase with increasing mass, as Δt will remain constant while t increases with mass. In MALDI, ionisation is achieved using a short pulse duration laser, typically a few ns or less, which would be expected to minimise this effect.

The initial spatial distribution of ions (parameter two) within the source region partially determines the kinetic energy of each ion in the drift region. Ions formed near to the backing plate (Fig.2.1) have greater potential energy than those of the same mass formed closer to the extraction grid, and are consequently ejected into the field free region with greater velocity. This distribution of velocities translates into a spread of arrival times at the detector, degrading the resolution. However, ions formed close to the backing plate will take longer to reach the drift region than those formed near the extraction grid. This counteracts the reduction in flight time within the drift region, and it is possible to adjust the extraction potentials such that a space focus is created at which ions of any given mass arrive at the same time, independent of initial position within the source region. More flexibility in the position of the space focus, and the strength of the extraction fields, can be achieved by using a two stage extraction field (Wiley and McLaren 1955), rather than the simple one stage shown in Fig.2.1. In MALDI the finite width of the ionising laser beam does not significantly contribute to this effect since ionisation is achieved through desorption from an equipotential surface.

However, uncertainties in the initial time and position of ion formation still exist due to the possibility of ion formation above the surface after the initial laser pulse. This is particularly relevant to MALDI where analyte ion formation is thought to occur by secondary reactions in the gas phase.

The initial kinetic energy distribution of ions (parameter three) again leads to a distribution of velocities within the drift region, and a spread of arrival times at the detector. However, this effect is the most difficult to correct in linear TOF mass spectrometers. This can be corrected in linear instruments by using a delayed extraction pulse (Wiley and McLaren 1955) but this method requires a large number of ionisation events to generate one well resolved spectrum and is not well suited to present day instrumentation.

The simplest means of correcting for an initial kinetic energy distribution is to use some type of energy focusing device. The system used by the author incorporated a reflectron to achieve this.

2.1.3 Reflectron TOF Mass Spectrometer

In a reflectron time-of-flight mass spectrometer, an electrostatic ion mirror (Mamyrin 1973) is used at the far end of the flight tube (Fig.2.2). This serves two fundamental purposes which both increase the achievable resolution: The ion flight path is approximately doubled, increasing the ion flight time and consequently reducing the effect of the initial temporal distribution on the resolution; Secondly, and most importantly, it compensates for any ion kinetic energy distributions (energy focusing). The basic principle of operation which produces energy focusing is as follows. For more detailed calculations see Appendix A.

Consider ions I_1 & I_2 produced in the source region of the spectrometer, but with different initial energies ($E_1 < E_2$). I_2 will spend less time in the drift region than I_1 due to its higher drift velocity. However, because I_2 has higher energy than I_1, it will penetrate further into the reflectron and hence spend more time in the reflectron than I_1. With the correct choice of system parameters, these time differences can be made to cancel (to

first or second order) allowing ions in an ion packet with a range of energies (E +/- ΔE) to arrive at the detector simultaneously. The resolution obtainable for an ideal ion source, producing ions with only an initial kinetic energy distribution, can be calculated theoretically (Eqn.A.11). Substituting the dimensions and operating parameters of the Glasgow reflectron TOF-MS (see Chapter 3.1 for description) into this equation gives

$$R_u \approx \frac{26}{\delta^2} \qquad \text{Eqn.2.5 (A.12)}$$

Where R_u is the system mass resolution and δ is the ratio between the initial energy spread in the ion packet, and the mean ion energy in the drift region (δ = 2ΔE/E). The typical MALDI mass resolution obtainable

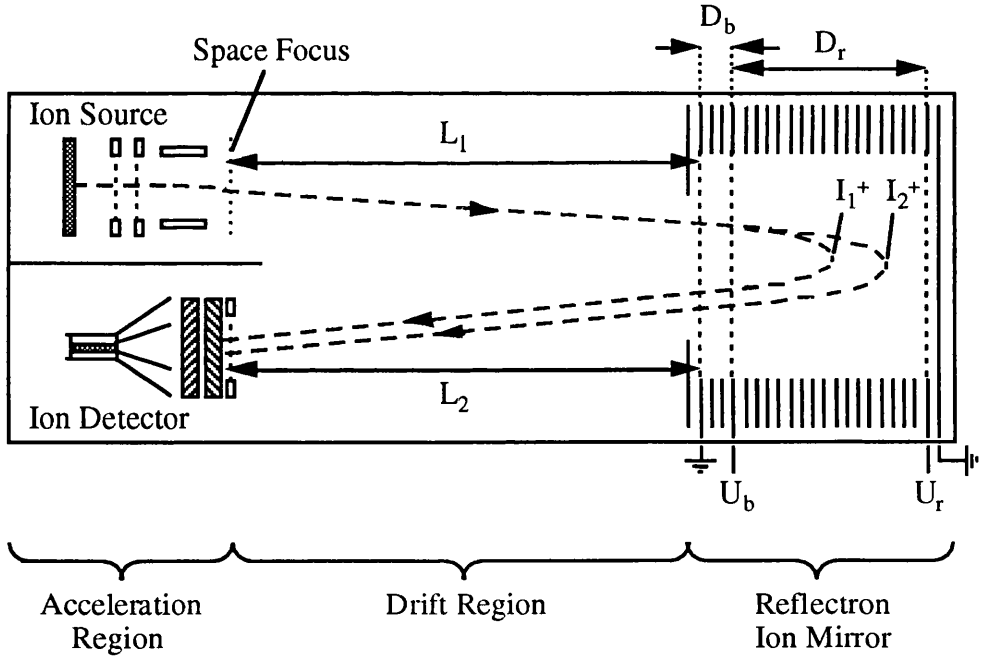

Fig.2.2 Schematic diagram of a reflectron TOF mass spectrometer.

over the range up to 2000 amu, was approximately 500. Given that the mean energy spread of ejected ions is typically a few eV (Dominic Chan 1994), then δ is of the order of 10^{-2} to 10^{-3}, and it is apparent from Eqn.2.5 that the initial energy spread at the space focus of the ion optics has

negligable effect on the overall mass resolution of the spectrometer. The mass resolution is limited by the temporal distribution of the ions arriving at the space focus. A good review of the theory and characteristics of reflectron TOF-MS has been written by Mamyrin (Mamyrin 1994).

2.2 Laser - Solid Interactions

Ablation is the generic term for liberation of material from a surface after irradiation by electromagnetic radiation, and is used to describe a wide range of techniques, even though the underlying physical processes are thought to be completely different. However, throughout all these different ablation phenomena, the interaction of the incident radiation with the material can be split into two separate phases;

i) Transmission of radiation into the material, and absorption by the constituent atoms or molecules.

ii) Energy redistribution processes leading to ejection of material from the sample surface.

In the technique of MALDI the first phase is relatively simple and outlined in section 2.2.1. However, the second phase is not well understood, and a number of theoretical models have been developed in an attempt to characterise this. These models can be split into effectively three categories depending on the fundamental physical mechanism thought to be underlying the ablation process; photothermal, photochemical or photomechanical. Section 2.2.2 outlines the differing ablation mechanisms in general terms, and discuss in greater depth the more substantive models published in the literature.

2.2.1 Absorption of Laser Light

Linear absorption of laser light by the matrix substrate is generally assumed to be the case in MALDI. Radiation is absorbed through electronic excitation and transitions of matrix molecules which are

initially in the ground electronic state. This absorption can be modelled classically (Demtroder 1982) by assuming that the atomic electrons in the absorbing medium act as damped harmonic oscillators, forced to oscillate by the electric field of the incident radiation, and consequently generate a macroscopic polarisation in the medium proportional to the strength of the incident electric field. This treatment results in a relation between the absorption and dispersion in the medium, introducing a complex refractive index, $n = n' - i\,\chi$.

The physical implications of this complex refractive index can seen by considering the transmission of an electromagnetic (E.M.) wave into the medium. The electric component of the wave in vacuum can be represented by

$$E = E_0 \exp[i(\omega_0 t - k_0 z)] \qquad \text{Eqn.2.6}$$

where E is the electric field strength, ω_0 is the frequency and k_0 is the wave number. On passing from the vacuum into the medium, the frequency of the E.M. wave remains unchanged but the wave number is changed to $k = k_0\, n = k_0\,(n' - i\,\chi)$. Inserting this into Eqn.2.6 gives

$$E = E_0 \exp\left[-\frac{2\pi\chi z}{\lambda_0}\right] \exp[i(\omega_0 t - k_0 n' z)] \qquad \text{Eqn.2.7}$$

Since the intensity is proportional to the amplitude squared, this leads to the Beer-Lambert law for linear absorption

$$I(z) = I_0 \exp[-\alpha z], \quad \text{with} \quad \alpha = \frac{4\pi\chi}{\lambda_0} \qquad \text{Eqn.2.8}$$

A commonly used parameter in the models outlined in section 2.2.2 is the absorption depth $\lambda_e = \alpha^{-1}$. This is the depth into the medium at which the intensity of a radiation field (incident normal to the surface) would be attenuated by a factor of e (the natural logarithm).

Recent work by Taranenko et al (Taranenko 1995) using a piezoelectric transducer to directly monitor absorption, has shown that linear

absorption is not valid for all wavelengths and matrices. This work is particularly relevant because the measurements were actually made during matrix ablation, at typical above threshold irradiances, rather than in solution at considerably lower irradiances. A non-linear dependence of acoustical signal on laser fluence was found for a number of matrices irradiated at 266 nm. This effect was attributed to non-linear absorption in the matrix crystals, due to multiphoton absorption by the matrix molecules. All the matrices tested showed near linear dependence at 355 nm, and it will be assumed in this thesis, as it is in most theoretical models described in the literature relating to MALDI, that linear absorption is the dominant mechanism for the matrices and wavelength (337 nm) used. It should be noted that the results of Taranenko et al were obtained using nanosecond laser pulses (10 ns) and that linear absorption may not be the case in ablation with picosecond, or shorter, laser pulses where non-linear multiphoton absorption may be dominant (Karas 1985).

The situation is entirely different for UV ablation of polymers (Lazare 1988, Srinivasan 1989) where it is known that the absorption coefficient shows a dynamic behaviour under relatively high irradiance conditions ($MWcm^{-2}$). Some authors (Kuper and Stuke 1987, D'Couto 1994) have attempted to introduce these non-linear absorption effects into their models for pulsed UV polymer ablation.

It is difficult to measure the absorption coefficients of the solids used as matrices in MALDI. As a consequence of this, the absorption of the material in solution is measured to give the molar extinction coefficient, ε ($l\ mol^{-1}\ cm^{-1}$), which is used to estimate the absorption of the material in its crystalline phase

$$\alpha = \frac{\varepsilon}{V_M} 10^3 \qquad \text{Eqn.2.9}$$

where V_M ($cm^3\ mol^{-1}$) is the molar volume. This gives a reasonable approximation to the correct value (Hillenkamp 1986, Dreisewerd 1995), although some degree of red shift occurs to the absorption curve of the solid phase (compared to the solution values).

Not all of the incident light is transmitted into the material, a fraction of the intensity being reflected from the surface of the material. The reflectivity (R) of a surface is defined as the ratio between the reflected irradiance and the incident irradiance, and can be modelled very accurately using Fresnel's laws of reflection. It is important to realise that the reflectivity of a surface depends on the polarisation of the incident light, the angle of incidence and the refractive index of the material (Lu 1994). In MALDI analysis both polarised lasers and polycrystalline, birefringent samples may be used. This presents considerable complications when attempting to model experimental data since the majority of models assume planar sample surfaces.

2.2.2 Models For Energy Redistribution

The primary product of absorbed laser light is not heat, but a non equilibrium energy distribution in the absorbing component of the irradiated material (i.e. excess particle energy, such as excitation energy of bound electrons, kinetic energy of free electrons (in a metal) or possibly excess phonons). The energy diagram of Fig.2.3 shows some of the elementary processes following the absorption of a single UV photon (Lazare 1989). Only the processes thought to be directly relevant are shown.

Upon absorption of a photon [1] the excited electron-vibrational state may lead to direct dissociation of molecular bonds [5] if the photon has sufficient energy. This may occur as almost instantaneous dissociation if the energy of the state is above the dissociation limit of the molecule, or via intersystem crossing to a repulsive state again leading to dissociation (Garrison 1985). Alternatively, part of the energy of the absorbed photon may be dissipated on a time scale of a few picoseconds (Bloembergen 1993, Luk'yanchuk 1993) via thermalisation [2] within the vibrational structure of the excited state. This may be followed by either dissociation [6] in a similar manner as described above, by internal conversion to a vibrationally excited ground state followed by rapid thermalisation [3], or by fluorescence [4], although the quantum yield of this will be small

(Vertes 1990a). Thermalisation of highly vibrationally excited states [2] & [3] will mainly occur via coupling to lattice vibrations (phonons), resulting in a rapid temperature rise of the matrix crystal.

It is evident that the rate constants for the different relaxation channels, and the wavelength of the ablation laser, will determine the relative importance of thermal or nonthermal mechanisms in material ablation. The complexity of the problem is further increased by the fact that laser ablation is typically performed with high intensity pulses, which will open up the possibility of multiphoton processes [7] and new relaxation channels. Due to the lack of reliable information on the energy relaxation processes of solid matrix materials, it is not possible to predict which type

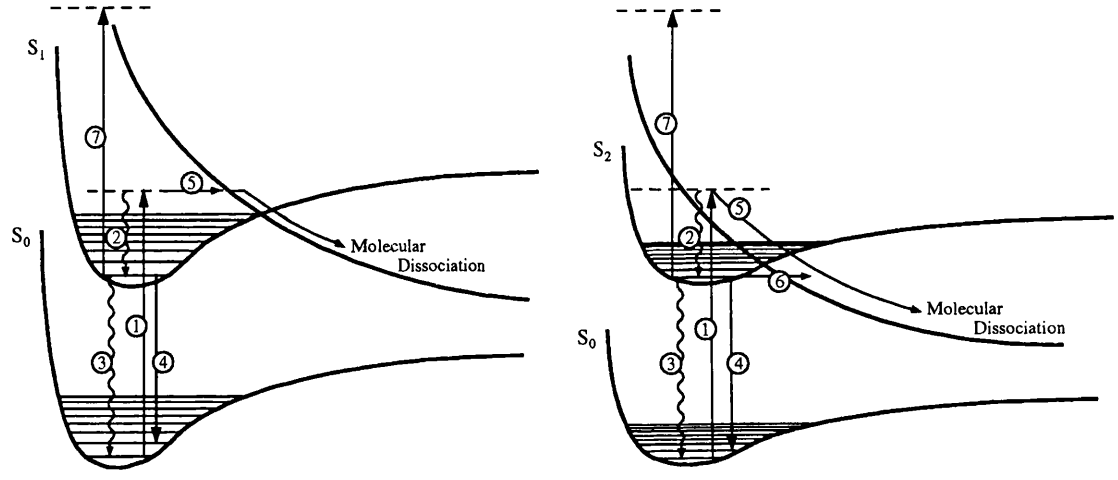

Fig.2.3 Energy diagrams showing electronic and vibrational states, and the elementary processes following the absorption of a UV photon by a matrix molecule. [1] Single photon absorption. [2] Vibrational relaxation within the 1st excited state. [3] Internal conversion to the ground state followed by rapid vibrational relaxation. [4] Fluorescence. [5] & [6] Molecular dissociation. [7] Absorption of a second photon.

of mechanism will dominate laser ablation. It is unlikely that a simple, general mechanism applies to all matrices for all wavelengths.

The wide range of ejection models described in the literature can be assigned to one of three categories, based on the fundamental nature of the mechanism leading to ablation. These categories can be broadly termed photothermal, photochemical or photomechanical. One of the basic questions related to MALDI is concerned with the relative

importance of each type of mechanism in the ablation process, as all three mechanisms may in fact work together to lead to ablation.

The successful ablation model must achieve two fundamental aims in relation to MALDI. It must;

i) properly describe the nature of the laser-induced processes leading to the transition from the solid phase to the gas, and

ii) explain how large molecules can escape fragmentation in an environment abruptly energised by the laser pulse.

The range of models published in the literature which attempt to explain the above two problems are outlined and discussed in the following sections.

The three different categories of ablation model are discussed in sections 2.2.2.1 to 2.2.2.3. It must be emphasised that these models relate to the mechanisms by which solid material is transformed to the gas phase. The expressions given for yield relate to the total number of particles (neutral molecules and ions) removed per laser pulse. This use of yield is based on the assumption that a co-operative ejection process occurs in MALDI (Ens 1991), as opposed to the situation in photon-stimulated desorption (Sundquist 1991) where the yield is given as particles ejected per photon absorbed. It is important to appreciate that the quantities for total particle yield predicted in these ablation models, do not necessarily have a direct connection with the behaviour of the molecular ion yield.

Angular dependence effects are included in a considerable number of the theoretical models published in the literature. However, this has generally been excluded from the discussions given in the following sections. MALDI samples are typically polycrystalline, and hence the concept of a well defined angle of incidence is not usually valid. Westman et al (Westman 1994b) attempted to investigate the dependence of the ion yield on laser beam incident angle, and make comparisons between various ablation models and the experimental data. They concluded

however, that a thorough analysis would require experiments on single crystals.

2.2.2.1 Photothermal Models

In this type of model, the main product of the laser energy deposited in the sample is material heating and phase transition. The main energy relaxation channels are internal conversion between electronic states and rapid thermalisation within the vibrational structure of these states. It is assumed that the overall time scale for relaxation is such that local thermal equilibrium is achieved during the laser pulse and the macroscopic concept of a material temperature is valid. The classical theory of heat conduction can therefore be used to model the temperature distribution within the sample.

The mathematical theory of heat conduction is based on the assumption that the heat flux $J(\mathbf{r},t)$ [Wm^{-2}] in a material is proportional to the local temperature gradient

$$J(\mathbf{r},t) = -K \nabla T(\mathbf{r},t) \qquad \text{Eqn.2.10}$$

where K [$Wm^{-1}K^{-1}$] is the thermal conductivity of the material. From Eqn.2.10, the principle of conservation of energy, and with the introduction of a laser heat source within the material, the general form of the differential equation for heat flow can be obtained (Von Allmen 1987)

$$\frac{\partial T(\mathbf{r},t)}{\partial t} = \kappa \nabla^2 T(\mathbf{r},t) + \frac{A(\mathbf{r},t)}{\rho C_v} \qquad \text{Eqn.2.11}$$

where ρC_v is the heat capacity per unit volume (product of the density and the specific heat capacity), and κ [m^2s^{-1}] is the thermal diffusivity ($\kappa = K/\rho C_v$). $A(\mathbf{r},t)$ [Wm^{-3}] is a heat source term representing laser heating

$$A(\mathbf{r},t) = \alpha (1-R) f' I(\mathbf{r},t) \exp(-\alpha \mathbf{n}.\mathbf{r}) \qquad \text{Eqn.2.12}$$

where the factor f' represents the fraction of the absorbed laser light which contributes to heat production within the material. Some molecules may fluoresce but the quantum yield of this will be small, and f' is usually assumed equal to unity. A material parameter which is crucial in determining the temperature profile generated by pulsed laser heating, is the thermal diffusion length. This is defined as

$$\delta = 2 (\kappa t)^{\frac{1}{2}} \qquad \text{Eqn.2.13}$$

and can be taken as representing the depth into a material to which heat diffuses in time t, following energy deposition in a plane at the surface.

A variety of different methods for solving Eqn.2.11 are described in the literature (Ready 1971, Lax 1977, Philippoz 1989, Vertes 1993b). To obtain analytical solutions of this equation, rather severe simplifications must be made. The simplest and commonest methods make the following assumptions; the material parameters K, C_v and κ are temperature independent, the laser is treated as a surface heat source ($\alpha^{-1} << \delta$), the thermal diffusion length is small compared to the laser spot diameter and the spatial irradiance profile of the laser spot is uniform. This allows the heat diffusion equation to be simplified to a one dimensional form, since heat flow parallel to the surface can be neglected. The analytical solution, based on these assumptions, is adequate to illustrate the basic characteristics of laser induced surface heating in metals, but more than qualitative agreement with experiment cannot be expected.

However, these assumptions are certainly not valid for typical matrix materials, where α^{-1} and δ are of similar magnitude, and K and C_v (and hence κ) may be highly temperature dependent (Von Allmen 1987). Although analytical models have been developed which can give good approximations to more complicated situations, such as a penetrating source (α^{-1} of the same magnitude, or greater, than δ), or a non-uniform spatial profile (gaussian laser spot) (Loza 1994, Von Allmen 1987), temperature dependent material properties cannot be incorporated into these models. In these circumstances, accurate solutions of Eqn.2.11 can only be obtained using numerical methods, with arbitrarily variable parameters [K(T) & C_v(T)]. Comparison between experimental

measurements and numerical calculations of surface temperature, have shown excellent agreement to within 10%, over the temperature evolution of the surface following irradiation (Philippoz 1989). Analytical solutions for a uniform non-penetrating source were shown to overestimate the rise in surface temperature by up to 50%, even with the most judicious choice of K and C_v.

MALDI Specific Photothermal Models

Vertes et al (Vertes 1993a & b) have developed a hydrodynamic model to describe MALDI. In this model the temperature of the material surface rises upon irradiation until a phase transition temperature is reached, being the transition between either surface heating and surface melting with evaporation (or sublimation), or surface heating and volume evaporation. After the phase transition is reached, material transport away from the surface commences, in the form of a hydrodynamic expansion. The model uses numerical methods to solve the 1-dimensional form of Eqn.2.11. The solution of this is then used as a boundary condition for the description of plume expansion, and coupled to a simplified set of hydrodynamic equations, via the Clausius-Clayperon equation for vapour pressure

$$\frac{dp}{d\tau} = \frac{L}{\tau \Delta v} \qquad \text{Eqn.2.14}$$

to give the temperature and density of the expanding plume as a function of time and distance from the laser solid interaction region. In Eqn.2.14, τ is the fundamental temperature, L is the latent heat of vaporisation or sublimation, p is the pressure and Δv is the change in volume in going from solid to gas.

Fig.2.4 shows the hydrodynamic model applied to ablation of a nicotinic acid sample (Vertes 1993a & b), where z is distance normal to the surface. The temperature and density distributions of the sample and plume are shown at three different times following the start of the laser pulse. It can be seen clearly from the temperature distribution curves that the surface

temperature drops rapidly following the end of the laser pulse. This is due to evaporative cooling of the surface, and is the reason the term 'thermal spike' is sometimes used to describe thermal models, due to the rapid temperature rise and fall of the sample surface. The estimated threshold fluence for neutral production is in relatively good agreement with experimental results. The plume density is relatively high (10% of the solid density 50 ns after the laser pulse) which supports the proposed gas phase ionisation mechanisms discussed in section 2.4.

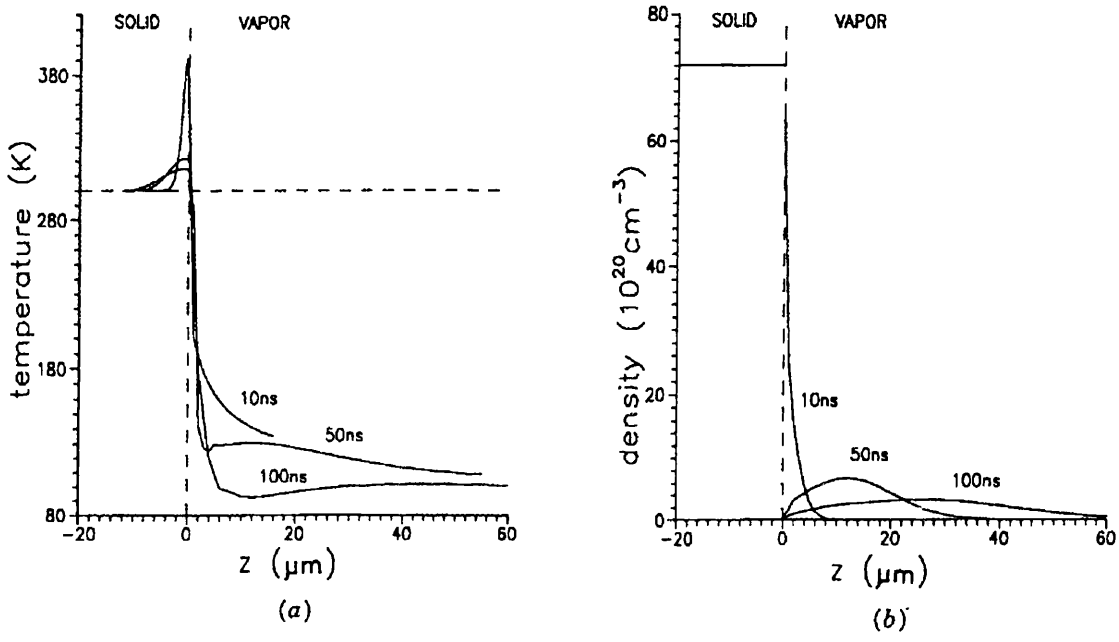

Fig.2.4 Graphs showing the calculated evolution of a) the temperature, and b) the density at the sample/vacuum interface as a function of time after the initial ablation laser pulse (Vertes 1993b).

However, the hydrodynamic model as proposed gives no satisfactory explanation of all the findings of UV MALDI experiments. The following are not explained by this model;

- The different ion and neutral production thresholds.
- That there is little apparent fragmentation of analyte molecules, yet there is considerable fragmentation of matrix molecules.
- The ionisation mechanism.
- The large energies of MALDI ions, compared to the matrix neutrals.

A particularly useful form of Eqn.2.14 is obtained (Kittel 1980) if the approximations are made that the volume occupied by an atom in the gas phase is very much larger than in the solid phase, and that the ideal gas law applies to the gas phase.

$$p(T) = p_0 \exp\left[\frac{-L_0}{k_B T}\right] \qquad \text{Eqn.2.15}$$

In the above equation p(T) is the vapour pressure, p_0 is a constant, L_0 is the latent heat per molecule and the fundamental temperature has been replaced by the Kelvin temperature through the relation $\tau = k_B T$. A number of thermal models have been developed where solutions to the heat diffusion equation have not been sought. Instead, attempts have simply been made to model the yield of sublimated material to some form of Eqn.2.15 (Dreisewerd 1995, Johnson 1991, Vertes 1990b). A typical form which is common in the literature is

$$N \propto \exp\left[\frac{-\Phi_0}{\Phi}\right] \qquad \text{Eqn.2.16}$$

where N is the number of ablated molecules, Φ is the laser photon fluence and Φ_0 represents an apparent 'threshold' fluence, determined by the cohesive (or sublimation) energy per molecule of the matrix, and the efficiency of the absorbed photon energy for causing material expansion.

It is immediately apparent from Eqn.2.16 that a thermal model for ablation will result in material transport across the solid/vacuum interface, regardless of the incident laser fluence or surface temperature. This is highly significant as it implies that the 'threshold' is not a real physical fluence threshold, but rather an apparent threshold determined by the detection efficiency of the system.

The fundamental difference between the photothermal model and the photochemical and photomechanical models described in the next two sections, is that the particle yield for the latter models exhibits a true threshold and goes to zero below some value of the fluence. Dreisewerd et al (Dreisewerd 1995) found that their experimental results could not be

fitted with any degree of accuracy to a model based on a real fluence threshold (pressure pulse), but were well interpreted within the framework of a thermal model based on Eqn.2.16 (Chapter 4, section 4.6). The model allowed for the prediction of absolute temperatures for the irradiated material. However, although fits to some of the experimental data give reasonable temperatures (similar to T_{sub} for the matrix), other fits predict surface temperatures of 10000 K, which are clearly unrealistic given that total fragmentation would be expected if the process occurred in a state of thermal equilibrium.

An obvious limitation of the simple sublimation model outlined by Dreisewerd stems from the fact that this model is based on an ideal interface between the solid and vacuum. However, this is certainly not the case as particles sublimated towards the latter end of the laser pulse will be ejected into a high density plume, rather than a vacuum.

2.2.2.2 Photochemical Models

In this type of model the main effect of the absorbed laser light is to cleave intra- or intermolecular chemical bonds. After a certain threshold in the density of broken bonds is reached, the internal stress due to the change in volume occupied by the fragments is enough for ablation to ensue. This type of model is typically used to describe UV ablation of organic polymers (Garrison 1985, Sutcliffe and Srinivasan 1986). Although most of the deposited energy is used in bond breakage, a fraction is inevitably converted to thermal energy, becoming increasingly significant at longer wavelengths (Brannon 1985).

The standard expression (Eqn.2.17) used by many researchers to model the yield of photochemical processes (Westman 1994b, Brannon 1985, Jellinek 1984) is not actually dependent on the type of mechanism, but merely relates to the deposition of energy within the solid according to the Beer-Lambert law of linear absorption (Eqn.2.8).

$$N \propto \frac{1}{\alpha} \ln\left[\frac{\Phi}{\Phi_0}\right] \qquad \text{Eqn.2.17}$$

N is the number of ablated particles, α is the linear absorption coefficient of the material, Φ is the laser photon fluence and Φ_0 is the threshold fluence above which the density of broken bonds is sufficient for ablation to occur. The use of Eqn.2.17 to model particle ablation resulting from the use of a quasi gaussian (spatially) laser pulse is obviously flawed since Eqn.2.17 implies a 'top hat' laser intensity profile on the sample surface, and simply relates the yield of ablated molecules to a depth into the material. A more accurate representation is to relate the yield to a volume of material over which some energy density has been exceeded. Assuming that the spatial intensity profile of the laser is gaussian, the following expression can be derived (Westman 1994b)

$$N \propto \frac{\Pi}{\alpha}\left[\sigma \ln\left[\frac{\Phi}{\Phi_0}\right]\right]^2 \qquad \text{Eqn.2.18}$$

where σ is the beam radius. This is essentially obtained by a combination of the Beavis model (section 2.2.4) with the Beer-Lambert law for linear absorption. The same logic can be applied to the sublimation equation of section 2.2.2.1 (Eqn.2.16) but it is found that the dependence of the photothermal yield on fluence does not change when this equation is integrated over the spatial and temporal profile of a gaussian laser pulse.

The threshold dissociation and ionisation energies of typical small organic molecules lie in the range between 7 and 9 eV. If single photon excitation is to be responsible for bond breaking, via channels [5] and [6] of Fig.2.3, then the photon energy has to be comparable with or greater than the molecular dissociation energy, which restricts this mechanism to far UV light. In fact, the role of photochemical processes arising from single photon excitation can be considered negligible for wavelengths greater than 250 nm (Oraevsky 1991). This process is thought to be the main mechanism involved in far UV ablation of polymers and is termed (Garrison 1985) ablative photodecomposition (APD).

Excitation to states lying above the molecular dissociation energy is possible for wavelengths greater than 250 nm following two step excitation. To achieve efficient two step excitation, the intermediate

electronic state has to be efficiently populated. A good approximation to the fluence (Φ_0) required to achieve this can be obtained by assuming that the excitation rate from the ground state must be equivalent to the relaxation rate from the intermediate state (Oraevsky 1991).

$$\Phi_0 = h\nu_L \left[\frac{\tau_p}{\tau_{rel}\sigma_1} \right] \qquad \text{Eqn.2.19}$$

In this expression $h\nu_L$ is the photon energy, τ_p the duration of the laser pulse, τ_{rel} the relaxation time of the intermediate electronic state and σ_1 the molecular absorption cross section ($\sigma_1 = \alpha V_M / N_A$). For UV ablation of DHB with a 3 ns pulse duration nitrogen laser (λ = 337 nm), and estimating $\alpha = 3.6 \times 10^4$ cm^{-1} , $V_M = 110$ cm^3 mol^{-1} (Strupat 1991) and τ_{rel} = 1 ns, the fluence threshold calculated from Equ.2.19 is $\Phi_0 = 270$ mJ cm^{-2}. This value is substantially higher than the threshold fluences published in the literature (Table.4.2, Chapter 4, section 4.6) which are for ion production. The threshold fluence values for neutral production will be a factor of approximately 3 lower than the values given in table.4.2. In the work of the author, the typical threshold fluence required for neutral production from ablation of DHB using a 4 ns nitrogen laser was approximately 12 mJ cm^{-2}.

The assumption used to determine Eqn.2.19 is an extreme simplification of the rate processes involved. In addition, there is considerable inaccuracy in calculating experimental fluences and solid absorption coefficients, and little reliable information exists on relaxation channels and rates for matrix materials. Eqn.2.19 is not expected to provide quantitative predictions of threshold fluences, but should instead provide a qualitative guide to the behaviour of the threshold fluence with laser pulse duration.

However, the photochemical model outlined above does not satisfactorily model the experimental data even qualitatively. In ablation of DHB with 4 ns and 300 ps pulsed nitrogen lasers (Chapter 4), it is suggested from the data that the threshold fluence for neutral production is independent of pulsewidth, or at least not a strong function of the pulsewidth. Similar behaviour was found with the ion production threshold. Demirev et al

found that the threshold fluences for ion production from a ferulic acid matrix using two different pulse length lasers (3 ns and 560 fs) were almost identical (Demirev 1992), and certainly did not vary by a factor of the order of 10^4 as predicted by Eqn.2.19 for the neutral threshold. It would be surprising if the behaviour of the ion prodution threshold with fluence, did not bear at least some similarity to that of the neutral threshold.

The experimental evidence of the author, and that of Demirev et al (Demirev 1992), suggests that the photochemical model outlined in this section is not adequate to describe the ablation process in MALDI. If indeed photochemical decomposition is the mechanism in UV MALDI, then the situation may be better described by a model incorporating both irradiance and fluence thresholds, such as that used to model UV polymer ablation (Sutcliffe and Srinivasan 1986), and modified to include a fluence, and irradiance dependent absorption coefficient (Kuper and Stuke 1987).

2.2.2.3 Photomechanical Models

A model for laser ablation in MALDI due to the generation of large pressure gradients within the irradiated matrix has been developed by Johnson and co-workers (Johnson 1991 & 1994). This model was based on applying concepts originally developed to describe MeV ion induced desorption (Johnson 1989). The model was referred to as the 'pressure pulse' model because the net impulse produced by the transiently pressurised cylindrical ion track resulted in sufficient momentum transfer to a volume of material bounded by the surface to allow ejection.

In the pressure pulse model applied to MALDI the laser energy is deposited as electronic excitation of matrix molecules, as in all models. However, this electronic energy is then mainly converted into energy which leads to material expansion, the details and timescale of which are not understood (Johnson 1993). This expansion results in an outwardly directed pressure pulse in the solid. Matrix and analyte molecules at the surface need to accumulate a net momentum from this pulse before

ejection commences. Although it is the momentum obtainable from the pressure pulse which determines the threshold fluence value, it is the local energy density (temperature) which will determine the degree of ionisation, and the internal energy of the ejected material.

The yield (N) of both neutrals and ions can be represented by the general expression (Johnson 1991)

$$N \propto n_m \, \Delta A_p \, \Delta z_{eff} \qquad \text{Eqn.2.20}$$

where n_m is a number density, ΔA_p is the laser pulse area on the sample surface and Δz_{eff} is an effective depth from which ejection occurs. An expression of this type could be used to describe the molecular yield for any model of laser ablation, the difference between each model apparent in the behaviour of Δz_{eff}.

When considering neutral matrix molecules, n_m is the number density of matrix molecules, and the effective depth is estimated as follows. If momentum dissipation effects are ignored, and the assumptions are made that; the net impulse is proportional to the photon fluence, Lambert-Beers law for absorption holds, and the momentum imparted must exceed some critical value, then the effective depth can be expressed as (Johnson 1991)

$$\Delta z_{eff} \approx \left[\frac{\cos \Theta'}{\alpha}\right] \ln\left[\frac{2\Phi}{\Phi + \Phi_0}\right] \qquad \text{Eqn.2.21}$$

where Θ' is the angle of refraction. The meaning of Φ and Φ_0 remain the same as used for the sublimation model (Eqn.2.16). The total yield is then proportional to

$$N \propto n_m \, \Delta A_p \left[\frac{\cos \Theta'}{\alpha}\right] \ln\left[\frac{2\Phi}{\Phi + \Phi_0}\right] \qquad \text{Eqn.2.22}$$

These expressions are developed for a 'top hat' laser profile. The form of Eqn.2.22 cannot be integrated analytically over a gaussian profile to find a general expression for the dependence of the yield on fluence from a

gaussian laser pulse profile (as is derived for the photochemical model). It is possible however, to derive the dependence of the yield near threshold fluence (Johnson 1994).

$$N \propto \left[\frac{\Phi - \Phi_0}{\Phi_0}\right]^2 \qquad \text{Eqn.2.23}$$

When considering the yield of analyte molecules, n_M is the number density of analyte molecules and Δz_{eff} takes the same form as Eqn.2.21, but with the threshold fluence value a factor of $(M/m)^{1/6}$ greater than that for the matrix molecules (M and m being the analyte and matrix masses respectively). This factor is obtained by assuming that the amount of momentum transfer is determined by the molecular area presented to the outflowing matrix material, that the matrix and analyte molecules are compact and that the cohesive energy per unit surface area is the same for both matrix and analyte molecules.

It has been reported in the literature (Vertes 1993b, Perera 1994) that the threshold fluence needed to observe analyte ions increases with the mass of the analyte. Westman et al (Westman 1994b) found that the threshold fluence for ion yield scaled with the mass of the analyte molecule as $\Phi_0 \propto M^{0.27}$. This shows a different exponent than that predicted for analyte neutrals ($\Phi_0 \propto M^{1/6}$), which is not unexpected since any mass or fluence dependence of the ionisation mechanism would be superimposed on the analyte molecular yield dependence. However this apparent increase in threshold fluence with analyte mass may be due to a decrease in detector efficiency, or a reduction in ion signal due the distribution of the analyte signal over an increased number of charged states (Vertes 1993b), as other authors have not observed such an increase (Hedin 1991).

If the pressure pulse model described above were valid then the velocity (momentum) of ejecta should increase with increasing fluence, and the relative velocity between matrix and analyte should scale as $(M/m)^{1/3}$. In a study by Beavis et al (Beavis 1991), the velocity of analyte molecular ions was found to be 35 % lower than that of the matrix ions, but no dependence on analyte mass was found over the range investigated (1 kDa - 16 kDa). Other studies have not found any difference between the velocities of

ablated matrix and analyte neutrals (Huth-Fehre 1991) or ions (Dominic Chan 1994).

The pressure pulse model was originally developed for MeV ion induced desorption, where the total energy deposition time is approximately 10^{-15} s. In MALDI the timescale for energy deposition is typically of the order of 10^{-8} s, and the assumption that dissipative processes are negligible may not be valid. A certain degree of relaxation of momentum from molecules may occur, in the form of heating (i.e. vibrational and rotational excitation of the molecules). However, these processes will not change the nature of the yield expressions, but would affect the ion formation probability and the degree of fragmentation (Johnson 1991).

Related Models

A number of related models which have been linked to, or suggested to play some part in the ablation process occurring in MALDI are outlined in the remainder of this section.

Spallation is a form of ablation where a surface layer is ejected from a material following laser irradiation above a threshold fluence. If the laser pulse width and the conversion time of absorbed laser energy to thermal energy are sufficiently short, then a surface layer of the material is heated such that it cannot undergo thermal expansion on the time scale of the laser pulse. The result of this is to induce a compressive stress pulse in the material whose amplitude is proportional to the absorbed fluence. Reflection of the outward directed stress pulse from the free surface of the material creates a tensile stress pulse which follows the inward directed compressive pulse into the material. If the tensile stress created is greater than the tensile strength of the material, then spallation will occur (Dingus 1991). From hydrodynamic models of the spallation process it can be shown that significant tensile stresses are generated at a depth comparable to the optical absorption depth (Albagli 1994). Damage craters of the order of α^{-1} in depth will be formed in the material following spallation. This is contrary to what is seen with MALDI, where little or no morphological change can be observed in the

sample surface following above threshold irradiation (Strupat 1991). Spallation can occur at fluences below that required for thermal vaporisation because the material is ejected in solid or liquid fragments, rather than as molecules or atoms. No evidence for this type of behaviour is evident in either the research of the author, or that published in the literature, and it can be concluded that spallation is unlikely to be the mechanism responsible for ablation in MALDI.

It has been suggested that shock heating may occur during MALDI and contribute to material ablation (Williams 1991). Following initial energy deposition at an interface, rapid heating of an extended volume of material is possible at a rate far exceeding that capable by thermal transport mechanisms. It is postulated by Williams et al that the shock wave generated by pulsed laser heating of an interface, rapidly moves through the bulk, causing material heating as it propagates and loses energy. The model is in fact a combination of thermal and mechanical effects and was proposed to explain results obtained in laser ablation of DNA loaded ice films on a copper substrate. The typical temperatures and pressures required to produce efficient volatilisation of the ice film were in the range 3600 - 6000 K and 30 - 50 kbar respectively. This mechanism is unlikely to have much significance in MALDI where the expected temperatures and pressures are orders of magnitude lower (Vertes 1993a & b).

The Laser-Induced Explosive Desorption (LITD) model was introduced to explain the experimentally observed molecular non-selective desorption of a surface adsorbate (Fain 1989). The adsorbate is assumed to form a van der Waals crystal on the substrate surface. Irradiation by UV light causes excitation of electronic levels of the adsorbate. The excited electronic state is coupled to vibronic states of either the ground level of the electronic state (internal conversion) or a different electronic state entirely (intersystem crosssing). These vibronic states can be strongly coupled to the phonon modes of the adsorbate crystal. Under certain conditions where the energy dissipation from the phonon modes is slower than the energy gain, exponential growth can occur in the phonon density, termed a 'phonon avalanche'. This would increase the effective temperature of the crystal leading to an explosive, nonselective desorption. This

complicated model has not been applied in detail to MALDI and is beyond the scope of this discussion.

2.2.3 Homogeneous Bottleneck Model

The homogeneous bottleneck model (Vertes 1990a & b) attempts to explain the production of intact, relatively internally cool analyte molecules and ions, from a volume of hot, excited matrix material. The model derives from a mechanism proposed to explain bond-selective processes in chemical reactivity, where it was hoped that 'bottlenecks' for intramolecular vibrational energy transfer following laser excitation, would lead to bond breakage other than that of the weakest molecular bond. This concept was modified to explain the laser desorption of internally cold molecules from hot substrates (Zare 1987), and has been further adapted by Vertes et al to describe the liberation of cold molecules from bulk solids.

In the case of molecular desorption (Zare 1987), labile molecules are bound to the substrate by weak van-der-Waal bonding. Surface phonons of the substrate will be well coupled to these low frequency bonds, which will rapidly absorb energy from the laser heated substrate. However, the van-der-Waal bonds are not well coupled to the stronger chemical bonds within the molecule, and the rate of energy transfer is slow (energy bottleneck). Thus, it is possible by sufficiently rapid laser heating to break the substrate-adsorbate bond without transferring significant amounts of vibrational energy to the adsorbate.

In the homogeneous bottleneck model (Vertes 1990a & b), volatilisation of the matrix occurs in a time short compared to that required for thermal equilibrium between the embedded analyte molecules, and the crystal lattice and matrix molecules. The model is homogeneous in that the deposited laser energy is uniformly spread over some volume of the matrix. Although this is clearly not the case, the most obvious objection being that the laser intensity decays exponentially with depth into the matrix, it is assumed for simplicity of argument. The bulk of the laser energy is initially deposited into the matrix, via electronic excitation, due

to the choice of laser wavelength. This is rapidly converted to internal vibrational excitation, and can then be redistributed between the lattice and analyte molecules. Most of the energy is transferred to the lattice, the energy density of which reaches that required for sublimation before significant amounts of energy can be transferred to the analyte molecules. The energy transfer bottleneck occurs in this case between the lattice phonons and analyte molecules, caused by the mismatch between the vibrational frequencies of the analyte molecules and the vibrational frequencies of the hydrogen bonds (between analyte and matrix molecules), which play the role of the van-der-Waal bonds in the surface desorption model (Zare 1987).

The qualitative predictions of this model are: the rate of matrix sublimation should be maximised, either by increasing the surface to volume ratio, or by choosing a matrix material with a low sublimation temperature; the concentration of analyte should be minimised, which has the detrimental effect that the ion signal is reduced, requiring a compromise between the two. The application of the model to 266 nm ablation of a protein doped nicotinic acid sample, using typing material parameters, shows that the most of the protein molecules ejected remain internally cold, and do not degrade (Vertes 1990b).

2.2.4 Phenomenological Model for MALDI

A phenomenological model was proposed by Beavis (Beavis 1992c) in an attempt to determine the relationship between the yield of desorbed particles and the laser fluence on the sample surface. The model is not based on any particular ablation mechanism, but only on the simple assumption that a fluence threshold exists for ion production, and that the illuminating laser beam has a gaussian profile at the sample surface.

$$F(r) = f \exp\left[\frac{-r^2}{2\sigma^2}\right] \qquad \text{Eqn.2.24}$$

F(r) is the fluence as a function of distance r from the beam centre, f is the fluence maximum and σ is the beam radius. Before the fluence threshold

has been reached, no ions are produced. After threshold, the yield of ions is directly proportional to the area of sample with an incident fluence greater than the threshold value. This model is based entirely on geometrical arguments. Based on the assumptions outlined above, the resulting expression for ion yield is essentially exactly the same form as that for the photochemical model, Eqn.2.17. The equation was in good agreement with the experimental results of Ens (Ens 1991). This model has recently been disproved by the results of Dreisewerd (Dreisewerd 1995), who used a flat-top spatial profile on the sample surface to investigate the fluence and spot size dependence of the ion signal, but still found a marked ion signal dependence on fluence.

Although this model is incorrect, it is clear from the adjustments required to the expressions for yield in the photochemical and photomechanical models, that the interpretation of the threshold behaviour can be affected significantly by the form of the laser pulse profile.

2.3 Plume Dynamics

Study of the gas phase evolution of ablated material has generated considerable interest in the field of laser ablation, and a number of authors have attempted to model the interaction processes involved in producing the observed plume distributions (NoorBatcha 1987, Kelly and Dreyfus 1988a & b, Kelly 1990, Kools 1992 & 1993, Vertes 1993a, Zimmerman and Ho 1994). Most of these studies have concentrated on analysis of the resultant plume from laser ablation of metal and semiconductor substrates, although the work of Vertes et al (Vertes 1993a) relates to ablation from MALDI matrices.

This section will outline the theory required to carry out a relatively simple analysis on the observed velocity distributions. A complete description of the plume is a complex problem of gas dynamics and is not treated in any depth by the author. The approach taken by the author will follow that of Kelly and Dreyfus (Kelly and Dreyfus 1988a & b), where a thermally activated ablation mechanism is assumed. However, identical

results can be obtained even if a non-thermal mechanism is assumed (Zimmerman and Ho 1994).

The development of the ablation plume can be divided into three stages, progression from one to the next being dependant on the average number of collisions occurring in the plume (proportional to the gas number density) and possibly the duration of the laser pulse (Kelly and Dreyfeus 1988a). The first stage is thermal emission of material from the substrate, where it is assumed that no gas phase collisions are occuring, and the velocity distribution immediately above the surface can be described by a half range Maxwell Boltzmann. If the particle number density is sufficiently high, then a hydrodynamic gas velocity will develop, onto which is superimposed a full range Maxwell Boltzmann. The region in which this develops is called the Knudsen layer (second stage). For even higher number densities, or where the pulse duration is long, an Unsteady Adiabatic Expansion (UAE) may develop (third stage). A description of the UAE, which may have consequences in terms of analyte cooling, will only be outlined in very general terms, as this does not significantly affect the interpretation of the authors experimental data.

2.3.1 Maxwell Boltzmann Velocity Distribution

The approach generally taken is to postulate that the velocity distribution of ejected material immediately above the sample surface may be described by an equation which takes a similar form to that used to describe an ideal gas in thermal equilibrium at temperature T.

$$\frac{dn}{n} = 4\pi v^2 \left[\frac{m}{2\pi k_B T}\right]^{\frac{3}{2}} \exp\left[\frac{-mv^2}{2 k_B T}\right] dv \qquad \text{Eqn.2.25}$$

This equation is the well known Maxwell Boltzmann distribution of particle velocities in a gas (Kittel 1980), where dn is the number of particles with velocities in the range v to v + dv, n is the total number of particles, m is the particle mass, k_B is Boltzmann's constant and T is the gas temperature. Throughout this work the word velocity will be used

where we actually mean speed, as no confusion is caused and it is traditional to refer to velocity distributions.

In laser ablation from a surface the particles are all directed into the hemisphere of space away from the surface. If the assumption is made that the particle number density in the plume is sufficiently low, such that essentially no collisions occur, then a flux weighted Maxwellian can be used to describe the velocity distribution (Kelly and Dreyfeus 1988a & b, Kittel 1980).

$$\frac{dn}{n} \propto v^3 \exp\left[\frac{-mv^2}{2k_BT}\right] dv \qquad \text{Eqn.2.26}$$

This is sometimes called the half-range Maxwell Boltzmann velocity distribution, since only positive values of v are allowed. It can be seen that this equation follows simply from Eqn.2.25 by weighting the faster particles with their velocity. However, this equation is usually derived by assuming a one dimensional energy distribution of the form

$$\frac{dn}{n} \propto \exp\left[\frac{-E}{k_BT}\right] dE \qquad \text{Eqn.2.27}$$

where E is the particle energy. A phase space factor of v^2 is incorporated when transforming to velocity and three dimensions (Kelly and Dreyfeus 1988b, Zimmerman 1994).

In practice, the distribution of particles in the plume is investigated by looking at either the flux, or density of particles as a function of time. The experimental arrangement used by the author is shown in Fig.2.5. A pulsed ionising laser is used to 'detect' the emitted material, the size of the resulting ion signal being proportional to the number density of particles in the detection region. Therefore, the velocity distribution given in Eqn.2.26 has to be transformed to time space and corrected for density dependant detection. The assumptions made in carrying out this transformation are that, i) the dimensions of both the laser ablation spot and detector (ionising laser volume) are small compared to their spacing,

ii) the ablation time is much less than the particle flight time and iii) the detector is on axis. The resultant distribution is

$$\frac{dn}{n} \propto \frac{1}{t^i} \exp\left[\left(\frac{-m}{2 k_B T_c}\right)\left(\frac{z}{t}\right)^2\right] dz \qquad \text{Eqn.2.28}$$

where i = 4, z is the distance to the ionising laser (normal to the surface), T_c is a characteristic temperature of the ablation process, t is the flight time of the particle and dz is the width of the focused laser beam (detector width).

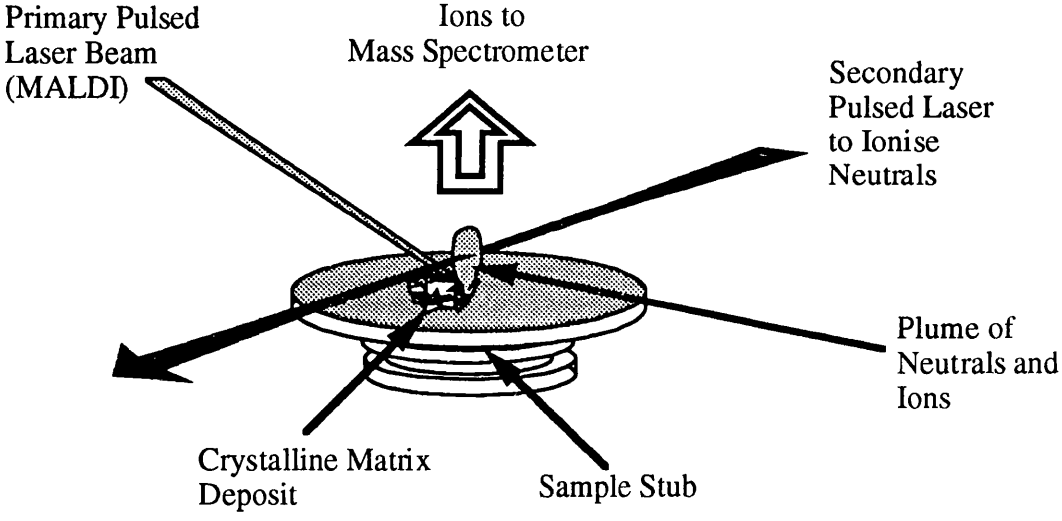

Fig.2.5 Schematic diagram showing experimental arrangment used for postionisation of ejected neutral particles.

The above expression should not be interpreted as an exact description of the time distribution of particles arriving at a distance z from the sample surface. It is derived from the assumption that the velocity distribution for an ideal gas is suitable to describe the plume formed following pulsed laser ablation from a surface under conditions where no collisions occur. It should be regarded as an empirical formula. The parameter T_c should be interpreted as a characteristic temperature of the ablation process, which may or may not reflect the actual surface temperature. There is considerable ambiguity over the value of i (the exponent of the time), and forms of Eqn.2.28 have been used with values of i between 2 and 5 (Lazneva 1991, Kelly and Dreyfeus 1988a, Kools 1992). However, it is difficult to

discriminate experimentally between differing values of i, since the distribution is more sensitive to the behaviour of the parameters in the exponential term (Kools 1992).

2.3.2 Knudsen Layer & Hydrodynamic Velocity

When the number density of particles emitted from the surface is sufficiently high that a significant number of collisions occur per particle, then some particles will develop negative values of v (i.e. move back towards the surface), and Eqn.2.28 is no longer appropriate. This is termed a Knudsen layer, the transition to which is usually controlled by the average number of collisions per particle in the plume, and has been calculated to occur for as few as 3 collisions per particle (NoorBatcha 1987). The plume can now best be described as a packet of particles moving with a hydrodynamic, or flow velocity, on top of which is superimposed a full range Maxwell Boltzmann velocity distribution (i.e. v can be positive or negative). The form of the resultant velocity distribution can be obtained by replacing the exponential term in Eqn.2.26 by

$$\exp\left[\frac{-m(v-u_K)^2}{2k_BT_K}\right] \qquad \text{Eqn.2.29}$$

where T_K is a characteristic temperature of the plume, u_K is the flow velocity and the other parameters are as defined for Eqn.2.28. The form of Eqn.2.29 remains similar to Eqn.2.28, since the half range Maxwell Boltzmann is still assumed to be valid at z = 0, prior to any collisions. An additional assumption to the three made in transforming from velocity to time (to obtain Eqn.2.28) is that the size of the Knudsen layer be small compared to the surface/detector spacing. This may not have been achieved in all the experimental work carried out by the author, some of which was performed with a separation between the sample surface and ionising laser of as little as 650 μm.

The relation between the characteristic temperature of the ablation process and the most probable time of flight is given by

$$k_B T_c = \frac{\hat{E}}{\eta_c} = \left(\frac{1}{2\eta_c}\right) m \left(\frac{z}{\hat{t}}\right)^2 \qquad \text{Eqn.2.30 (B.7)}$$

where $\hat{t}$ is the most probable time of flight, $\hat{E}$ the most probable particle energy and the parameter η_c ranges between 2.52 (monatomic species) to 3.28 (polyatomic species with many internal degrees of freedom). The dependence of η_c on the number of degrees of freedom j is given in Appendix B (Eqn.B.8), where the theory of the Knudsen layer model is outlined in more detail.

The value of η_c is essentially constant for molecules containing more than seven or eight atoms. The number of vibrational modes in a polyatomic molecule with N atoms is 3N - 6 (Eisberg and Resnick 1985). Assigning 2 degrees of freedom to each vibrational mode, and including the three rotational degrees of freedom (Kelly and Dreyfeus 1988a), the total number of degrees of freedom is given by

$$j = 2(3N - 6) + 3 \qquad \text{Eqn.2.31}$$

From Eqn.B.8 the value of η_c for DHB (with N = 17 and j = 93) is equal to 3.254. The maximum value, for a molecule with infinite degrees of freedom, is less than 1% greater than this, with $\eta_c = 3.281$.

2.3.3 Unsteady Adiabatic Expansion

It is apparent that the assumption of collisionless particle emission, used in Section 2.3.1, is rather unphysical when considering the typical ablation conditions used in MALDI. The transition between an essentially collision free plume, and formation of a Knudsen layer, has been established (experimentally and theoretically) to correspond to a removal rate of approximately 0.5 monolayers in a 10 ns duration pulse (Kelly 1990). Material removal rates in MALDI depend strongly on the incident fluence, but are typically orders of magnitude greater than this (Strupat 1991). When the average number of particle collisions in the plume exceeds more than approximately 3, a planar Unsteady Adiabatic Expansion begins (Kelly 1990). This will only be mentioned briefly since it

is a complex problem of gas dynamics. The essential point is that although the adiabatic expansion leads to a decrease in the width of the velocity distribution, there is essentially no change to the most probable velocity. Thus, the Knudsen layer theory relating the most probable velocity to the characteristic temperature, is still valid in calculating T_c.

2.4 Ionisation Mechanisms

It is widely accepted that the matrix plays an essential role in analyte ionisation in addition to facilitating the desorption process. However, the exact processes which lead to the production of analyte ions are as yet unclear. Although there have been suggestions that analyte ionisation may occur in the solid state (Zhu 1995) with laser desorption leading to the ejection of preformed ions, the majority of researchers believe that a gas phase ionisation mechanism is responsible. Most of the experimental results published in the literature support this belief. Of the ideas discussed in the literature, two distinct models have emerged. Discussion of these models in depth is beyond the scope of this thesis, and in this section only the fundamentals of each will be described. A relatively thorough discussion of these ionisation models is given by Liao (Liao 1995).

Excited State Proton Transfer (ESPT)

Most useful matrix materials are compounds which are strong acids in the excited state. It has been proposed (Gimon 1992) that the ionisation mechanism operating in MALDI is that of ESPT. Absorption of a UV photon by ground state matrix molecules in the gas and/or solid phase results in excitation to the lowest level singlet state. The increased acidity of excited state (singlet) matrix molecules leads to a proton transfer reaction with ground state analyte molecules following molecular collisions in the dense ablation plume. The mechanism of ESPT has been suggested previously in laser desorption ionisation (LDI) of aromatic amino acids (Karas 1985), the increased acidity of excited state aromatic amino acids in solution being well known. In addition, direct evidence for the occurrence of ESPT in the solid state has been reported for UV LDI of

several fluorene and hydroxy aromatic acids (Chiarelli 1993). However, it is difficult to reconcile this ionisation mechanism with the delayed extraction experiments described below.

Radical Molecular Ion Photochemistry

In this model (Ehring 1992) it is proposed that during the lifetime of the ablation laser pulse, photo-ionisation of ejected gas phase matrix molecules occurs. This results in the production of radical molecular ion species which then play an active role in analyte ionisation via ion/molecule reactions in the dense ablation plume. The model results from a study of the LDI spectra from a large variety of different organic compounds, where it was found that the majority of useful matrices produced ion signals corresponding to both radical molecular species (odd-electron) and the protonated parent (even-electron). Further evidence for a protonation mechanism based on ion/molecule reactions comes from experimental results published by Wang (Wang 1993) where it was reported that enhancement in the abundance of protonated and cationated (alkaline ion adducts) analyte ion species occurred following delayed ion extraction. The results strongly suggest that this ion signal enhancement was due to the increased time interval during which ion/molecule reactions could take place, prior to ion extraction from the plume.

Chapter Three

Instrumentation & Experimental

3.1 Mass Spectrometer

The mass spectrometer used by the author is of the reflectron time-of-flight (TOF) type and is one of three designed and assembled in Glasgow. The fundamental requirement for a TOF mass spectrometer is a vacuum environment in which to create and manipulate ions on a microsecond timescale. A reflectron TOF mass spectrometer is built up of a range of different elements to achieve this. A chamber is needed to contain the vacuum, and pumps are required to create and maintain it. Ion optics are required, to collect, accelerate and collimate ions from the source region, and to form an electrostatic mirror to direct the ions through 180 degrees onto the detector. Plan and elevation views of the mass spectrometer are given in Fig.3.1 and Fig.3.2 respectively.

Main Chamber and Time-Of Flight Arm

The core of the system is a spherical stainless steel chamber, 30 cm in diameter. Numerous ports are situated in the chamber walls, onto which a variety of flanges and equipment have been fitted. The TOF arm of the spectrometer consists of a 1.5 meter long steel cylinder fitted onto one of the main chamber ports.

Samples for analysis are deposited on a stainless steel sample stub which is then positioned on a manipulator arm in the centre of the main chamber. The sample manipulator (Kratos WG-194) allows movements to be made of the sample stub in three orthogonal planes (X,Y & Z) and allows the sample to be rotated about the vertical (Z) axis. Micrometers control the movement in each axis and allow the sample position to be moved accurately and reproducibly.

Sample stubs can be inserted and removed from the manipulator using the sample insert probe (Kratos WG 707). The insertion system contains a

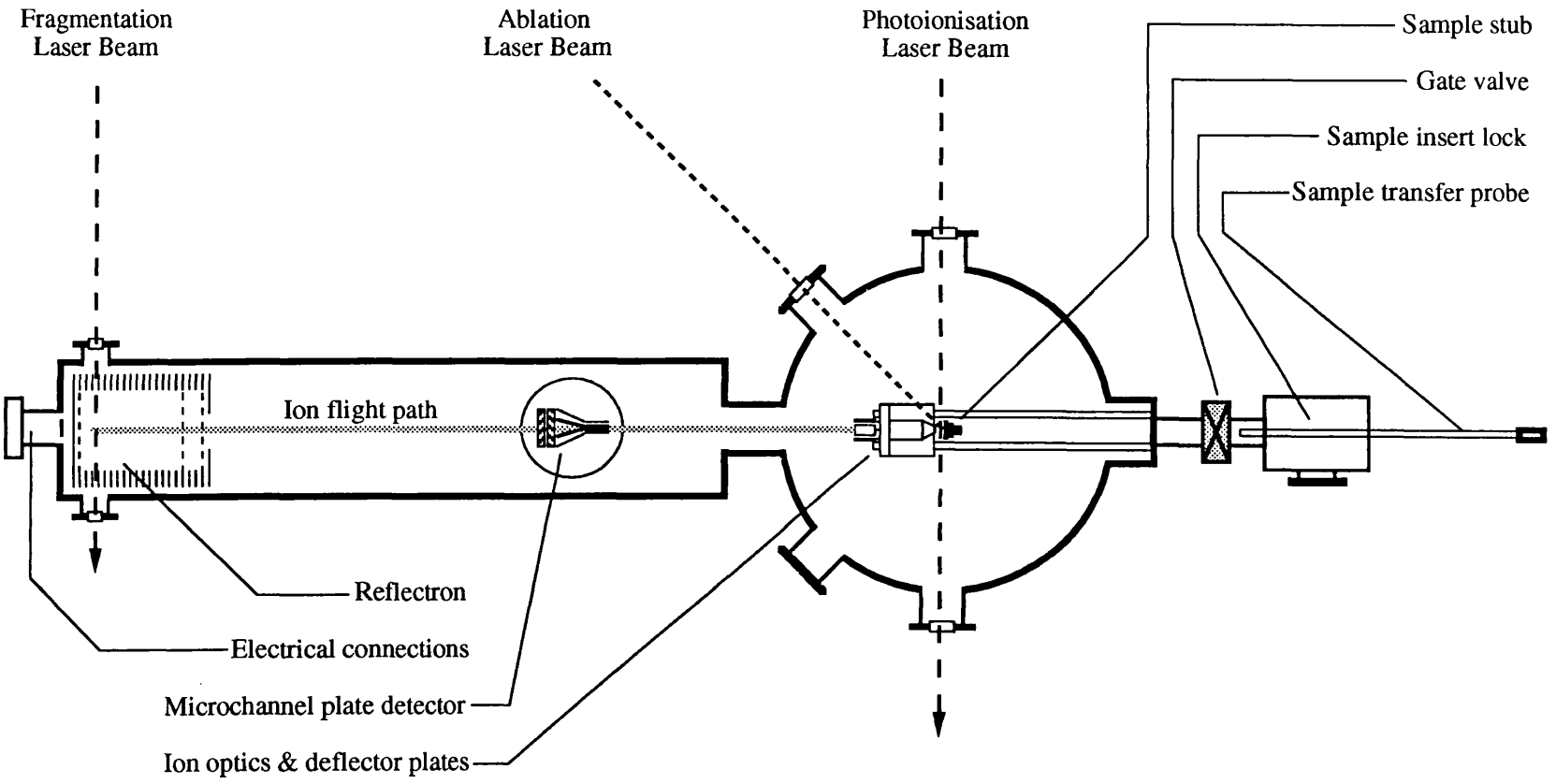

Fig.3.1 Plan view of the mass spectrometer

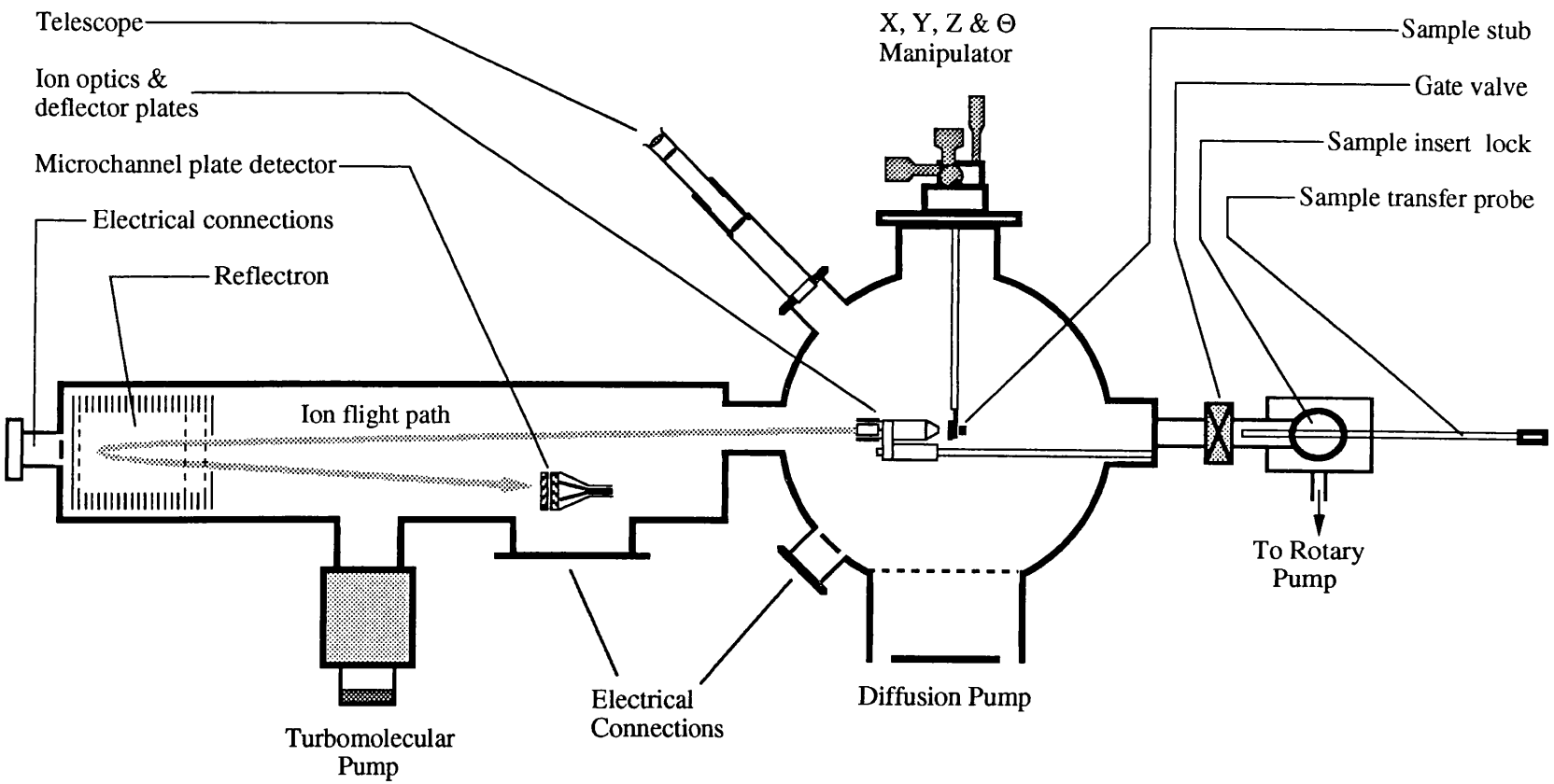

Fig.3.2 Elevation view of the mass spectrometer

small vacuum chamber which is pumped out before the probe is admitted to the main chamber. Using this system allows the pressure in the main chamber to return to normal within 5 minutes of a sample changeover occurring.

The majority of the ports on the main chamber have been fitted with fused quartz windows and are used to admit laser beams to the sample stub region and to allow direct viewing of the chamber interior. A telescope has been fitted to the viewing port directly above the TOF arm. This allows for more discrimination in the choice of ablation analysis area on the sample stub surface.

Two small ports were added to the TOF arm, at the far end of the reflectron. These are fitted with quartz glass windows and allow access for a laser beam to the ion turnaround point in the reflectron. These ports were installed to facilitate the ion fragmentation studies mentioned briefly in Chapter 1, initial results of which are shown in Chapter 7.

Vacuum Pumps

The pressure in the mass spectrometer is normally constant at a base of approximately 10^{-9} torr. During ablation analysis this base pressure can rise by an order of magnitude. The system operating pressure is maintained using a variety of vacuum pumps. Most of the work is performed by a diffusion pump (Edwards Diffstak Mk2, model 160) which has a pumping speed of 700 litres per second. This pump is located at the base of the main chamber. The TOF arm does not require this level of pumping and is serviced by a turbo-molecular pump (Edwards ETP6), which has a pumping speed of 200 litres per second. Both of these pumps are backed by rotary pumps.

Ion Optics

The ion source optics are shown in Fig.3.3. These ion optics were designed by the author using the software package SIMION4 and installed in the mass spectrometer early in the authors work. All data taken by the author was obtained using these optics. The first four

elements of the optics are designed to extract ions created near to the sample stub surface and produce a collimated beam of ions. The plates at the rear of the optics are designed to deflect the ion beam, both in the horizontal and vertical, by applying a small voltage to each set. This deflection of the beam is required to direct the ions down the TOF arm to the reflectron, and subsequently the detector.

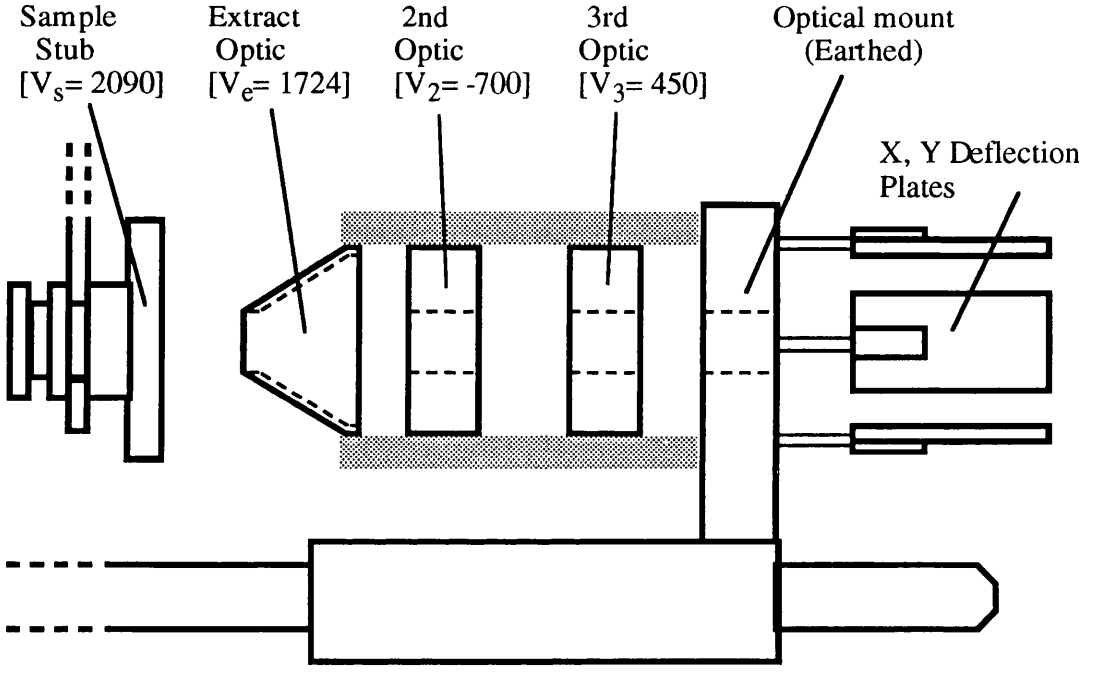

Fig.3.3 Ion optics and voltage biasing

The electrostatic lens, or reflectron, is located at the far end the TOF arm. This reflectron is shown in Fig.2.2 (Chapter 2, section 2.1.3) along with details in the text describing the operation and theory of the reflectron.

Previous to the installation of the new ion optics an 'electrostatic particle guide' had been used when the spectrometer was operated with an ion acceleration potential of less than 3 kilovolts. This was designed to increase the transmission of the system and took the form of a fine wire strung along the ion beam path. A small negative voltage (< -30 volts) was applied to this wire, forming a small potential well around the wire, which helped to correct for any radial dispersion of the ion beam packet.

Following characterisation of the mass spectrometer with the new ion optics, it was found that both the resolution and the transmission of the system were improved if the wire was grounded, despite the fact that the acceleration voltage used was 2.1 kilovolts. The wire was subsequently removed at a later stage when the TOF arm was opened for maintenance.

Detector

A dual microchannel plate (MCP) ion detector (Gallileo Electro Optics, model FTD-2003) was used in the mass spectrometer. This is shown in Fig.3.4 along with the voltage biasing of the plates. This particular model has a 50 Ω impedance matched anode/vacuum feedthrough, which insures optimum time resolution with minimum pulse reflections. Single ion pulse width is quoted at 1 ns with a pulse rise time of less than 1 ns. Although the diameter of each microchannel plate is 25 mm, the active area of the collection anode is slightly less, having a diameter of 20 mm. This detector was installed in the system at the same time as the ion optics described above. The resistance of the detector (both plates) was measured on installation as 340 MΩ.

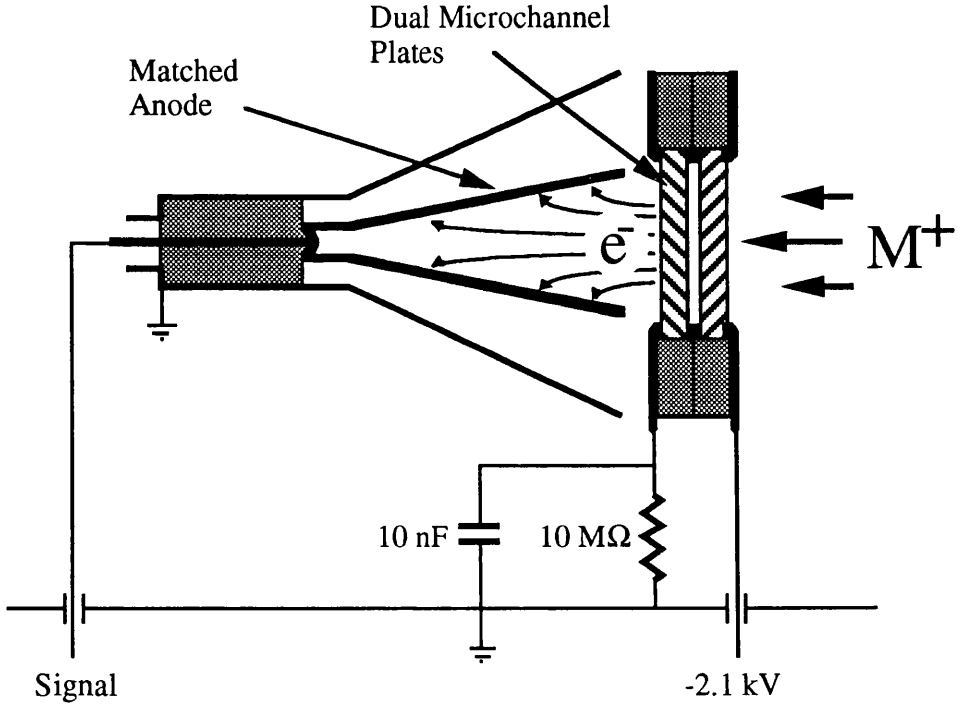

Fig.3.4 Gallileo dual microchannelplate detector

The voltage applied to the MCP was often varied in order to a) reduce the size of the detector output signal when large numbers of ions were incident on the detector, and hence minimise any saturation effects and b) increase the sensitivity of the detector when small numbers of ions were expected. The dependence of the detector signal on the applied voltage was determined in order that data obtained at reduced, or increased operating voltages could be related to that obtained under normal operating conditions.

3.2 Lasers

A wide variety of lasers were used for the experimental work carried out by the author. These were used in two particular areas of application; ablation and photoionisation.

Ablation is the first step in the MALDI process and is generally performed using lasers operating at wavelengths in the ultraviolet, although infrared or visible lasers can be used as well. The wavelength is the most important characteristic of the ablation laser, and should be matched to a strong absorption in the matrix material. The temporal and energy stability of the laser pulse, and the spatial profile of the beam, are secondary considerations in most applications of MALDI. However, these parameters become important when investigating the fundamental physics of the technique. Nitrogen lasers are used in most laboratories and commercial MALDI machines, because of their operating wavelength, low cost and reliability. Nitrogen lasers were used almost exclusively in the MALDI ablation work performed by the author.

A range of different wavelengths were required for photoionisation. To probe the neutral species present in the MALDI generated plume, non resonant photoionisation was performed, primarily using the quadrupled output from a Nd:YAG laser (266 nm) and the doubled output from a dye laser. The ideal technique to use in plume analysis of this type is a non-selective method of ionisation (i.e. ionisation efficiency does not vary between different molecules), but in practice this is very difficult to achieve. At the wavelengths available to the author, a considerable degree

of selectivity was apparent between different neutral species in the ablation plume.

Some of the plume analysis was performed using resonant multiphoton photoionisation (Chapter 6). This is where the wavelength of the laser is set at a value dependent on the particular atom to be analysed. This atom can then be selectively ionised, as the ionisation efficiency has been enhanced by many orders of magnitude. A tuneable dye laser operating in the visible was used to achieve this. All the photoionisation work was performed at wavelengths in the UV, and frequency doubling was employed to produce these wavelengths from visible or infrared lasers.

Ablation Lasers

Two nitrogen lasers were used over the course of the work detailed in this thesis. The initial work was performed using a Nitromite Laser, model LN 100 (Photochemical Research Associates Inc, Canada). This is a pulsed laser producing laser pulses of 300 ps duration and approximately 50 μJ. The laser cavity operates under atmospheric pressure with a steady stream of nitrogen passing through the cavity (flowing head design). Pulse triggering is controlled by a spark gap which operates at a nitrogen pressure of 30 psi. The output from the laser cavity has poor temporal stability (100-200 ns jitter between trigger and pulse output) and has a considerable beam divergence (approaching 8 mrad in both horizontal and vertical). However, this was not a problem for the basic MALDI experiments performed, which required only one laser. A second laser was purchased for two reasons; to investigate the differences in MALDI characteristics using an ablation laser with a different pulse duration, and to perform detailed analysis of the MALDI plume. This second study required a laser with good temporal stability, as it was anticipated to use time delays of less than 1 μs between the ablation and probe laser.

The laser purchased was a Laser Photonics, LN 300 Sealed Nitrogen Laser (Laser Photonics Inc, Florida). The laser pulse duration of 4 ns is over an order of magnitude larger than the Nitromite Laser, and the output power of 240 μJ per pulse, is also significantly greater. The laser

tube and optics are sealed removing the need for a nitrogen supply and gas lines. Instead of a spark gap, the laser output is triggered using a low jitter thyratron which gives the laser a command jitter of +/- 2 ns (laser pulse jitter of ~5 ns). This is ideal for crucial timing applications. Due to the design of the optical cavity, the laser output has a low beam divergence (1.6 x 0.7 mrad, horizontal x vertical) which allows it to be focused to a smaller focal spot than the Nitromite.

Photoionisation Lasers

The laser system used comprises of two Spectralase 4000 dye lasers (Spectron Laser Systems, Rugby, UK) and a Spectron SL2Q & SL3A Q-Switched Nd:YAG laser.

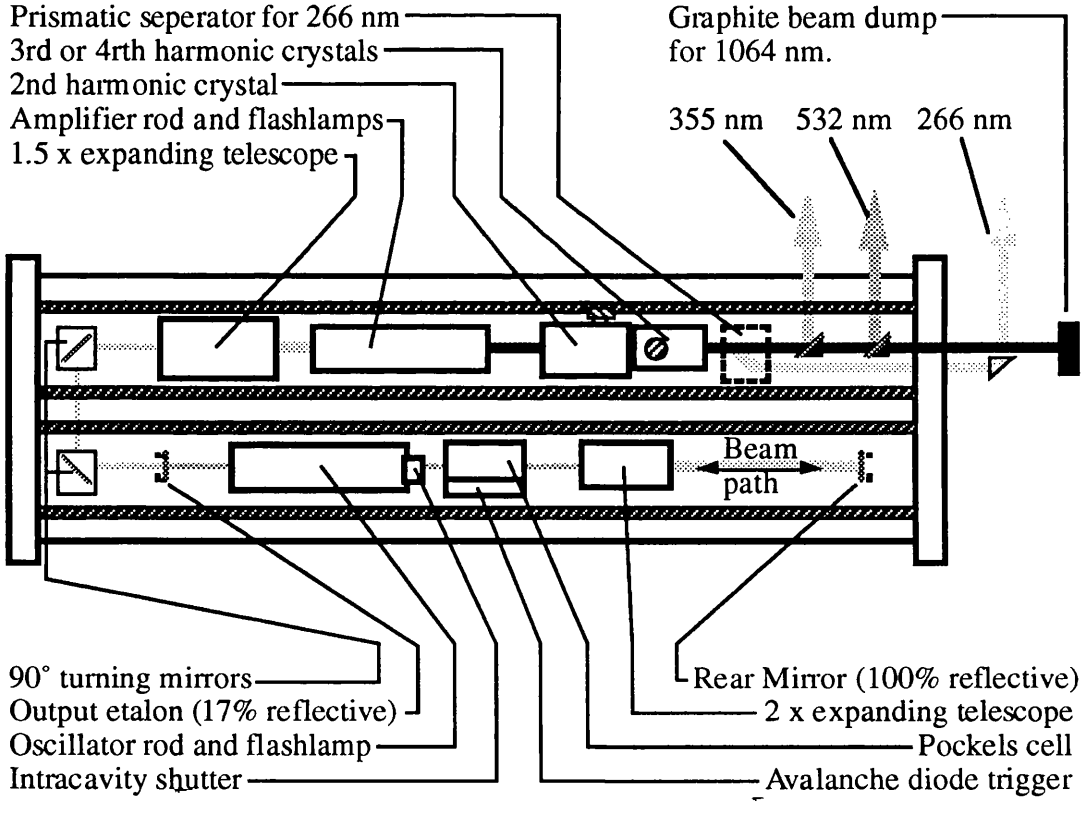

Fig.3.5 Schematic diagram of the Spectron Nd:YAG laser

The Nd:YAG laser is shown schematically in Fig.3.5. It can be separated into two parts; the oscillator cavity and the amplifier and harmonic generation crystals. The laser cavity contains a Nd:YAG crystal rod pumped by a single flashlamp, a pockels cell and a beam expanding telescope. The pockels cell was initially triggered using a krytron valve housed in the laser control rack. This proved to be unreliable, and was replace by an avalanche diode chain triggering system in May 1994. The oscillator cavity is formed using mirrors of unequal curvature (plano/concave). Using this geometry, the addition of a beam expanding telescope is necessary in order to form a stable resonator with reasonable physical dimensions (1 m long in this case).

The output from the oscillator cavity is turned through two 90° mirrors before passing through the amplifier rod, which is pumped by two flashlamps. The laser output after the amplifier rod (1064 nm) is approximately 800 mJ per pulse, with the laser operating at 10 hertz. Through a variety of potassium di-deuterium phosphate (KDP) crystals it is possible to generate light at 532, 355 or 266 nm, although simultaneous generation of the third and fourth harmonics is not possible in this laser. The laser pulselengths are approximately; 16 ns at 1064 nm, 10 ns at 532 nm, 6 ns at 355 nm and 5 ns at 266 nm. The harmonic generation crystals are maintained at 55° C to provide optimum stability in the harmonic outputs. The second and third harmonic outputs can be selectively filtered from the fundamental beam using coated mirrors. These mirrors are removed when the fourth harmonic is required, and replaced with a prismatic separator.

Both Spectrolase 4000 dye lasers were used by the author. These two lasers are very similar and they will be referred to hereafter as the red or blue dye laser for the following reasons. The red dye laser is designed to be pumped by the second harmonic of a Nd:YAG (532 nm) and can cover the full wavelength range 540-750 nm, using a variety of different laser dyes. The layout of the red dye laser is shown in Fig.3.6. The blue dye laser is designed to be pumped by the third harmonic of a Nd:YAG (355 nm) and can cover the wavelength range 400-750 nm, although it is only used for wavelengths below 540 nm because of the lower energy available in the pump laser. A secondary consequence of the lower energy pump

pump beam is that the blue dye laser has only one amplifier cell compared to the two fitted in the red dye laser. Wavelength selection is achieved by rotating the mirror opposite the diffraction grating. The mirror mount is connected to a sine drive unit which is operated by entering the necessary wavelength and scan speed into the controller terminal. The dye lasers were specified to have a resetability of 1 pm and an accuracy of 5 pm, but in practice this was not found to be the case. The laser wavelength varied considerably with room temperature and changed by 25 pm depending on whether the wavelength was scanned to longer of shorter wavelengths (due to slack or wear in the sine drive mechanism).

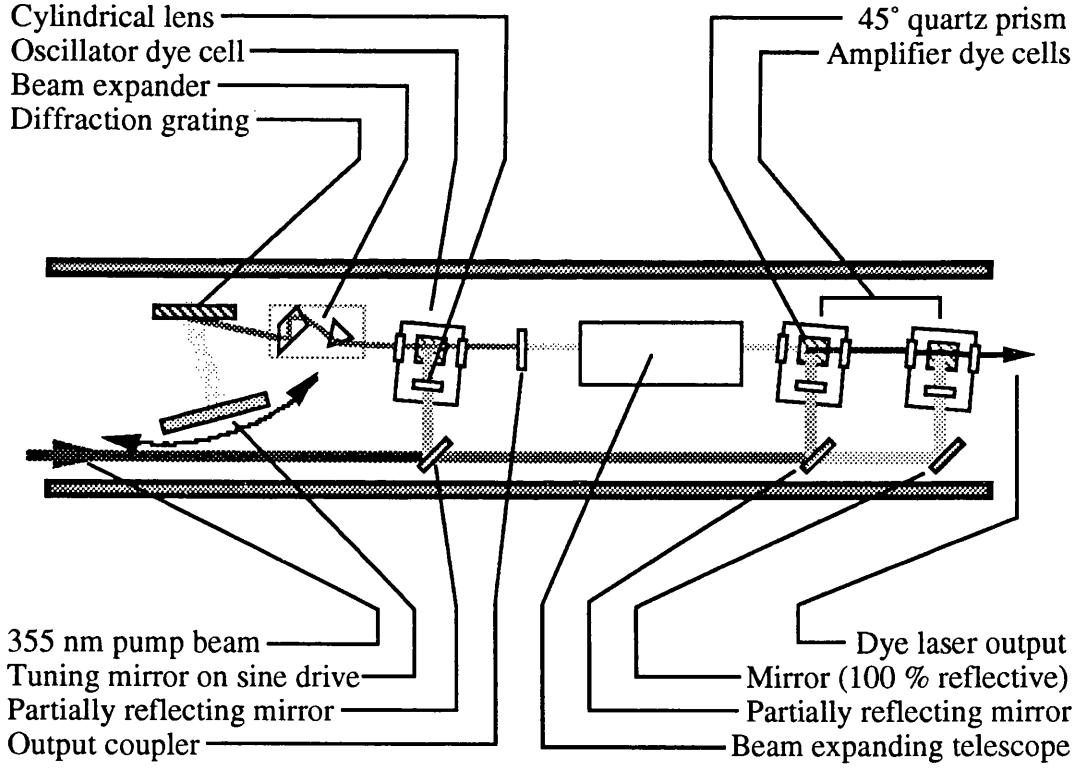

Fig.3.6 Schematic diagram of the Spectrolase 4000 red dye laser

Some of the photoionisation work was performed using the 266 nm radiation from a Quantel YG 580 (Quantel, Cedex, France) Nd:YAG. This laser operates in a similar manner to the Spectron Nd:YAG. It only became necessary to use this laser in experiments where ablation was

being performed with the dye laser output, and a second YAG was required to perform postionisation at 266 nm.

3.3 Optical Equipment

A combination of mirrors and 45° quartz prisms were used to transfer the Nd:YAG and dye laser beams to the sample chamber. All optical mounts were affixed to the optical bench using magnetic bases. The nitrogen lasers were situated in such a way that the output was directly incident on the sample stub, through the 45° analysis port. The photoionising lasers (plume probe) were focused into the system using a 47 cm quartz lens (for 266 nm) and a 25 cm quartz lens (for 243 nm and 310 - 350 nm). A 22 cm quartz lens was used to focus the nitrogen ablation lasers onto the sample. All lenses were mounted to allow micrometer adjustment in both the horizontal and vertical planes.

Control of the laser pulse energy was achieved using a precision optical attenuator (Newport model M-935-5-Opt)). This was used on both ablation and photoionisation lasers. While the attenuator was being used to control the photoionisation laser, the power of the ablation laser could be adjusted using glass plates, in a stepwise fashion.

Frequency Doubling of Dye Lasers

As mentioned previously, each dye laser can only produce laser light in the wavelength region above 400 nm. All photoionisation work required wavelengths in the region below 355 nm, and to achieve this, frequency doubling of the dye laser output was necessary. A SHG Autotracker (Inrad model 5-12, Northvale, NJ, USA) was used when it was necessary to scan the laser wavelength. The autotracker continuously monitors the UV output from the doubling crystal, and adjusts its angle such that the optimum UV output is maintained as the wavelength is scanned. When wavelength scanning was not required, the frequency doubling crystal was placed in a mount (Inrad model 820-360) and angle tuned manually using a micrometer.

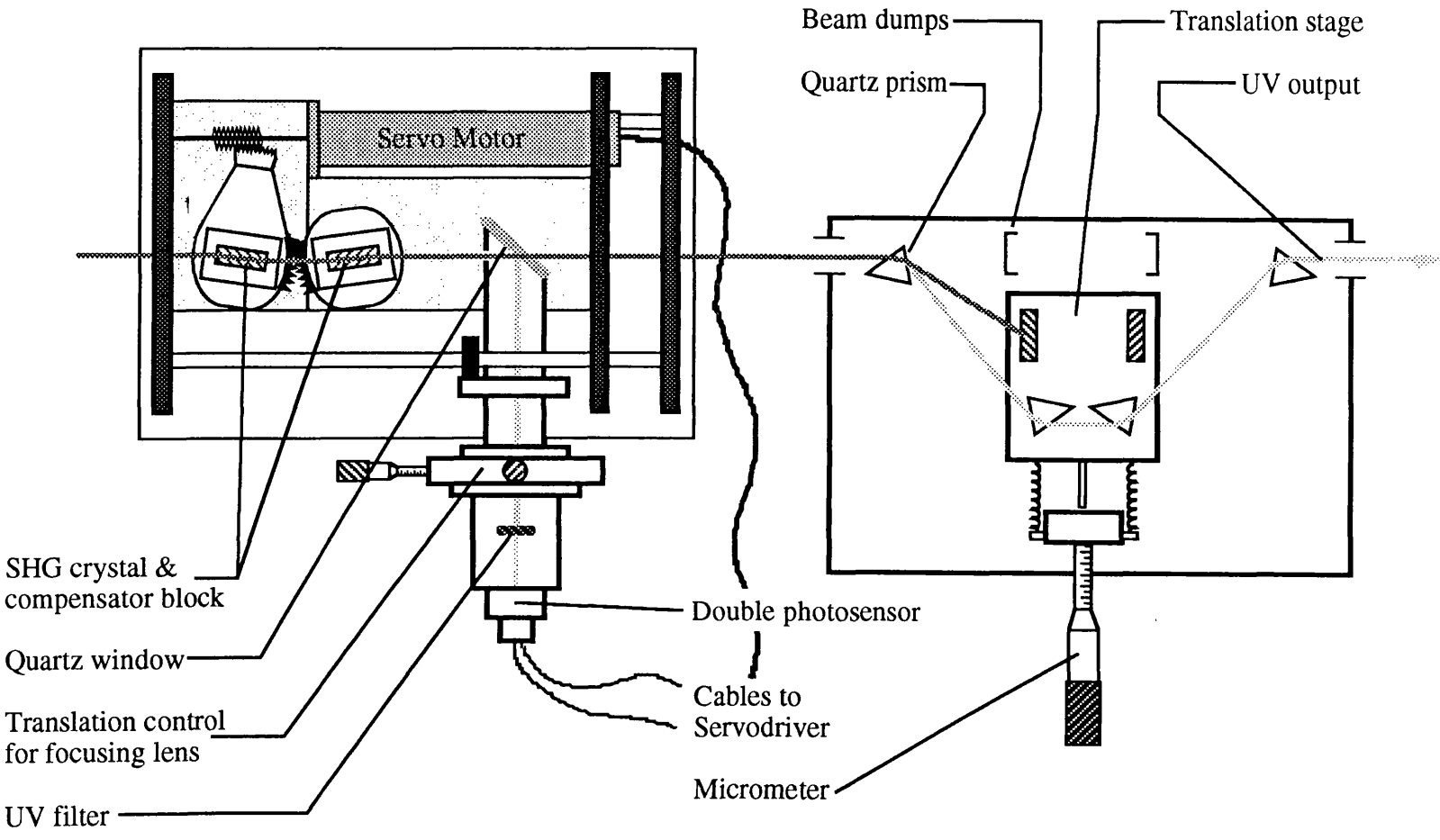

Fig.3.7 The Inrad Autotracker used in wavelength scanning experiments coupled with the Inrad Prismatic Seperator

The doubled UV output from the autotracker was separated from the fundamental using a harmonic separator (Inrad model 752-104). A schematic of the autotracker and separator is shown in Fig.3.7. This separator is highly efficient at transmitting plane polarised light. The laser beam is refracted in four prisms before being emitted along the original flight path. The separator is designed so that the angle of incidence in each prism is close to Brewsters angle. If the prismatic separator is oriented such that the direction of the electric field oscillation of the laser beam lies in the plane of incidence, then nearly 100% of the laser beam is refracted into each prism. Although some of the light is internally reflected at the exit face, most of the beam is refracted out of the prism giving the separator an overall transmission of approximately 95%. This compares very well with the typically poor transmission through most available UV filters (20-30 % for 210-250 nm and 50-80 % for 250-350 nm).

Detectors

Three different types of photodetectors were used by the author. Measurements of the actual ablation and photoionisation laser pulse energies were made using two pyroelectric joulemeters (Molectron Corp., CA, USA), models J3-09 (response of 1.25 volts per millijoule) and J4-09 (response of 0.79 volts per millijoule). This type of detector integrates the output from an optical sensor over the duration of the laser pulse, and emits an output pulse with a peak voltage proportional to the energy in the incident laser pulse.

During initial setting up and optimisation of both the Nd:YAG lasers and the dye lasers, a bolometer was used to measure mean power output (Detector model 03A-p-cal and meter model DGX, Ophir-Aryt Optronics Ltd, Israel).

Fast photodiodes were used to provide the trigger signals for the data analysis system (digital oscilloscope and PC) and for the laser pulse generator, used to control the timing sequences between the ablation and photoionisation lasers.

3.4 Data Acquisition and Control System

Laser Control

A system was needed to accurately control the timing between ablation and photoionisation lasers, where variable delays in the range 0 to 15 microseconds were required. A custom delay unit was used to perform this function. A Stanford DG535 digital gate and delay generator (SRS, Sunnyvale, CA) was used to provide the trigger signal to the delay unit, and a trigger pulse to the Nitromite laser. A variety of different lasers was used for both ablation and photoionisation, each laser requiring a different set of trigger pulses. As a consequence of this, the delay unit timing sequence was not fixed, and had to be constantly altered to reflect the lasers in use at the time. Timed outputs were required for Q-switching, flashlamp and laser pulse triggering, and sometimes even to recharge capacitor banks depending on laser type.

A temporal drift on the unit output was identified during the course of the work, and was due to the type of electronics used to generate the delays. This drift was of no significance during work with the LN 300 ablation laser due to the particular timing sequences used, but did however affect work with the Nitromite laser. When photoionisation experiments were performed using the Nitromite laser for ablation, the timing between laser pulses had to be monitored in real time on an oscilloscope to ensure that the correct delays were indeed being used. For all other work the delay could reliably be set on a micrometer control at the front of the delay unit.

Data Acquisition

Data acquisition was performed using a digital storage oscilloscope (9410, LeCroy Corp., NY, USA) coupled to an IBM compatible personal computer (PC). The oscilloscope features; dual signal input (100 megasamples per second analogue to digital conversions (ADC) systems), wide bandwidth (150 MHz), two 10 thousand byte memories for waveform acquisition, four 10 thousand byte memories for waveform processing, a variety of different acquisition modes and a library of mathematical

processing routines for waveform analysis. All waveform analysis was performed using these routines. The detector ion signal was fed directly to the oscilloscope from the MCP without any form of amplification. Large matrix and analyte ion signals are a characteristic of MALDI, and as a consequence all ion signals of interest were well above the noise level even without signal amplification.

The 9410 oscilloscope has an optional facility for data storage, but this was not installed on the equipment used by the author. To enable data storage the oscilloscope was interfaced to a PC using an RS-232 bus. Software was written by the author (programme LECGPIB) to allow the transfer of files between the oscilloscope and the computer hard drive. The files generated by the oscilloscope were stored in a format particular to LeCroy. Before waveforms could be transferred to a graphics package, they first had to be reformatted using a program called 93REM (LeCroy Corp.) to a default file format, with one data value per line.

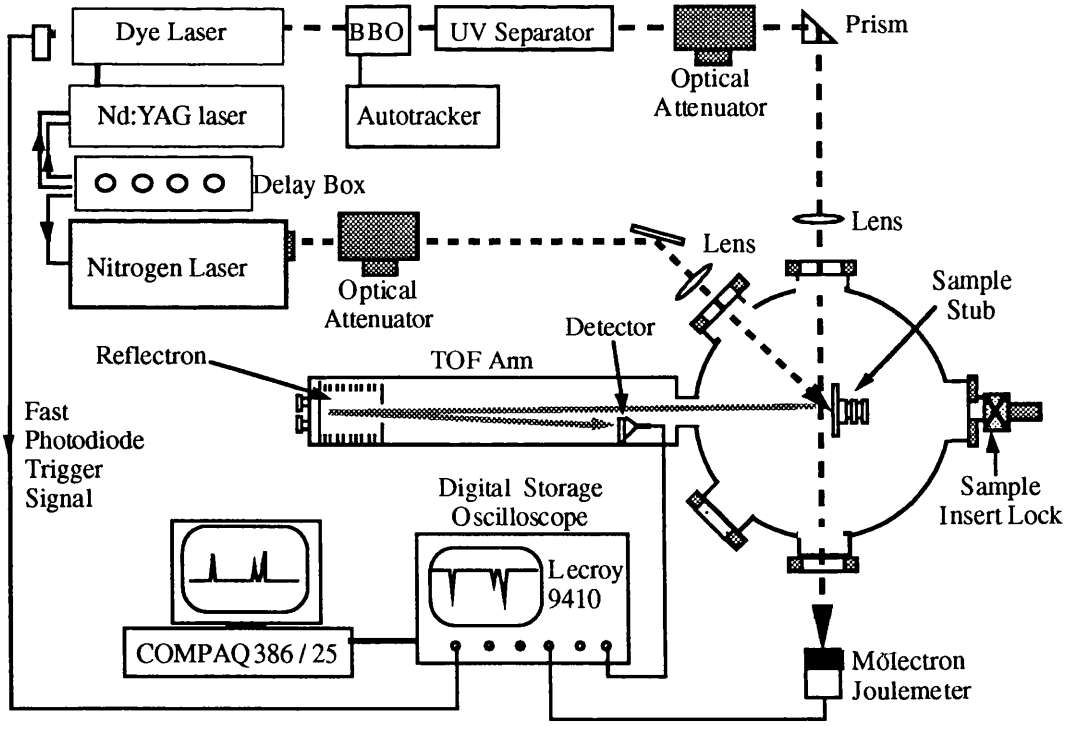

Fig.3.8 Complete system showing typical arrangement for PAI experimental work

A typical arrangement of the experimental equipment described in sections 3.1 to 3.4 is shown schematically in Fig.3.8. This particular arrangement was used in the PAI and hydrogen work described in Chapters 5 and 6.

3.5 Samples and Preparation Techniques

Compounds Used

Two different matrices were used in this study. The majority of the work was carried out with the matrix 2,5-dihydroxybenzoic acid (DHB). DHB was chosen for the bulk of the work as it is an excellent matrix and can be prepared in the form of single crystals with relative ease, which was an essential requirement due to the nature of the plume analysis work which would be carried out. Some work was also carried out using the matrix sinapinic acid, although not nearly to the same extent as that with DHB.

The compounds used as analytes were substance P, bovine insulin and tyrothricin. These particular compounds were chosen because of their widespread use as standard test samples, and are well documented in the literature. All matrices and analytes were obtained from Sigma Chemical Company Ltd (Poole, Dorset, UK) and were used without further purification. Absorption spectra were obtained for all matrix and analyte compounds used in the authors work and are shown in Fig.3.9. It is immediately apparent that only the two matrix compounds show strong absorption in the wavelength range used for ablation in most UV MALDI experiments.

A variety of solvents were tried during the initial stages of the work. The solvents tried during the preparation of different mixtures were; methanol, ethanol, propanol, acetone and water in varying proportions. The solvent mixture finally chosen for most subsequent sample preparations was that used by Karas and Hillenkamp (Strupat 1991) namely a mixture of water and ethanol in the proportions 9:1. All solvents used in sample preparation were analytical grade and were obtained from a variety of sources, while the water used was doubly de-

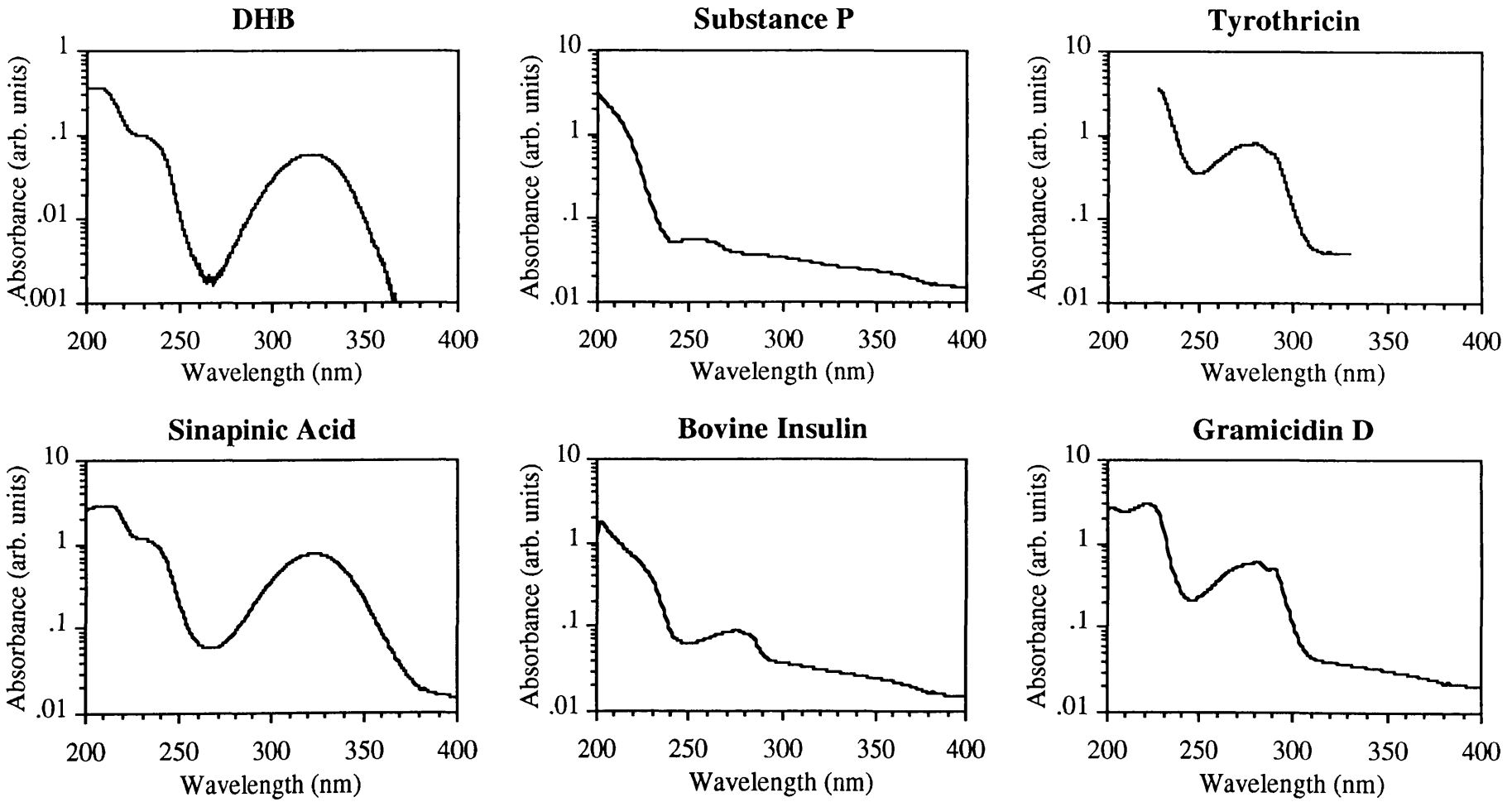

Fig.3.9 Absorption spectra of the matrices and analytes used

ionised and prepared in house. Small quantities of trifluoroacetic acid (TFA) (Sigma Chemical Company Ltd) were often added to sample preparations in order to enhance the solubility of analyte molecules.

Sample Preparation

Samples were prepared in a number of different ways in order to investigate the effect on the quality, stability and general form of the spectra. This is described in more detail in Chapter 4. The methods used to prepare samples can essentially be split into five;

i) Vacuum drying (extremely rapid).
ii) Drying in stream of warm air or nitrogen (rapid).
iii) Drying in laboratory atmosphere at room temperature (slow).
iv) Drying in fridge atmosphere at a few degrees Celsius (very slow).
v) Growing single crystal samples from solution in fridge.

Methods one to four all involved placing an aliquot of sample solution on the prepared sample stub.

Glassware and sample stubs were cleaned rigorously to avoid 'memory' effects. All equipment was washed with detergent in hot water, then thoroughly rinsed with tap water. The glassware was cleaned of biological contaminants by washing in a bath of chromate cleaning solution, while the sample stub was lightly polished using fine emery paper. The chromate cleaning solution was prepared by mixing 35 ml of saturated aqueous chromium (vi) oxide in one litre of concentrated sulphuric acid. Glassware and sample stubs were then washed three to four times in distilled water, followed by a final rinse in analytical grade ethanol prior to either blow drying using a heat gun or compressed nitrogen, or oven drying in a vacuum oven.

Chapter Four

Preliminary Investigation of MALDI Characteristics

4.1 Introduction

The technique of MALDI was novel to the author's research group in Glasgow. This Chapter details the initial characterisation work performed on the mass spectrometer and describes some of the basic properties of MALDI. Comparison is made with similar work described in the literature.

4.2 System Calibration and Miscellaneous

As detailed in the instrumentation chapter, new ion optics were installed in the mass spectrometer at the beginning of the author's program of work. As a consequence of this a full system calibration was required. It was decided to use caesium iodide (CsI) as a standard sample in order to obtain an approximate mass calibration for the system, and to determine whether the optimum experimental operating parameters corresponded with those calculated using SIMION4. CsI is a commonly used mass calibrant for TOF mass spectrometers (Grundwurmer 1994), and is usually used in conjunction with an absorbing matrix. Sucrose, lactose and DHB were tried as matrices, with the best results obtained using a 1:1 mixture (by mass) of lactose and CsI. Ablation was performed using a 300 ps nitrogen laser. No cluster ion signals could be obtained from ablation of a pure CsI sample. A typical mass spectrum is shown in Fig.4.1.

In some spectra the fifth member of the series, $[(CsI)_4Cs]^+$, can just be determined above the noise level. The mass of cluster which can be observed depends on both the sample preparation technique and the acceleration (or post-acceleration) potential. A series of spectra was taken to investigate the effect varying the voltage settings of the ion optics and reflectron had on the resolution and transmission of the

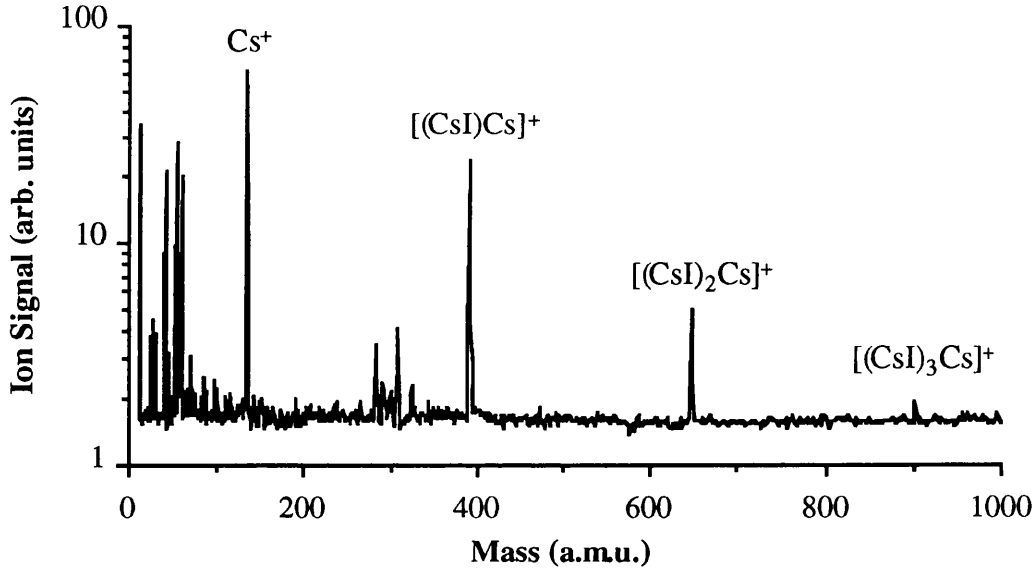

Fig.4.1 Mass spectrum from sample of CsI and lactose (1:1 ratio by mass). Ablation using a 300 ps nitrogen laser with a fluence of 37 $mJcm^{-2}$.

spectrometer. The optimum voltage settings obtained (given in chapter 3) were comparable with those predicted using SIMION4, and resulted in a spectrometer mass resolution of between 1400 and 1500 at 393 amu (Cs_2I) for single shot spectra. However, due to a shot-to-shot variation in peak position, the mass resolution of summed spectra was not more than 500. It was initially thought that this was a triggering problem, as the oscilloscope was triggered using the laser trigger out signal, for which a temporal variation was observed in relation to the actual laser pulse, and consequently triggering was changed to a fast photodiode. Paradoxically, this resulted in a slightly worsened mass resolution. The reason for this was never satisfactorily explained, but was believed to be due to laser power fluctuations directly related to the temporal jitter. This resolution degradation effect is not the same as that observed in MALDI, where even for single shot spectra the mass resolution is typically low.

The mass calibration constant for the spectrometer (ratio of the square of the flight time (μs) to the ion mass-charge ratio (amu/z)) is approximately 31.3, but varies with each spectrum due to small variations in ion source conditions, and must be calculated anew for each spectrum. Spectra were calibrated internally using ion peaks of known mass, usually matrix

specific peaks. In real analyses of unknown compounds, known internal calibrants of similar mass to the unknown molecule can be added to the sample to achieve greater accuracy of mass determination.

The majority of the low mass ion peaks observed in Fig.4.1 are due to ablation from the steel substrate and are not specific to the lactose matrix. These peaks are observed sporadically in MALDI spectra, their appearance dependent on both the sample preparation method used and the ablation laser pulse energy. Part of a typical mass spectrum from ablation of the steel sample stub alone is shown in Fig.4.2.

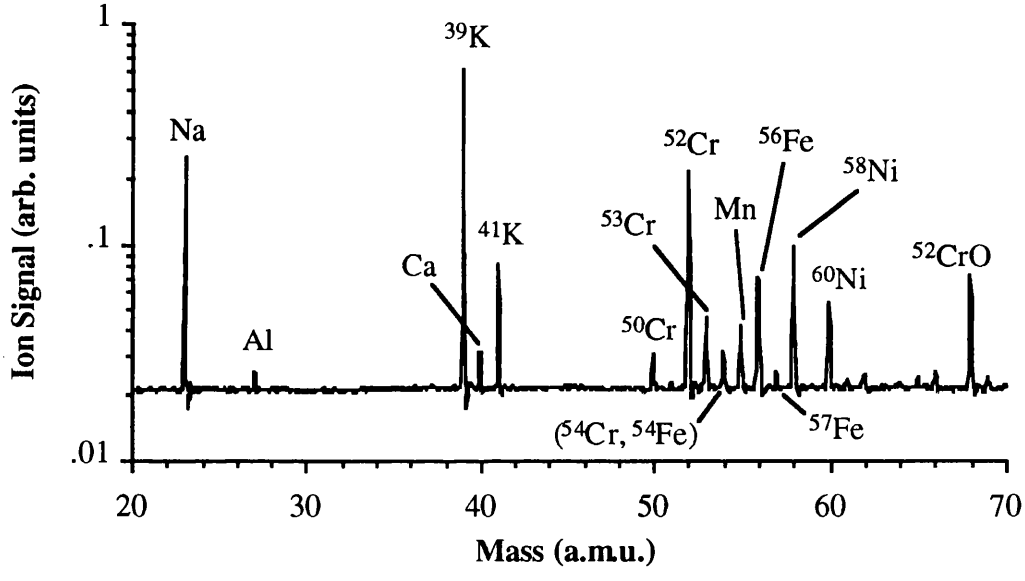

Fig.4.2 Mass spectrum from steel substrate. Ablation using a 300 ps nitrogen laser with a fluence of 58 $mJcm^{-2}$.

During the course of the work it was necessary on occasion to reduce the microchannel plate detector voltage in order to avoid detector saturation. A series of DHB mass spectra were taken to investigate the ion signal dependence on detector voltage and allow a direct comparison to be made between spectra taken with different detector voltages. Single crystal DHB samples were used in order to obtain good signal reproducibility. The results of this are shown in Fig.4.3. The detector response is exponential over most of the voltage range investigated, but shows a slight fall off in response above approximately 1900 volts.

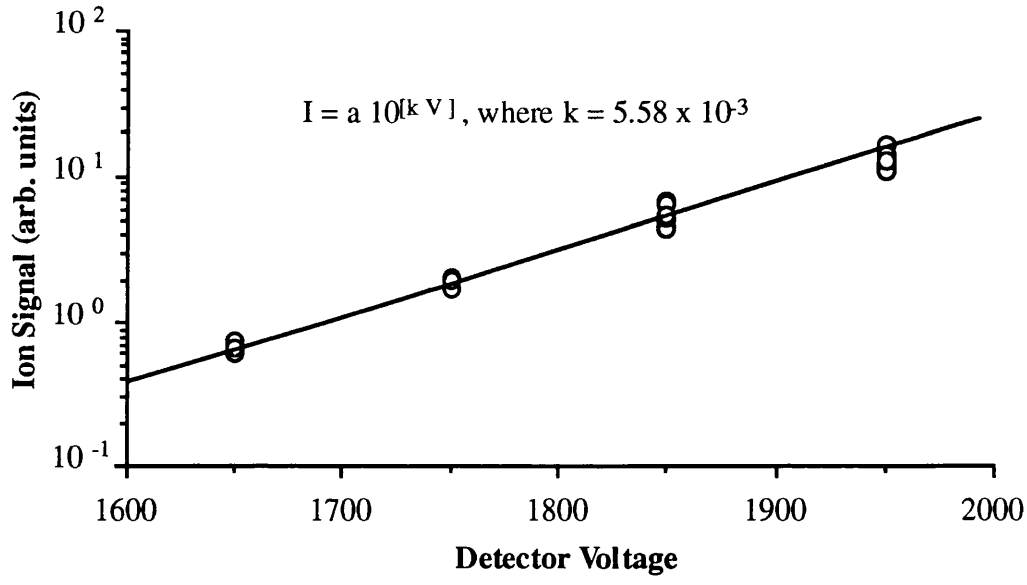

Fig.4.3 Graph showing response of microchannel plate detector (I) as a function of applied voltage (V).

Throughout the course of the experimental work, an ion signal at a mass of 354 amu was occasionally observed in spectra (Fig.4.4). This was eventually identified as apiezon A (average molecular mass 354 amu)

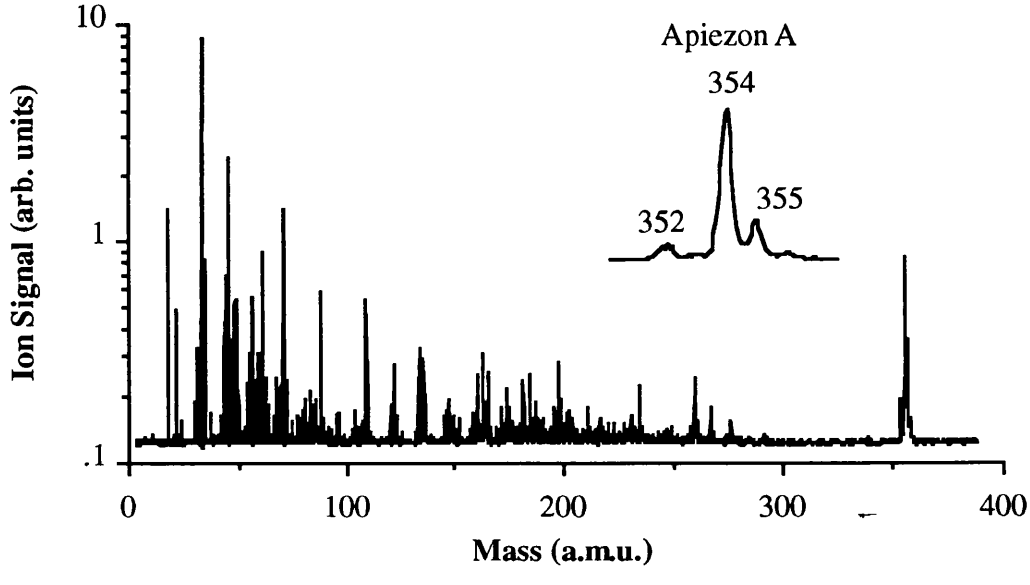

Fig.4.4 Mass spectrum from steel substrate showing contamination from the medium vapour pressure diffusion pump oil, apiezon A. Ablation using the quadrupled output (266 nm) from a Nd:YAG laser with a fluence of 42 $mJcm^{-2}$.

which was present as a contaminant in the low vapour pressure oil (santovac 5) used in the vacuum system diffusion pump. However, the presence of this contaminant on the sample stub and the internal surfaces of the mass spectrometer did not interfere with the experimental results.

4.3 Basic Matrix and Analyte Spectra

Typical mass spectra obtained from the compounds used in the experimental work are shown and discussed in the following sections.

4.3.1 Matrix Spectra

The mass spectra of pure matrix materials generally exhibit rather simple structure. This is apparent from the spectra shown in Fig.4.5 and Fig.4.6, obtained by the author from ablation of pure DHB. The spectrum shown in Fig.4.5 is obtained from a vacuum dried preparation of DHB, with the ablation laser fluence close to the threshold fluence for production of matrix ions ($F_{th(ion)}$). It can be seen that individual ion peaks are relatively well resolved. This is typical of ablation from vacuum dried samples, or ablation from the crystals formed in standard sample preparations at a fluence just above $F_{th(ion)}$. In the spectrum shown in Fig.4.6 the ion peaks are no longer well resolved, and matrix cluster ion species make a significant contribution to the ion signal. This is typical of ablation at fluences significantly above $F_{th(ion)}$, or ablation following a large number of laser shots from the same site. The identity of these ion peaks is discussed further below.

Until a number of years ago it was generally assumed that even-electron molecular ions were the predominant ion species produced following laser desorption of polar organic molecules (Strupat-1991). It was believed that polar organic molecules were desorbed as preformed ions, resulting in spectra containing only even-electron ions such as the protonated molecular ion or fragments resulting from the loss of small neutral molecules such as H_2O, CO_2 or NH_3. However, a systematic investigation of the ion signals obtained from a large selection of UV absorbing

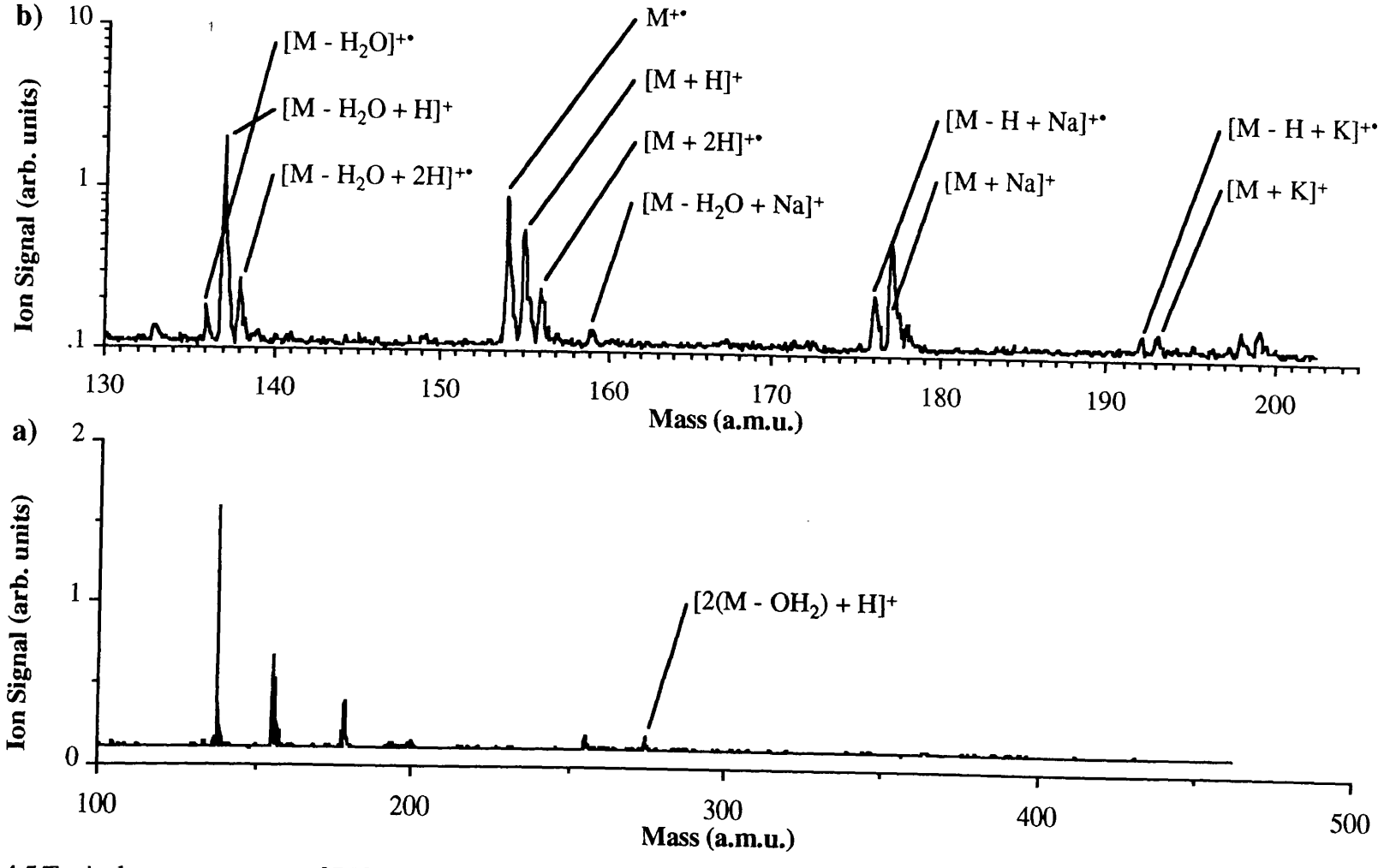

Fig.4.5 Typical mass spectrum of DHB from vacuum dried preparations, or using low ablation fluence* showing well resolved peaks. Ablation using a 300 ps nitrogen laser with a fluence of 13 $mJcm^{-2}$. The full spectrum is shown in a), with the parent and cation adduct ion peaks expanded in b). $M^{+\bullet}$ represents the radical matrix parent ion. [* NB alkaline cation adduct ions are not present in ablation of crystal preparations]

compounds (Ehring 1992) showed that in fact the appearance of odd-electron molecular ion signals was not uncommon. Sinapinic acid and DHB were both found to produce even-electron ions and radical odd-electron ions.

There are several ionisation models which have been proposed in an attempt to explain the observed ions in MALDI. Most of the discussion in the literature centres on the following two ionisation mechanisms: excited state proton transfer reactions between matrix and analyte molecules due to an increased acidity of matrix molecule in the excited state, and; photochemical reactions between neutral analyte molecules and radical odd-electron matrix ions formed by photoionisation of neutral matrix molecules. This is discussed in more detail in Chapter 2, section 2.4.

Discrimination between the even and odd-electron ion signals can best be observed in Fig.4.5. The spectrum shown in Fig.4.5 contains only three groups of sizeable intensity which are related to DHB, each of which contains both even and odd-electron ions: a group around the parent ion at 154 amu; a group around the dehydroxylated parent ion at 137 amu, and a group around the matrix parent plus sodium ion at 177 amu. This sodium adduct ion is generally not present in spectra obtained from ablation of samples containing macroscopic DHB crystals, as the crystallisation process excludes low mass contaminants from the resulting matrix crystals. Low intensity dimer ion peaks can usually be discerned centred around the protonated dimer of two dehydroxylated DHB molecules at 273 amu. Sodium and potassium peaks are always present in spectra from vacuum dried samples, but are not shown in Fig.4.5. It has been postulated (Ehring 1992) that the main peak in the spectrum, the dehydroxylated parent ion at M-17, is assumed to be formed from both the loss of H_2O from the protonated parent molecular ion and the loss of the an OH radical from the radical molecular ion. However, there is evidence that this ion signal may result from protonation of the ($M\text{-}OH_2$) neutral species found in the ablation plume (Chapter 5, section 5.3 & 5.4).

Fig.4.6 shows the mass spectrum following ablation from a single crystal sample of DHB at a fluence significantly greater than $F_{th(ion)}$, or following

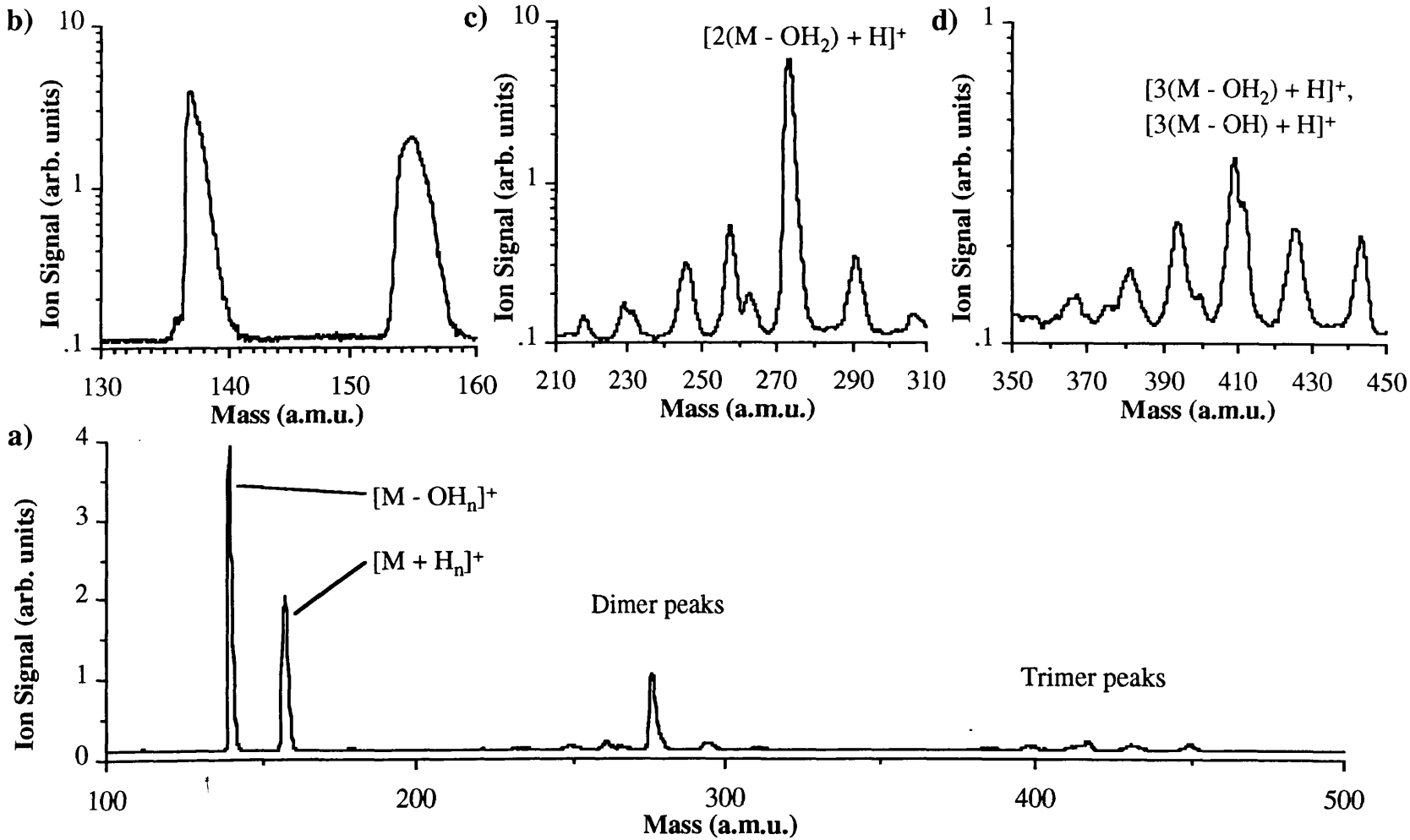

Fig.4.6 Typical mass spectrum of DHB using high laser ablation fluence, or after a considerable number of shots from the same spot, showing poorly resolved peaks. Ablation using a 300 ps nitrogen laser with a fluence of 40 $mJcm^{-2}$. The full spectrum is shown in a), and parent , dimer and trimer ion peaks are expanded in b), c) and d) respectively. $M^{+\bullet}$ represents the radical matrix parent ion, $n \in \{0,1,2\}$.

a large number of laser shots. It is immediately apparent that the resolution has degraded to the extent that discrimination between even and odd-electron ion peaks is no longer possible. In addition, there is now a significant contribution to the total ion signal from dimer and trimer cluster peaks. This is also observed for sinapinic acid (see below) and 4-nitroaniline (Gimon 1992). The dimer $(2(M\text{-}OH_2)+H)^+$ and trimer $(3(M\text{-}OH_2)+H)^+$ signals form the main ion signals of each group, surrounded by lower intensity signals corresponding to loss or addition of mOH_n and/or CO_2 from the dehydroxylated dimer or trimer.

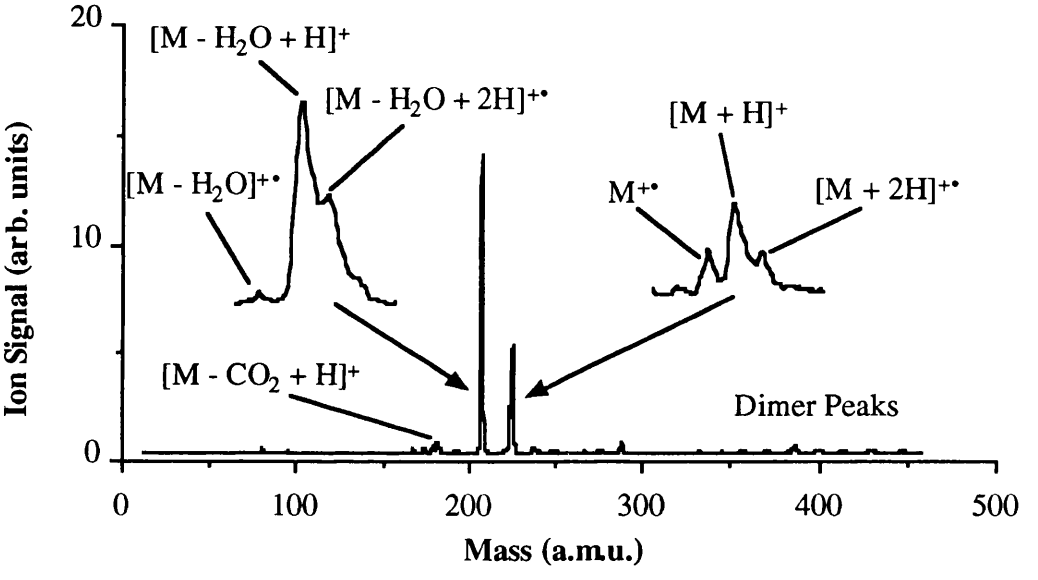

Fig.4.7 Mass spectrum of sinapinic acid from a standard sample preparation. Ablation using a 300 ps nitrogen laser with a fluence of 18 $mJcm^{-2}$. The inserts show an expansion of the parent and dehydroxylated parent, and associated peaks.

The mass spectra obtained from sinapinic acid exhibit very similar characteristics to those obtained from DHB, a typical example of which is shown in Fig.4.7. The main difference in the spectra from sinapinic acid lies in the change in relative intensities between even and odd-electron ion signals in the parent and dehydroxylated parent ion groups. In addition, a low intensity signal is observable due to the decarboxylated parent molecular ion. As with DHB, good mass resolution is obtained at low ablation laser fluence, and abundant dimer and trimer production occurs at high ablation fluences or following a large number of laser shots from the same spot.

4.3.2 Analyte Spectra

As mentioned in Chapter 3 the main analytes used in the authors work were tyrothricin, substance P and bovine insulin. Typical MALDI mass spectra of all three compounds are shown in Fig.4.8, the spectra restricted to the regions containing the analyte molecular ion signals.

Tyrothricin is a mixture of cyclic decapeptides extracted from cultures of the bacteria *Bacillus brevis* (McIver 1994) and has been used as an antibiotic. The mass spectrum of tyrothricin has been well characterised and the three most significant ion signals in MALDI spectra from standard sample preparations correspond to the protonated tyrocidine component of the mixture (tyrocidine A, B & C) at 1271, 1310 and 1349 amu respectively. Substance P is a linear decapeptide found in the brain of all vertebrates. The base ion signal associated with substance P is the protonated parent molecular peak at 1347.7 amu (mass given for the monoisotopic protonated molecule). Quasi-molecular peaks (loss of H_2O or NH_3, M - 8 or the sodium cation adduct) are always present at lower intensities than the base peak, although the relative intensities between these depends on both sample preparation and the laser fluence used. Similar ion peaks are found in the mass spectrum of bovine insulin (average molecular mass of the protonated molecule 5734.7 amu), with peaks due to the loss of CO_2 in addition to those due to loss of H_2O or NH_3. In MALDI spectra of the three analytes used, ion signals resulting from fragmentation of covalent bonds in the molecular backbone were only observed with substance P. This is discussed at the end of this section.

The bovine insulin ion peaks observed in the author's work were very small in relation to the ion signals of lower mass analytes. This is a consequence of the relatively low acceleration voltage (2090 V) and the fact that no post-acceleration of ions was carried out. In light of this it is perhaps surprising that of the analytes used, bovine insulin was the only one for which cluster ions were observed by the author (up to the quadrumer ion at mass 22940 amu).

Laser ablation of the pure analyte was carried out in order to demonstrate that the analyte ion signals observed in mass spectra obtained from

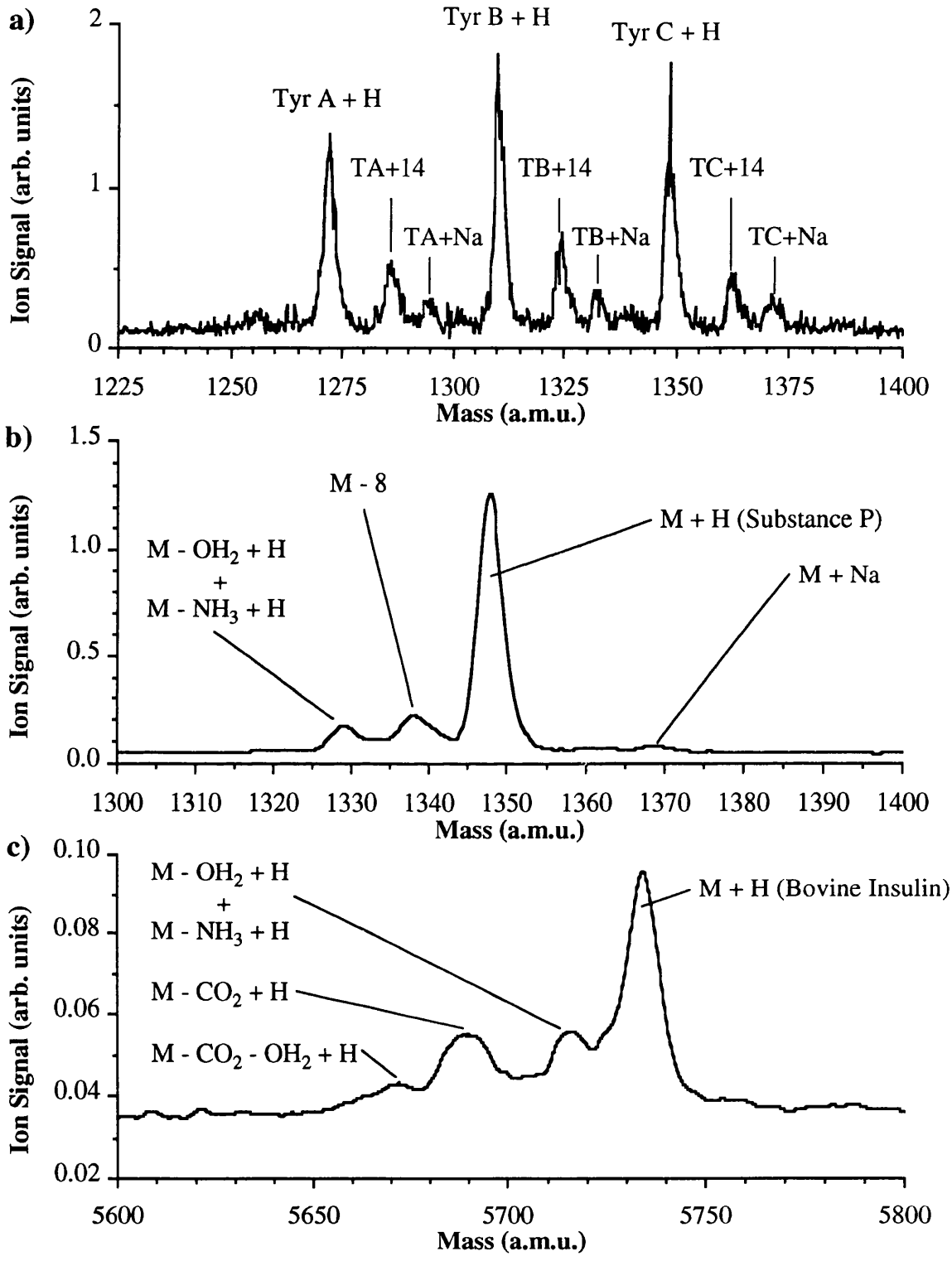

Fig.4.8 MALDI mass spectra of the molecular ion regions of a) Tyrothricin, b) Substance P and c) Bovine Insulin. A certain degree of peak smoothing has been carried out on the spectra for substance P and bovine insulin. Structure is detectable in the molecular ion peaks of the raw data, but the resolution of the spectrometer is insufficient to fully resolve the isotopic distribution. The isotopic distribution of a large molecule must be considered when calculating the mass resolution of the spectrometer, which is significantly better than that obtained from the FWHM of the peaks above.

MALDI preparations occurred solely as a result of the presence of the matrix material in the mixture. Mass spectra obtained from ablation of, a) a mixture of each analyte with the matrix DHB, and b) a sample of the pure analyte, are shown in Fig.4.9A, B & C. It is interesting to note that in the mass spectra obtained from ablation of pure substance P, fragment ions specific to the analyte form the main ion signals, while the mass spectra from pure bovine insulin or tyrothricin show only unspecific low mass fragments. The ion at 133 amu in Fig.4.9B(b) can be identified as the Z_1 fragment of substance P (methionine with the loss of NH_2) using the terminology of Roepstorff and Fohlman (Roepstorff 1984), which correlates well with the appearance of the C_{10} fragment as the most intense substance P fragment ion seen in MALDI spectra (Fig.4.10).

For large mass molecules (approximately > 1000 amu) the monoisotopic ion peak is no longer the only significant parent ion signal in the spectrum. If the mass resolution of the spectrometer is insufficient to resolve unit mass separations at the mass of the molecule of interest, then the FWHM of the ion peak is mainly determined by the isotopic envelope of the molecule, and only partly due to the instrumental mass resolution (Werlen 1994, Vestal 1995). In other words, the resolution of the mass spectrometer is significantly greater than that calculated from simply considering the FWHM of one of the analyte peaks. Some isotopic structure can be detected in single shot spectra of substance P and tyrothricin samples. However, this structure is lost in the majority of spectra which are obtained by summing a number of laser shots.

Ion signals originating from fragmentation of the substance P molecular backbone have been observed in MALDI spectra as mentioned earlier. The fragmentation pattern observed is shown in Fig.4.10. Although it is not apparent from Fig.4.10, the fragment peak SP 2 is a double peak, and has been resolved in other spectra. The measured masses of each fragment peak were calculated from the spectra using the protonated substance P ion peak as a calibrant, and are given in table.4.1. Also given are calculated masses of possible fragments (where the calculated mass is that of the monoisotopic molecule) and the calculated masses of residues found following a carboxypeptidase digest of substance P (Vorm 1994b).

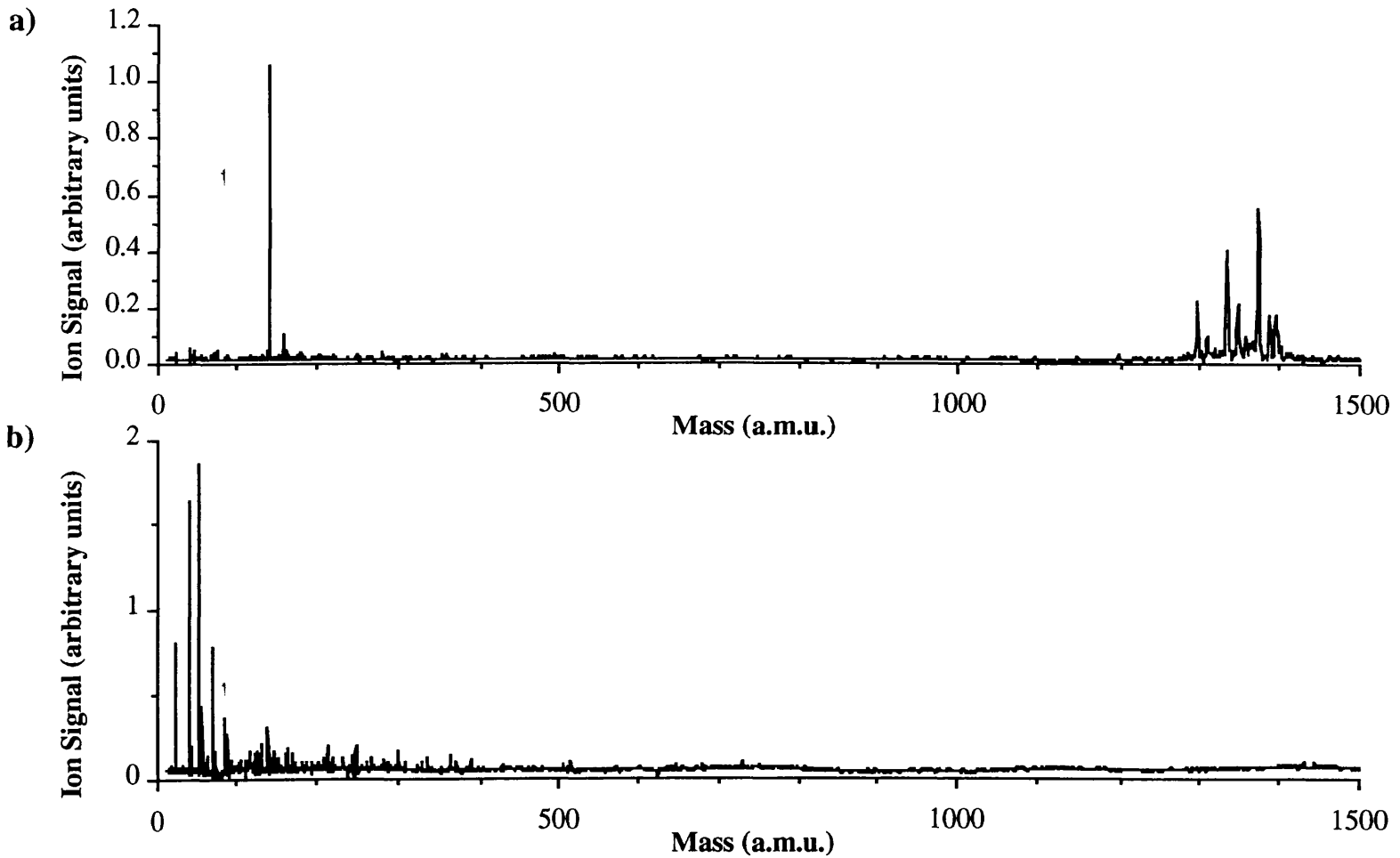

Fig.4.9A Mass spectra showing: a) The MALDI mass spectrum from a vacuum dried sample of tyrothricin in DHB (M/A approximately 350). Ablation using a 300 ps nitrogen laser with a fluence of 37 $mJcm^{-2}$. b) The Laser Desorption Ionisation (LDI) mass spectrum of a vacuum dried sample of tyrothricin. Ablation using a 300 ps nitrogen laser with a fluence of 11 $mJcm^{-2}$.

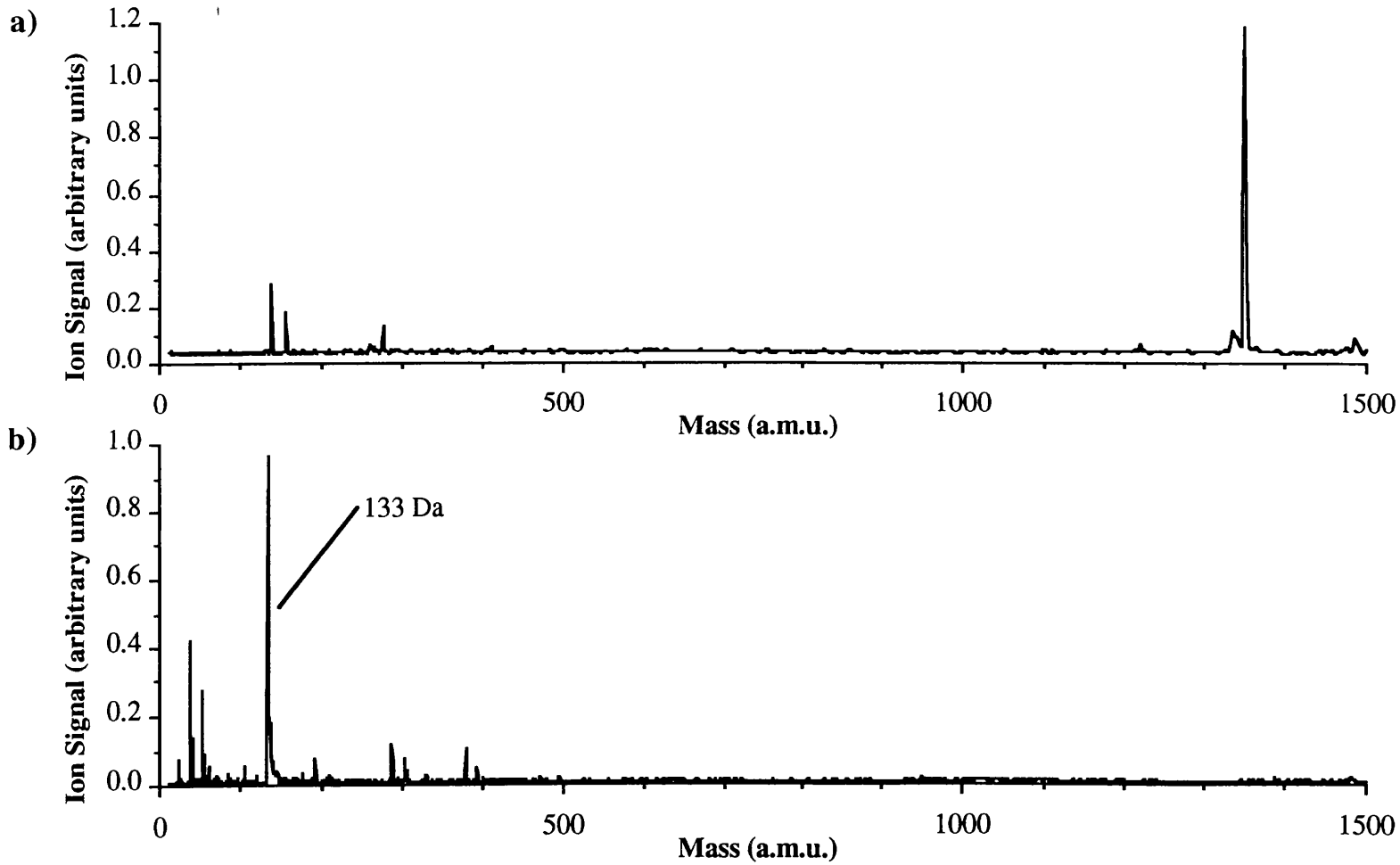

Fig.4.9B Mass spectra showing: a) The MALDI mass spectrum from the crystals formed around the edge of a standard sample preparation of substance P in DHB (M/A = 440). Ablation using a 300 ps nitrogen laser with a fluence of 21 $mJcm^{-2}$. b) The Laser Desorption Ionisation (LDI) mass spectrum of a vacuum dried sample of substance P. Ablation using a 300 ps nitrogen laser with a fluence of 22 $mJcm^{-2}$.

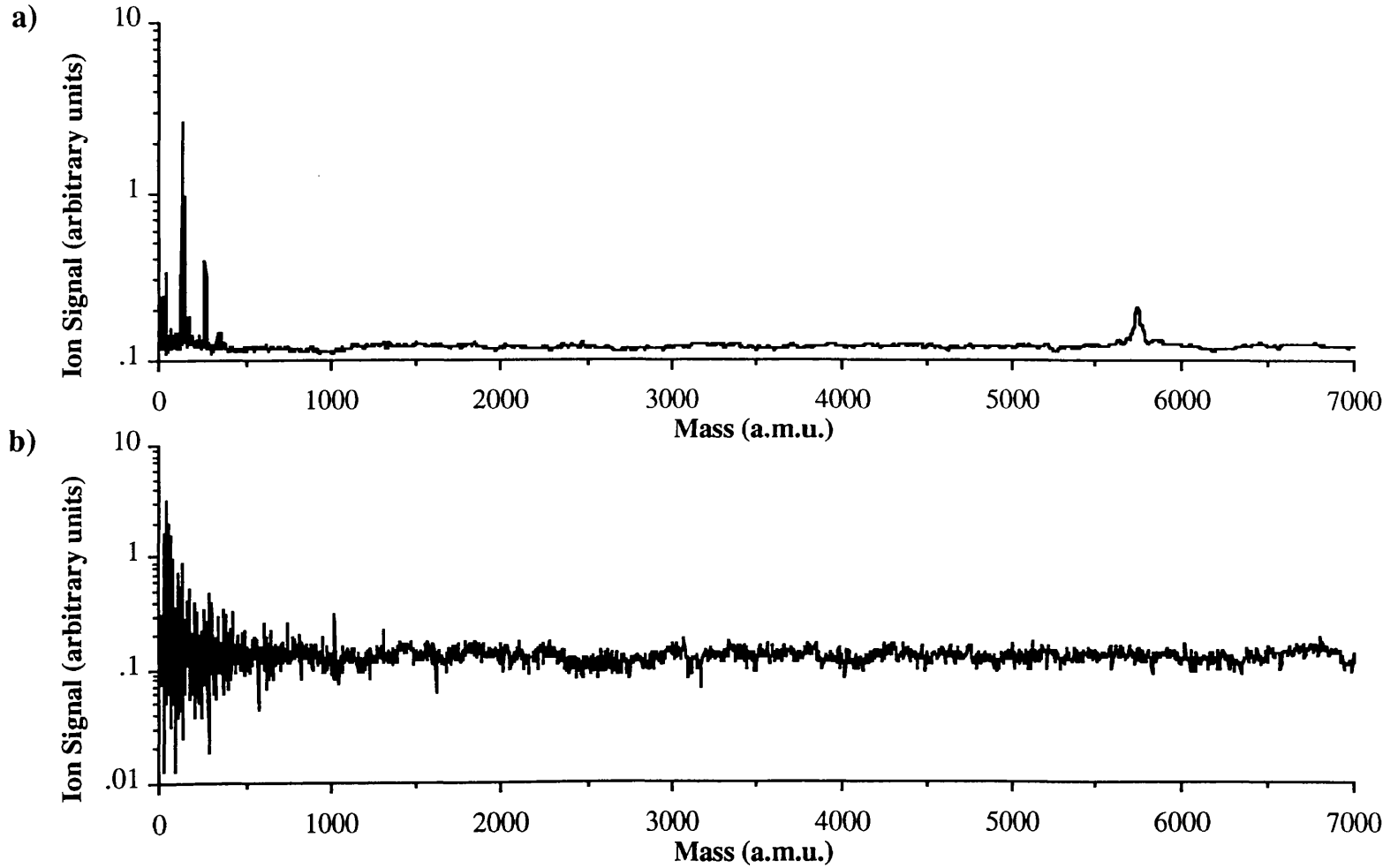

Fig.4.9C Mass spectra showing: a) The MALDI mass spectrum from a vacuum dried sample of bovine insulin in DHB (M/A = 1500). Ablation using a 300 ps nitrogen laser with a fluence of 21 $mJcm^{-2}$. b) The Laser Desorption Ionisation (LDI) mass spectrum of a vacuum dried sample of bovine insulin. Ablation using a 300 ps nitrogen laser with a fluence of 27 $mJcm^{-2}$.

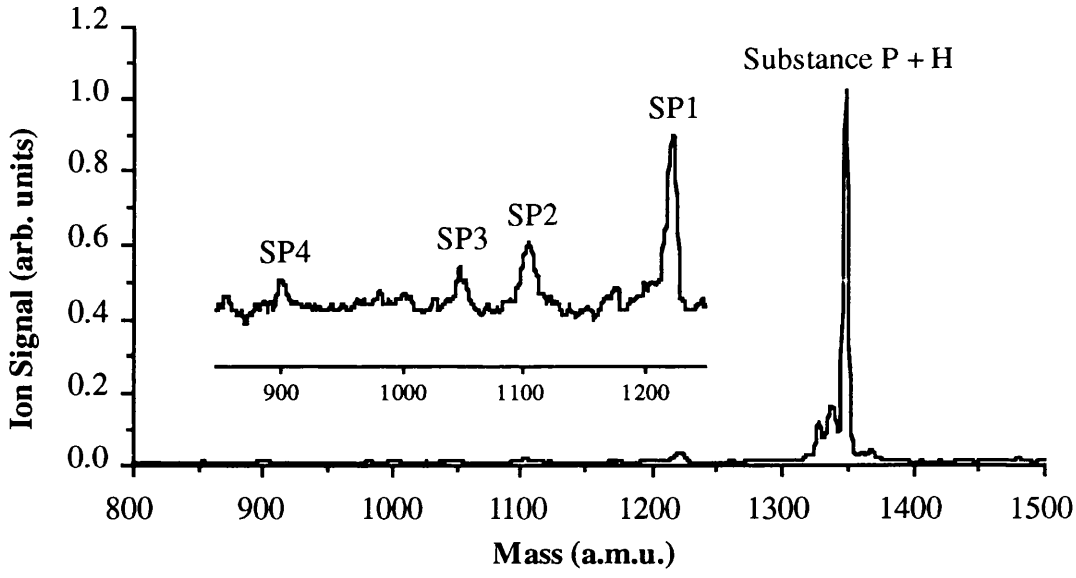

Fig.4.10 Mass spectrum showing the fragment ions associated with substance P. The identity and mass of each fragment is given in table.4.1. Ablation using a 300 ps nitrogen laser with a fluence of 32 $mJcm^{-2}$ from a sample of substance P in DHB (M/A ~ 350). Sample was prepared by blow drying with a stream of warm air, with ablation from the crystals formed around the edge.

In Table.4.1 the nomenclature used to identify the fragments is that of Roepstorff and Fohlman (Roepstorff 1984). The amino acid sequence of substance P has been identified as

Arg-Pro-Lys-Pro-Gln-Gln-Phe-Phe-Gly-Leu-Met(NH_2)

or

RPKPQQFFGLM(NH_2)

using the standard naming convention for polypeptide chains (sequence of amino acids written with amino-terminal residue at the start) and the conventional abbreviations for amino acids (Stryer 1988).

The results obtained by the author are intriguing. The main ion signals seen in the spectra are C_n series amino-terminal fragments formed due to loss of carboxyl-terminal residues (Roepstorff 1984), although a low intensity carboxyl-terminal fragment can sometimes be resolved in the

spectra (Y_9) due to the loss of Arg and Pro residues from the amino-terminal of substance P.

However, results published in the literature on the typical fragmentation patterns found following MALDI of peptides, and specifically substance P (Kaufmann 1994, Lee 1995), show only A_n and B_n series amino-terminal fragments. No carboxyl-terminal specific ions were found in the mass spectra. The experimental parameters (type of matrix, sample preparation, ablation laser and ablation fluence) used by both Kaufmann and Lee were identical or very similar to those used by the author, and it is expected that the ion source conditions would be similar to those generated in the author's experiments. It is therefore difficult to explain the completely different fragmentation patterns found if the ion signals observed by the author do indeed result from fragmentation of substance P during or after material ejection.

Table.4.1

Peak	Measured Mass (amu)	Mass Error	Frag.	Calculated Mass (amu)	AAR*	Calculated Mass (amu)
SP 1	1220.0	3.2	C_{10}	1214.7	1 - 10	1217.7
SP 2a	1103.7	2.2	C_9	1101.6	1 - 9	1104.6
SP 2b	1095.2	3.0	Y_9	1092.4		
SP 3	1047.0	2.9	C_8	1044.6	1 - 8	1047.6
SP 4	899.7	1.9	C_7	897.4	1 - 7	900.5

* AAR - Amino Acid Residue left following chemical removal of carboxyl-terminal residues (Vorm 1994). Calculated mass is that of the protonated AAR.

However, the mass spectra obtained by the author (Fig.4.10) are similar to those observed following MALDI of a peptide mixture obtained following a combined carboxypeptidase Y and P digest of substance P (Vorm 1994b), the main difference between the spectra being the relative intensities of the ion peaks. It is possible that partial hydrolysis of a small fraction of the substance P sample has occurred during preparation, which has resulted in residues similar to those seen in the work of Vorm. Table 4.1 shows the measured masses of the ions in Fig.4.10, the calculated

masses of the fragment ions C_{10} to C_7 and the calculated masses of the residues obtained following the carboxypeptidase digest (Vorm 1994b).

4.4 Effect of Sample Preparation Method

In order to work with the optimal source conditions for both post-ionisation of neutrals and tandem MS of ions, a cursory investigation was carried out upon the influence which the sample preparation technique had on the ablation characteristics and MALDI spectra obtained. DHB was used as the matrix material. Samples were prepared by a variety of different methods, the main physical effect of which was to alter the rate at which crystallisation occurred, thus changing the form and distribution of matrix/analyte crystals over the area of the sample drop. The samples analysed can be separated into the following groups;

i) Standard MALDI sample preparations.
   - Blow dried (heat gun or compressed nitrogen stream).
   - Dried at ~20°C with no evaporative assistance.
   - Dried at ~4°C with no evaporative assistance.

ii) Vacuum dried samples.

iii) Single crystals grown in solution at ~4°C.

The results of the investigations on each type of sample are discussed in the following section.

Standard Sample Preparations

The standard sample preparation method used in MALDI analysis is generally described as the 'dried droplet' method and involves the relatively slow drying of a drop of the sample solution on the sample stub (as described in Chapter 1, section 1.4.2) which typically results in a ring of small crystals forming around the edge of the sample spot (DHB). Ion signals from samples produced via the dried droplet method exhibit large variations in ion signal intensity, both as a function of laser beam position on the sample, and from shot to shot on the same spot. In addition both the fluence threshold for ion production and the rate at which ion signals

become exhausted are found to vary considerably (see next sections). To obtain the best spectra, the laser beam has to be scanned over the crystalline rim until a suitable site is found ('hot spot'). Spectra from poor locations on the sample are generally characterised by the appearance of alkaline ion signals and adducts, low ion signal intensity of matrix and analyte ions, and an abundance of non-specific low mass ions.

The size and quality of the crystals formed around the rim is a function of the rate at which the solvent was evaporated from the initial sample drop. The largest and best quality crystals were observed for those samples which were dried in the fridge at approximately 4°C. The mass spectrum from such a crystal is shown in Fig.4.9B(a). Spectra from fridge dried samples generally exhibited smaller variations in ion signal intensity and ion production threshold, probably due to the superior quality of the matrix crystals formed.

A number of solutions were prepared containing a mixture of both substance P and bovine insulin in DHB, samples of which were prepared by blow drying. Analysis of these samples produced interesting results, a typical example of which is shown in Fig.4.11. The largest ion signals for each analyte were not obtained from the same type of sample region. The best substance P ion signals were obtained from the crystals around the rim of the sample drop. However, these crystals yielded little or no bovine insulin ion signals. In contrast to this, the residue which was left in the centre of each dried sample drop produced the best bovine insulin ion signals, with a much reduced signal for substance P. This result was reproducible in all the samples and over the full range of fluences investigated. It is probable that this effect is directly related to the ability of the matrix to incorporate a particular protein/peptide molecule within the matrix crystal lattice. Time lapse photography of drying matrix/bovine insulin samples by Doktycz et al (Doktycz 1991) suggests that the bulk of the bovine insulin does not solidify until most of the solvent has evaporated, and concentrates in the centre region of the sample drop, supporting the above view. However, it is also possible that the poor solubility of bovine insulin in the solvent mixture used may have resulted in the bulk of the protein remaining in suspension, unavailable for

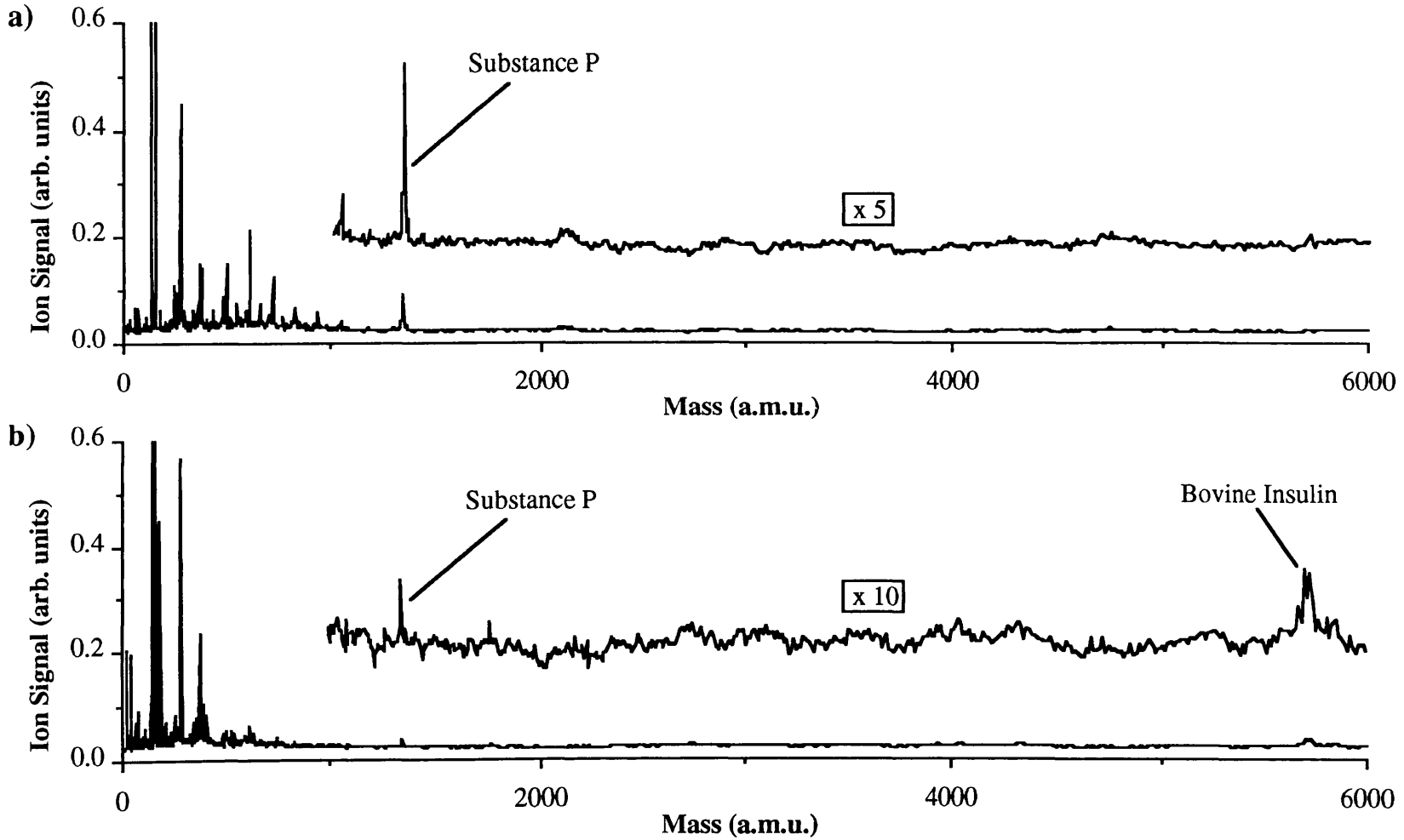

Fig.4.11 Mass spectra from a sample of substance P (M/A ~ 87 500) and bovine insulin (M/A ~ 150 000) in DHB. Mass spectrum a) was taken from the crystals which formed around the rim of the spot. Mass spectrum b) was taken from the residue which was left in the centre of the sample spot. In both spectra the DHB parent ion peak signals are saturated. The TFA cluster peaks are visible in a).

inclusion within the matrix crystals, and left as a residue over the sample spot once the solvent has evaporated.

Vacuum Dried Samples

Samples were prepared by extremely rapid evaporation of the solvent using a rotary pump. The resulting samples were homogeneous to the eye, although under the optical microscope it was observed that the sample was actually polycrystalline with micrometer sized DHB crystals. The ion signals obtained from these samples showed only minor signal variation, both in terms of shot-to-shot reproducibility and from one sample position to another, in marked contrast to spectra obtained from standard sample preparations. However, the matrix and analyte specific ion signals are of lower intensity than those from standard sample preparations, and exhibit relatively rapid ion signal decay, with ion signal

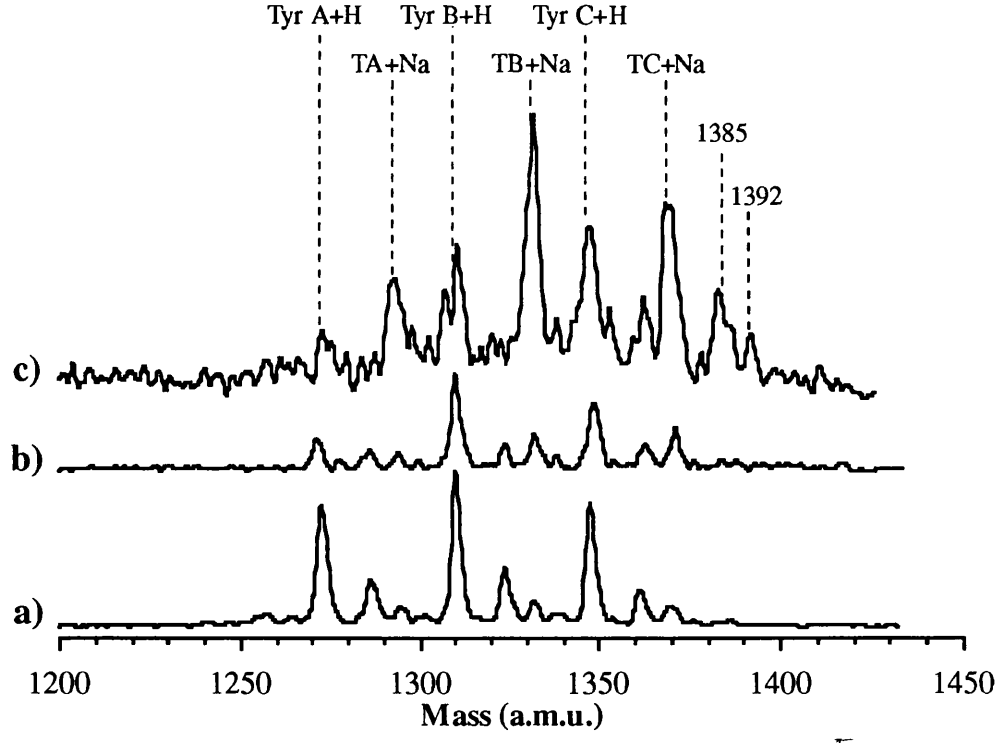

Fig.4.12 Spectra showing the effect of sample preparation method on the observed ion signals. All samples are tyrothricin in DHB (M/A ~ 350). The spectra shown are: a) air dried sample at a fluence of 41 $mJcm^{-2}$ (the intensity of this ion signal has been reduced by a factor of 10), b) vacuum dried sample at a fluence of 14 $mJcm^{-2}$ (marginally above threshold), and c) vacuum dried sample at a fluence of 40 $mJcm^{-2}$. Ablation was performed using a 300 ps nitrogen laser.

intensities dropping a factor of two following a few 10's of laser shots (depending on ablation fluence). This loss of signal is not necessarily due to exhaustion of the sample material, and very often total loss of ion signal at a certain fluence can occur with no apparent damage to the surface of the sample (this occurs regardless of sample preparation technique).

A significant contribution to the total ion current is due to alkaline ions and adducts. Comparison between the mass spectra obtained from ablation of vacuum dried and air dried samples of tyrothricin in DHB is made in Fig.4.12. Enhancement of the Na adduct ion signal (Tyr 'x' + Na) relative to the parent ion signal (Tyr 'x') can clearly be seen in spectra from the vacuum dried sample. This enhancement is small for an ablation fluence marginally above the threshold fluence value, but rapidly increases with fluence such that the adduct ion signals are the predominant ion species for ablation significantly above the threshold fluence. This has a major effect on mass calibration of large analytes where the mass resolution of the spectrometer may be insufficient to resolve adduct peaks from the parent ion species, resulting in an overestimation of the analyte mass (Strupat 1991).

Single Crystals.

Large single crystals of DHB were grown from a solution of DHB and substance P (M/A = 440). A glass vial of the sample solution was placed in a fridge at approximately 4°C for one to two days, resulting in the formation of relatively large (1 to 2 mm), flat crystals on the bottom of the vial. The highest quality crystals were removed from the solution and fixed to a steel sample stub simply by drying the solution remaining between the crystal and stub. Alkaline cation or adduct ions were never observed in mass spectra obtained from ablation of the surface of single crystal samples. The stability of ion signals was generally very good once above the ion production threshold. The shot-to-shot and spatial variation of the ion signal over the sample surface was better than that obtained from standard blow dried sample preparations, but still considerably worse than that obtained from vacuum dried samples. Perhaps the most surprising result was that the mass resolution obtained in spectra from single crystal samples was worse than that from samples prepared by the

dried droplet method. This has also been observed in ablation from sinapinic acid (Xiang 1993) but has not been satisfactorily explained. The best resolved spectra were in fact obtained from vacuum dried samples, although comparable quality mass spectra were obtained from dried droplet samples for ablation fluences marginally above the threshold value.

A number of researchers have carried out more exhaustive investigations into the role of sample morphology in MALDI in an attempt to obtain more information on the processes involved, and produce more reproducible and better resolved spectra (Westman 1995, Perera 1995, Gusev 1995, Xiang 1994, Vorm 1994a, Doktycz 1991). All these studies describe essentially similar observations; ablation from polycrystalline samples where the typical crystal dimension is much smaller than the laser focal spot results in spectra which exhibit less variation (fluence threshold value, spot-to-spot, shot-to-shot) and typically show increased mass resolution than spectra obtained from ablation of crystals macroscopic on the scale of the laser focal spot. It is likely that in polycrystalline samples the intensity of ion signal from each microcrystal varies considerably, but averaging over the large number of crystals results in a relatively reproducible ion signal. The reason for the large fluctuations from apparently similar regions on single crystal samples is unknown.

In the authors work the polycrystalline samples (vacuum dried preparations) exhibited large ion signals due to the presence of contaminants. This suggests that attempting to produce highly homogeneous samples of this nature has its drawbacks, as this will negate the benefits of the purification process inherent in MALDI (i.e. the inclusion of only the analyte molecules into the matrix crystals) by creating a morphology of matrix microcrystals interspaced with contaminant residue, ablation from both of which will occur. However, sample preparation techniques have been developed (Vorm 1994a, Xiang 1994) which allow rigorous washing of the sample, resulting in less interference from salts and impurities than observed from standard dried droplet preparations.

4.5 Sample Exposure Effects

Based on the results of the study into sample preparation techniques it was decided that single crystal samples would be ideally suited for the post ablation ionisation (PAI) investigations reported in Chapter 5. The techniques used to obtain the majority of PAI information result in repeated exposures being made upon the sample. It was therefore crucial that the effects of repeated laser exposure on single crystal samples were investigated prior to carrying out the work detailed in Chapter 5. The effect of repeated laser exposure on the primary ion yield and mass resolution was investigated for ablation fluences above the fluence threshold for ion production. Investigation of the time evolution of the neutral species via PAI was carried out in tandem to the MALDI ion investigation, for ablation both above and below the ion production threshold fluence, the results of which are reported in Chapter 5.

The ion yield from a single crystal of DHB doped with substance P (M/A ~ 440) is shown in Fig.4.13 for ablation fluences of approximately 2 and 3 times the threshold fluence for ion production ($F_{th(ion)}$), where $F_{th(ion)}$ ~ 14 $mJcm^{-2}$. The general behaviour of the ion signals with the number of ablation shots is relatively reproducible, and exhibits characteristic features such as the hump in the dehydroxylated parent matrix (M-OH) and dimer species, and the rise in signal intensity of the dimer relative to the M-OH signal. Similar behaviour has been found with other matrices (Gimon 1992). However, the actual intensity of the ion signals and their rate of decrease were found to vary considerably even from different ablation positions on the same crystal, as also found by Westman et al (Westman 1995). Ablation at a fluence of ~$2F_{th(ion)}$ results in a twofold reduction in ion signal over the range 300 to 600 laser shots. Increasing the ablation fluence generally results in both an increased initial ion signal intensity and an increased rate of ion signal reduction with exposure, which has been observed in all exposure studies (Quist 1994, Westman 1994a). The effect of repeated exposure on the resolution of the ion peaks is shown in Fig.4.14, where the full width at half maximum (FWHM) of the dimer and dehydroxylated parent matrix species from the data shown in Fig.4.13a, is displayed as a function of the number of ablation shots. This behaviour is typical and can be attributed to a

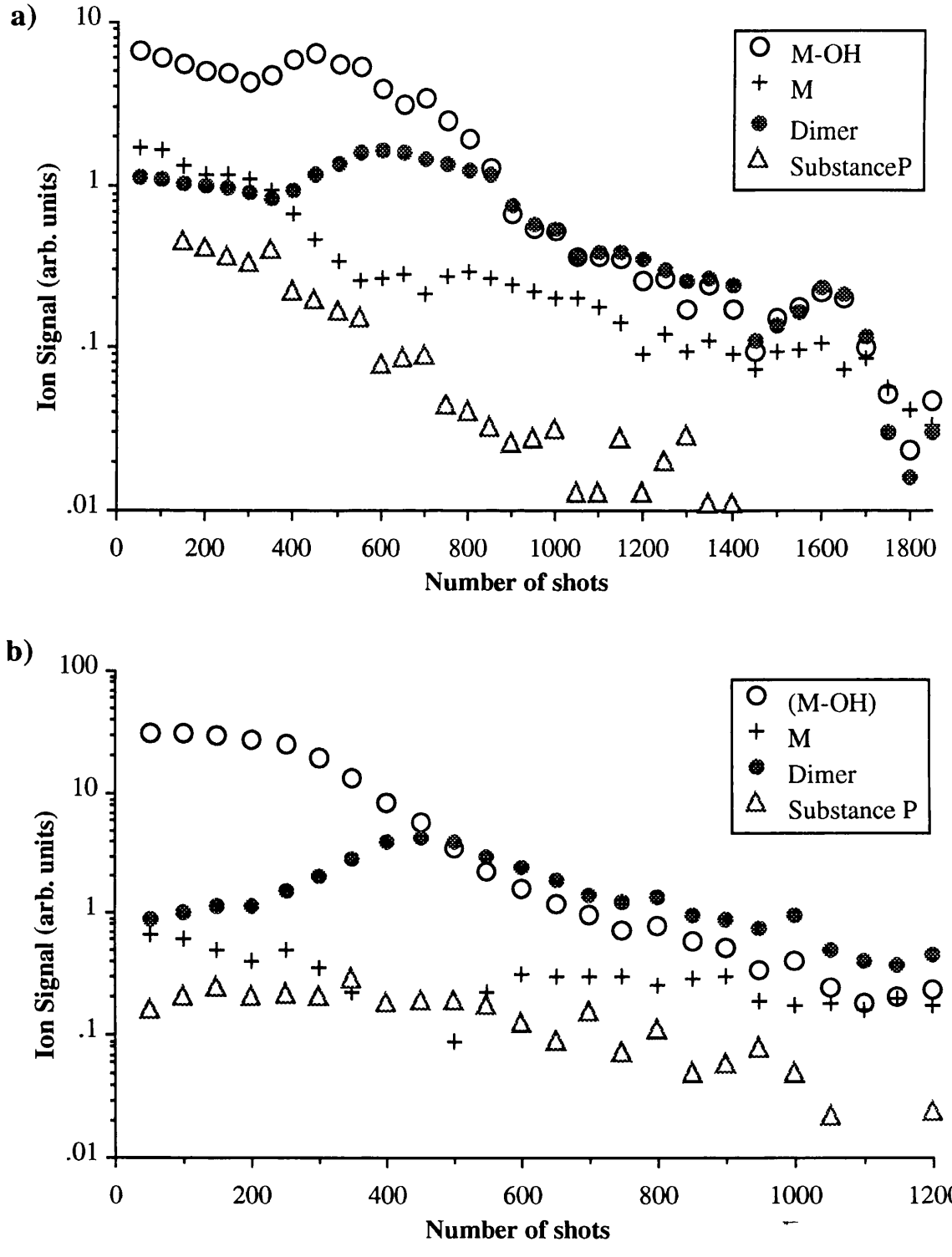

Fig.4.13 Ion yield as a function of exposure from a single crystal of DHB doped with substance P (M/A ~ 440). Run a) was taken with an ablation fluence of 26 $mJcm^{-2}$, run b) with a fluence of 45 $mJcm^{-2}$. The threshold fluence for ion production was approximately 14 $mJcm^{-2}$.

reduction in the plume density as a function of exposure, which will reduce the effect of the ion source parameters on which the overall mass resolution is dependent.

The graph shown in Fig.4.15 shows the behaviour of the ion signal from the same sample spot over an extended analysis which consisted of: letting the ion signal at the initial ablation fluence ($1.9F_{th(ion)}$) fall to zero; a half hour delay followed by ablation at the same fluence ($1.9F_{th(ion)}$); increasing the ablation fluence to $2.5F_{th(ion)}$ and letting the ion signal fall to zero; and finally increasing the ablation fluence to $3.3F_{th(ion)}$ and letting the ion signal fall to zero. The effects illustrated by Fig.4.15 are typical, and were routinely observed throughout the author's work. If the ablation fluence is increased following exhaustion of the ion signal at a particular ablation fluence, a point is reached where a second fluence threshold is observed, above which large ion signals can again be obtained. This effect has been observed in ablation from polycrystalline samples (Westman 1994a) where it was postulated that the threshold fluence for polycrystalline samples is a function of the size of the crystal (due to

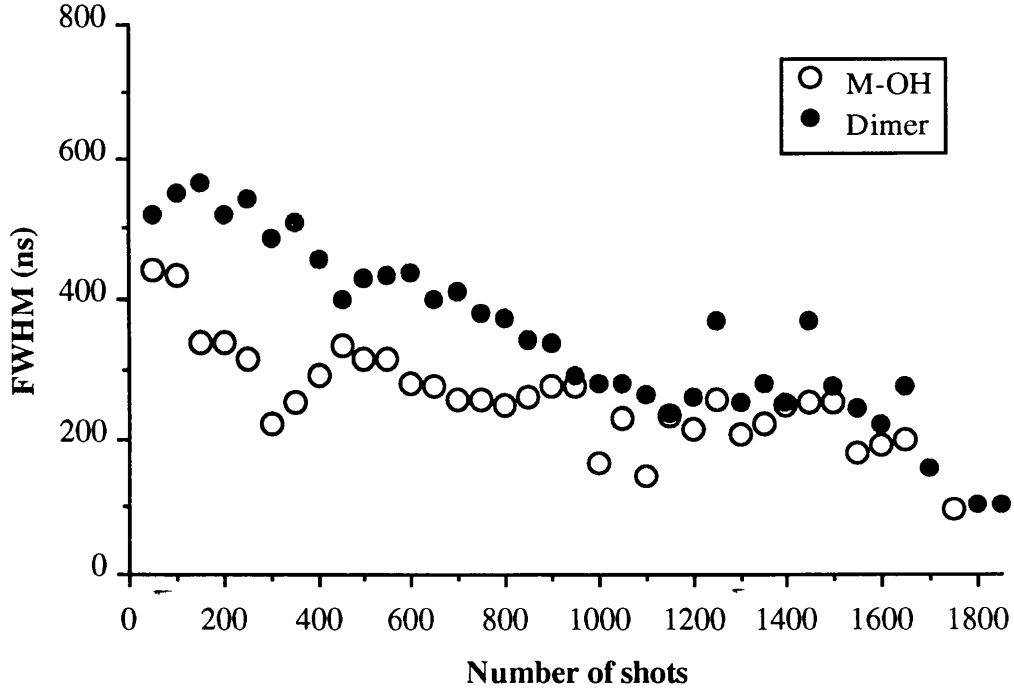

Fig.4.14 Graph showing the full width at half maximum (FWHM) as a function of exposure for matrix ion species. The data in this figure corresponds to that displayed in Fig.4.13a.

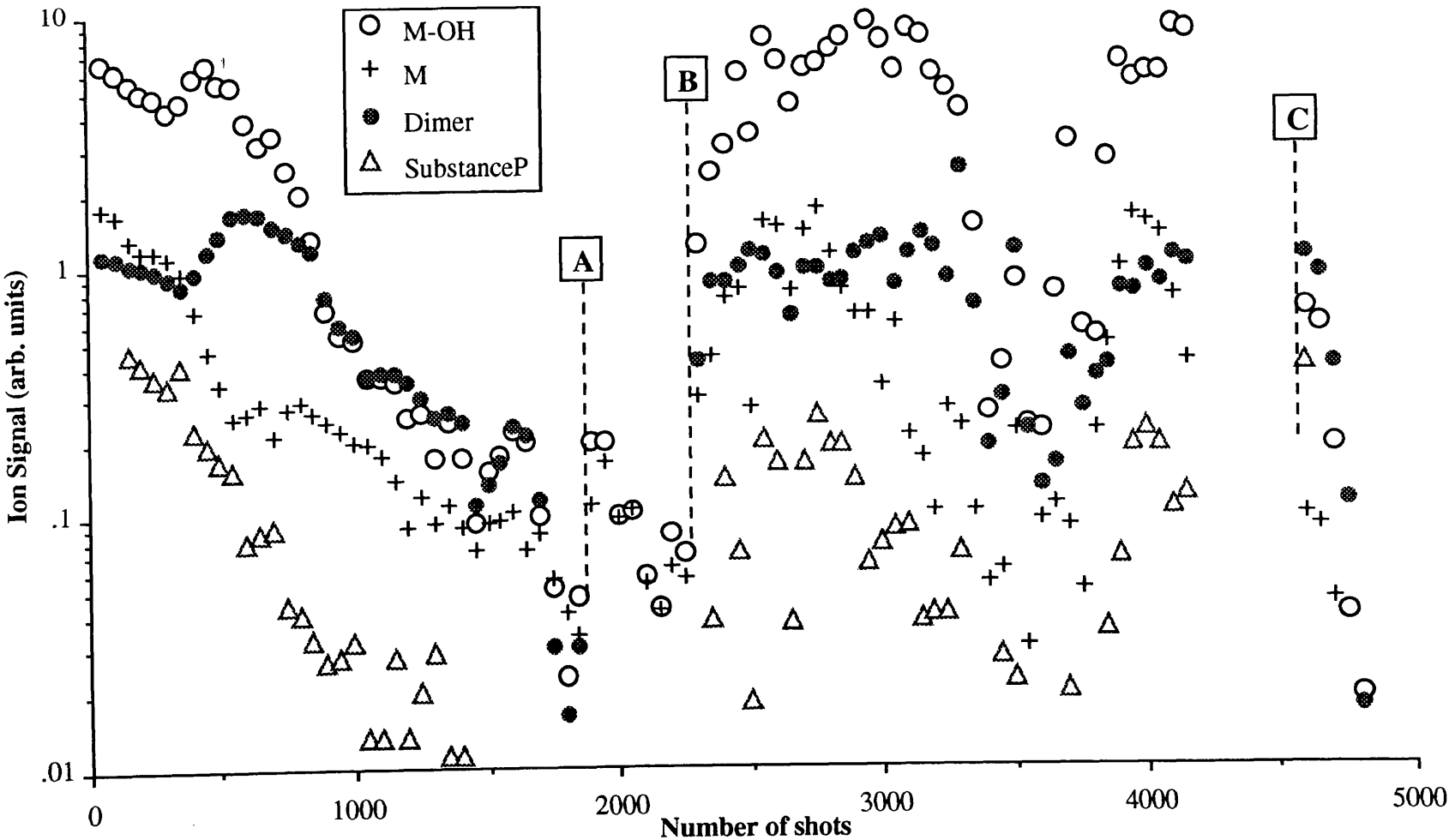

Fig.4.15 Ion yield over an extended analysis at a number of ablation fluences. The ion yield to **A** is the same as that shown in Fig.4.13a). The ion yield fell below the detection threshold at **A**, and the sample was left for a half hour before continuing ablation at the same fluence ($1.9F_{th(ion)}$) until the ion signal again dropped to below detection threshold at **B**. The fluence was increased to $2.5F_{th(ion)}$ and $3.3F_{th(ion)}$ at **B** and **C** respectively, and ablation continued at these fluences until the ion signals dropped below the detection threshold.

energy transfer rates). However, this explanation is not valid for single crystal samples.

It has been suggested that the decrease in ion yield with sample exposure may be related to photochemically induced changes within the matrix, specifically for the cinnamic acid derivatives (Westman 1995). Photochemical modification in UV irradiated cinnamic acid derivatives results in the production of dimers and trimers which have significantly higher melting points than the corresponding monomer. The formation of a surface layer on the irradiated matrix crystal containing a significant fraction of dimers and trimers may have the effect of increasing the threshold fluence required for ablation. Although it has been reported that DHB undergoes photodissociation rather than dimerisation (Westman 1995), this is not supported by the experimental results obtained by the author. Fig.4.16. shows the matrix specific ion signals obtained from ablation of a single crystal of DHB at consecutively low, high, then back to low fluences. The yield of dimer and trimer species in Fig.4.16c is considerably enhanced over that in Fig.4.16a, the normal low fluence ablation spectrum obtained from single crystal DHB. The quadrumer ion signal was also present but is not displayed in the mass spectrum shown in Fig.4.16c. This data suggests that polymerisation of DHB matrix monomers to dimers, trimers and even quadrumers, does occur in the solid state following exposure to high levels of UV. The relative intensity of the dimer and trimer ion signals in Fig.4.16c is enhanced over that in Fig.4.16b most likely due to a reduced probability of fragmentation (lower internal energy and smaller collisional cross section within the ablation plume at fluences closer to threshold). Evidence for a similar mechanism of dimer/trimer production in both DHB and sinapinic acid (a cinnamic acid derivative) is not surprising given the similarity between the matrix spectra.

4.6 Fluence Dependence of MALDI Spectra

In an attempt to quantify the nature of the material ejection process in MALDI, studies were carried out on both the yield of ejected neutral matrix material, and the yield of matrix and analyte ions following UV

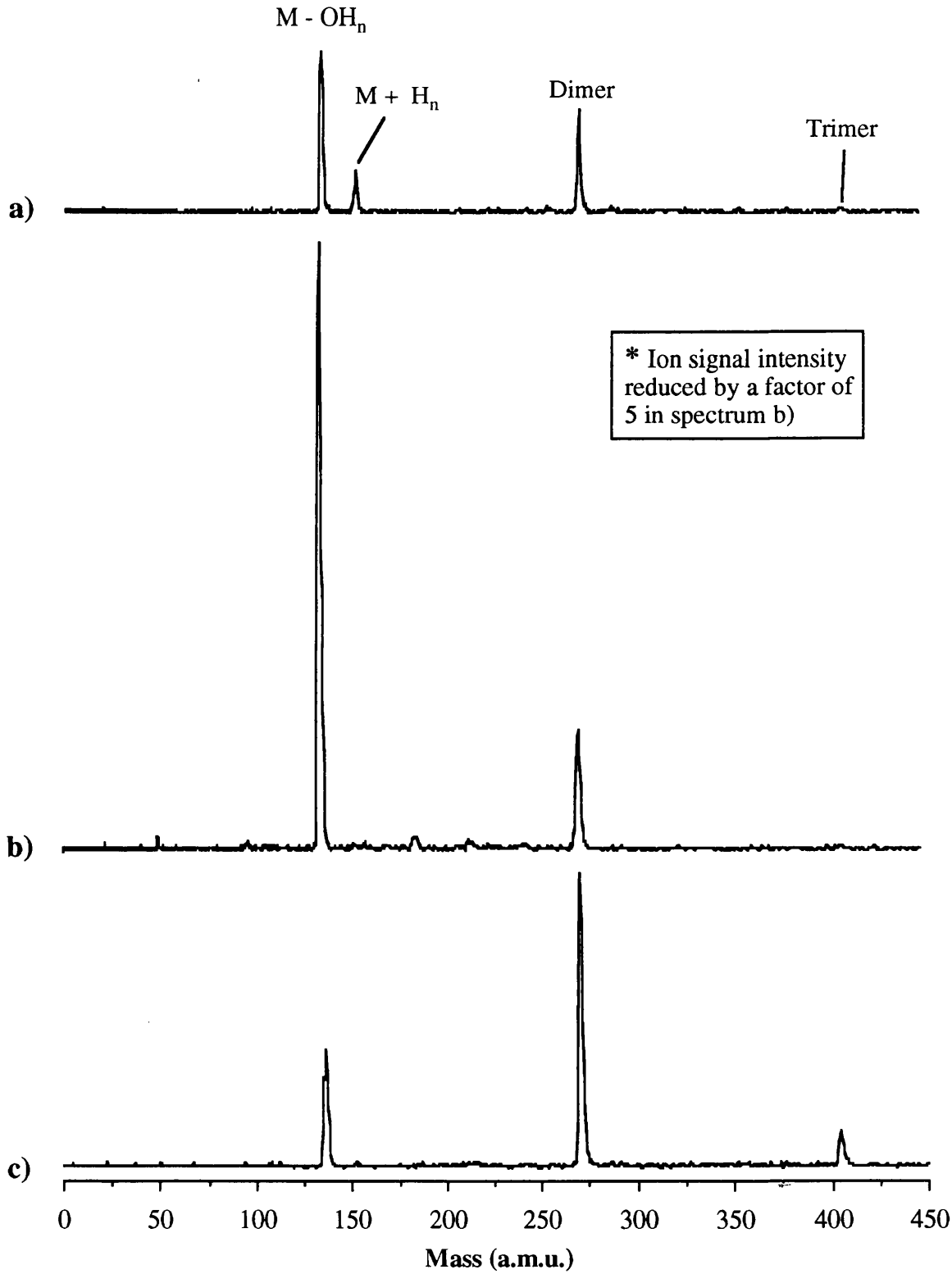

Fig.4.16 Variation in ion signal intensities as a function of exposure and fluence. The mass spectra were taken consecutively from the same sample spot with ablation fluences of a) 51 $mJcm^{-2}$, b) 130 $mJcm^{-2}$ and c) 50 $mJcm^{-2}$. Each spectrum is summed from 20 shots and 60 shots were incident on the crystal at the high fluence prior to accumulating spectrum b). Ablation was from a single crystal of DHB using a 4 ns nitrogen laser, $F_{th(ion)}$ approximately 34 $mJcm^{-2}$.

laser ablation. The matrix neutral particle yield was monitored using the post-ablation ionisation (PAI) technique which is described in Chapter 2 and used extensively in the studies on the dynamics of the MALDI plume (Chapter 5 & 6). This section details the results obtained by the author, and makes comparison to relevant published results followed by discussion of the author's results in relation to the models for neutral particle ejection described in section 2.2.2 of Chapter 2.

4.6.1 DHB Fluence Dependence

A range of samples were used in these studies. The fluence dependence of the ion yield was investigated from standard dried droplet preparations, vacuum dried preparations and single crystals of DHB grown from solution. However, studies of the neutral yield were carried out only using single crystal samples. Some of the results of the analysis are shown in Fig.4.17 to 4.21. Most of the data is obtained by summing the ion signal from 5 to 10 laser shots. All the PAI data was corrected for fluctuations in the energy of the post ionisation laser using the known power dependence of each ion signal (Chapter 5). In Fig.4.19a each data point represents a single shot spectrum with an individual fluence measurement made for each laser shot. The large signal fluctuation described in section 4.4 of this Chapter can clearly be seen for ablation with fluences of less than twice the threshold fluence for ion production, $2F_{th(ion)}$. The C_2H_2 PAI signal in Fig.4.20 & 4.21 originates from PAI laser induced fragmentation of neutral M and M-OH_2 species in the ablation plume. The behaviour of the C_2H_2 ion signal was representative of all the carbon fragment species seen in the mass spectra. The slight difference in the ratio between the M-OH_2 and C_2H_2 PAI signals as a function of ablation laser fluence, observed in some of the data in Fig.4.20 and Fig.4.21, is probably related to the increase in internal energy of matrix neutrals with ablation fluence.

The ablation laser fluence at which the detection threshold for ion production is reached ($F_{th(ion)}$) is higher than the threshold for matrix neutral production ($F_{th(neut)}$) by a factor which lies in the range 2.7 to 3.5 independent of the ablation laser pulsewidth. Results published in the

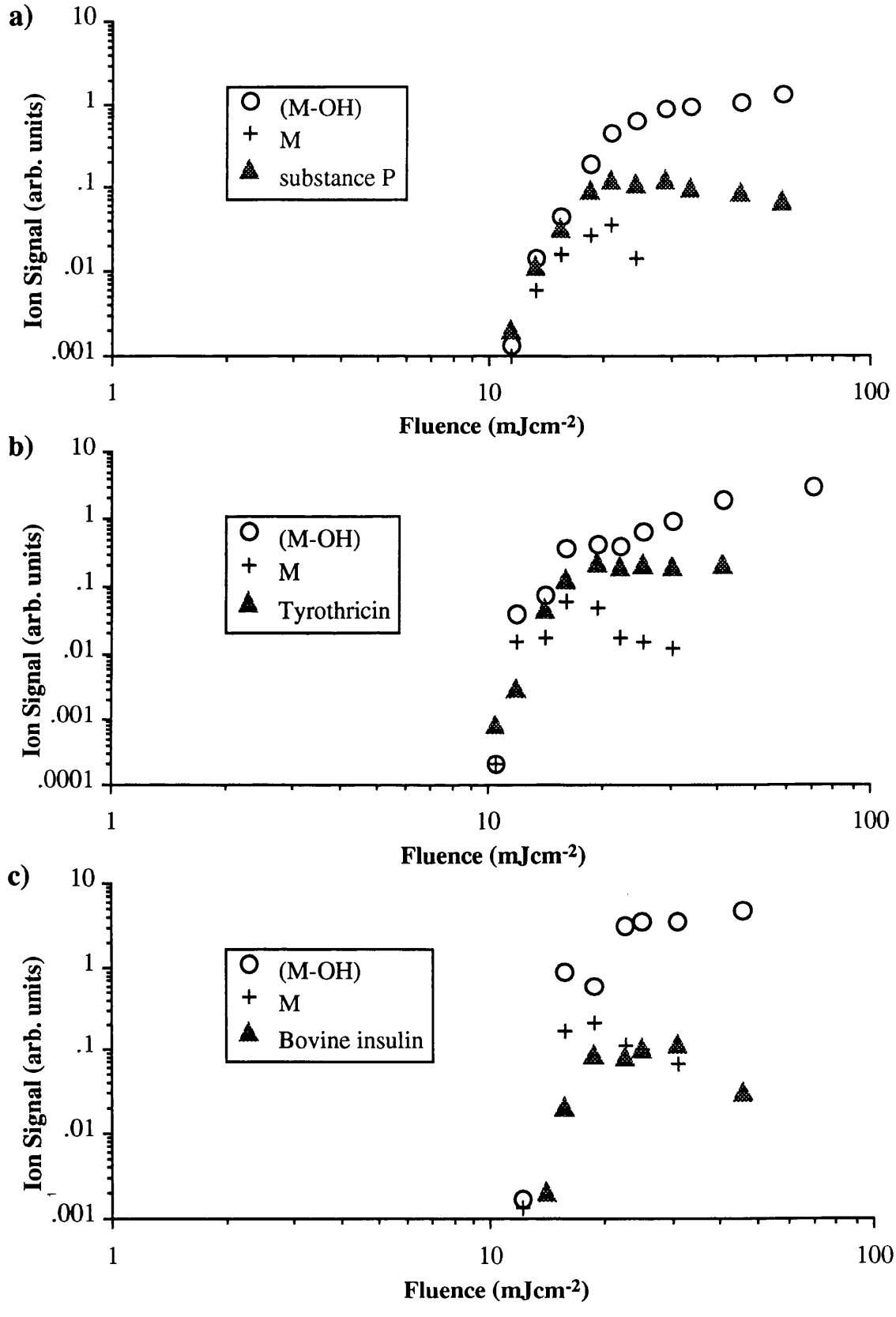

Fig.4.17 Graphs showing the fluence dependence (300 ps N_2 laser) of the ion signals from vacuum dried preparations of a) substance P in DHB (M/A ~ 440), b) tyrothricin in DHB (M/A ~ 360), and c) bovine insulin in DHB (M/A ~ 1500).

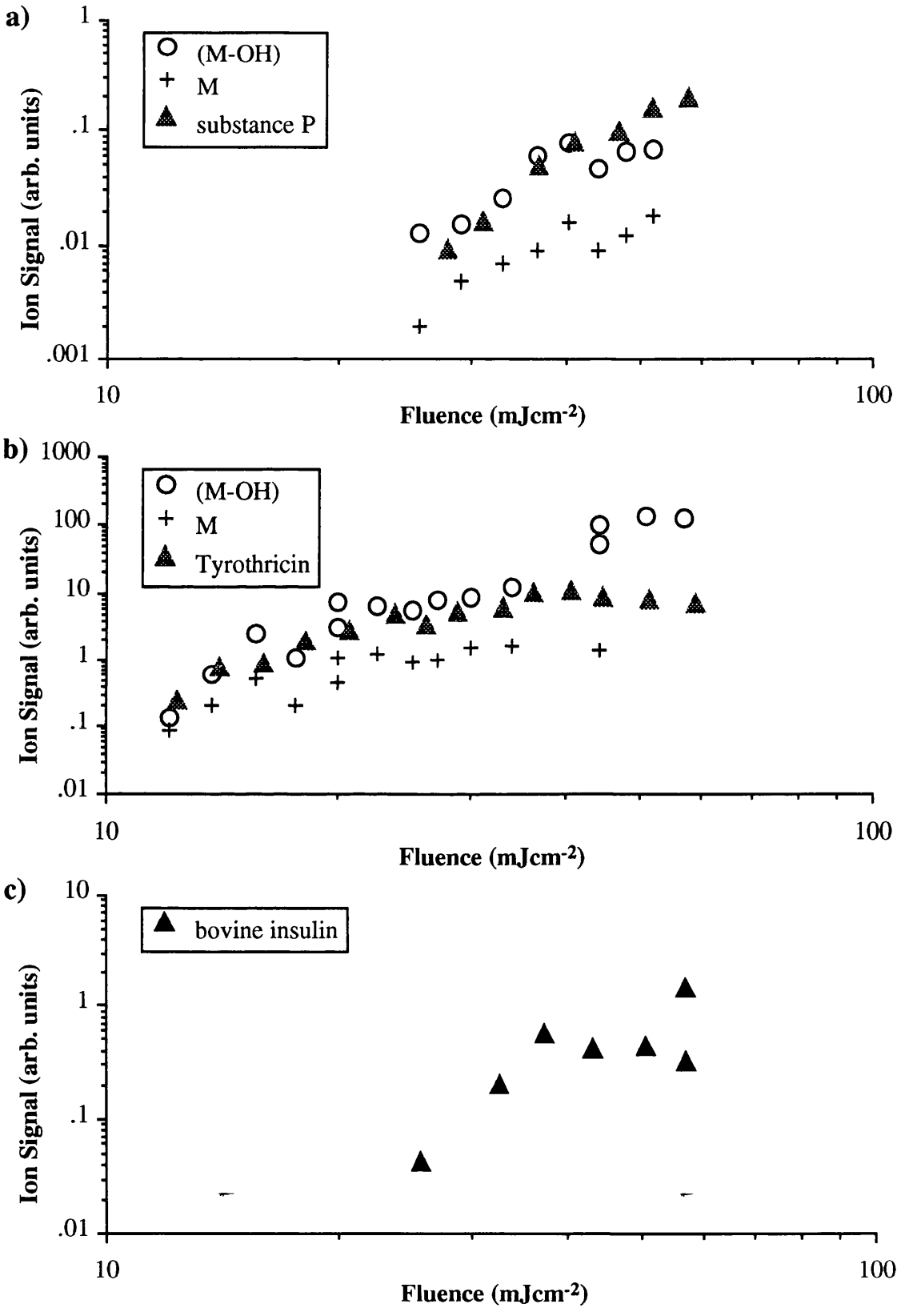

Fig.4.18 Graphs showing the fluence dependence (300 ps N_2 laser) of the ion signals from standard dried droplet preparations of a) substance P in DHB (M/A ~ 440), b) tyrothricin in DHB (M/A ~ 360), and c) bovine insulin in DHB (M/A ~ 1500). No matrix crystals formed in the bovine insulin sample and the ion signals exhibited poor reproducibility.

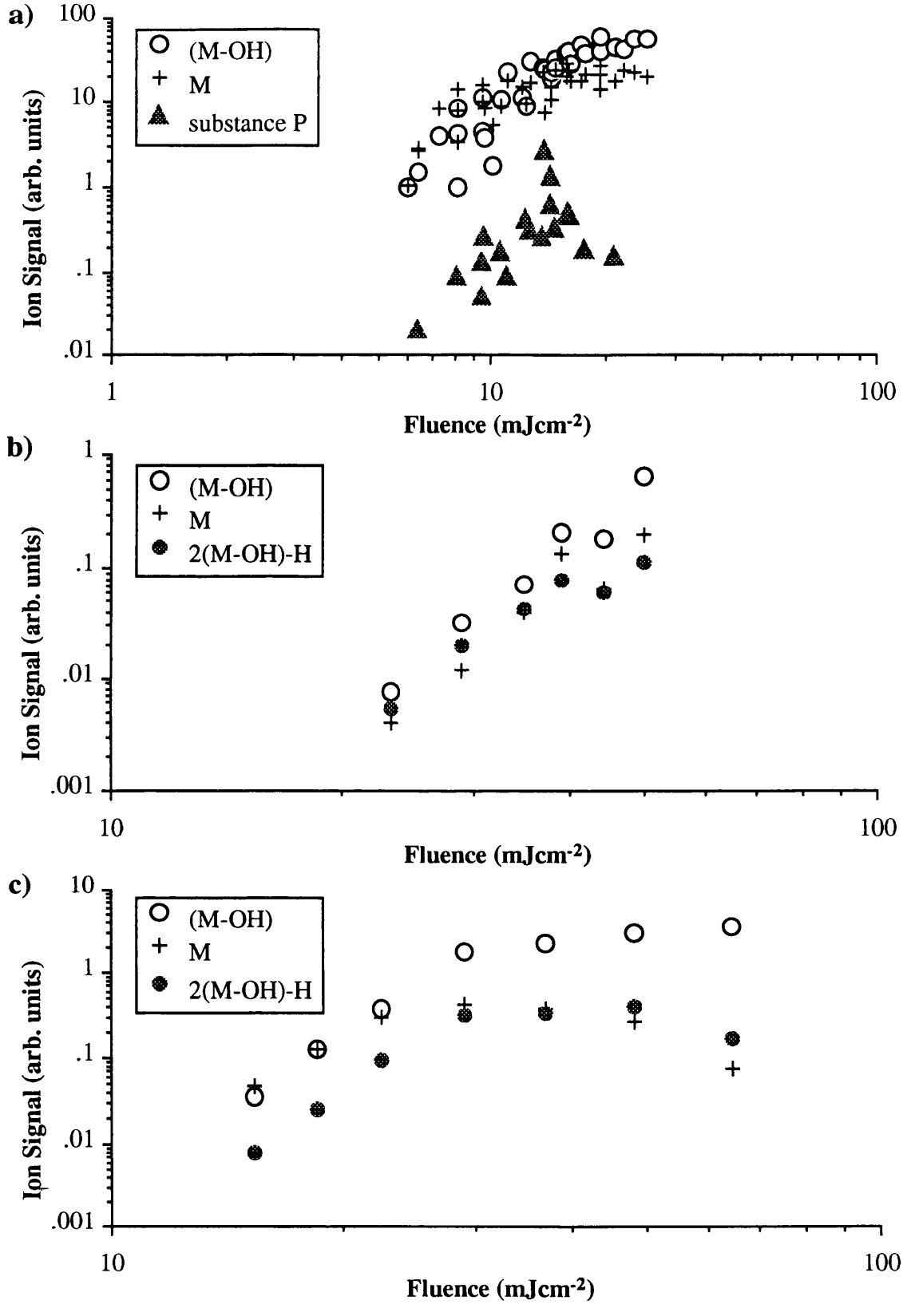

Fig.4.19 Graphs showing the fluence dependence (300 ps N_2 laser) of the ion signals from, a) a single crystal grown from a solution of DHB and substance P (M/A ~ 440), and a standard dried droplet preparation of DHB, from b) the crystals formed around the edge, and c) the residue left in the centre of the sample spot.

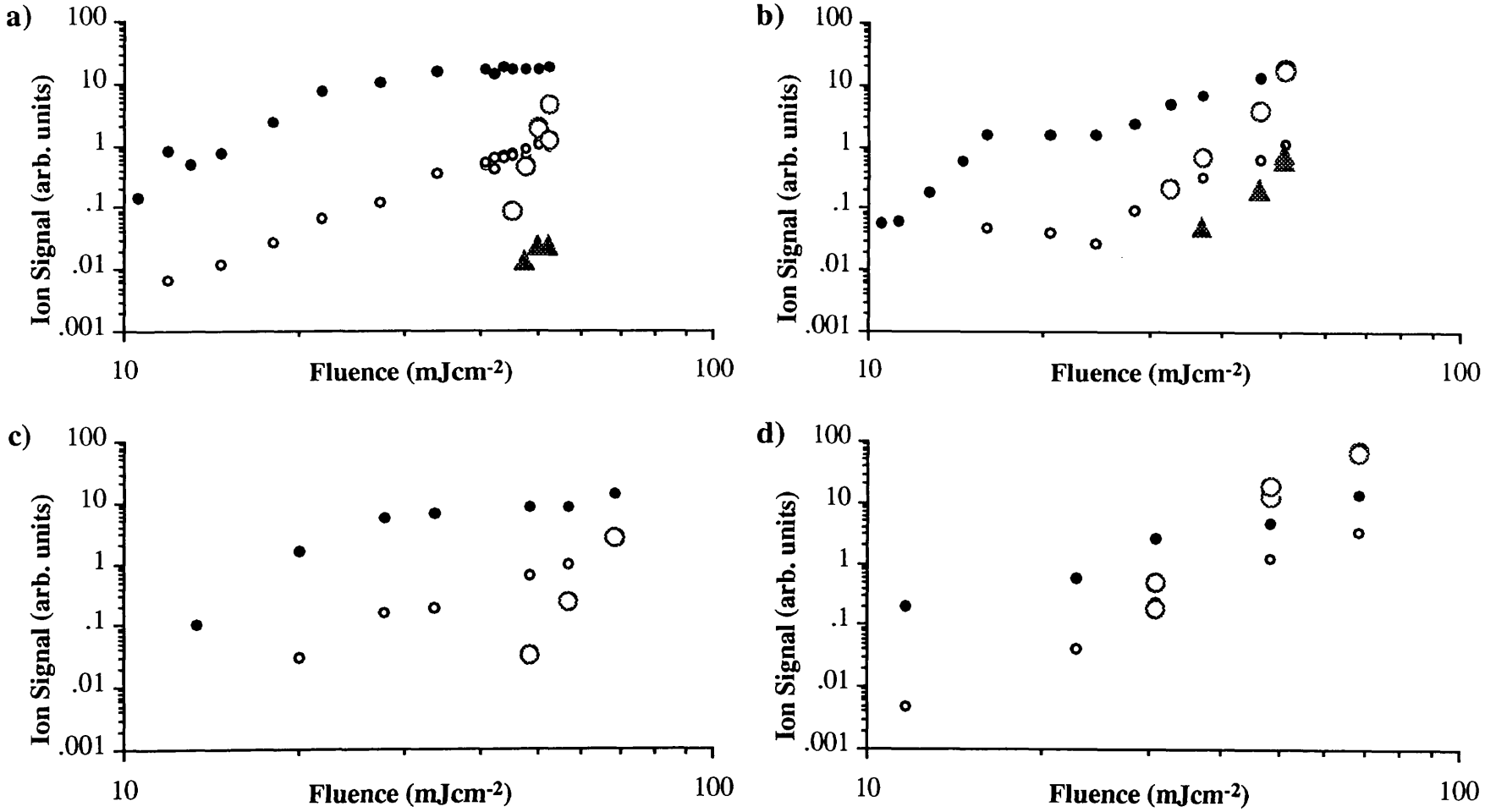

Fig.4.20 Graphs showing the dependence of both the PAI signal and the primary ion signal on the ablation laser fluence (300 ps N_2 laser). Graphs a) & b) are from a standard dried droplet preparation of DHB and substance P (M/A ~ 440) [PAI; 266nm,1 mJ (2.1×10^9 Wcm^{-2}), 2 mm in front of the sample, 4.2 μs delay]. Graphs c) & d) are from a single crystal of DHB [PAI; 266nm, 0.57 mJ (1.2×10^9 Wcm^{-2}), 1.5 mm in front of the sample, 3.3 μs delay].

literature for a variety of matrices give similar values for this ratio; for both gramicidin S and the matrix ferulic acid a ratio of approximately 3 (Huth Fehre 1991) was found, while Dreisewerd (Dreisewerd 1995) found similar ratio's for DHB (~ 3.5) and sinapinic acid (~ 2.5). In addition the MALDI ion signal dependence on ablation laser fluence is much higher than that for the photoionised neutrals, in agreement with published results (Dreisewerd 1995). In the authors work $F_{th(ion)}$ was typically found to vary in the range 10 to 30 mJcm^{-2} for ablation with the 300 ps N_2 laser, and in the range 30 to 50 mJcm^{-2} for the 4ns N_2 laser, although values outwith this range were not uncommon (Fig.4.19a, Fig.4.20a & c and Fig.4.21). Surprisingly, the largest variation in the value of $F_{th(ion)}$ was obtained from ablation of single crystal samples. This has been reported previously, where variations of +/- 30% (Strupat 1991) and +/- 50% (Westman 1995) were found in the value of $F_{th(ion)}$.

The absolute value of the fluence is subject to considerable error due to uncertainty in the size of the laser spot on the sample and will in fact vary over the sample due to the spatial intensity profile of the laser beam used. For this reason many authors give pulse energy instead (a well defined quantity), or give the laser fluence in arbitrary units when comparing

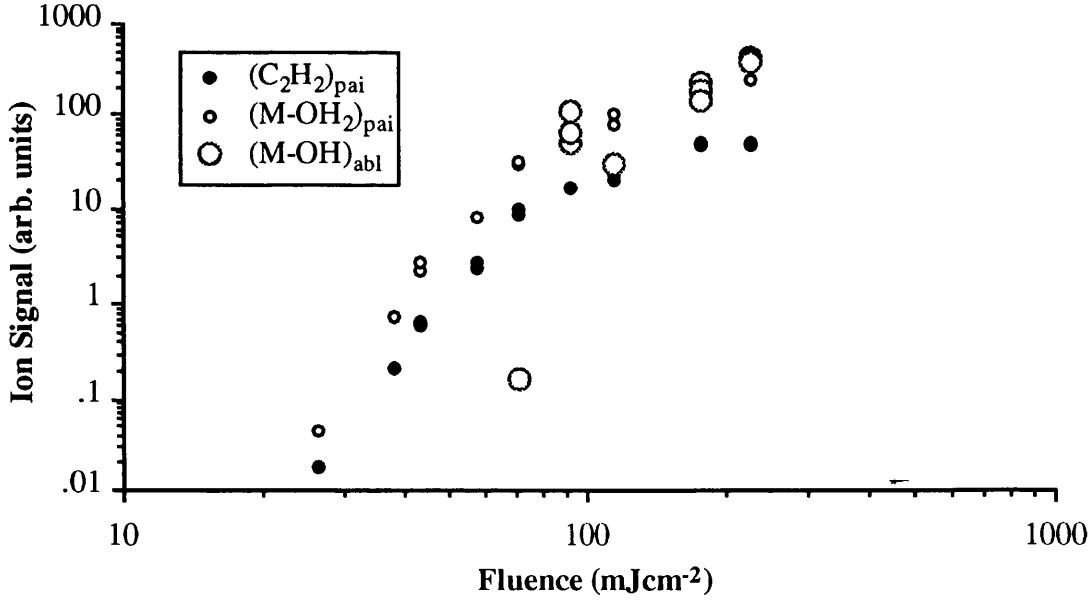

Fig.4.21 Graph showing the dependence of both the PAI signal and the primary ion signal on the ablation laser fluence (4 ns N_2 laser). The sample used was a single crystal of DHB [PAI; 243.03 nm, 9.1 x 10^7 Wcm^{-2}, 1 mm in front of the sample, 2.1 μs delay].

different threshold values. However, for the purposes of intercomparison threshold fluence values for the appearance of analyte ions obtained from published results are given in table.4.2. The wide variation in reported values is due in part to the inaccuracy in determining the actual fluence used, and the criterion used in defining the threshold fluence, but will be mainly due to the variety of ablation laser wavelengths used and the range of experimental conditions, given the known threshold fluence dependence on laser spot size (Dreisewerd 1995) and matrix to analyte molar ratio (Medina 1994). Whether the threshold fluences for detection of ions and neutrals actually correspond to real production thresholds is dependent on the physical process governing particle ejection (Chapter 2, section 2.2.2).

In the authors work the ion signals from analyte species exhibited the same fluence dependence as the matrix ion signals, and analyte and matrix ions appeared at essentially the same value of $F_{th(ion)}$. Although this is in agreement with the results of some researchers (Hedin 1991, Demirev 1992, Yau 1993, Dreisewerd 1995), others have found the value of $F_{th(ion)}$ for analyte species to be greater than that for matrix ions (Liao 1995, Westman 1994b, Medina 1994). Further research is clearly required to clarify these apparent inconsistencies. It is possible that a shift towards apparently higher threshold fluence values with increasing molecular mass is caused by a combination of the reduction in detection efficiency and the increase in ion signal peak width which will result in a reduced signal-to-noise ratio for higher mass analyte ion signals.

4.6.2 Photothermal Fit to Data

In a thermal ablation model the experimentally observed fluence threshold is interpreted as a detection threshold rather than a real physical fluence threshold. The yield of ablated neutral species is given by an expression of the form given in Eqn.2.16. Rewriting Eqn.2.16 using the nomenclature of Dreisewerd et al (Dreisewerd 1995) gives the expression

$$N = P\, f(A) \exp\left[\frac{-E_a}{k_B T}\right] \quad \text{where} \quad T = T_0 + \eta\, \Phi \qquad \text{Eqn.4.1}$$

Principle Author	Year	Laser Parameters				Matrix Material	Analyte		
		Wavelength (nm)	Pulse Duration (ns)	Angle of Incidence	Estimated Spot Area (cm^2)		Material	Threshold Fluence ($mJ\ cm^{-2}$)	Threshold Irradiance ($W\ cm^{-2}$)
Beavis	1989a	266	10	70°	3×10^{-4}	NA & Various Others	Various	5 - 10	5×10^5 - 10^6
Ehring	1992	266 337	8 4	45°	10^{-6} - 10^{-5}	Various	Bovine Insulin	12 - 160	3×10^6 - 2×10^7
Ingendoh	1994	355	5	15° (also 80°)	Over the range 8×10^{-7} to 6×10^{-4}	DHB & SA	Various [Range of masses]	Over the range 150 to 10	Over the range 3×10^7 to 2×10^6
Dreisewerd	1995	337	3	30	Over the range 9×10^{-7} to 3.6×10^{-4}	DHB	Substance P Bovine Insulin Cytochrome C Bovine Albumin	Over the range 160 to 7	Over the range 5.3×10^7 to 2.3×10^6
					3.6×10^{-4}	SA	Bovine Insulin	5	1.7×10^6
Demirev	1992	337	3	75°	1.9×10^{-2}	SA	Bovine Insulin	0.95	3.2×10^5
		248	5.6×10^{-4}		1.3×10^{-2}	FA		1.33	2.37×10^9
Ens	1991	308	10 - 20	45°	4×10^{-5}	SA	Bovine Insulin	20 - 40	2×10^6
Medina	1994	337	3	45°	2×10^{-6}	SA	Bovine Insulin Porcine Trypsin Cytochrome C	Only arbitrary units given. NB Analyte threshold approximately twice that of the matrix.	
Quist	1994	355				FA	None	11 & 31 [2 thresholds]	
Westman	1994a	337	3	40°	8×10^{-4}	FA	Bovine Insulin	50	1.7×10^7
Yau	1993	266	17	45°		SA	Bovine Insulin	24	1.4×10^6
						3-NBA		14	8.2×10^5
Huth-Fehre	1991	266	5		$\sim 4 \times 10^{-4}$	FA	Gramicidin S	32.5	6.5×10^6
Hedin	1991	266	10	45°	$\sim 3.5 \times 10^{-3}$	FA	Bovine Insulin	~ 10	$\sim 10^6$
Riahi	1994	337	3	20°	Over the range 2.6×10^{-4} to 1.4×10^{-3}	SA	Bovine Insulin	27	9×10^6

Table.4.2 Threshold fluence and irradiance values published in the literature [Matrices; NA - nicotinic acid, DHB - 2,5-dihydroxybenzoic acid, SA - sinapinic acid, FA - ferulic acid, 3-NBA - 3-nitrobenzyl alcohol]

where P is a constant, f(A) is an area dependent term [Pf(A) is a constant in the authors analysis], E_a is an activation or sublimation energy, T_0 is the ambient temperature (taken as 293°K), Φ is the ablation laser fluence, and η is a factor which describes the conversion of the transmitted fluence into a temperature increase in the irradiated matrix volume.

If the assumptions are made that complete thermal equilibrium is reached on a timescale comparable to the laser pulse length, and negligible thermal conduction occurs outwith the laser irradiated volume, then η can be given as

$$\eta = \frac{(1 - R)\,\alpha}{\rho\, c_p} \qquad \text{Eqn.4.2}$$

where R is the matrix reflectivity, α is the linear absorption coefficient, ρ is the matrix density and c_p is the specific heat capacity of the matrix. Assuming $\alpha = 4 \times 10^6\ m^{-1}$ (337 nm), R = 0.2, $\rho = 1.57 \times 10^3\ kgm^{-3}$ and $c_p = 1.045 \times 10^3\ JK^{-1}kg^{-1}$ for DHB, the value of η obtained is $\eta = 1.95\ m^2KJ^{-1}$.

Eqn.4.1 was fitted to the neutral PAI data obtained following ablation with both the 4 ns and 300 ps N_2 lasers (shown in Fig.4.20 & Fig.4.21). Two fits to each data set were attempted and are shown in Fig.4.22 as Arrhenius plots; the first where the values of both E_a and η were variable, the second where only E_a was variable with $\eta = 1.95\ m^2KJ^{-1}$. The values obtained from the graphs are shown in table.4.3. It is clear that the data obtained

Table.4.3

PAI Data Set	E_a & η variable		E_a variable $\eta = 1.95\ m^2KJ^{-1}$
	E_a (eV)	η (m^2KJ^{-1})	E_a (eV)
C_2H_2 [300 ps N_2]	n/a*	n/a*	0.32
M-OH_2 [300 ps N_2]	0.36	0.98	0.40
C_2H_2 & M-OH_2 [4 ns N_2]	n/a*	n/a*	0.66

* Data fit is unphysical. The best fit is obtained with a negative value of T_0.

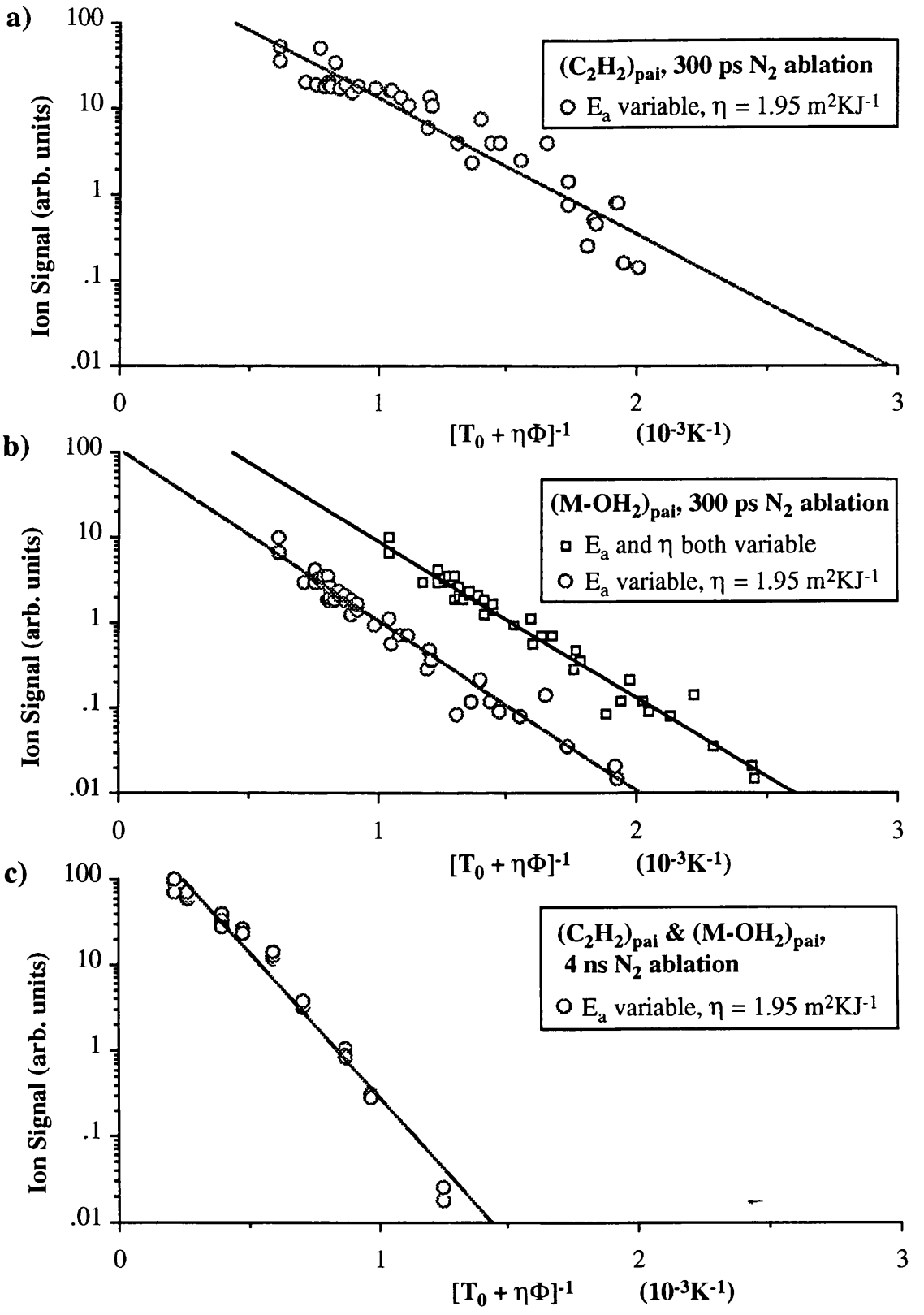

Fig.4.22 Graphs showing fits to the ablation laser power dependence data assuming a photothermal ablation model and a neutral yield expression of the form given in Eqn.4.1; a) C_2H_2 PAI ion signal shown in Fig4.20 (a-d) [300 ps N_2 ablation], b) M-OH_2 PAI ion signal shown in Fig.4.20 (a-d) [300 ps N_2 ablation], and c) Combined C_2H_2 & M-OH_2 PAI ion signal shown in Fig.4.21 [4 ns N_2 ablation].

by the author can be fitted with reasonable accuracy using a thermal ablation model.

When both E_a & η were allowed to vary an optimum fit could only be obtained using the data set for the post ionised M-OH_2 neutrals (300 ps N_2 ablation). The fact that each data set was obtained with a constant laser spot size coupled with the observed degree of variation in the ion signal intensity results in a relatively arbitrary choice of E_a and η as demonstrated by the graphs shown in Fig.4.23, where the degree of fit, χ^2, and best fit value for E_a are plotted as a function of η.

The value of E_a = 0.66 eV obtained from the 4 ns N_2 ablation data is remarkably close to the value obtained by Dreisewerd et al (Dreisewerd 1995), who found a best fit to their data with E_a = 0.62 eV, following ablation of DHB by a 3 ns N_2 laser. These values are close to the range of sublimation energies estimated for typical matrix compounds (0.7 to 1 eV). It is not possible to say whether the lower value obtained for E_a (0.32 to 0.4 eV) from the 300 ps N_2 ablation data has any significance towards the ablation mechanism. The values obtained for E_a are dependent on the fluence, the conversion to which from laser pulse energy is subject to considerable error, as discussed earlier.

From the range of observed threshold fluences for neutral production, with both the 300 ps and 4 ns N_2 lasers, an estimate can be made for the average energy per DHB molecule at threshold; 0.1 to 0.4 eV per molecule from the 300 ps data, and 0.4 to 0.67 eV per molecule from the 4 ns data. These ranges include the typical values found for E_a which may indicate that complete thermal equilibrium has been approached prior to the commencement of ablation.

Absolute temperatures can be extracted from the graphs shown in Fig.4.22. For the 300 ps N_2 data a value of approximately 500°K (207°C) is found at the ablation threshold, which is reasonable given the typical sublimation temperatures of matrix compounds (Vertes 1993b). For the 4 ns N_2 data a value of approximately 800°K (507°C) is obtained at threshold which is much larger than would be expected. However, the considerable inaccuracy in the value of η could easily account for this.

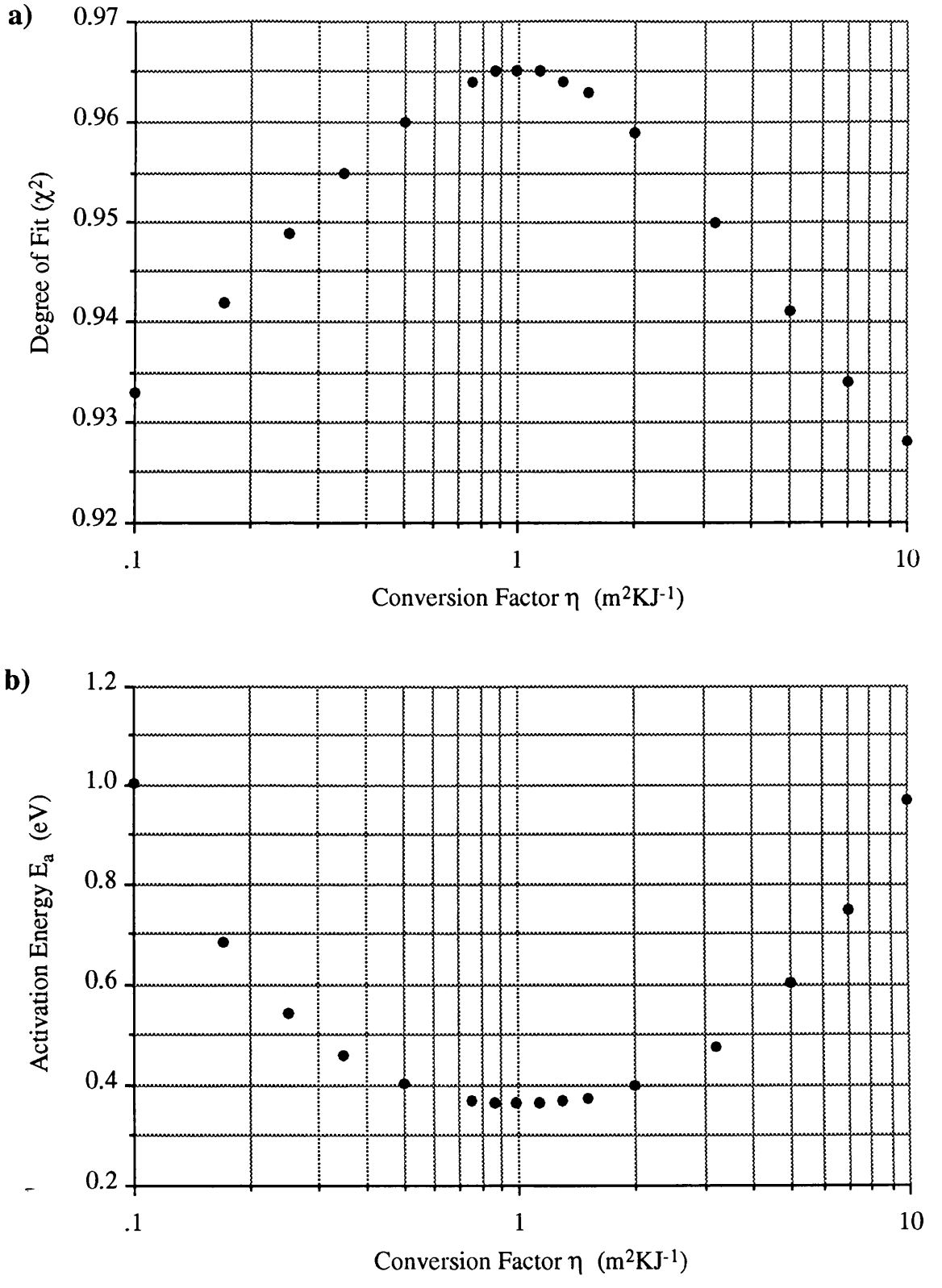

Fig.4.23 Graphs showing a) the degree of fit (χ^2), and b) the activation energy E_a as a function of the conversion factor η. The data used is that shown in Fig.4.22b.

4.6.3 Photochemical and Photomechanical Fit to Data

In the photochemical and photomechanical models the observed threshold fluence is interpreted as a real physical fluence threshold. The yield of ablated neutral species is described by equations of the form given in Eqn.2.18 (photochemical) and Eqn.2.23 (photomechanical). The data obtained by the author was fitted to both of these equations, the results of which are shown in Fig.4.24 and Fig.4.25. In both graphs the solid line fit to the data is the best fit obtained by computer analysis (minimum value of χ^2). However, for both models one data fit could be satisfactorily applied to both the C_2H_2 and M-OH_2 data as expected (dotted line in Fig.4.24b & Fig.4.25b). The degree of fit obtained using both models was less than that obtained using the thermal model. In particular, neither model could fit the data obtained from 4 ns N_2 ablation close to the threshold fluence value with any reasonable accuracy.

It has been reported that pre-irradiation of matrix crystals at a fluence just below the threshold fluence for ion production does not lead to any noticeable change in the eventual threshold fluence value (Westman 1994a). This is difficult to explain in terms of the photochemical model where some form of exposure effect would be expected as the density of broken bonds in the matrix builds up from shot-to-shot. Given the discussions detailed in Chapter 2 and those above, it is considered highly unlikely that the simple photochemical model outlined in Chapter 2 is the mechanism responsible for ablation of neutral material in MALDI.

Some of the best fits to the data were achieved assuming a power law dependence. This is not predicted by any of the models described in Chapter 2. However, the thermal model can often be well approximated (at least close to threshold) by a power law (Johnson 1994) and the predicted neutral yield in the hydrodynamic model of Vertes (Vertes 1993a) was well fitted in the near threshold fluence region (<5 x the threshold fluence) by a power law with an exponent of 6.8, while the experimental ion yield was fitted by a power law with exponent 6. For comparison, Fig.4.26 shows the M-OH_2 PAI data fitted using a power law dependence. The dependence obtained by the author was less steep than

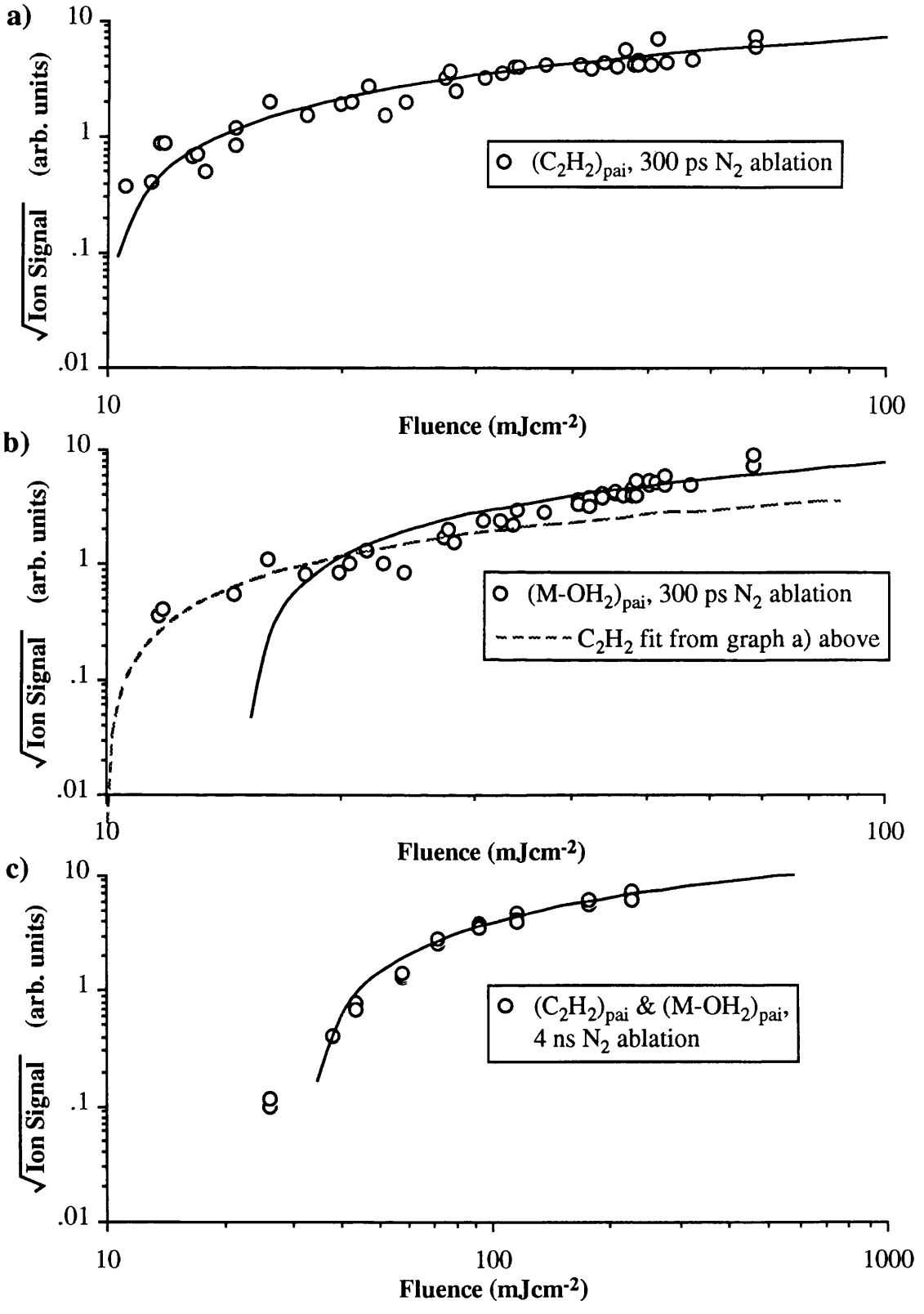

Fig.4.24 Graphs showing best fits to the ablation laser power dependence data assuming a photochemical ablation model and a neutral yield expression of the form given in Equn.2.18; a) C_2H_2 PAI ion signal shown in Fig4.20 (a-d) [300 ps N_2 ablation], b) M-OH_2 PAI ion signal shown in Fig.4.20 (a-d) [300 ps N_2 ablation], and c) Combined C_2H_2 & M-OH_2 PAI ion signal shown in Fig.4.21 [4 ns N_2 ablation].

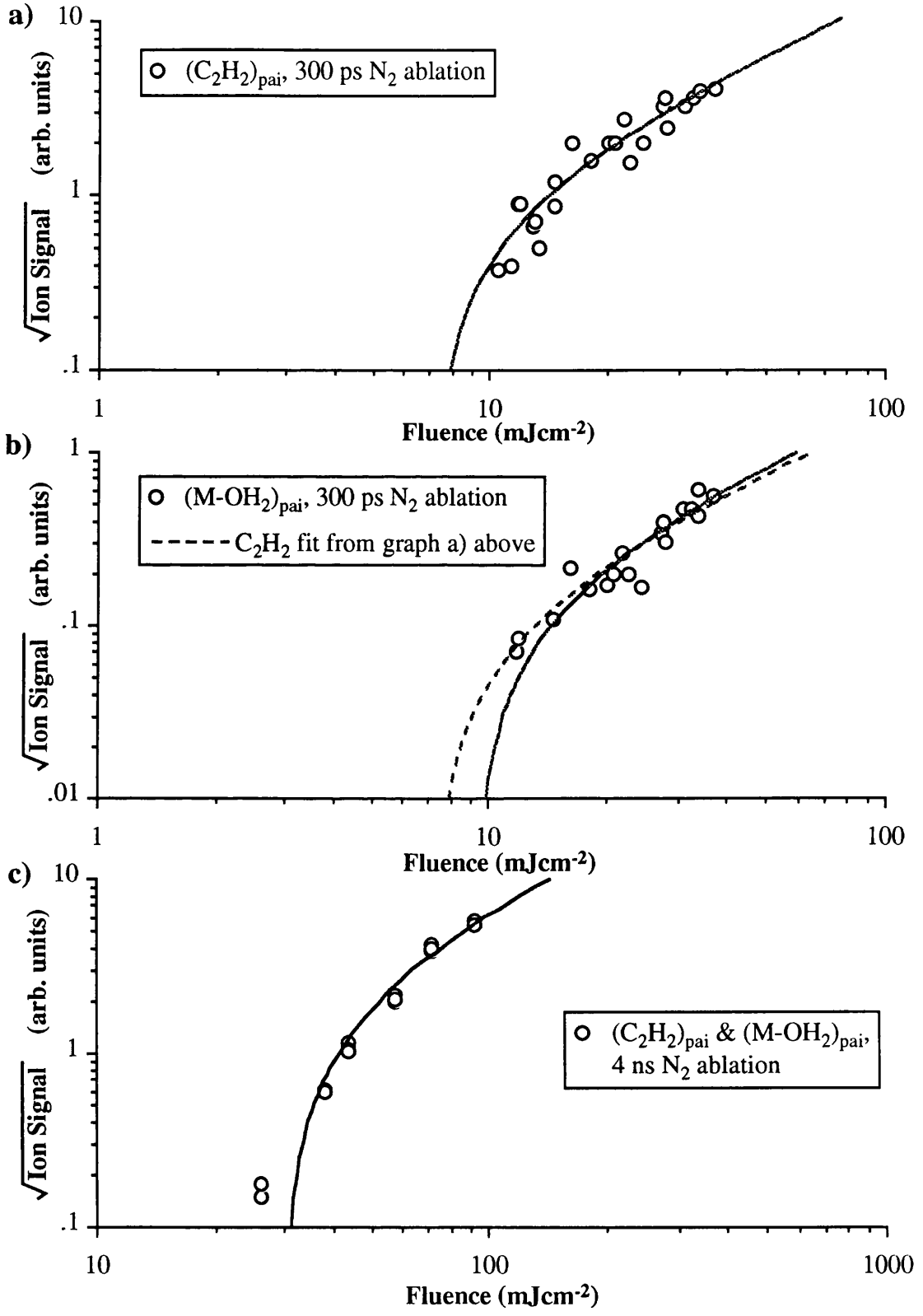

Fig.4.25 Graphs showing best fits to the ablation laser power dependence data assuming a photomechanical ablation model and a neutral yield expression of the form given in Equn.2.23. Only data obtained with an ablation fluence of $< 4F_{th(neut)}$ is used in the fit; a) C_2H_2 PAI ion signal shown in Fig4.20 (a-d) [300 ps N_2 ablation], b) M-OH_2 PAI ion signal shown in Fig.4.20 (a-d) [300 ps N_2 ablation], and c) Combined C_2H_2 & M-OH_2 PAI ion signal shown in Fig.4.21 [4 ns N_2 ablation].

that predicted using the hydrodynamic model of Vertes, an exponent of 3.47 obtained for the data shown in Fig.4.26.

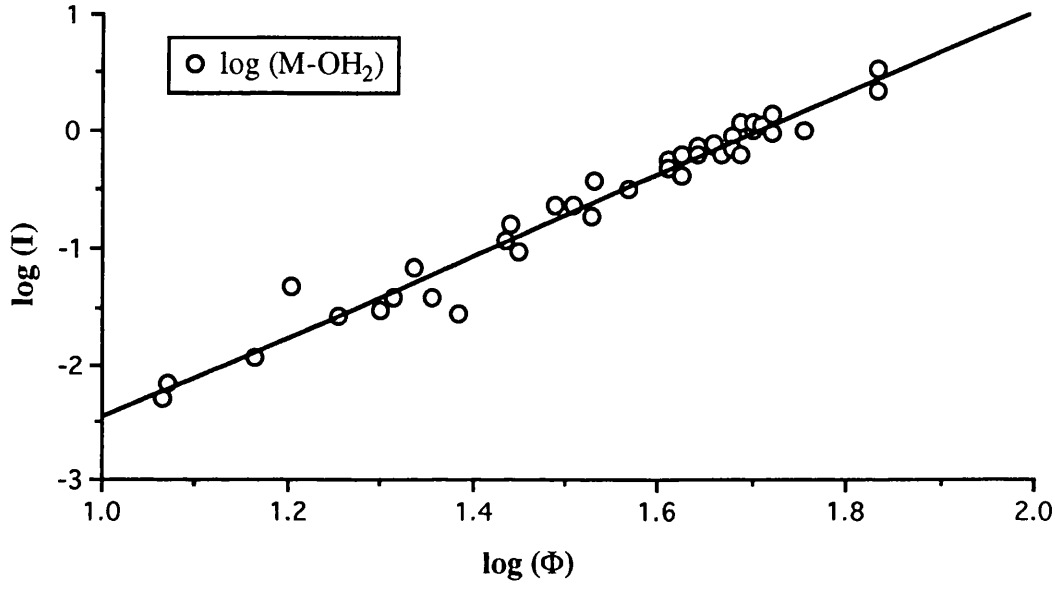

Fig.4.26 Graph showing the (M-OH2) PAI ion signal intensity as a function of ablation laser fluence (Fig.4.20 a-d), the curve fit assuming a power law dependence $I \propto F^x$. Best fit was obtained with a value of x = 3.47.

4.7 Molar Ratio

A series of experiments were carried out to investigate the effect varying the molar ratio of MALDI samples had on the strength of ion signals, the mass resolution, the ion production threshold and the quality of crystals formed in the sample. It was decided to carry out these experiments using substance P as the analyte, with DHB as the matrix. Samples were made up with various molar ratios of matrix to analyte over the range M/A = 350 to 3 500 000. The samples were prepared by either vacuum drying, or by the standard preparation technique of blow drying. Analysis of the blow dried samples was carried out from both the crystals formed around the edge of the sample and the residue left in the centre.

The first experiment to be carried out was to investigate whether the ion production threshold for matrix and analyte ions was a function of the molar ratio. It was found that the threshold fluence for matrix specific

ions showed no dependence on analyte concentration over the range of molar ratios investigated by the author. The value of this threshold fluence was estimated from the results to be approximately 12 (+/-2) $mJcm^{-2}$. Analyte ions were found to have an identical threshold fluence for the low molar ratios, which increased once the molar ratio was increased above approximately M/A = 10^5. This increase should not be seen as a real increase in the physical fluence threshold, but is actually caused by the detection efficiency of the system. Similar work by Sundquist et al (Medina 1994) showed a small but reproducible increase in the threshold fluence towards lower M/A values, changing to a rapid increase as the molar ratio was reduced to the extent that 'dilution' of the matrix occurred. This was well modelled by assuming that the 'dilution' of the matrix results in a lower energy density within the sample crystals for the same incident fluence. That this variation was not seen in the work described above is not surprising given that relatively large ion signal fluctuations were observed (20% error in the estimated value of the threshold fluence), and that the effect would be less significant over the molar ratio range investigated by the author due to the lower mass of analyte investigated.

On the basis of the power dependence work the second set of samples were analysed at two ablation laser fluences; ~50 % above $F_{th(ion)}$ at 19 $mJcm^{-2}$, and ~200 % above $F_{th(ion)}$ at 34 $mJcm^{-2}$. The variation of the substance P and DHB dimer ion signals with molar ratio is shown in Fig.4.27 for ablation with the high fluence from both the sample crystals (a), and the residue left in the centre of the sample (b). The variation of the matrix M-OH_n and M+H_n peaks with molar ratio was essentially the same as that of the matrix dimer. The data obtained with the lower fluence is not shown, but follows an identical pattern with an overall lower ion signal intensity. Analysis of the vacuum dried samples produced similar results to those for the residue.

From Fig.4.27 a) & b) it can clearly be seen that at large molar ratios (M/A>$3x10^4$) the intensity of matrix specific peaks remains essentially constant while that of the substance P ion signal falls approximately inversely proportional to the molar ratio. The substance P ion signal at M/A = 3.5 x 10^6 appears to contradict this behaviour, but is actually larger

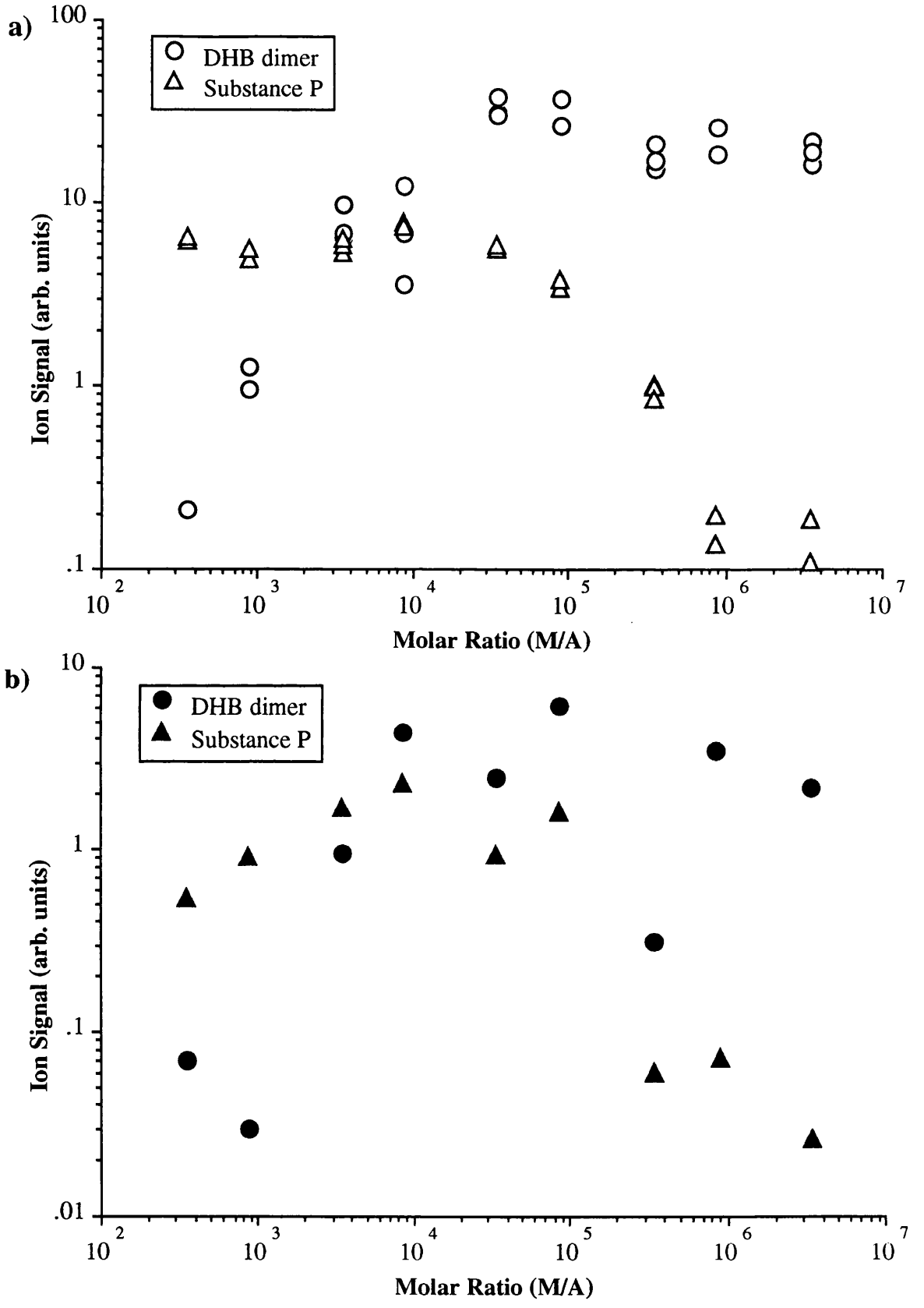

Fig.4.27 Plots showing the variation of the DHB dimer (specifically the ion 2(M - OH_2) + H where M represents the matrix parent) and substance P ion signals as a function of the matrix to analyte molar ratio for ablation from a) the cystals formed around the edge of a standard blow dried sample preparation, and b) the residue left in the centre of the same sample spot. Ablation using a 300 ps nitrogen laser with a fluence of 34 $mJcm^{-2}$.

than expected due to the presence of a small amount of substance P contamination in either the DHB solution, or on the sample stub itself. For molar ratios of less than M/A = 3 x 10^4 the opposite was found; the intensity of the substance P ion signal remained constant, while the intensity of matrix specific peaks dropped with the molar ratio. This suppression of low mass matrix specific peaks has been previously observed (Dominic Chan 1991, Strupat 1991) and is thought to be linked to the rate of intermolecular reactions occurring in the gas phase. Results published by Perera (Perera 1995) show that if the molar ratio is decreased further, below some optimum value, then the substance P ion signal suffers a gradual reduction to zero from the plateau value. This was explained by assuming that as the molar ratio is decreased below the optimum value, an increasing number of analyte molecules are not included in matrix crystals and do not contribute to the MALDI ion signal.

The full width at half maximum (FWHM) of the DHB dimer and substance P ion peaks, from ablation of both crystals and the residue in the centre of a standard sample spot, are shown in Fig.4.28 as a function of the molar ratio. It can clearly be seen that the FWHM of all the ion signals does not show any strong dependence on the molar ratio of the sample. It is interesting to note that although the DHB dimer ion signal shows an increased temporal width for both ablation from matrix crystals, and ablation with an increased fluence, this behaviour is not exhibited by the substance P ion signal. This may imply a different ion production mechanism or significantly different ion source kinematics between analyte and matrix dimer.

The quality of crystals formed around the edges of the blow dried samples was significantly reduced for the two samples with molar ratio M/A = 350 and 875. Of the few crystals that formed, all were very small in comparison to those from pure DHB solutions. On the basis of the authors work, the optimum molar ratio for substance P in DHB lies in the range M/A = 3 x 10^3 to 3 x 10^4 which compares favourably to that found by Karas et al (Strupat 1991).

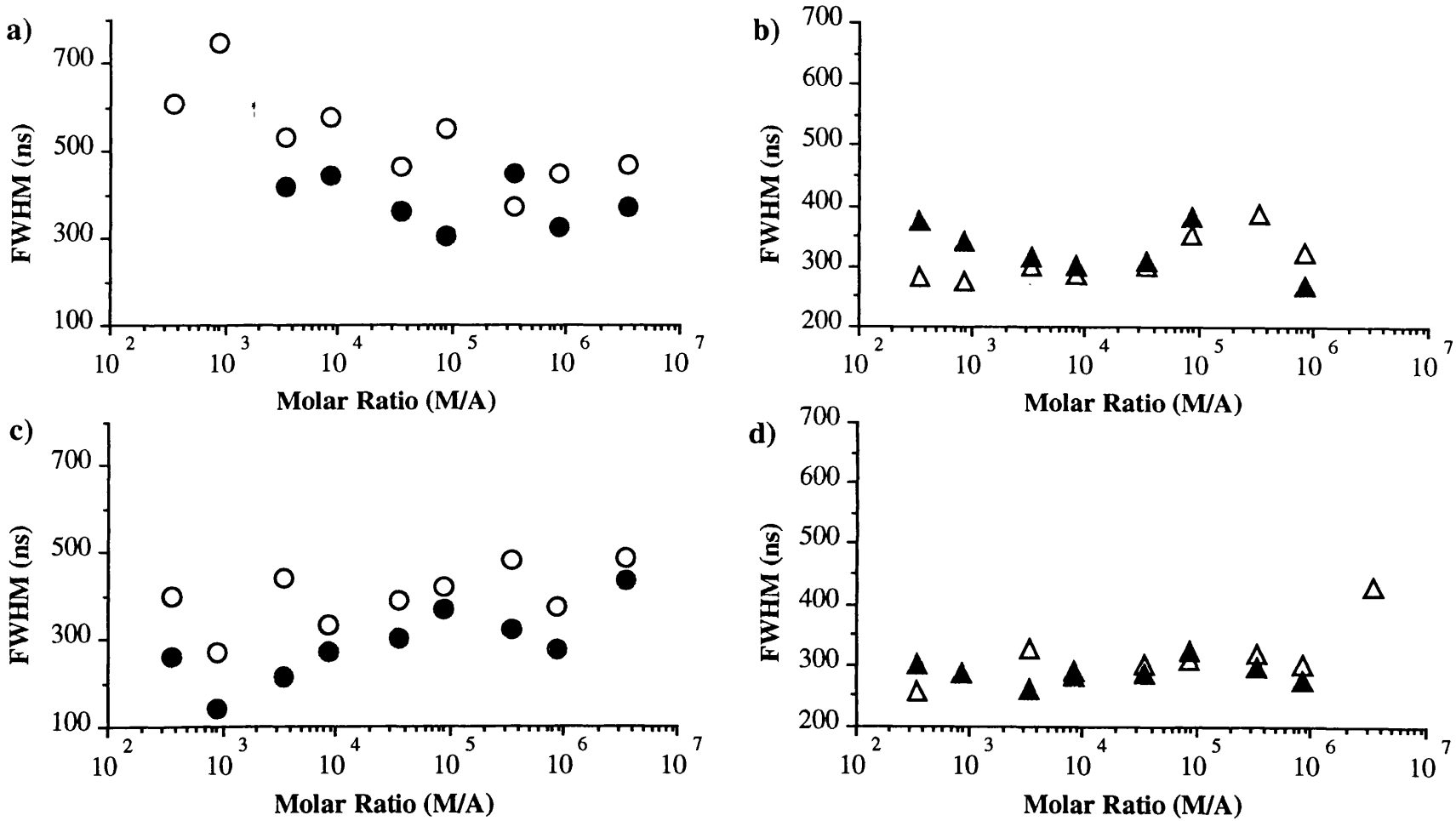

Fig.4.28 Plots showing the variation in temporal width of ion signals as a function of molar ratio for the two ablation laser fluences of 34 $mJcm^{-2}$, a) & b), and 19 $mJcm^{-2}$, c) & d). Ablation using a 300 ps N_2 laser. [Circles - DHB dimer signal from; O crystals, ● residue in centre. Triangles - substance P signal from; Δ crystals, ▲ residue in centre.]

4.8 TFA Cluster Ions

During the course of the experiments looking at the effects of varying the matrix to analyte molar ratio of MALDI samples, cluster ion peaks were occasionally observed in the mass spectral region between the matrix dimer and substance P ion peaks (Fig.4.29). The appearance of these peaks could always be correlated with the use of trifluoroacetic acid (TFA) in the preparation of the analyte solution. The masses of the cluster peaks observed from crystal samples were unambiguously determined as M_c = 260 + 113n, where n $\in$ {1,2,...,7}. The 'monomer' unit of this cluster ion sequence can easily be identified as a deprotonated TFA molecule (the molecular mass of TFA is 114 amu). The ion signal obtained from a sample stub which had been prepared using an aqueous solution of TFA is shown in Fig.4.30. The peak at 113 amu forms the main TFA related ion signal, although a number of quasimolecular fragment ions are also present, which may be connected with the lower intensity peaks spread around each cluster ion peak in the mass spectrum shown in Fig.4.29. The identity of the cluster series 'base' unit (mass 260 amu) is not known but may be tentatively identified as some form of DHB dimer species, such as [2(M - OH + H) - OH +H]. The formation of the TFA cluster peaks was impaired for samples with a molar ratio of approximately 9000 or less,

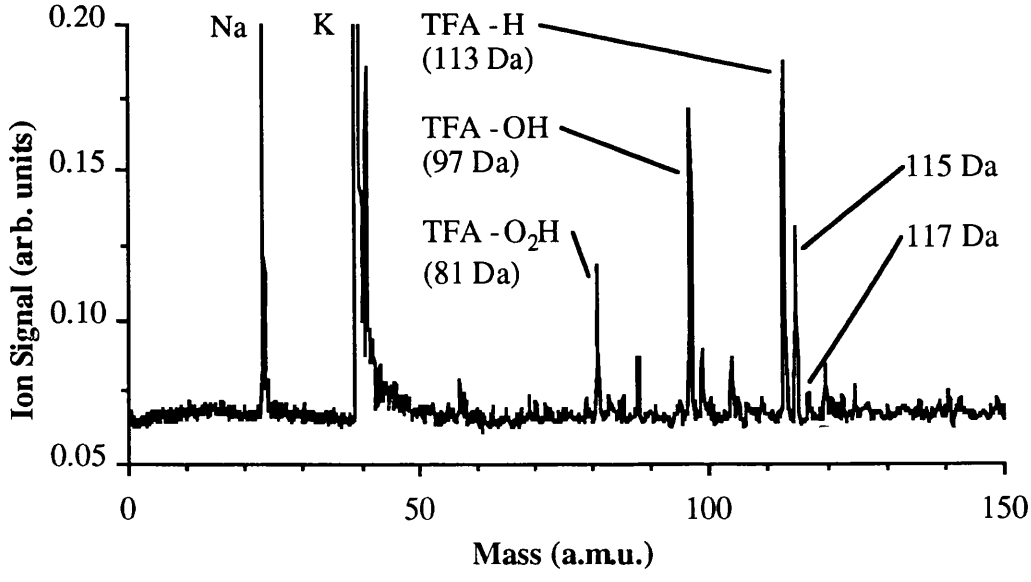

Fig.4.30 Mass spectrum showing the ion signal obtained following ablation from the surface of a steel sample stub onto which an aliquot of solution consisting of 0.1% TFA in de-ionised water had been deposited and dried. Ablation using a 300 ps N_2 laser.

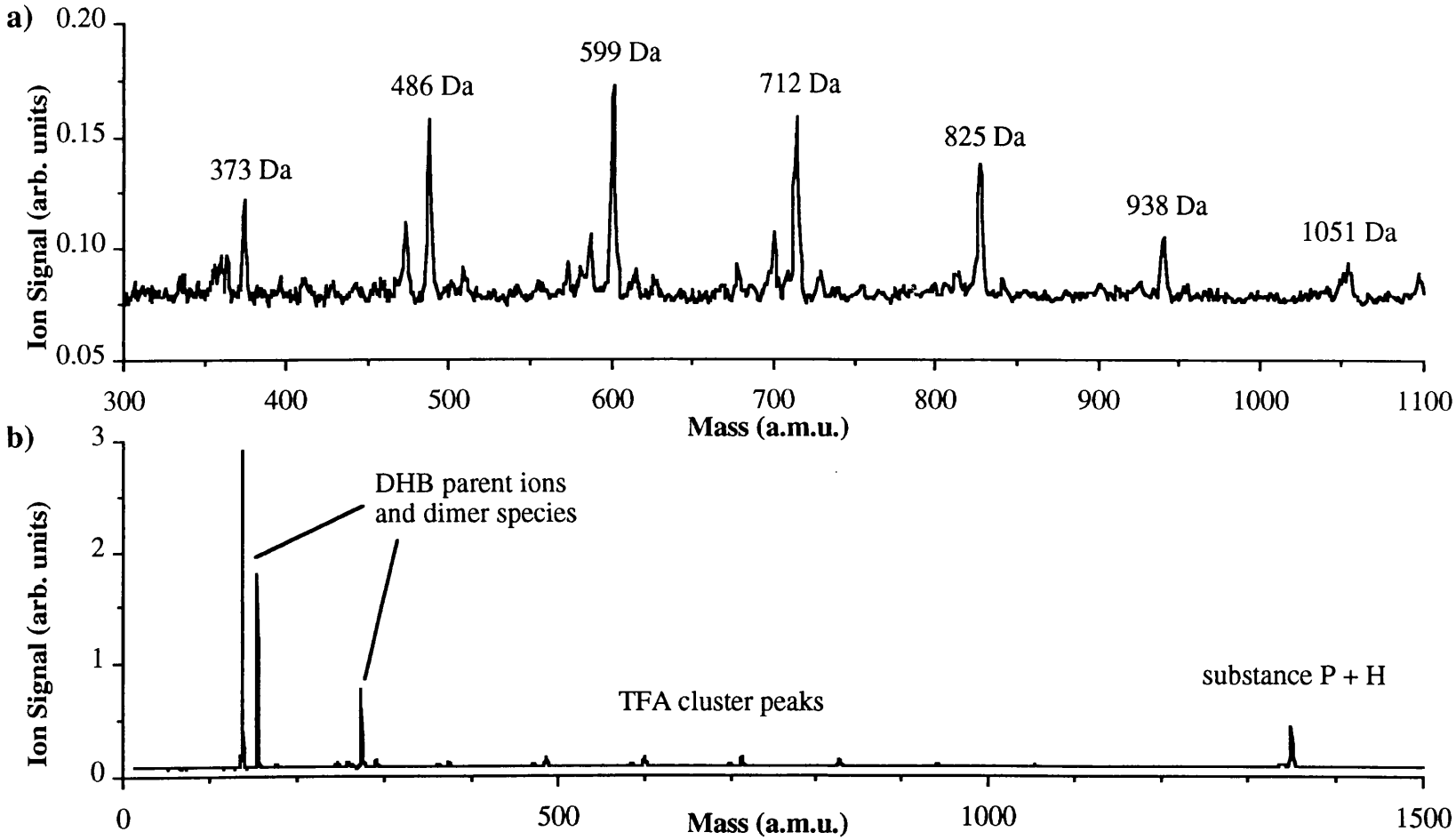

Fig.4.29 Mass spectra showing the ion signals associated with the use of trifluoroacetic acid in sample preparation. The spectrum shown in a) above is an expansion of the region labelled 'TFA cluster peaks' in the mass spectrum shown in b). Ablation using a 300 ps nitrogen laser with a fluence of 23 $mJcm^{-2}$ from a sample of substance P in DHB (molar ratio M/A = 35 000) with the addition of a small amount of TFA. The mass spectrum was summed from 200 laser shots.

and ceased altogether when the molar ratio was reduced to approximately 900 or less.

Similar cluster peaks were also observed in ablation from the residue left in the centre of the sample, and the samples prepared by vacuum drying. However, the appearance of these peaks was sporadic and when the peaks could be observed, the ion signals were small in comparison to those obtained from the matrix/analyte crystals. The envelope of the cluster peaks from the residue was heavily skewed towards the lower masses, and the mass of each cluster peak was increased by 20 and 21 amu, believed to be some form of sodium adduct of the cluster series base unit.

It was thought that the cluster ion series would provide excellent internal calibration for mass analysis of small peptides. However, this was limited by the poor mass resolution of MALDI spectra compared to that achievable with post-ionisation techniques. The mass of the substance P ion peak was calculated from a number of spectra containing TFA cluster peaks as 1347.5 +/- 0.8 amu. This compares well with the actual mass of the protonated monoisotopic molecule (1347.7 amu). This relatively accurate mass calibration did not extend to higher masses. Poor reproducibility of calculated mass was encountered when the TFA peaks were used to calibrate spectra also containing bovine insulin. Accurate calibration of high mass analytes using reflectron TOF analysis alone, can only be ensured with the addition of known compounds to the sample, of similar mass to the unknown analyte.

Chapter Five

Post Ablation Ionisation

5.1 Introduction

This Chapter is concerned with investigations into the plume of neutral material ejected from the sample surface following laser ablation. The particular technique used by the author is called Post Ablation Ionisation (PAI) and involves probing the ablation plume with a second laser to ionise neutral species (called photo-ionisation) which can then be detected in the mass spectrometer. A schematic of the interaction region and sample stub is shown in Fig.2.5 (Chapter 2). The density of neutral material in the ablation plume can be investigated as a function of time by varying the delay between the ablation and PAI laser, with the PAI laser kept at a constant distance from the sample surface. A description of the instrumentation used to carry out this work is given in Chapter 3. Only single crystal samples were used in this work to ensure relatively good signal reproducibility combined with slow signal decay as a function of sample exposure.

The nature of the PAI work carried out by the author facilitates the separation of the particle distribution data into two essentially separate sections (Section 5.3 & 5.4): The first section describes PAI work carried out 'far' from the sample surface, at typical separations of 1 mm or greater. Modelling of the experimental results is attempted using the theory described in Chapter 2, Section 2.3 (Plume Dynamics); The second section in this Chapter describes PAI work carried out at very small distances from the sample surface where the theory described in Chapter 2 could not be expected to apply.

5.2 Photo-Ionisation Spectra of DHB

Typical PAI mass spectra obtained following ablation of DHB are shown in Fig.5.1a & b. In the spectrum shown in Fig.5.1b the ablation fluence

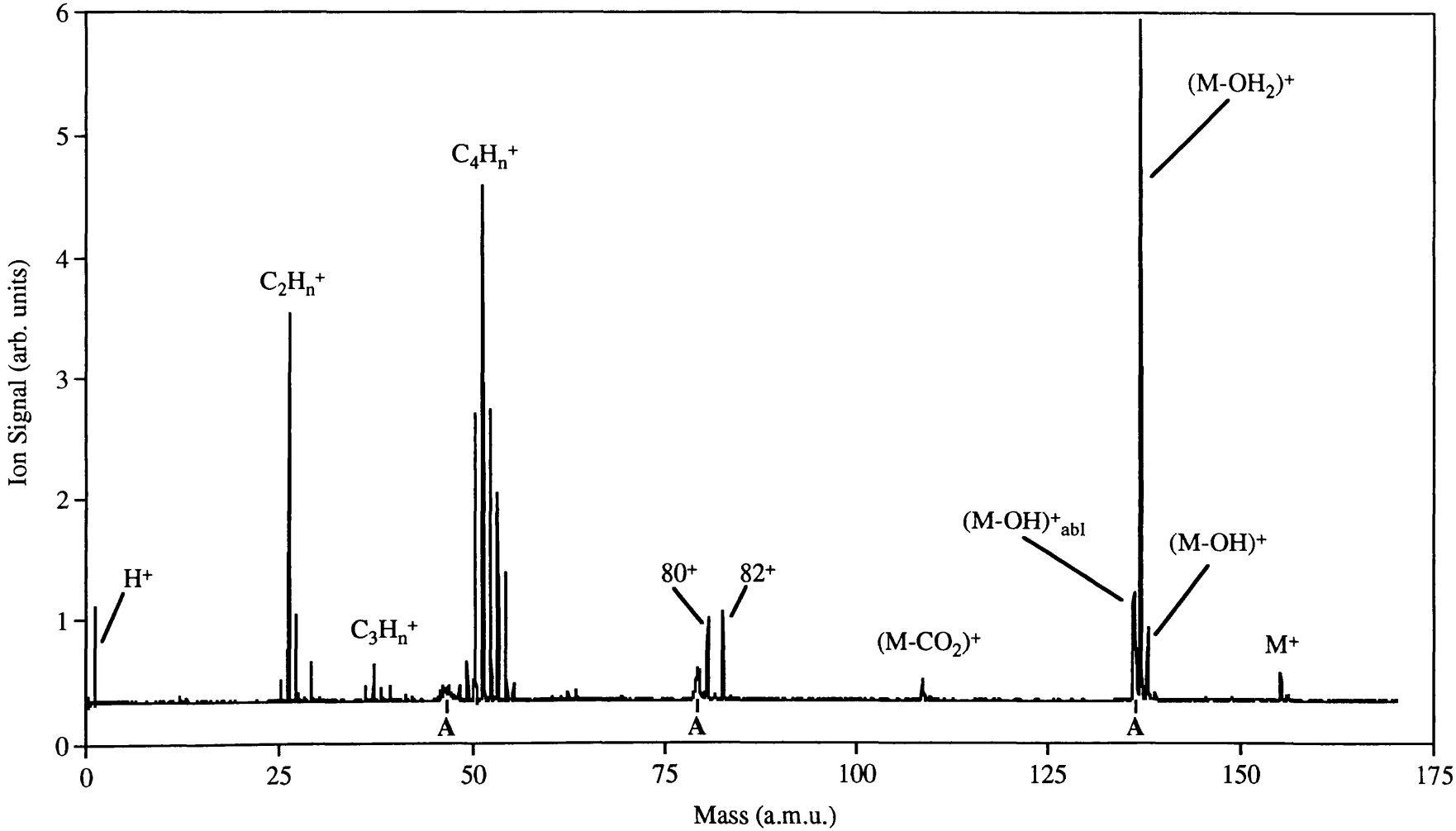

Fig.5.1a PAI mass spectrum obtained following ablation of DHB using a 4 ns N_2 laser with a fluence of 35 $mJcm^{-2}$ (just above the ion production threshold). PAI carried out at 243.13 nm with an intensity of 4.5 x 10^7 Wcm^{-2}. When the PAI laser is blocked, only the small ablation peaks marked '**A**' remain in the spectrum.

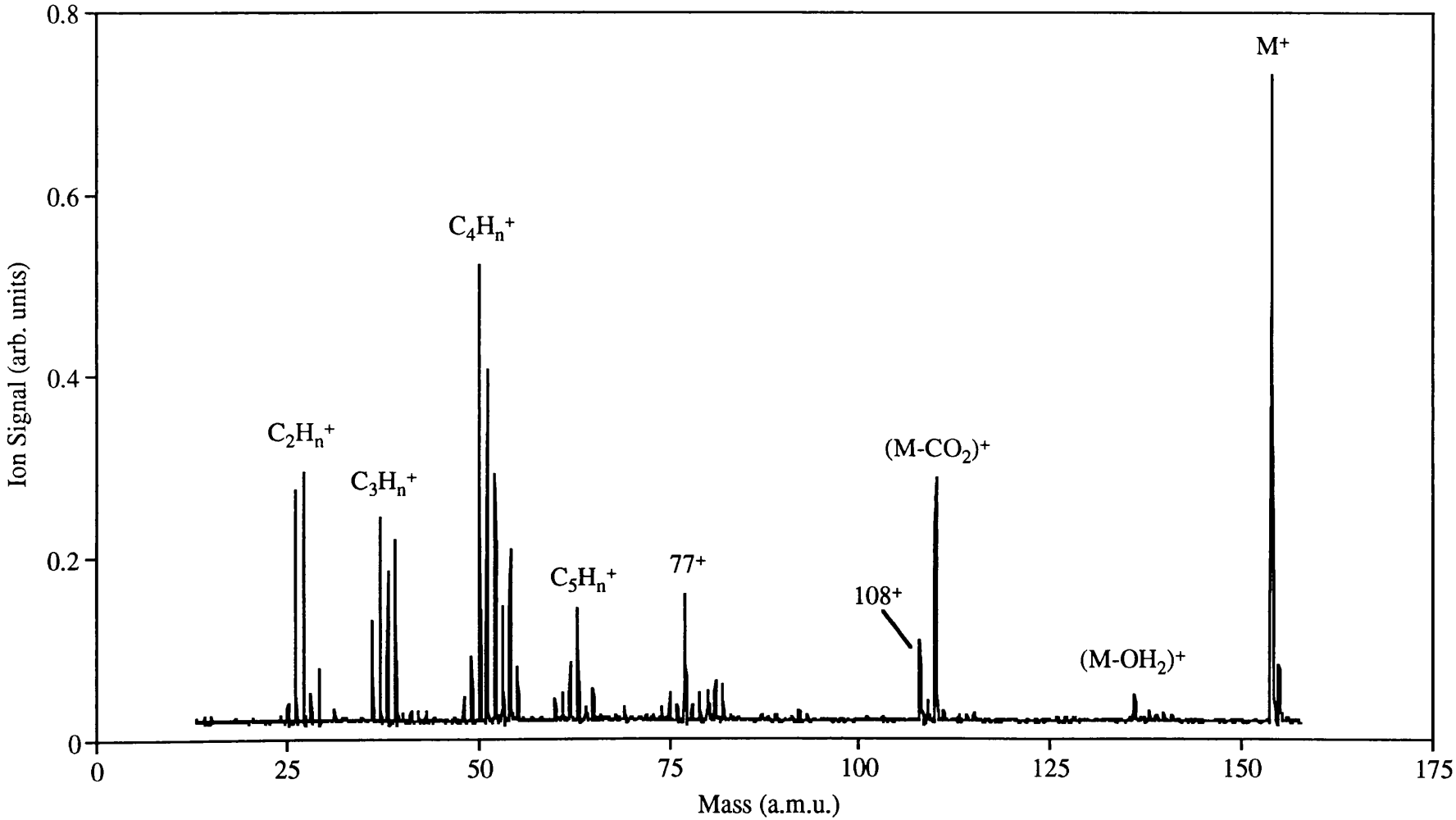

Fig.5.1b PAI mass spectrum obtained following ablation of DHB using a 300 ps N_2 laser with a fluence of 22.5 $mJcm^{-2}$ (below the ion production threshold). PAI carried out at 266 nm with an intensity of 1.3 x 10^9 Wcm^{-2}. When the PAI laser is blocked, no ion signals can be observed.

was just above the threshold fluence for ion production and small ablation ion signals can be seen superimposed on the PAI spectrum.

It is immediately apparent from the spectra shown in Fig.5.1a & b that the absorption cross sections and fragmentation pathways for the neutral species present in the plume are markedly different at the two PAI wavelengths used. With PAI at 243.13 nm, $(M\text{-}OH_2)^{+\bullet}$ is the main quasimolecular ion signal, while PAI at 266 nm produces M^+ as the main peak. The dependence's of the ion species shown in Fig.5.1a & b on the PAI laser intensity are shown in Fig.5.2. It can be seen that the matrix parent (M) and dehydroxylated parent ($M\text{-}OH_2$) ion signals have an essentially identical power dependence of approximately unity, with no sign of signal saturation at the higher intensity values. The gas phase ionisation potentials of polar organic molecules typically lie in the range 7-9 eV (Oraevsky 1991, Ehring 1992) while the photon energies used in the PAI work are 4.7 eV (266 nm) and 5.1 eV (243 nm). It is most likely that the M^+ and $(M\text{-}OH_2)^{+\bullet}$ ion signals originate from two photon ionisation of the respective neutral species, the first excitation step of which is saturated at the laser intensities shown in Fig.5.2. Fragmentation of M^* after the initial excitation step with subsequent photo-ionisation of neutral ($M\text{-}OH_2$) can be excluded since an increased PAI power dependence would be expected for the $(M\text{-}OH_2)^{+\bullet}$ ion signal over that for M^+. Likewise, dissociation of M^+ to form H_2O and $(M\text{-}OH_2)^{+\bullet}$ or a similar ion dissociation channel is not considered likely as discussed in section 5.3. The $(M\text{-}CO_2)^+$ signal has a PAI laser power dependence of < 1 over the range of intensities shown in Fig.5.2, and is also assumed to be present in the ablation plume as the neutral species. The lower mass fragments (less than 108 amu) shown in Fig.5.1a & b all show PAI laser power dependence's of > 1 and are believed to originate mainly from PAI laser induced fragmentation. This is not expected to hold for ablation at fluences significantly above the threshold fluence for ion production where laser generated plasmas will form and considerable matrix fragmentation occurs (Fig.6.10). It can be postulated that the significantly different fragmentation patterns apparent between Fig.5.1a & b may be a consequence of a different parent species depending on the PAI wavelength chosen (ie Fig.5.1a may show mainly the fragmentation pattern from ($M\text{-}OH_2$) and similarly for Fig.5.1b and M).

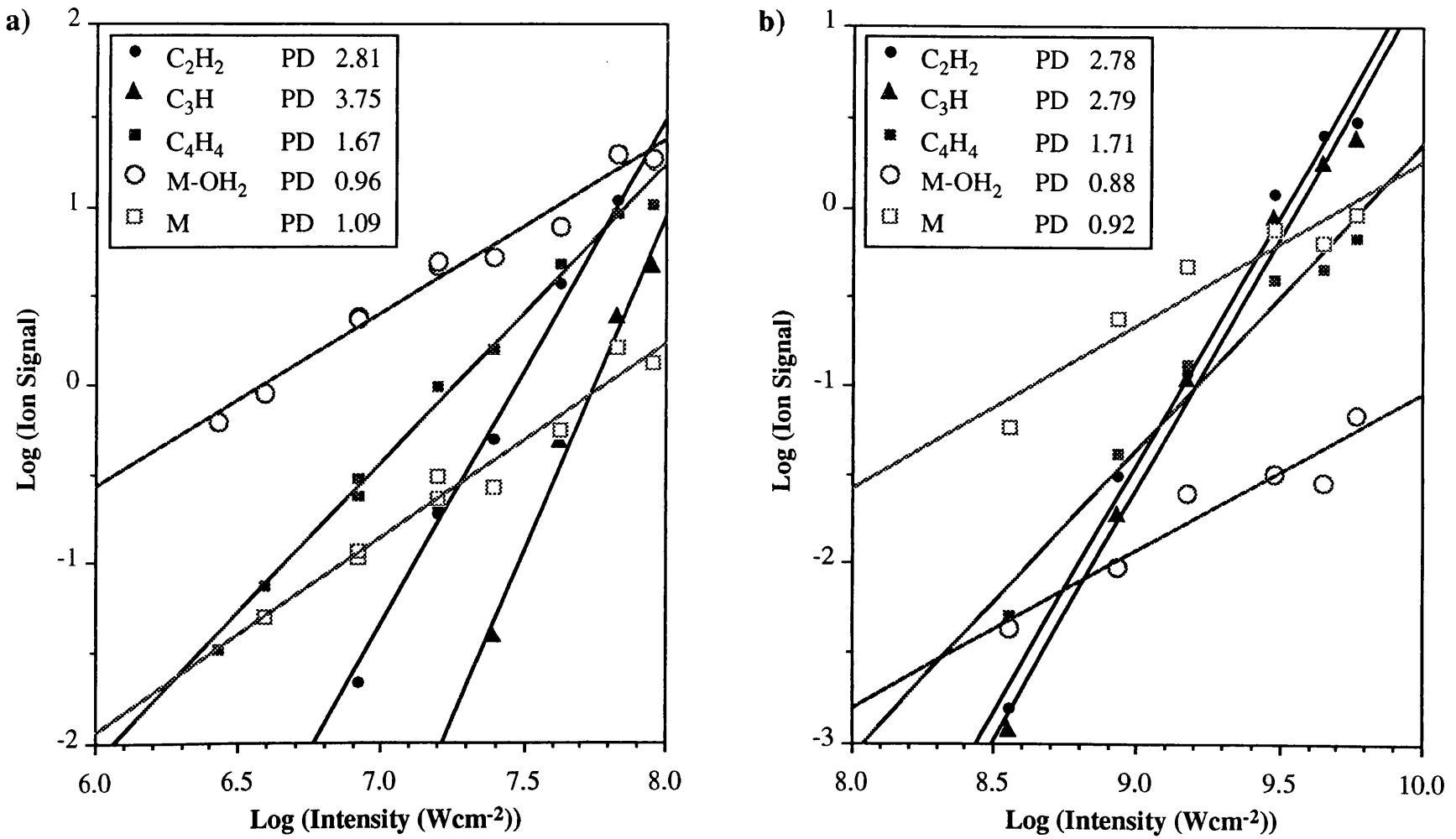

Fig.5.2 Graphs showing the PAI signal power dependence for a) PAI at 243.13 nm and ablation using a 4 ns N_2 laser with a fluence of 42 mJcm^{-2}, and b) PAI at 266 nm and ablation using a 300 ps N_2 laser with a fluence of 22 mJcm^{-2}. The data has been corrected for decay in signal size as a function of the number of laser shots on the sample using the known dependences at the above fluences.

The presence of $(M\text{-}OH_2)$ as one of the main neutral species in the plume is not surprising. One of the main mechanisms proposed to explain the production of ions in MALDI is that of a proton-transfer reaction. Proton transfer to neutral $(M\text{-}OH_2)$ in the dense ablation plume would result in the appearance of $(M\text{-}OH)^+$, the main matrix ion signal seen in the MALDI spectra from DHB.

5.3 Particle Distributions Far from the Sample Surface

Investigations were carried out into the plume particle distributions produced following N_2 laser ablation using both the 4 ns and 300 ps lasers, with PAI performed using 243.13 nm (doubled dye laser output) and 266 nm (quadrupled Nd:YAG output) respectively. The ablation plume was probed at a variety of PAI/sample separations within the range 0.65 to 3.2 mm. Some of the data obtained are shown in Fig.5.3a to Fig.5.3h in the form of time distributions. The PAI pulse energy was monitored for each individual data point and the data subsequently corrected for variations using the known power dependence of each ion signal (Fig.5.2). In addition the data was also corrected for the known variation of the PAI signals as a function of the number of ablation pulses on the sample. In spite of this, it should be emphasised that accurate data is difficult to produce given that laser ablation does not result in highly stable signals as a function of time. Some of the data obtained by the author could not be used due to sudden changes which occurred in the flux of ejected material during the course of a run, believed to result from sample inhomogeneities.

In the time distributions shown in Fig.5.3a to Fig.5.3h the only carbon fragments shown are $(C_3H_n)^+$. and $(C_4H_n)^+$. All the other carbon fragments shown in Fig.5.1a & b followed a similar behaviour. The most striking feature in the distributions shown in Fig.5.3a to Fig.5.3h is the relative behaviour of the M^+ and $(M\text{-}OH_2)^{+\bullet}$ signals. In the data obtained following 4 ns N_2 ablation (Fig.5.3f to Fig.5.3h) all ion signals exhibit the same behaviour. However, in the data obtained following 300 ps N_2 ablation (Fig.5.3a to Fig.5.3e) the behaviour of the $(M\text{-}OH_2)^{+\bullet}$ signal is

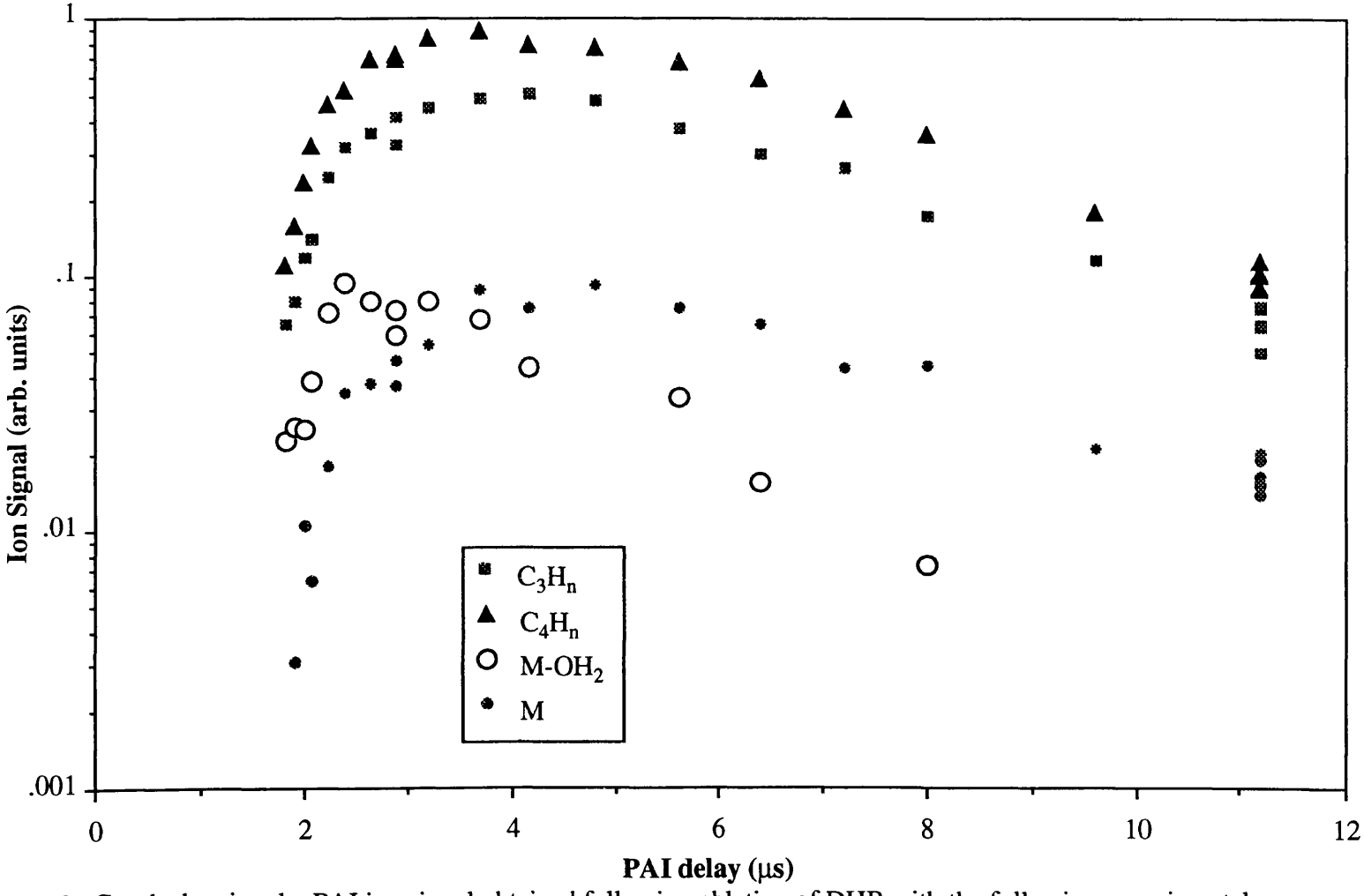

Fig.5.3a Graph showing the PAI ion signal obtained following ablation of DHB with the following experimental parameters: Ablation using a 300 ps N_2 laser with a fluence of 39 $mJcm^{-2}$; PAI at 266 nm, 3.2 mm from the sample and with an intensity of 6.6 x 10^9 Wcm^{-2}. M represent the matrix parent molecule.

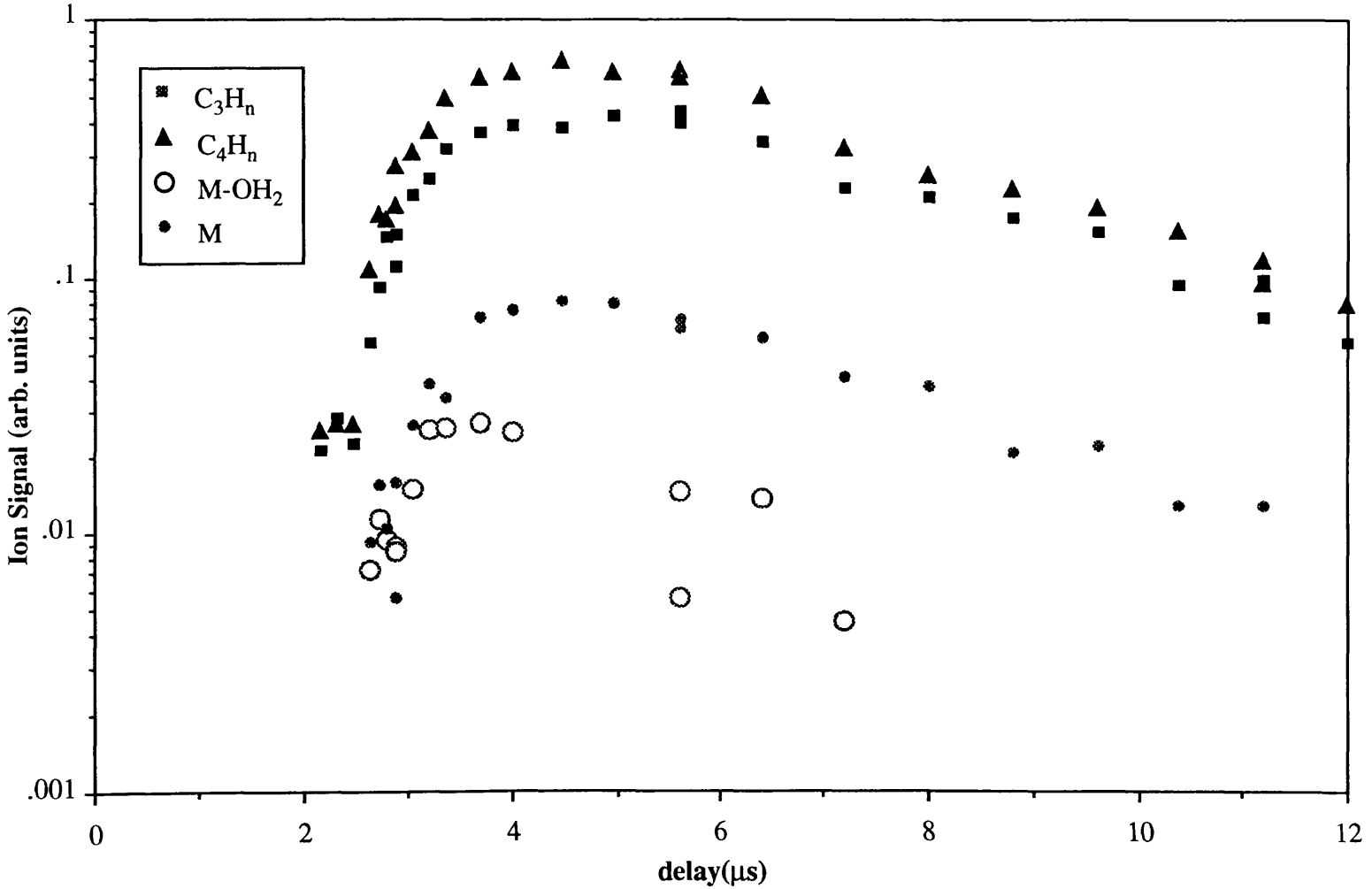

Fig.5.3b Graph showing the PAI ion signal obtained following ablation of DHB with the following experimental parameters: Ablation using a 300 ps N_2 laser with a fluence of 16.5 $mJcm^{-2}$; PAI at 266 nm, 3.2 mm from the sample and with an intensity of 6.6 x 10^9 Wcm^{-2}. M represent the matrix parent molecule.

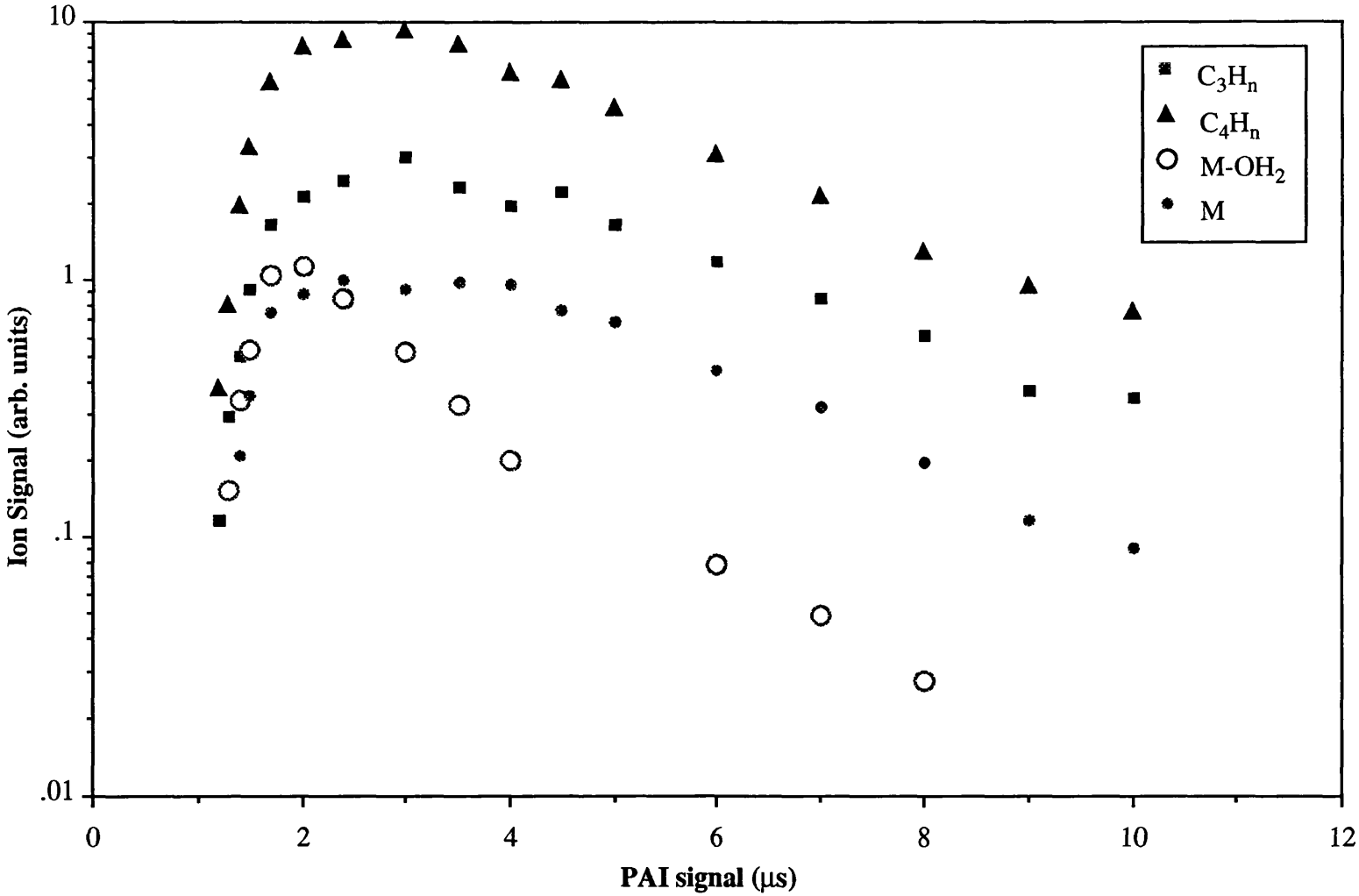

Fig.5.3c Graph showing the PAI ion signal obtained following ablation of DHB with the following experimental parameters: Ablation using a 300 ps N_2 laser with a fluence of 44 $mJcm^{-2}$; PAI at 266 nm, 2 mm from the sample and with an intensity of 4.2 x 10^9 Wcm^{-2}. M represent the matrix parent molecule.

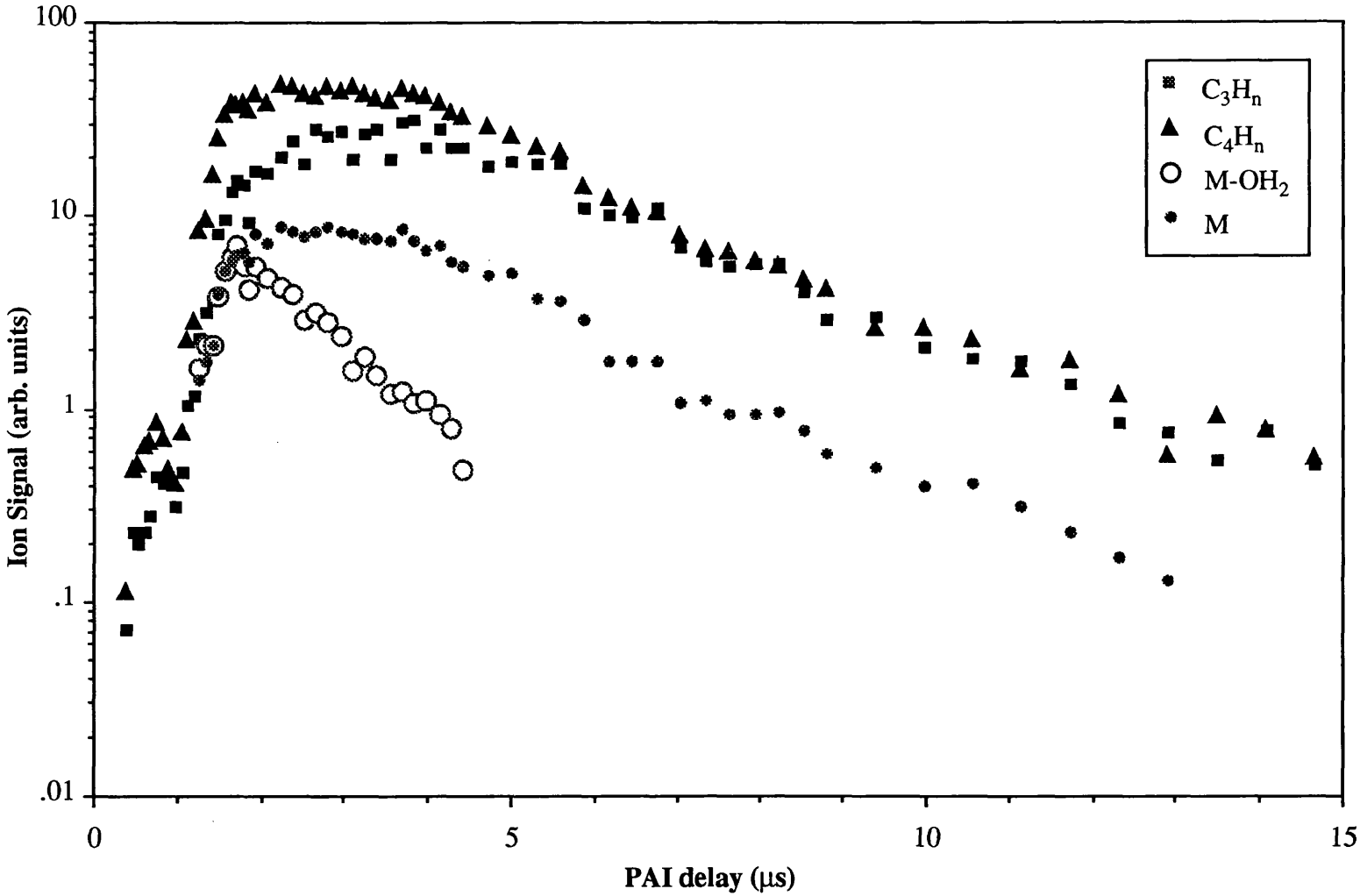

Fig.5.3d Graph showing the PAI ion signal obtained following ablation of DHB with the following experimental parameters: Ablation using a 300 ps N_2 laser with a fluence of 57 $mJcm^{-2}$; PAI at 266 nm, 1.5 mm from the sample and with an intensity of 1.4 x 10^9 Wcm^{-2}. M represent the matrix parent molecule.

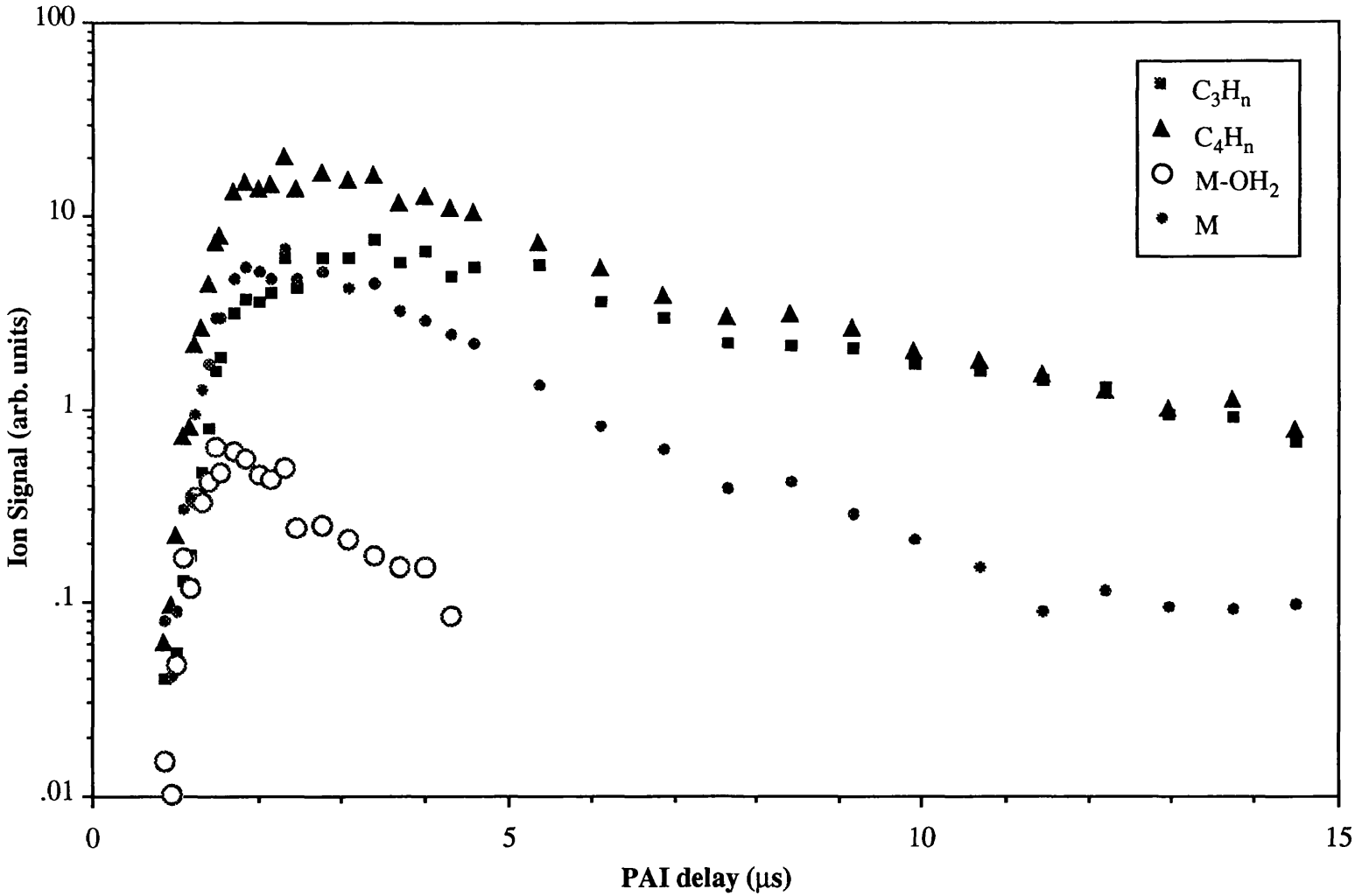

Fig.5.3e Graph showing the PAI ion signal obtained following ablation of DHB with the following experimental parameters: Ablation using a 300 ps N_2 laser with a fluence of 23 $mJcm^{-2}$; PAI at 266 nm, 1.5 mm from the sample and with an intensity of 1.4×10^9 Wcm^{-2}. M represent the matrix parent molecule.

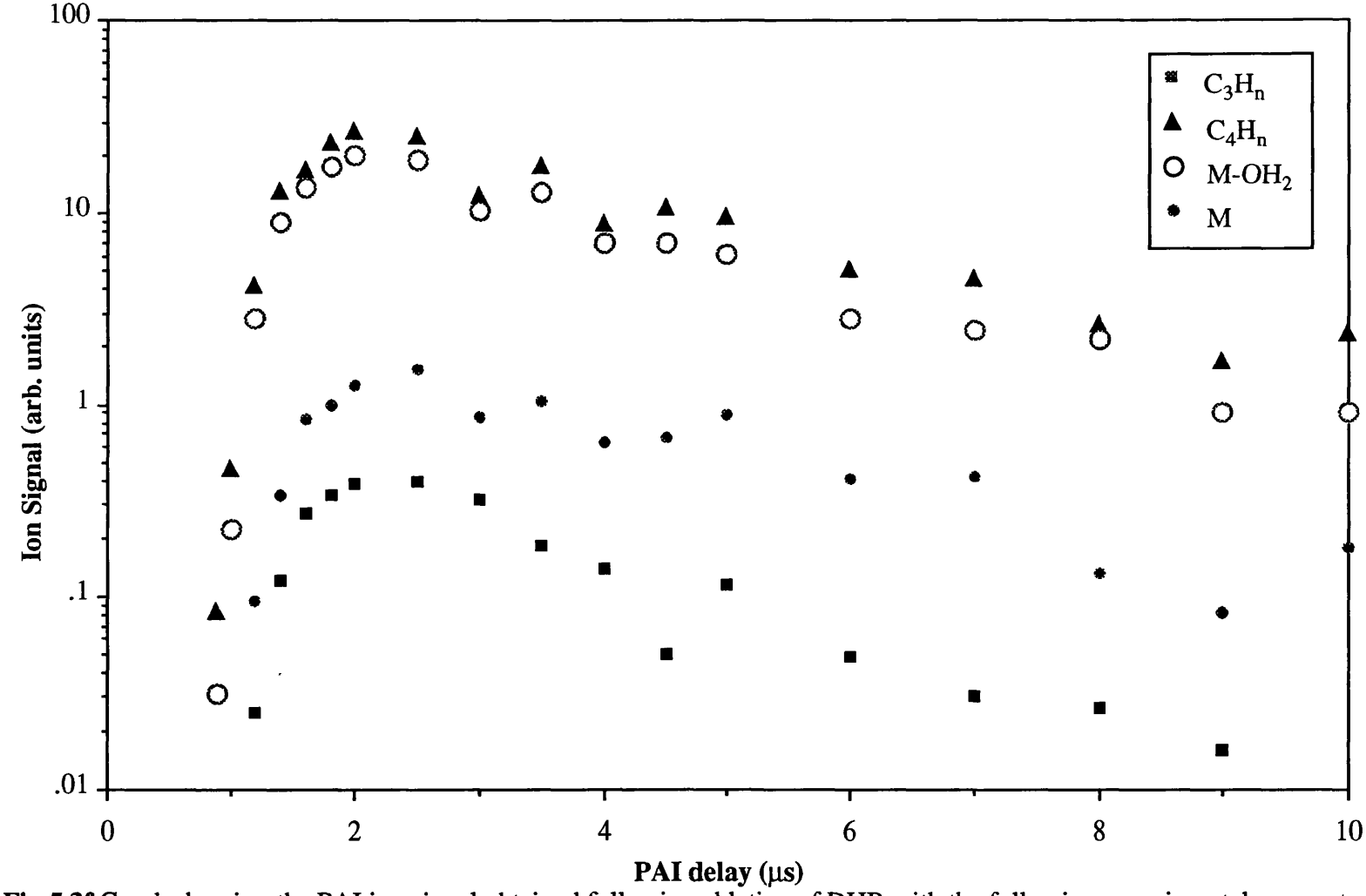

Fig.5.3f Graph showing the PAI ion signal obtained following ablation of DHB with the following experimental parameters: Ablation using a 4 ns N_2 laser with a fluence of 61 $mJcm^{-2}$; PAI at 243.13 nm, 1.1 mm from the sample and with an intensity of 3.1×10^7 Wcm^{-2}. M represent the matrix parent molecule.

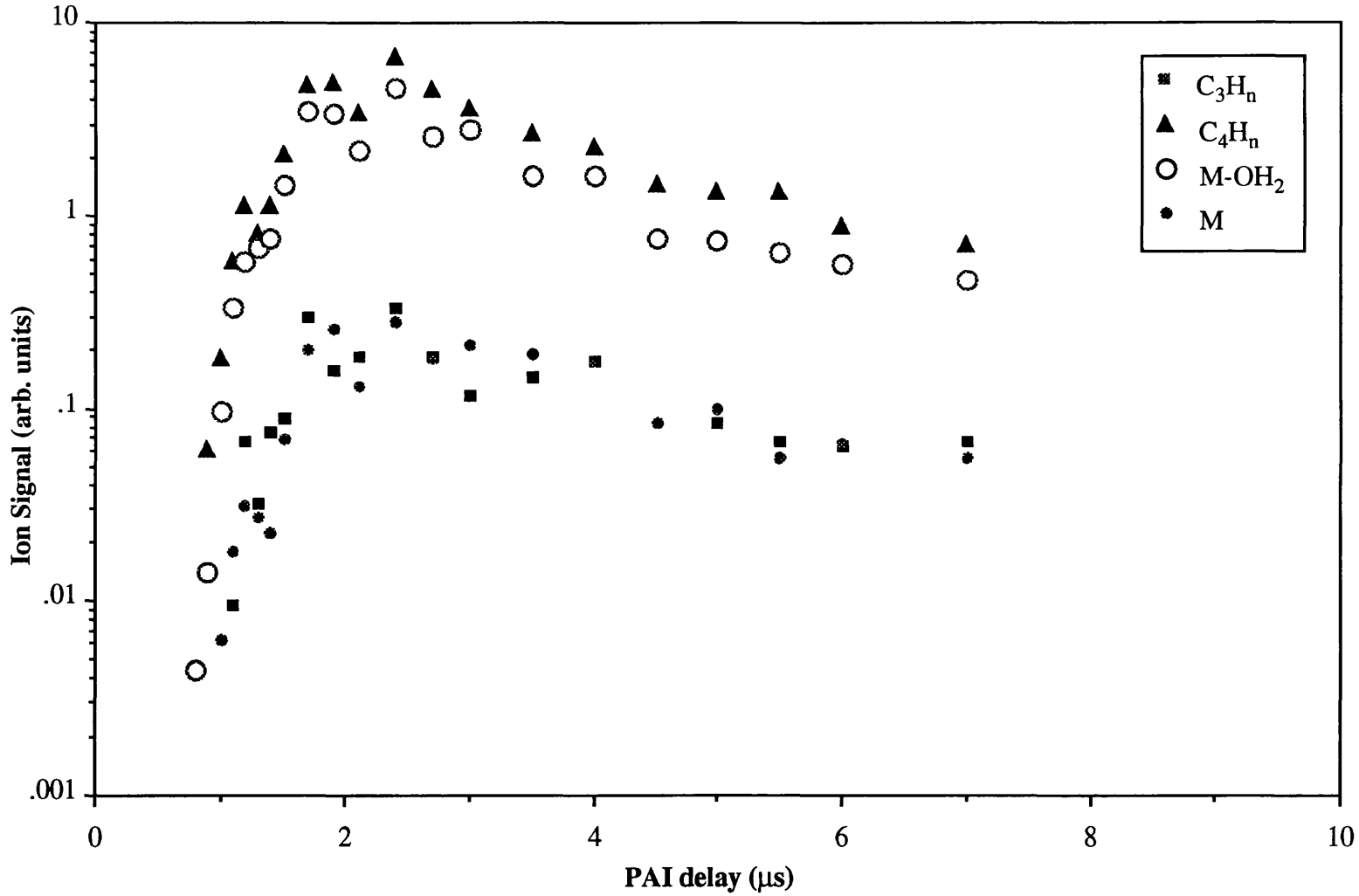

Fig.5.3g Graph showing the PAI ion signal obtained following ablation of DHB with the following experimental parameters: Ablation using a 4 ns N_2 laser with a fluence of 28 $mJcm^{-2}$; PAI at 243.13 nm, 1.1 mm from the sample and with an intensity of 3.1 x 10^7 Wcm^{-2}. M represent the matrix parent molecule.

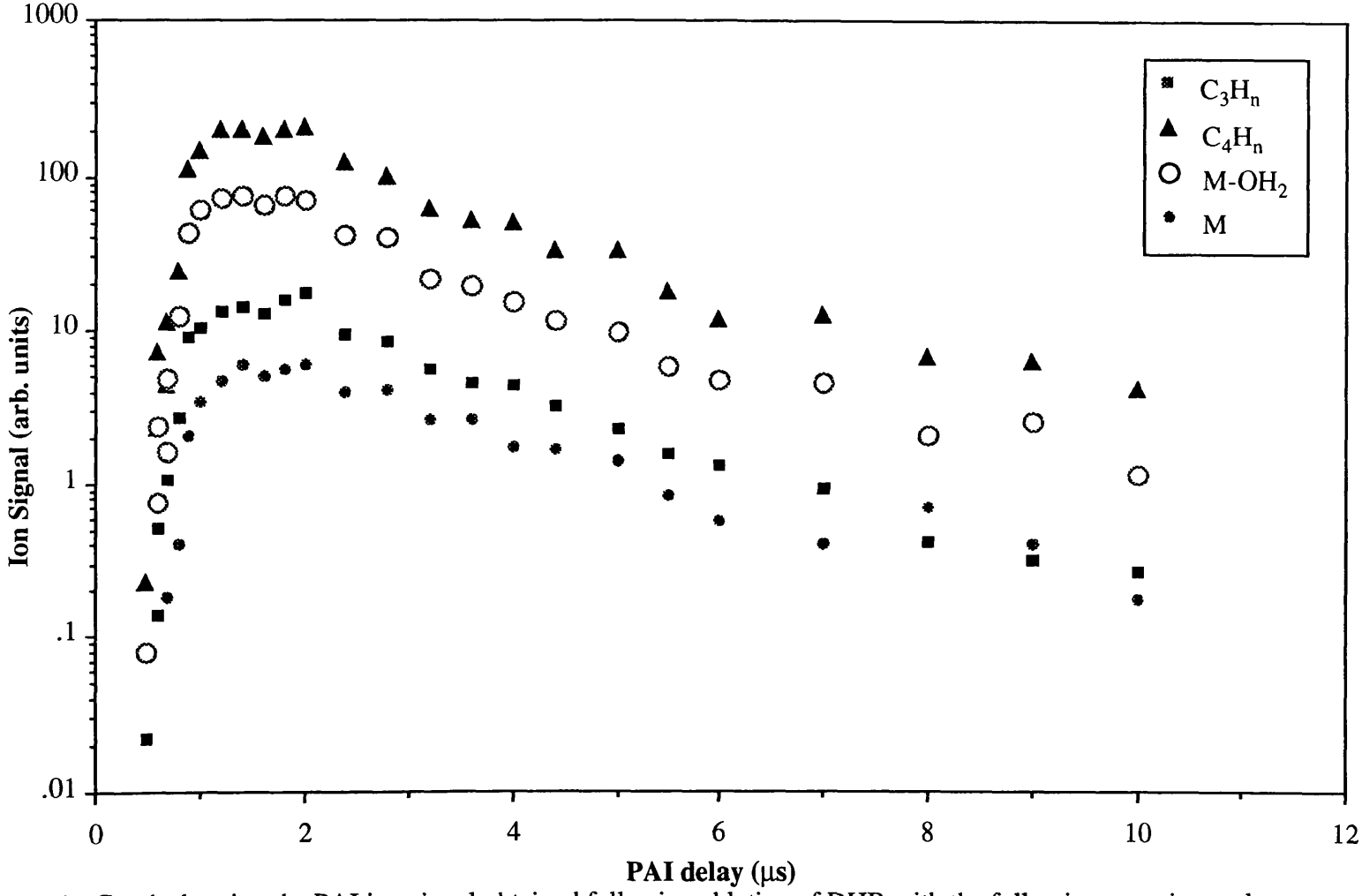

Fig.5.3h Graph showing the PAI ion signal obtained following ablation of DHB with the following experimental parameters: Ablation using a 4 ns N_2 laser with a fluence of 28 $mJcm^{-2}$; PAI at 243.13 nm, 650 μm from the sample and with an intensity of 7.8 x 10^7 Wcm^{-2}. M represent the matrix parent molecule.

markedly different from that of the M^+ or carbon fragment ion signals, reaching a maximum at shorter delay times and falling to the noise level at an increased rate. If picosecond laser ablation resulted in the production of excited neutral $M\text{-}OH_2$ species which subsequently fragmented with a lifetime on the order of a few microseconds, this could explain the observed behaviour. However, such an effect would result in a reduction of the $(M\text{-}OH_2)^{+\bullet}$ signal with respect to the M^+ signal as the PAI/sample separation, and hence the delay time at the distribution maximum, was increased. Such an effect is not evident in the data shown in Fig.5.3a to Fig.5.3e. The observed behaviour of the $(M\text{-}OH_2)^{+\bullet}$ signal in the ablation plume from the 300 ps N_2 has been interpreted by the author as an indication that neutral $M\text{-}OH_2$ species are ejected with a higher mean energy than that of the neutral M species. This is not apparent in ablation with a 4 ns N_2 laser.

The data has been modelled using the half-range Maxwell Boltzman and Knudsen layer models outlined in Chapter 2, section 2.3 and Appendix B. These models predict that the particle distribution in the ablation plume can be described by the equation

$$I \propto \frac{1}{t^i} \exp\left[\left(\frac{-m}{2 k_B T'}\right)\left(\frac{z}{t} - u_K\right)^2\right] \qquad \text{Eqn.5.1 (2.28 \& 29)}$$

where; $u_K = 0$ and $T' = T_c$ in the half-range Maxwell Boltzman (MB) model, and $T' = T_K$ in the Knudsen layer model. All parameters in Eqn.5.1 are known apart from T_c & i in the MB model, and T_K, i & u_K in the Knudsen layer model. The flow velocity (u_K) in the Knudsen layer model can be obtained from the most probable particle velocity in the plume (Appendix B), and the Knudsen temperature can be related to the characteristic temperature via Eqn.B.2. Thus it is possible to choose a value for i and solve Eqn.5.1 for the characteristic temperature. This was done by taking the logarithm of Eqn.5.1, re-arranging to give

$$\ln (I) - \ln (t^{-i}) + \text{constant} = \left(\frac{-m}{2 k_B T'}\right)\left(\frac{z}{t} - u_K\right)^2 \qquad \text{Eqn.5.2}$$

and plotting the left hand side against either t^{-2} (MB model) or $(z/t - u_K)^2$ (Knudsen layer model).

Eqn.5.2 was fitted to the M and M-OH_2 particle distributions shown in Fig.5.3a to Fig.5.3h for both the MB and Knudsen layer models, using four values of i for each ($i \in \{2,3,4,5\}$). Examples of this are given in Fig.5.4a & b for some of the data shown in Fig.5.3h. Although considerable variation was found in the value of i which produced the best fit to each curve, it was generally found that the best results were obtained with a value of i=3 for 4 ns N_2 ablation, and i=4 for 300 ps N_2 ablation. Best fit curves are shown in Fig.5.5a, b & c superimposed on the time distributions obtained using 300 ps N_2 ablation, above and below the ion production threshold, and using 4 ns N_2 ablation below the ion production threshold. The half-range Maxwell Boltzman model was found to provide a relatively good fit to all the data obtained by the author. Although the Knudsen layer model also fits the data well at short PAI delays, the 'tail' of the data at long delays is not fitted well by this model.

The characteristic temperatures (T_c) obtained from the analysis described above are shown in table.5.1 (for the half-range Maxwell Boltzman model) and table.5.2 (for the Knudsen layer model). The introduction of a hydrodynamic velocity (u_K) in the Knudsen layer model significantly reduces the characteristic temperature calculated from the observed particle distributions (40 to 25 % reduction). Even although the Knudsen layer model does not provide as good a fit to the data as the MB model, it is expected to provide a more physical description of material ejection since to some extent it takes into account particle collisions within the plume. As discussed in Chapter 2, T_c should not be interpreted as the surface temperature, but rather some temperature characteristic of the ablation process. If the theory is to satisfactorily describe material ejection then it would be expected that T_c would be the same order of magnitude as the sublimation temperature for DHB (T_{sub} ~ 500 °K).

With reference to table.5.1 it can be seen that for ablation of DHB with the 4 ns N_2 laser the values of T_c (using i=3) are only a factor of ~ 2.5 greater than T_{sub} for the MB fit, and only a factor of ~1.8 greater than T_{sub} for the Knudsen layer fit. Thus it would appear that for 4 ns N_2 ablation a

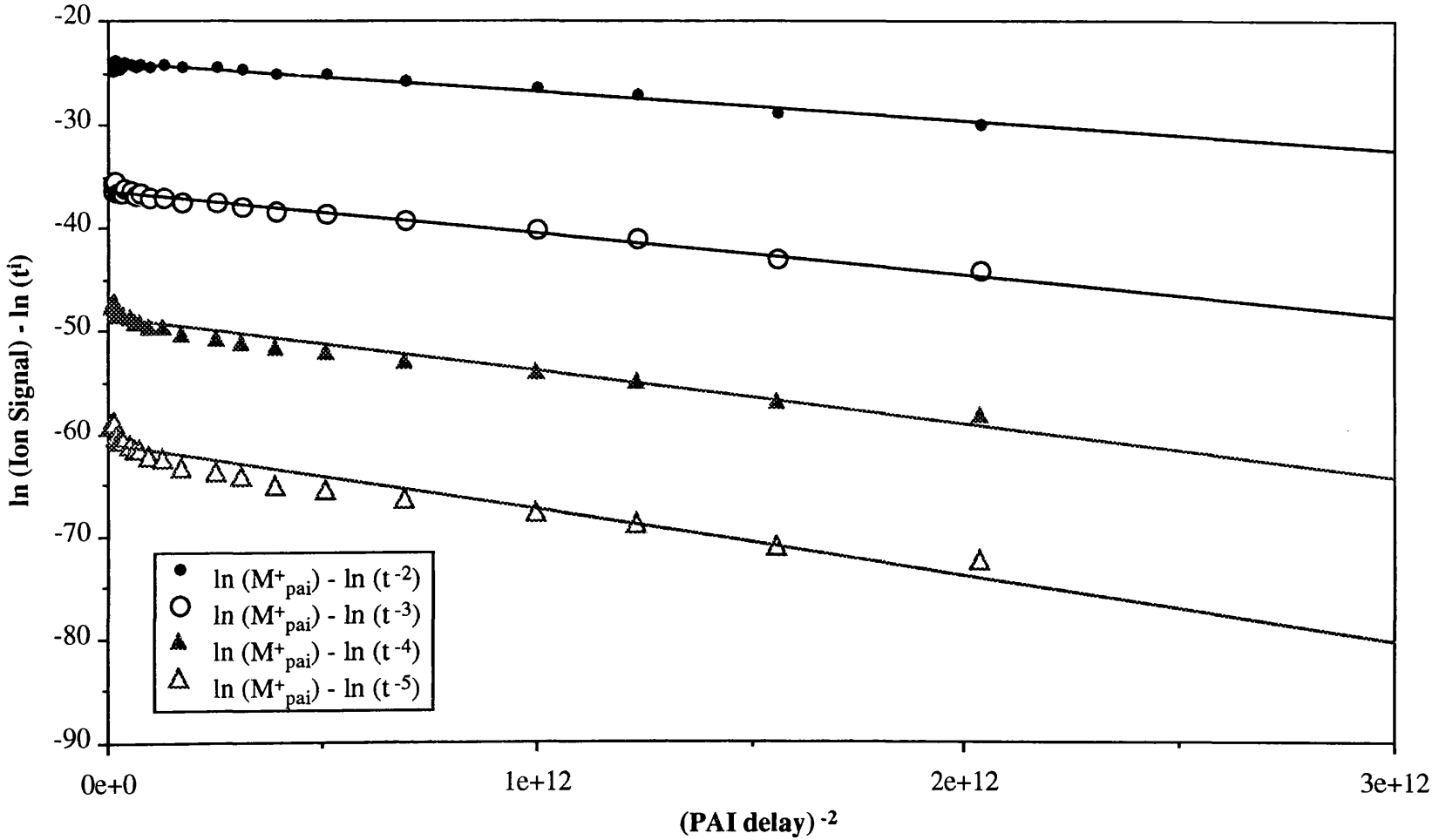

Fig.5.4a Graph showing the application of the half-range Maxwell Boltzman model (Eqn.5.1) to the matrix parent PAI signal from the data shown in Fig.5.3h. Four different values of i = {1,2,3,4} were fitted to the data resulting in the four curves shown above. For the data shown z = 650 μm.

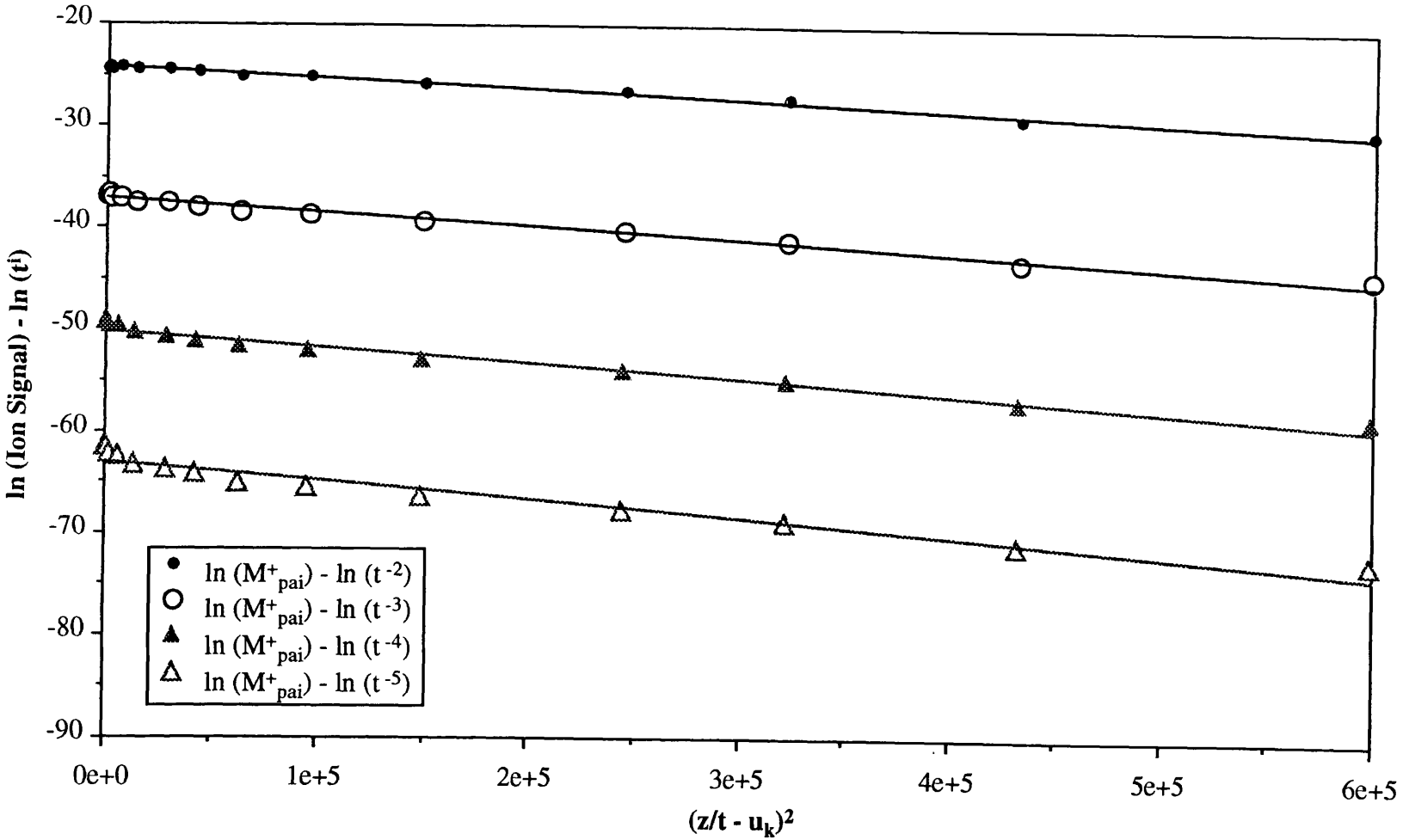

Fig.5.4b Graph showing the application of the Knudsen layer model (Eqn.5.2) to the matrix parent PAI signal from the data shown in Fig.5.3h. Four different values of i = {1,2,3,4} were fitted to the data resulting in the four curves shown above. For the data shown z = 650 μm and u_k = 155 ms^{-1}. The PAI laser delay is denoted by t.

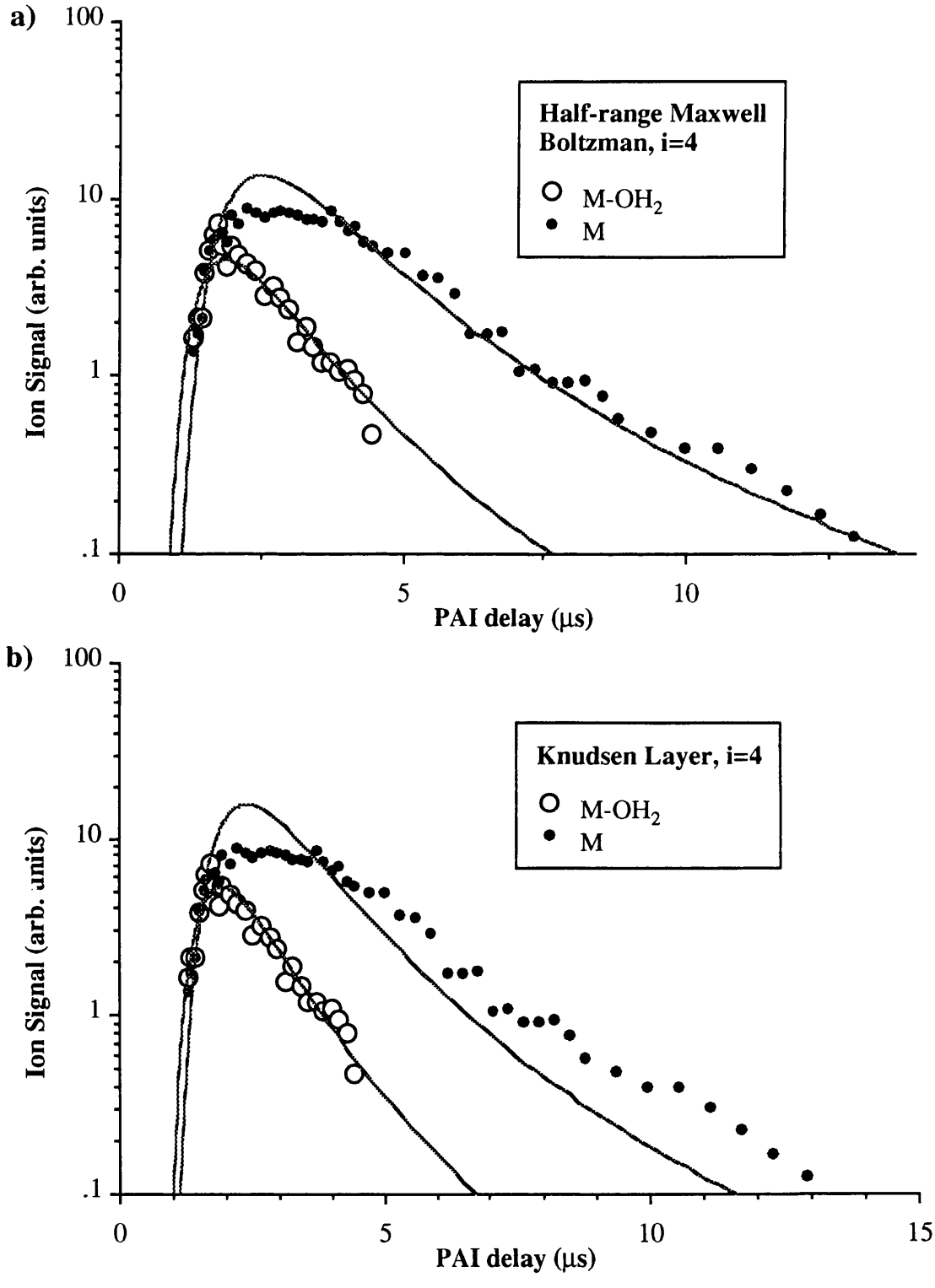

Fig.5.5a The PAI signal obtained using an ablation fluence above the threshold fluence for ion production shown as a time distribution, and fitted assuming a) a half-range Maxwell Boltzman distribution, and b) formation of a Knudsen layer. A 300 ps N_2 laser was used for ablation with an incident fluence of 57 $mJcm^{-2}$. PAI was carried out at 266 nm, 1.5 mm from the sample, and with a laser intensity of approximately 1.4×10^9 Wcm^{-2}. M represents the matrix parent ion.

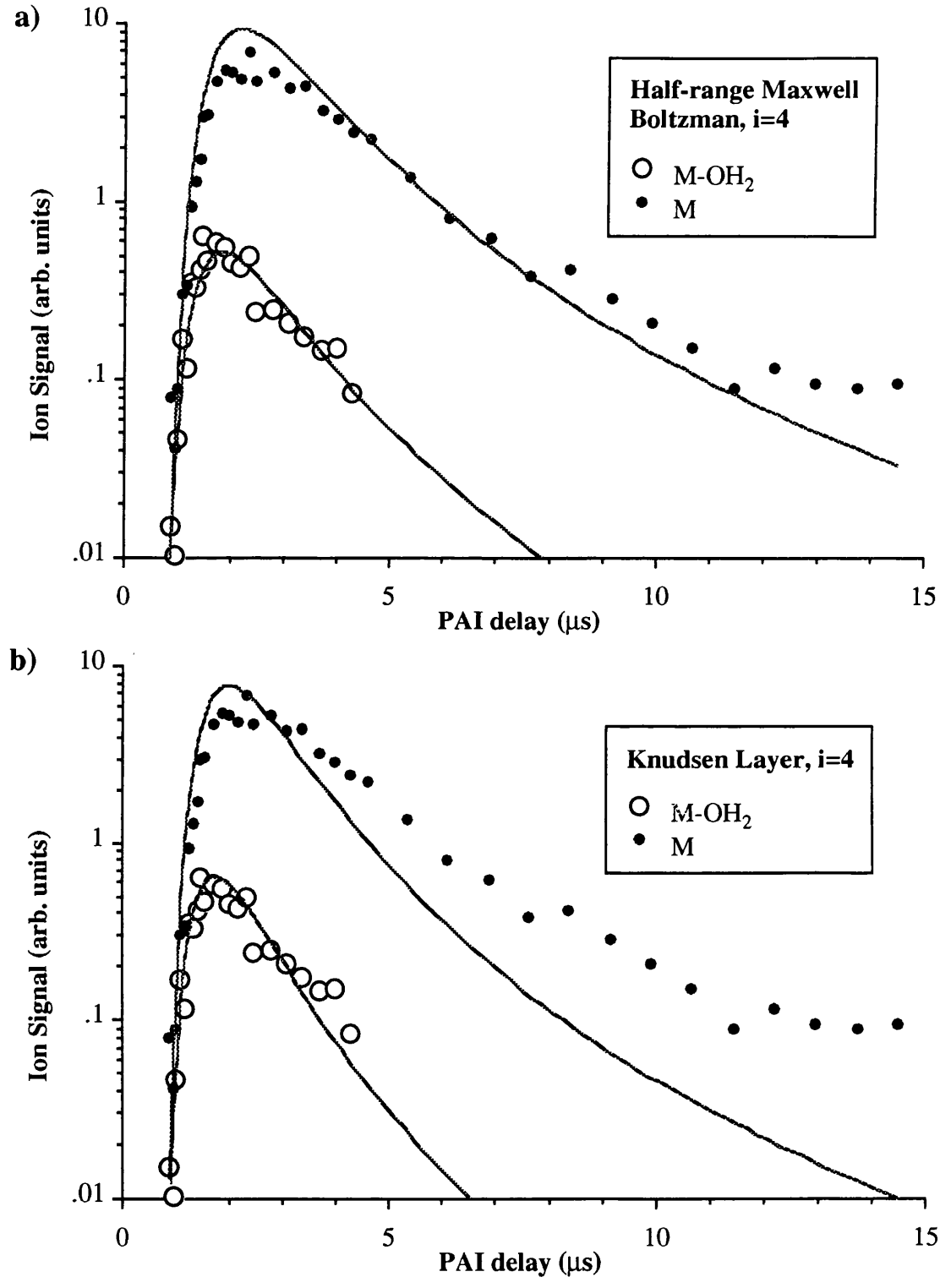

Fig.5.5b The PAI signal obtained using an ablation fluence below the threshold fluence for ion production shown as a time distribution, and fitted assuming a) a half-range Maxwell Boltzman distribution, and b) formation of a Knudsen layer. A 300 ps N_2 laser was used for ablation with an incident fluence of 23 $mJcm^{-2}$. PAI was carried out at 266 nm, 1.5 mm from the sample, and with a laser intensity of approximately 1.4×10^9 Wcm^{-2}. M represents the matrix parent ion.

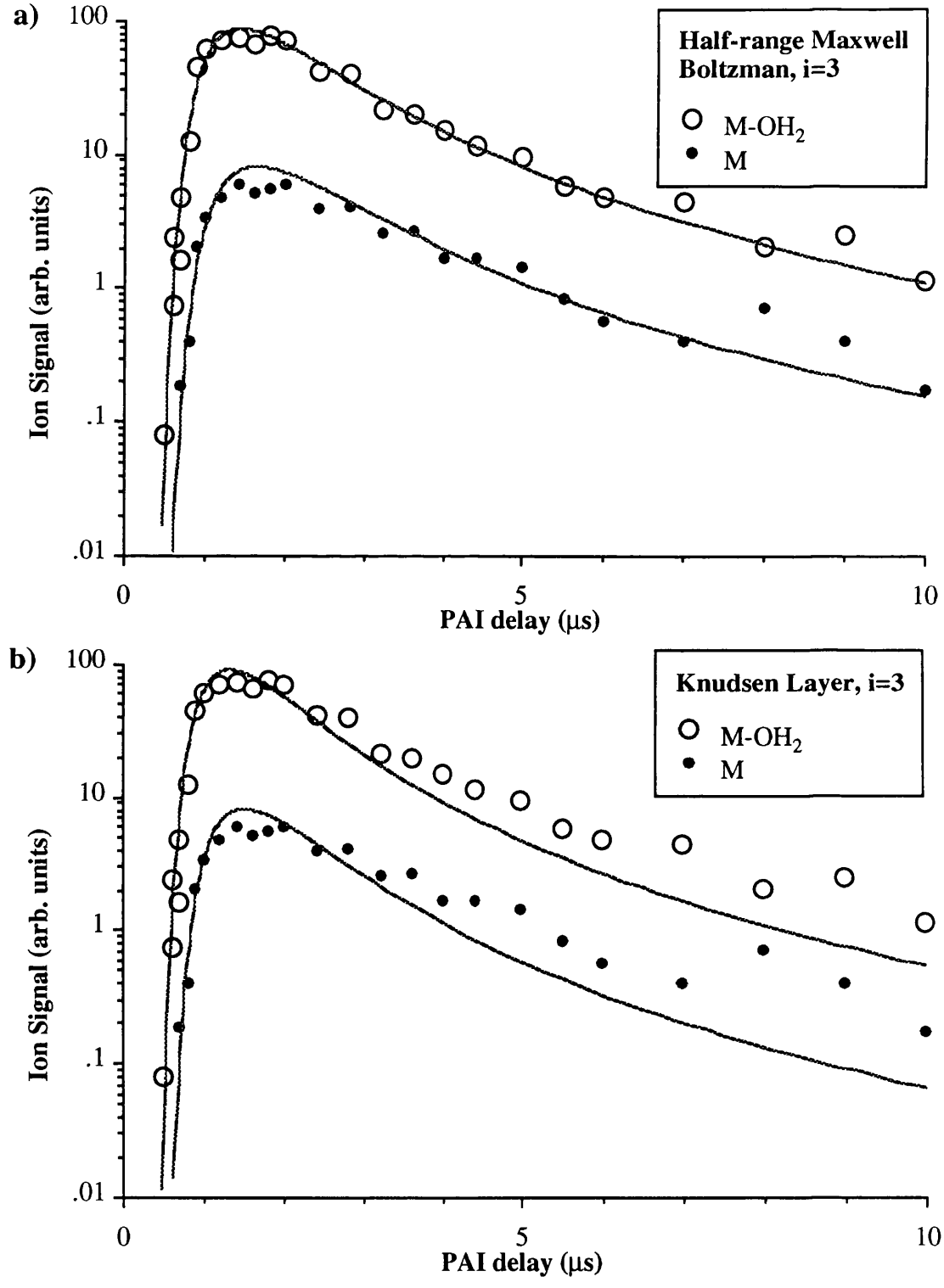

Fig.5.5c The PAI signal obtained using an ablation fluence below the threshold fluence for ion production shown as a time distribution, and fitted assuming a) a half-range Maxwell Boltzman distribution, and b) formation of a Knudsen layer. A 4 ns N_2 laser was used for ablation with an incident fluence of 28 $mJcm^{-2}$. PAI was carried out at 243.13 nm, 650 μm from the sample, and with a laser intensity of approximately 7.8 x 10^7 Wcm^{-2}. M represents the matrix parent ion.

Ablation Laser Pulsewidth	Incident Fluence ($mJcm^{-2}$)	Relation to Threshold Fluence	PAI/sample Separation (mm)	Characteristic Temperature (°K)			
				M		$M\text{-}OH_2$	
				i = 3	i = 4	i = 3	i = 4
4 ns	28	$< F_{th(ion)}$	0.65	990	760	1160	935
4 ns	60	$> F_{th(ion)}$	1.1	1230	930	1225	1000
4 ns	28	$< F_{th(ion)}$	1.1	1365	1110	1390	1170
				1200	**930**	**1260**	**1035**
300 ps	57	$> F_{th(ion)}$	1.5	2470	1730	3940	2780
300 ps	23	$< F_{th(ion)}$	1.5	2890	2240	3430	2810
300 ps	43	$> F_{th(ion)}$	2.0	3650	2710	5530	3760
300 ps	39	$> F_{th(ion)}$	3.2	3790	2980	6650	4900
300 ps	16	$< F_{th(ion)}$	3.2	2650	2090	3820	2840
				3090	**2350**	**4670**	**3420**

Table.5.1 The table above shows the characteristic temperatures (T_c) obtained by using the half-range Maxwell Boltzman model to fit the data shown in Fig.5.3a to Fig.5.3h. Both the M and $M\text{-}OH_2$ distributions are fitted using the values of $i \in \{3,4\}$. The mean of the temperatures obtained for each specific set of variables (pulselength, neutral species, value of i) are shown in bold at the foot of each column.

Ablation Laser Pulsewidth	Incident Fluence ($mJcm^{-2}$)	Relation to Threshold Fluence	PAI/sample Separation (mm)	Characteristic Temperature (°K)			
				M		$M\text{-}OH_2$	
				i = 3	i = 4	i = 3	i = 4
4 ns	28	$< F_{th(ion)}$	0.65	754	621	925	793
4 ns	60	$> F_{th(ion)}$	1.1	834	679	887	767
4 ns	28	$< F_{th(ion)}$	1.1	999	831	1051	905
				860	**710**	**955**	**820**
300 ps	57	$> F_{th(ion)}$	1.5	1625	1250	2240	1545
300 ps	23	$< F_{th(ion)}$	1.5	2180	1845	2260	1875
300 ps	43	$> F_{th(ion)}$	2.0	2490	1945	3030	2350
300 ps	39	$> F_{th(ion)}$	3.2	2730	2160	3820	2960
300 ps	16	$< F_{th(ion)}$	3.2	1670	1330	2200	1650
				2140	**1710**	**2710**	**2080**

Table.5.2 The table above shows the characteristic temperatures (T_c) obtained by using the Knudsen layer model to fit the data shown in Fig.5.3a to Fig.5.3h. Both the M and $M\text{-}OH_2$ distributions are fitted using the values of $i \in \{3,4\}$. The mean of the temperatures obtained for each specific set of variables (pulselength, neutral species, value of i) are shown in bold at the foot of each column.

thermal mechanism for ejection could be reconciled with the observed particle distributions. The fact that no significant difference in T_c is apparent between ablation with a fluence of 28 $mJcm^{-2}$ (below the ion production threshold) and 60 $mJcm^{-2}$ (above the ion production threshold) is perhaps indicative of evaporative cooling of the surface during material ejection (Vertes 1993a).

However, for ablation of DHB with the 300 ps N_2 laser the values of T_c (using i=4) for; a) the neutral M species are a factor of ~ 5 (MB fit) to ~ 3.5 (Knudsen layer) greater than T_{sub} , and b) the neutral M-OH_2 species are a factor of ~ 7 (MB fit) to ~ 4 (Knudsen layer) greater than T_{sub}. These values are considerably greater than T_{sub} and would result in considerable fragmentation of the matrix quasimolecular species were thermal equilibrium to have occurred in the irradiated volume.

The hydrodynamic model of MALDI developed by Vertes (Vertes 1993a) predicts a drift velocity for the centre of mass (v_{drift}) of approximately 250 ms^{-1} (for both ferulic and sinapinic acid ablated using nanosecond laser pulses). This model is essentially a thermal model. The results obtained by the author give a measured maximum in PAI signal intensity at particle velocities of; a) v_{max} ~ 440 ms^{-1} for both M and M-OH_2 following 4 ns N_2 ablation, and b) v_{max} ~ 650 ms^{-1} for M, and v_{max} ~ 950 ms^{-1} for M-OH_2 following 300 ps N_2 ablation. Other similar work reported in the literature (Huth-Fehre 1991) gave a value of v_{max} ~ 350 ms^{-1} following 5 ns ablation with the quadrupled output of a Nd:YAG.

The results discussed above suggest that the material interrogated by the PAI laser has not been liberated by a thermal mechanism alone. As might be expected this becomes more apparent with shorter pulselength ablation. However, it is difficult to reconcile a photochemical ablation mechanism with the results of Demirev et al (Demirev 1992) who found that the threshold fluence for ion production was essentially identical for ablation with 3 ns and 560 fs lasers. The author also found similar fluence thresholds for ion production regardless of whether 4 ns or 300 ps pulselength lasers were used for ablation (Chapter 4, section 4.6).

5.4 High Plume Density PAI - Short Time Scales

In order to probe the ablation plume dynamics in the dense gas phase produced immediately following ablation, post-ionisation was carried out with the PAI laser at various distances from the sample, ranging from 250 μm to as close as possible without producing ablation signals. It was thought that this work would produce new insights into the ionisation mechanism which is believed to occur via gas phase reactions in this region.

In addition, it was thought that the higher concentration of analyte neutrals in the focused PAI laser volume close to the sample surface might result in a detectable ion signal. No evidence of analyte photo-ionisation was found during the PAI work carried out at distances of greater than 650 μm from the surface of single crystals doped with substance P. Although the PAI wavelengths used (266 nm & 243.13 nm) were not ideal for photo-ionisation of large labile molecules (Huth-Fehre 1991) it was believed that photo-ionisation of neutral analyte molecules may be occurring but that the ion signal size was too small to be seen above the detection threshold. At the time of the experiments it was not feasible to deflect low mass matrix species which would have resulted in a reduction in detector saturation effects, and permitted the use of higher detector voltages giving a significant increase in detection sensitivity.

Initial investigations of the ablation plume were carried out with the ablation laser fluence on the sample below the ion production threshold fluence in order to simplify the resultant PAI spectra (ie PAI ions only). A typical example of PAI spectra obtained 'far' from the sample surface is shown in Fig.5.6 as a function of PAI laser delay. This data was obtained following ablation of a single crystal sample of DHB at a PAI laser/sample separation of 250 μm. It can be seen from Fig.5.6 that spectral shape remains essentially constant as a function of PAI laser delay, the only change being in the absolute ion signal magnitude. The apparent reduction in the M^+ signal at short PAI delays relative to all other ion signals in the spectrum is an artefact of the particular data set shown in Fig.5.6. The observed variation in PAI spectra taken 'close' to the surface of the same sample is shown in Fig.5.7a also as a function of PAI laser

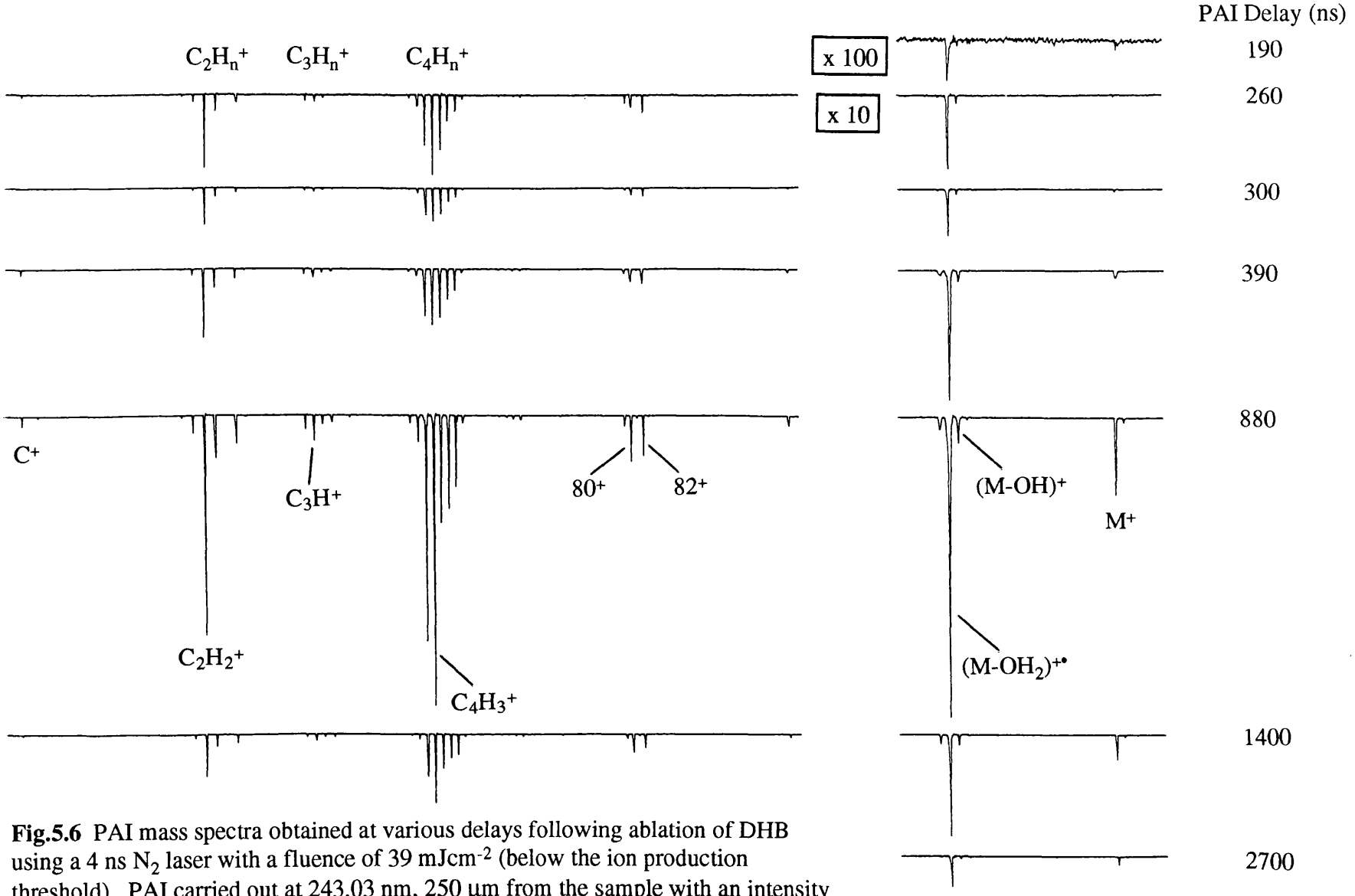

Fig.5.6 PAI mass spectra obtained at various delays following ablation of DHB using a 4 ns N_2 laser with a fluence of 39 mJcm^{-2} (below the ion production threshold). PAI carried out at 243.03 nm, 250 μm from the sample with an intensity of 9.1 x 10^7 Wcm^{-2}. When the PAI laser was blocked, no ion signals could be obtained.

PAI Delay (ns)

Na^+_{abl} K^+_{abl} x 10 $(M\text{-}OH_2)^{+\bullet}$ $(M\text{-}OH)^+$ M^+ 50

60

70

C^+ C_3H^+ $C_2H_2^+$ $C_4H_3^+$ $(M\text{-}OH_2)^{+\bullet}$ $(M\text{-}OH)^+$ M^+ 80

100

120

180

250

300

400

$(M\text{-}OH_2)^{+\bullet}$ $(M\text{-}OH)^+$ M^+ 500

Fig.5.7a

delay. Ablation was carried out using a 4 ns N_2 laser with a fluence of 42 $mJcm^{-2}$ on the sample; PAI was carried out at 243.03 nm with an intensity of 2 x 10^8 Wcm^{-2}. The PAI laser was moved towards the sample until a slight clipping of the laser beam was observed, whereupon the laser was moved back approximately 10 μm. The dye laser focal spot size above the sample was estimated to be approximately 70 μm diameter by passing a sharp edge through the laser beam whilst observing the intensity of the transmitted beam.

It is immediately apparent from Fig.5.7a that a dynamic behaviour is exhibited by the quasimolecular matrix ion species. At very short delay times (50 ns), corresponding to the low particle density, high particle velocity region of the ablation plume, the only PAI ion signals present in the spectra are those corresponding to the matrix parent (M) and dehydroxylated parent (M-OH & $M-OH_2$). No carbon fragment species are observed. The relative intensities of the quasimolecular ion species at short delays are identical to those found at long PAI delays, or for PAI 'far' from the sample (Fig.5.6). As the PAI laser delay is increased, the particle density rises in the region of the ablation plume intersecting the PAI laser volume, resulting in a general increase in all ion signals. However, the $(M-OH)^+$ signal exhibits a dramatic increase relative to the M^+ and carbon fragment ion signals whilst the $(M-OH_2)^{+\bullet}$ signal suffers a reduction in intensity relative to the M^+ and carbon fragment ion signals. It would appear that the $(M-OH)^+$ signal is enhanced at the expense of the $(M-OH_2)^{+\bullet}$ signal. The $(M+H)^{+\bullet}$ ion signal can be seen to increase in size at the same time as the $(M-OH)^+$ signal enhancement occurs, although this is slight when compared to the increase exhibited by the $(M-OH)^+$ signal.

As the PAI laser delay is increased still further (100 to 180 ns), the particle density in the probed plume region increases to such an extent that significant collisional broadening of the PAI ion signals occurs, and the $(M-OH)^+$ and $(M-OH_2)^{+\bullet}$ signals merge. However, it is still possible to observe that as the PAI laser delay is increased from 180 to 300 ns, the enhancement of the $(M-OH)^+$ signal at the expense of the $(M-OH_2)^{+\bullet}$ signal is reduced, returning to standard quasimolecular ion signal intensity ratios for PAI laser delays greater than 400 ns. This type of behaviour

was found to be absolutely reproducible, although the degree of enhancement observed varied between experiments and was thought to depend critically on the relative overlap between the PAI laser volume and the ablation plume. When PAI was carried out using a laser wavelength of 266 nm, similar results were obtained although the enhancement was confined to the dehydroxylated quasimolecular ions alone, with much reduced overall absolute ion signal intensities of $(M\text{-}OH)^+$ and $(M\text{-}OH_2)^{+\bullet}$ relative to the M^+ signal as would be expected (Fig.5.1a & b). A set of spectra obtained under similar conditions to those described for Fig.5.7a are shown in Fig.5.7b where the dynamic behaviour between the $(M\text{-}OH)^+$ and $(M\text{-}OH_2)^{+\bullet}$ signals is more apparent.

In some of the experiments performed it was observed that if ion signals could be obtained at extremely short PAI laser delays (20 to 30 ns) then the intensity of the $(M\text{-}OH)^+$ and $(M\text{-}OH_2)^{+\bullet}$ signals dropped drastically resulting in spectra containing essentially only the parent ion signal (Fig.5.8).

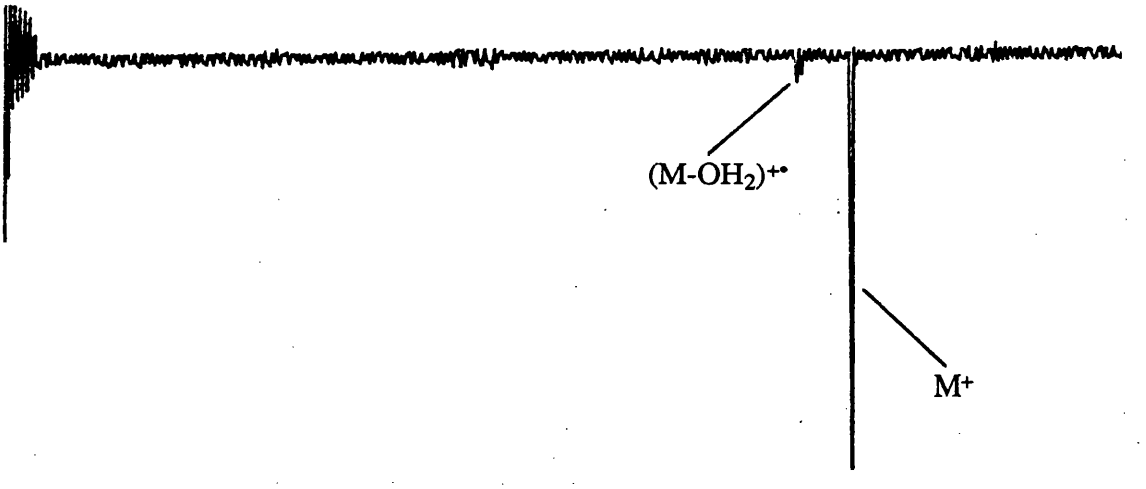

Fig.5.8 PAI spectrum obtained 20 ns following ablation of DHB using a 4 ns N_2 laser with a fluence of 39 $mJcm^{-2}$ (below the ion production threshold). PAI carried out at 243.03 nm, immediately above the sample surface with an intensity of 6.8×10^7 Wcm^{-2}.

The Na and K ions present in the spectra (most obvious at a PAI delay of 50 ns) are generated from ablation as a result of the PAI laser beam grazing the edge of the sample crystal. With the N_2 ablation laser blocked, only the Na and K ion signals are observed. The ion and neutral production threshold fluences (N_2 ablation laser) were investigated as a

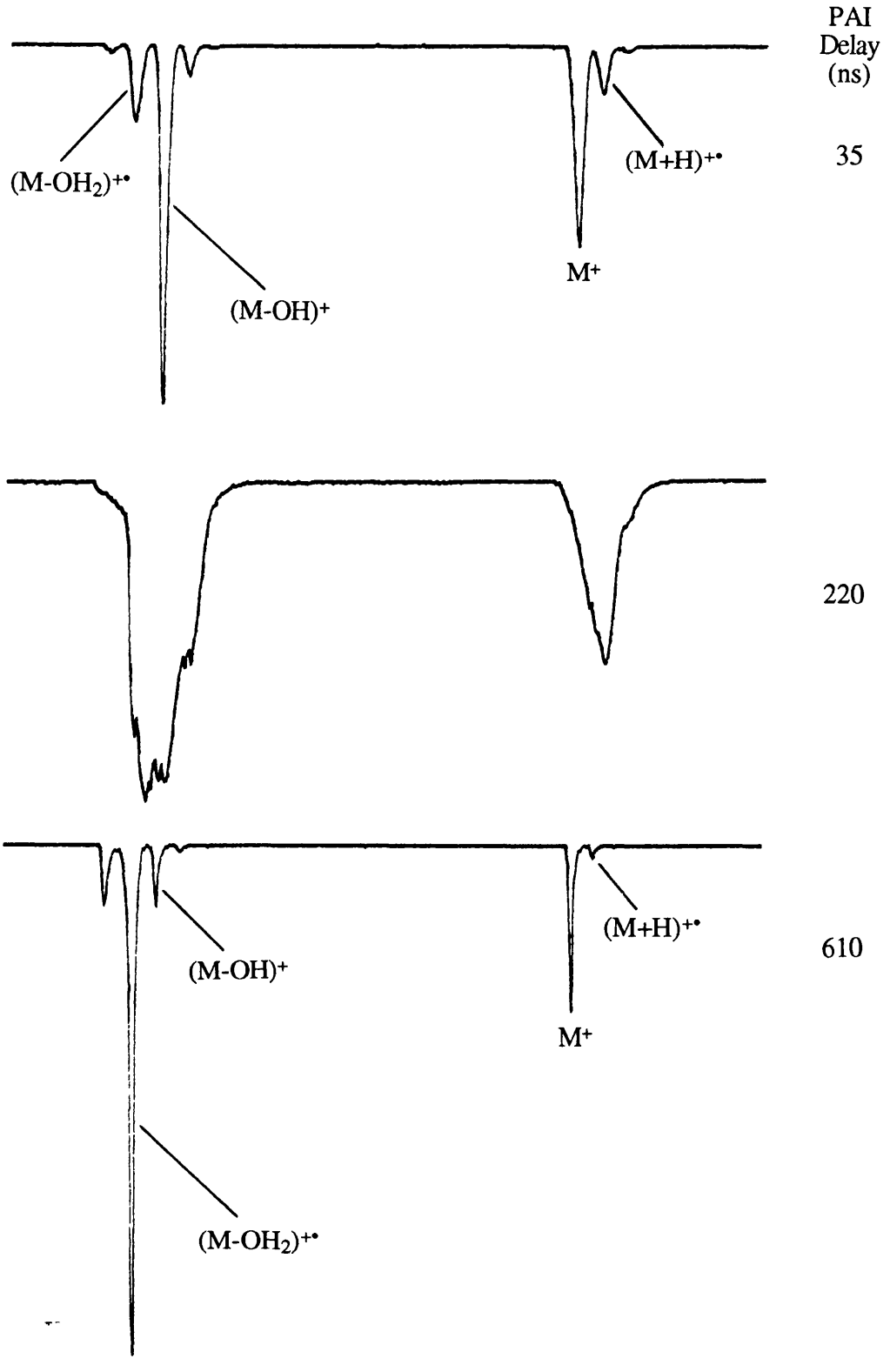

Fig.5.7b PAI mass spectra obtained at various delays following ablation of DHB using a 4 ns N_2 laser with a fluence of 39 $mJcm^{-2}$ (below the ion production threshold). Only the quasimolecular parent ion region of the spectra is shown. PAI carried out at 243.03 nm, immediately above the surface with an intensity of 6.8×10^7 Wcm^{-2}.

function of PAI laser delay over the range -100 ns to +100 ns in order to check whether energy from the PAI laser was contributing to the ablation process, following absorption in the sample from the very edge of the PAI laser beam. The threshold fluence values were found to be independent of the PAI delay, indicating that the PAI laser did not contribute to ablation.

Some of the experiments were carried out using single crystals of DHB doped with substance P in an attempt to post-ionise analyte molecules. However, no evidence of analyte photoionisation was observed and it was concluded that deflection of low mass matrix species was a necessity in order to observe such ions, provided that they are produced in postionisation with relatively long wavelengths such as 243 nm (Huth-Fehre 1991).

Investigations were also carried out with the PAI laser as close as possible to the sample and the ablation laser fluence above the ion production threshold. PAI spectra obtained under such conditions are much more complicated, containing a superposition of both ablation and PAI ions. Indeed, if the ablation ions are actually formed in the gas phase, as indicated by the experimental evidence and believed by the majority of researchers (Zhou 1992, Ehring 1992, Vertes 1993a, Wang 1993, Liao 1995), then the PAI laser beam will inevitably perturb the ablation ion formation process in addition to providing additional ionisation mechanisms. A series of spectra taken using a PAI laser wavelength of 266 nm are shown in Fig.5.9 as a function of PAI laser delay. Similar behaviour to that described previously for below threshold fluence ablation can be observed in this series of spectra with a large enhancement in the $(M\text{-}OH)^+$ signal occurring at a PAI delay of the order of 100 ns. The ion signals exhibit collisional broadening and possible charge shielding effects for considerably larger PAI delays than observed in the below threshold work (Fig.5.7a & b) presumably due to the increased particle and charge density produced following above threshold ablation.

Experiments carried out using a PAI wavelength of 243.03 nm produce similar spectra and enhancement effects, the main difference being that the main PAI ion is $(M\text{-}OH_2)^{+\bullet}$ rather than M^+ (see Fig.5.1a & b) resulting in slightly more complicated spectra. A brief investigation was made of

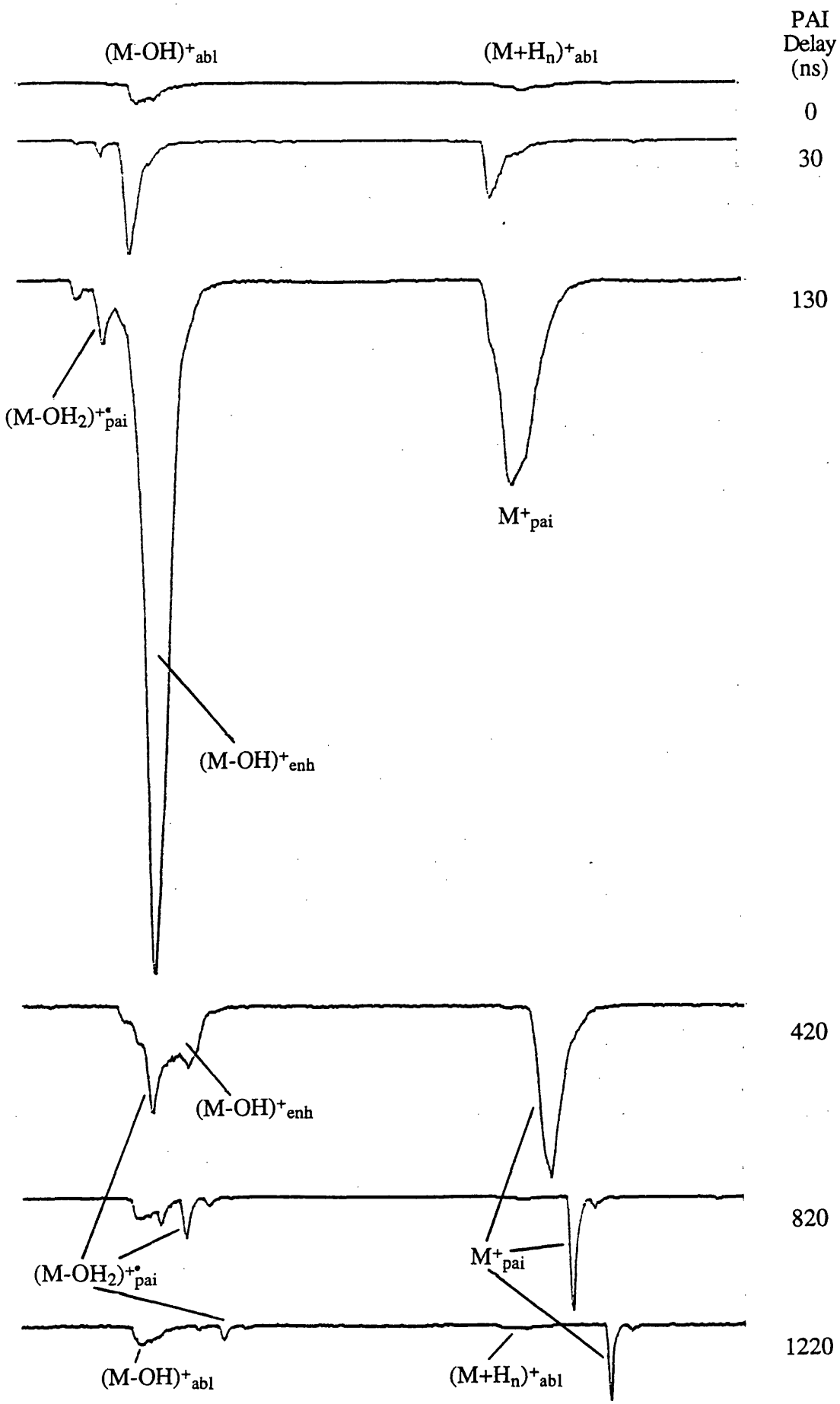

Fig.5.9 Series of spectra obtained using PAI at various delays following ablation of DHB using a 4 ns laser with a fluence of 65 $mJcm^{-2}$ (above the ion production threshold). PAI carried out at 266 nm, immediately above the sample surface with an intensity of 2.3×10^8 Wcm^{-2}.

PAI spectra obtained at short delays close to the surface of sinapinic acid samples where a similar type of ion signal behaviour was observed.

The enhancement of the $(M\text{-}OH)^+$ signal in the data shown in Fig.5.7a & b can not be explained by photoionisation alone. The enhancement is only seen in PAI spectra obtained very close to the sample surface and at relatively short delays. As the PAI laser separation is increased the degree of enhancement observed falls till essentially no enhancement is seen for distances greater than approximately 100 to 200 μm, even for the same PAI delay time. This implies that the enhancement originates from particle collisions facilitated by the high particle density which occurs in the early ablation plume, although the involvement of relatively short lived (10's of ns) excited state matrix species produced following ablation cannot be ruled out. This view is supported by the work of Vertes (Vertes 1993b) where calculations of plume density following ablation from typical matrix materials give densities approximately 5% of the solid phase value, 30 μm from the surface and 100 ns after the ablation event (see Fig.2.4), similar to the delay times and PAI/sample separation where $(M\text{-}OH)^+$ enhancement was found to occur. Further expansion of the plume results in a rapid decrease in density.

The main mechanistic models used to explain the formation of protonated ions in MALDI spectra are based on either excited state acid-base chemistry, or on matrix photoionisation followed by some form of ion-molecule reaction, both requiring particle collision in the gas phase (Liao 1995). One possible explanation for the ion signal enhancement behaviour found in PAI spectra following ablation with fluences below $F_{th(ion)}$ is as follows; Photoionisation of neutral $(M\text{-}OH_2)$ results in the production of $(M\text{-}OH_2)^{+\bullet}$, the radical dehydroxylated matrix ion. When the plume density is sufficiently high that particle collisions are likely, ion/molecule reactions occur, protonating neutral M and $(M\text{-}OH_2)$ to produce enhanced $(M+H)^{+\bullet}$ and $(M\text{-}OH)^+$ ion signals over that expected due to photoionisation alone, and resulting in a decreased $(M\text{-}OH_2)^{+\bullet}$ signal. The size of the $(M\text{-}OH)^+$ enhancement in relation to that observed for $(M+H)^{+\bullet}$ could be due to a lower ion/molecule reaction cross section. This mechanism can be used to explain the matrix ions found in ablation with fluences above $F_{th(ion)}$.

The mechanism outlined above is only one possibility, and indeed it has be concluded by some (Liao 1995) that numerous mechanisms may be operative in producing the observed spectra. The study carried out by the author is still at an early stage and although the results detailed in this section are likely to be of significance with regards to analyte protonation mechanisms, it is clear that further work is required.

Chapter Six

Hydrogen Ejection From Matrix Materials

6.1 Introduction

It is well known that the predominant analyte ion observed is that of the protonated parent $[A + H]^+$. As described in Chapter 2, the production of this ion is usually explained in the literature by a proton-transfer reaction between a radical matrix ion and an analyte molecule (Ehring 1992, Gimon 1992)

$$M^{+\bullet} + A \rightarrow [M - H]^{\bullet} + [A + H]^+$$

It has also been suggested that the observed protonation could be attributed to a high abundance of atomic hydrogen in the reactive mixture of ionic and neutral species formed following ablation above the threshold fluence for ion production (Ehring 1992).

It was decided to probe the MALDI generated plume in an attempt to investigate for the presence of neutral atomic hydrogen in the ejected material.

6.2 Resonance Ionisation Mass Spectrometry

The large ionisation potential of hydrogen coupled with the uncertainty in the likely abundance (if any) of hydrogen in the plume called for a highly sensitive gas phase ionisation technique. The technique of Resonant Ionisation Spectroscopy (RIS) (Hurst 1988) provides such a sensitive technique and has been used extensively by the Glasgow group (Towrie 1990, Wang 1991, Clark 1992, Scott 1994). In the RIS scheme used by the author, ionisation of atomic hydrogen is achieved with high efficiency at 243.13 nm via a two-photon resonant excitation step ($1s^2S_{1/2} \rightarrow 2s^2S_{1/2}$) followed by the absorption of a further photon to ionise ((2 + 1) multiphoton resonant excitation/ionisation scheme). This ionisation process has a

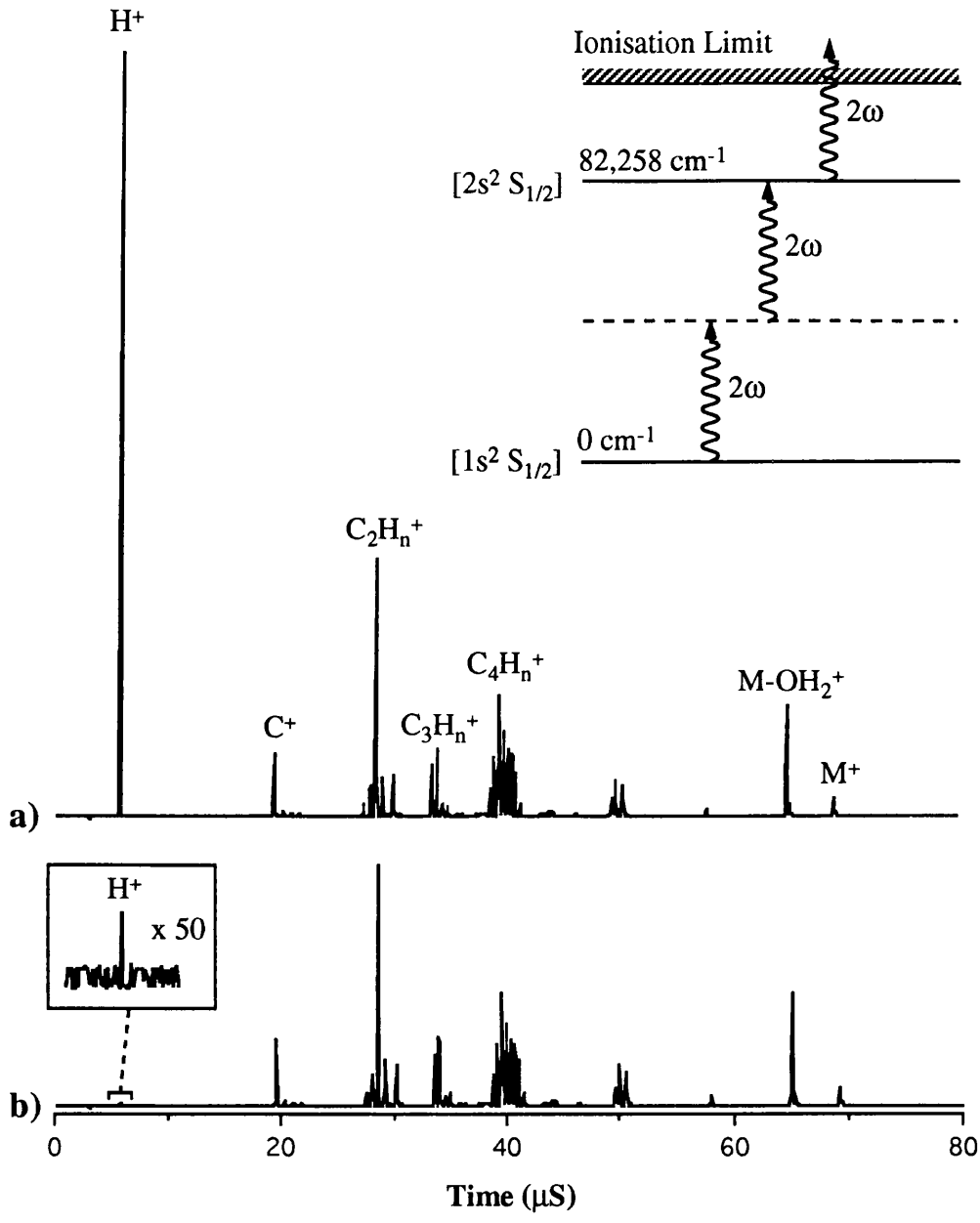

Fig.6.1 Graph showing the PAI spectra obtained following laser ablation of DHB below the ion production threshold fluence, with PAI laser a) on-resonance at 243.13 nm, and b) off-resonance at 243.03 nm. A 4 ns N_2 laser was used for ablation with an incident fluence of 21 $mJcm^{-2}$. PAI was carried out at 400 μm from the sample with a laser intensity of approximately 3.9 x 10^8 Wcm^{-2}. M represents the matrix parent ion.

power dependence of ≤ 3 on the ionisation laser intensity, and is shown as a schematic in the insert in Fig.6.1.

Fig.6.1 compares the PAI mass spectrum of the matrix species in the ablation plume (nitrogen laser below ionisation threshold) (a) taken on-resonance at 243.13 nm with that (b) taken off-resonance at 243.03 nm. A very large resonant enhancement in the hydrogen ion signal is clearly seen when on-resonance. From previous work by the author (Chapter 5) it is known that the bulk of the material in the plume from the ablation of DHB is composed of matrix parent molecules and large daughter fragments. The hydrogen signal in the spectrum shown in Fig.6.1 is attributed mainly to atomic hydrogen from PAI laser induced fragmentation of matrix species. This process is well known in UV photodissociation of gas phase organic molecules (Clark 1993). The dependence of the hydrogen ion signal on the PAI laser power (Fig.6.8a) with a slope of 4.3 ± 0.3 also supports this, indicating that at least five photons are required to produce these hydrogen ions (≥ 2 photons required to produce atomic hydrogen from molecular fragmentation, and 3 photons required for ionisation of the atomic hydrogen using the scheme shown in Fig.6.1). In both the spectra shown in Fig.6.1, substantial fragmentation is apparent with large ion signals present from a number of carbon fragment groups ($[C_xH_y]^+$, x=1,2,3..., y=0,1,2,3...) along with the ions $[M]^+$ and $[M\text{-}OH_2]^+$.

6.3 Investigation of the Ablation Plume

In previous studies of the velocity distributions of ejected neutrals from MALDI, the observed velocities have been similar, independent of mass (Beavis 1991, Huth-Fehre 1991). If this were generally the case, any hydrogen atoms from the ablation process could not be distinguished from those produced by fragmentation of the matrix species using PAI at 243.13 nm. However it was thought likely that the velocity of hydrogen atoms produced directly from ablation would be different from that of the matrix species and hence permit discrimination from hydrogen produced by fragmentation.

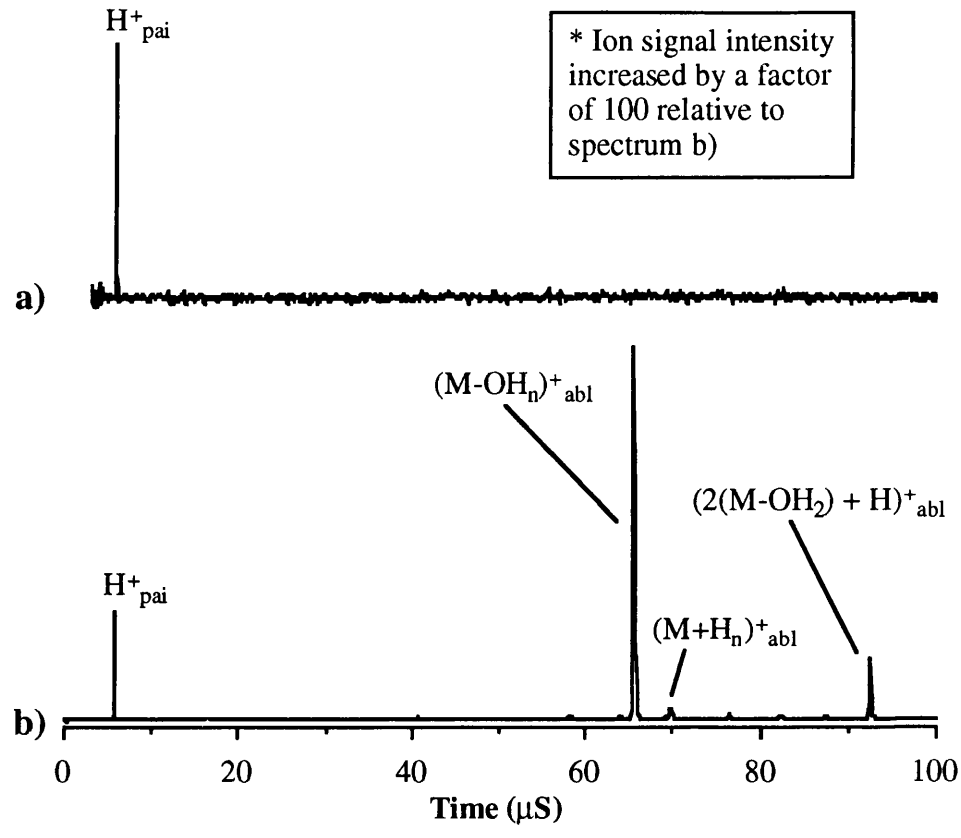

Fig.6.2 Mass spectra obtained following PAI at short delays in the plume generated by laser ablation a) below the ion production threshold fluence (22 $mJcm^{-2}$), and b) above the ion production threshold fluence (90 $mJcm^{-2}$). A 4 ns N_2 laser was used for ablation. PAI was carried out at 243.13 nm, 300 μm from the sample, and in spectrum a) intensity 1.7 x 10^8 Wcm^{-2}, PAI delay 160 ns, and b) intensity 1.2 x 10^8 Wcm^{-2}, PAI delay 60 ns.

It was found that neutral hydrogen is ejected from matrix materials with velocities considerably greater than those found for matrix neutrals. Mass spectra obtained using on-resonant PAI following ablation of DHB below and above the ion production threshold fluence are shown in Fig.6.2. Fig.6.3 shows on-resonant PAI at long (a) and short (b) delays following ablation of sinapinic acid above the threshold fluence for ion production. It can clearly be seen that at short delays the only PAI ion signal present is that of elemental hydrogen (for comparison see the ablation spectra from DHB and sinapinic acid shown in Chapter 4).

Velocity distributions from DHB were obtained with the ablation laser fluence both above and below the ionisation threshold for the MALDI process, and the PAI laser on-resonance for atomic hydrogen. However,

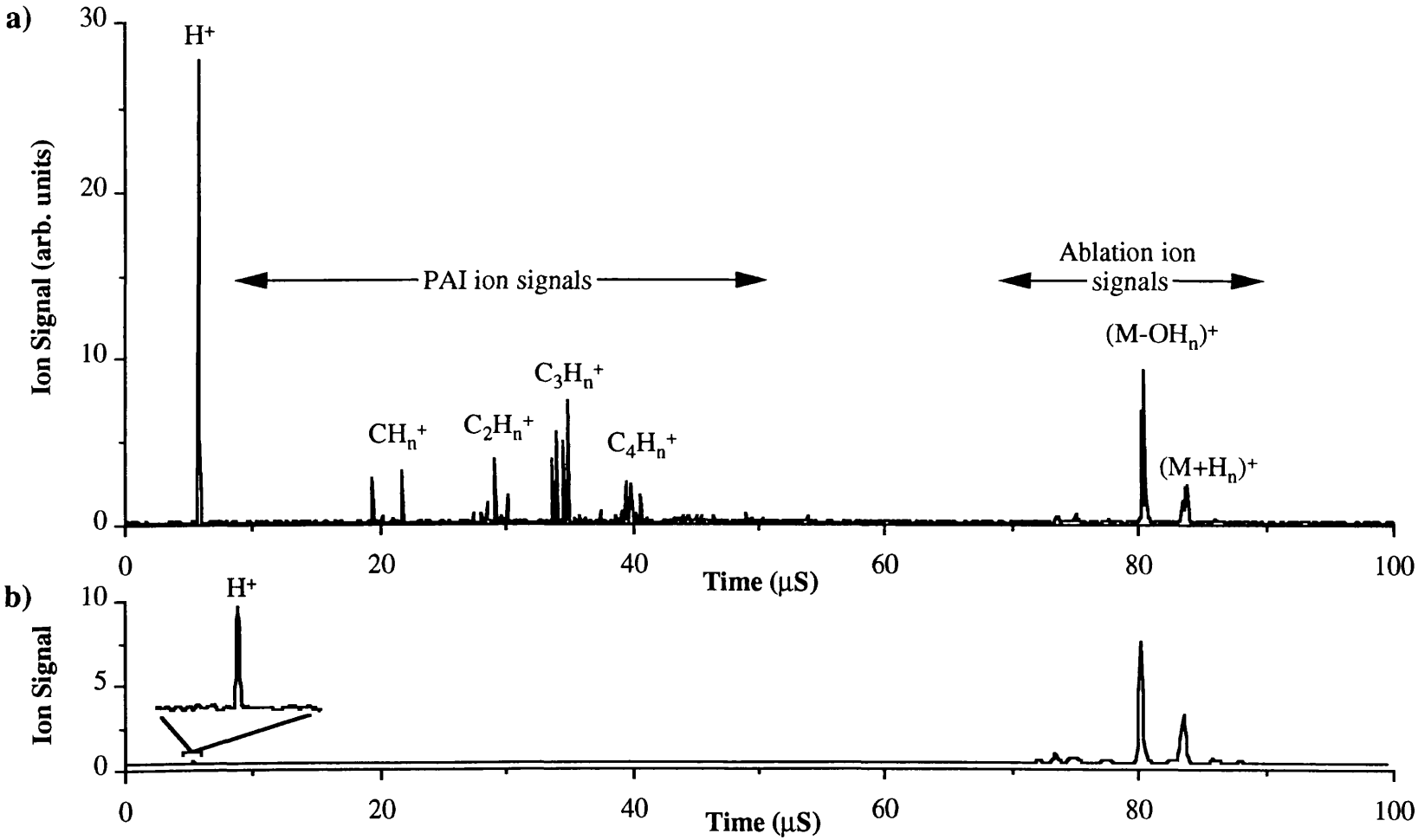

Fig.6.3 Mass spectra obtained following laser ablation of sinapinic acid above the ion production threshold fluence, with PAI laser on resonance at 243.13 nm a delays of a) 240 ns, and b) 60 ns. A 4 ns N_2 laser was used for ablation with an incident fluence of 67 $mJcm^{-2}$. PAI was carried out 300 μm from the sample with a laser intensity of approximately 1.4×10^8 Wcm^{-2}.

for sinapinic acid the fast hydrogen component of the plume could only be detected for ablation above the ion production threshold. The observed distributions are shown in Fig.6.4 to Fig.6.7 as both time and velocity distributions. The fast hydrogen ion signal obtained from ablation of sinapinic acid was less stable than that observed from DHB, and two separate particle distributions are shown (Fig.6.6 and Fig.6.7).

It is clear from Fig.6.4 to Fig.6.7 that the distributions can be separated into two regions: one where the hydrogen and carbon fragment ion signals clearly follow the same distribution as that of the parent matrix molecules, further indicating that they are products of fragmentation by the PAI laser; the other where the hydrogen ion signal rises through a second maximum after reaching a minimum point at which the matrix parent and carbon fragment ion signals fall to zero. This is clear evidence for atomic hydrogen production during the ablation process which may be connected with the MALDI protonation process.

The PAI pulse energy was monitored for each data point, and the data shown in Fig.6.4 to Fig.6.7 has been corrected for observed fluctuations in the PAI laser intensity using the known power dependence of each ion signal. In addition the data has also been corrected for the variation in neutral particle abundance as a function of the number of ablation shots incident on the sample. Fig.6.8 shows a typical power dependence (a) and ablation shot dependence (b) for ablation of DHB below the ion production threshold.

A series of experiments were carried out using DHB to determine the relationship between the ablation laser fluence, and the optimum delay time and maximum hydrogen signal intensity at this delay time. It was found that a large increase occurred in the particle density of ejected neutral hydrogen as the ablation fluence was increased above the threshold fluence for ion production. The results of this are shown in Fig.6.9. The threshold fluence for production of ions from ablation lies between 70 and 80 $mJcm^{-2}$.

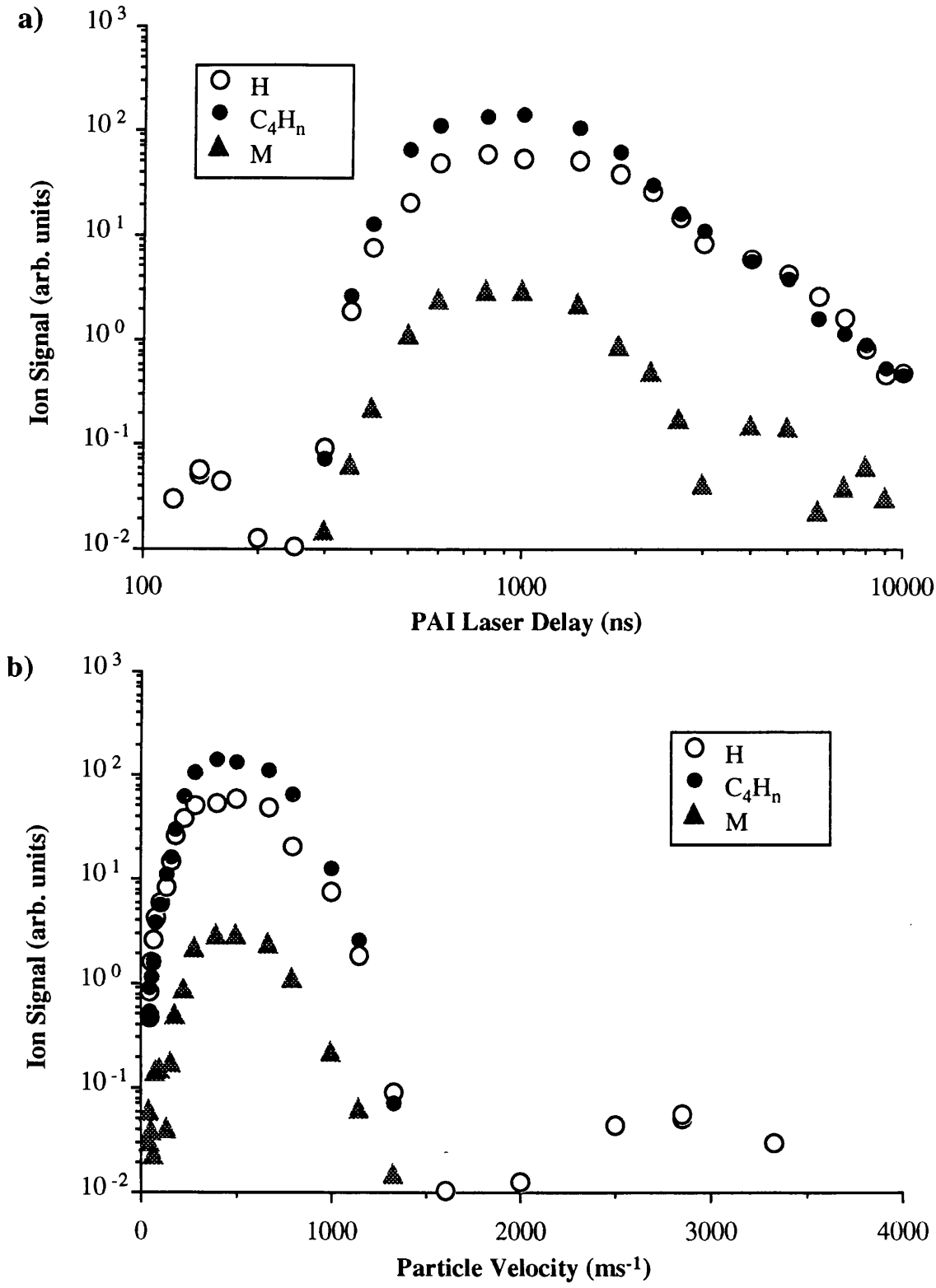

Fig.6.4 Graph showing the plume particle distribution observed following laser ablation of DHB below the ion production threshold fluence, shown as a) a time distribution and b) as a velocity distribution. A 4 ns N_2 laser was used for ablation with an incident fluence of 21 $mJcm^{-2}$. PAI was carried out at 243.13 nm, 400 μm from the sample, and with a laser intensity of approximately 2.2 x 10^8 Wcm^{-2}. M represents the matrix parent ion.

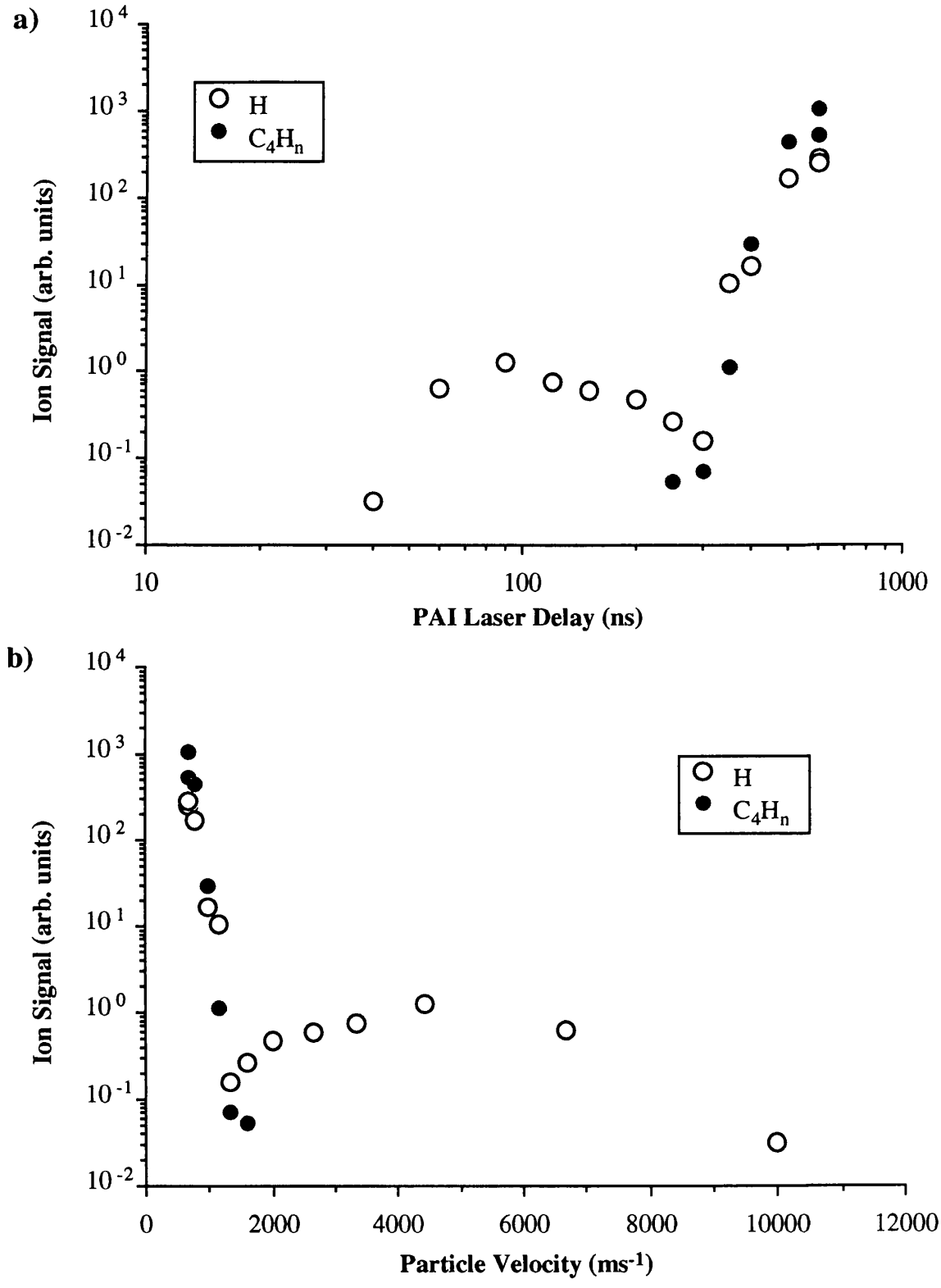

Fig.6.5 Graph showing the plume particle distribution observed following laser ablation of DHB above the ion production threshold fluence, shown as a) a time distribution and b) as a velocity distribution. A 4 ns N_2 laser was used for ablation with an incident fluence of 58 $mJcm^{-2}$. PAI was carried out at 243.13 nm, 400 μm from the sample, and with a laser intensity of approximately 1.8 x 10^8 Wcm^{-2}. Only the front edge of the matrix plume is shown, represented by the C_4H_n signal.

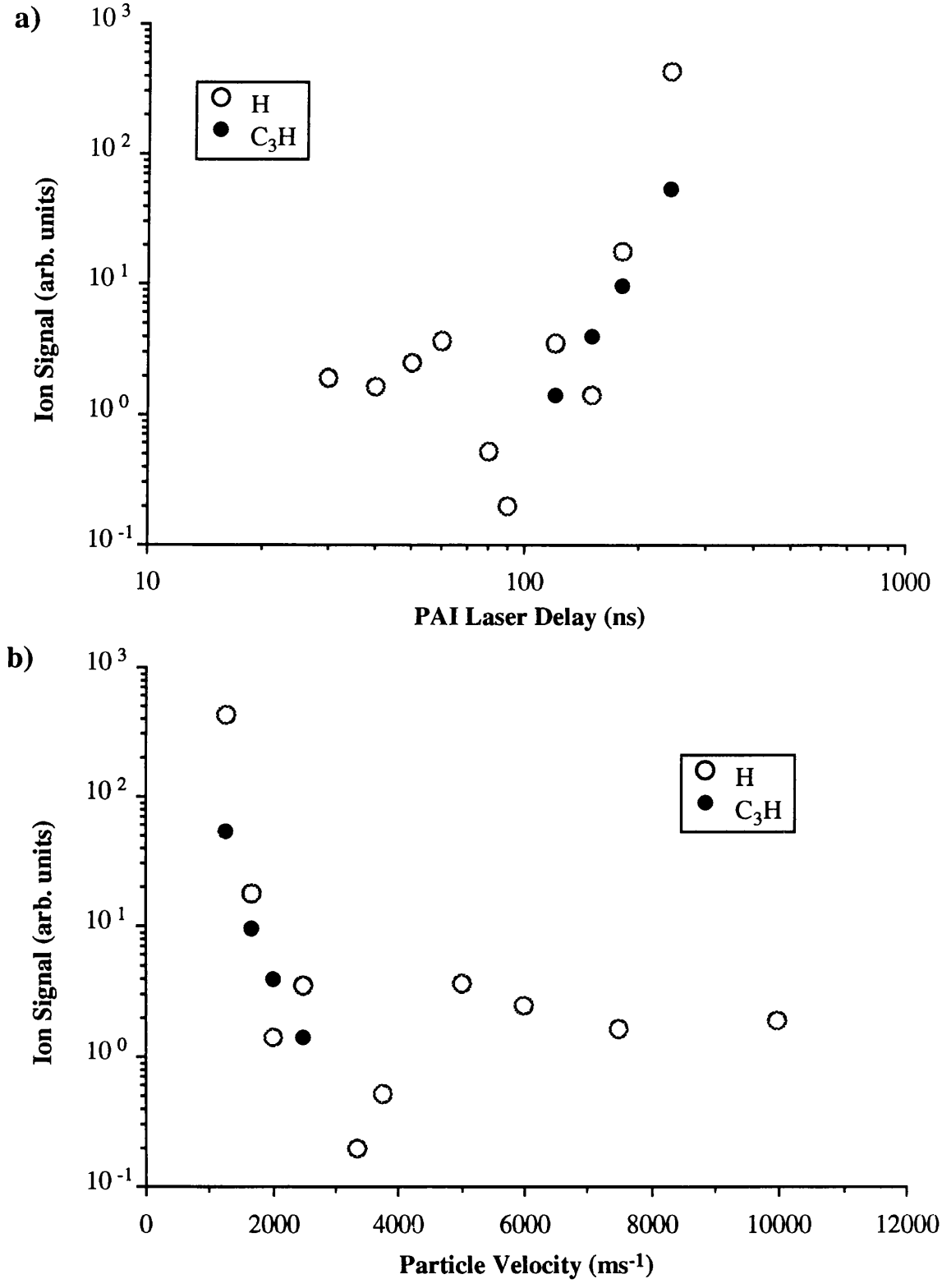

Fig.6.6 Graph showing the plume hydrogen distribution observed following laser ablation of sinapinic acid above the ion production threshold fluence, shown as a) a time distribution and b) as a velocity distribution. A 4 ns N_2 laser was used for ablation with an incident fluence of 67 mJcm^{-2}. PAI was carried out at 243.13 nm, 300 μm from the sample, and with a laser intensity of approximately 1.4 x 10^8 Wcm^{-2}. Only the front edge of the matrix plume is shown, represented by the C_3H signal.

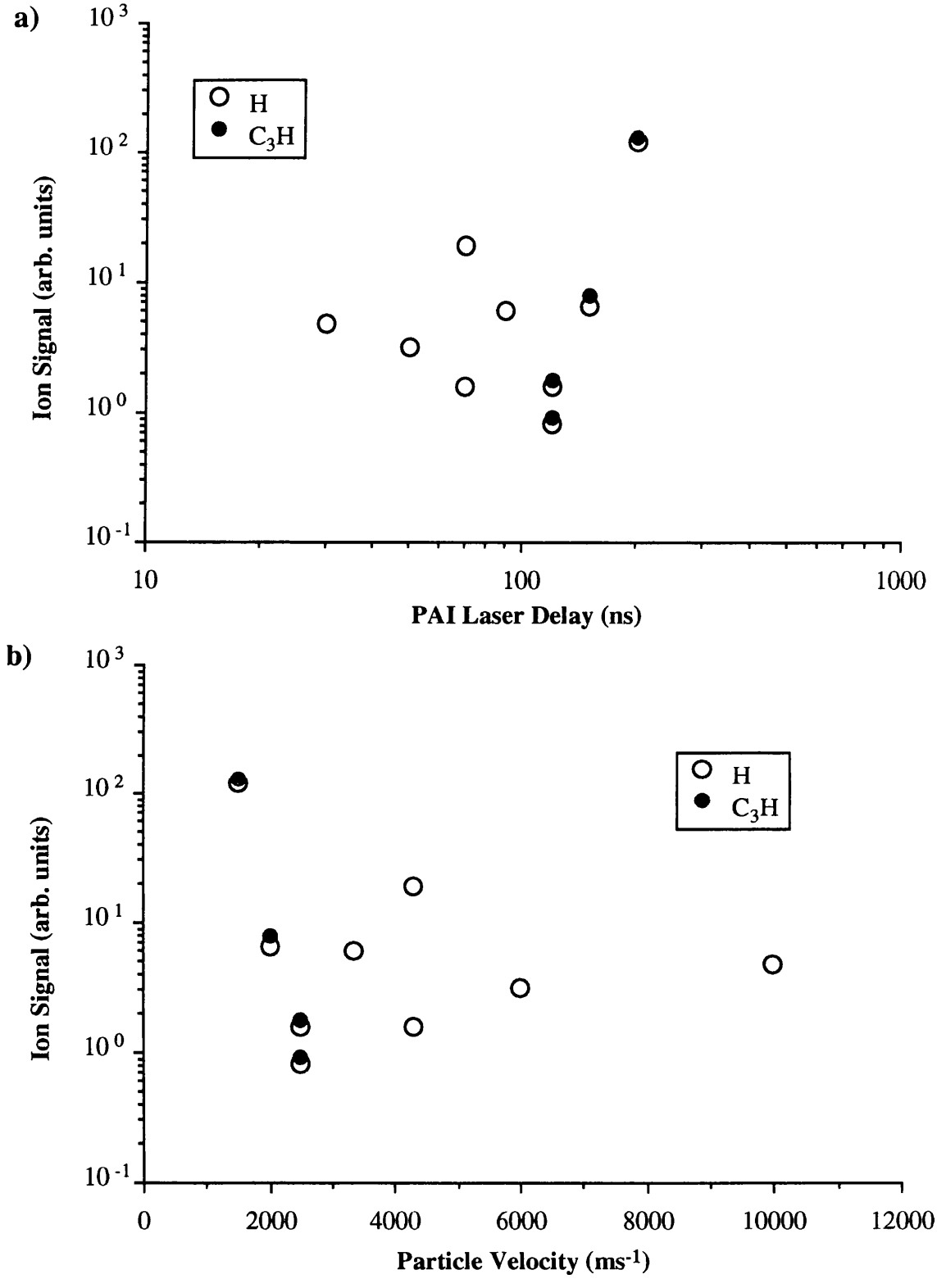

Fig.6.7 This diagram shows a second set of results taken using the same conditions described for Fig.6.6.

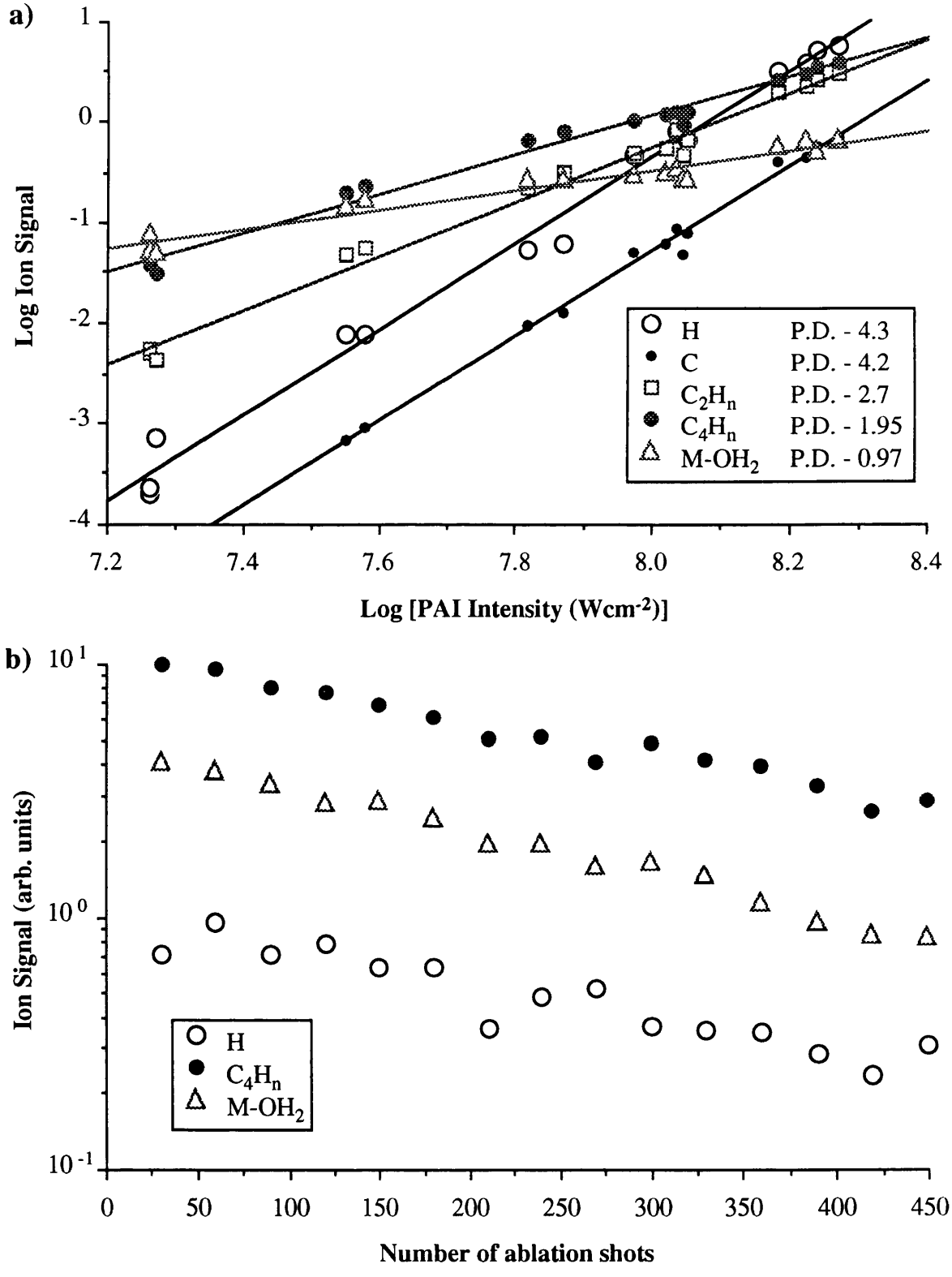

Fig.6.8 Graphs showing a) the PAI power dependence of a number of fragments, and b) the PAI ion signal dependence on number of ablation shots. Both sets of data were taken with an ablation fluence below the ion production threshold fluence (fluence 28 $mJcm^{-2}$). PAI was carried out at 243.13 nm and 1.1 mm from the sample. The PAI intensity in the shot dependence data was 5.5 x 10^7 Wcm^{-2}.

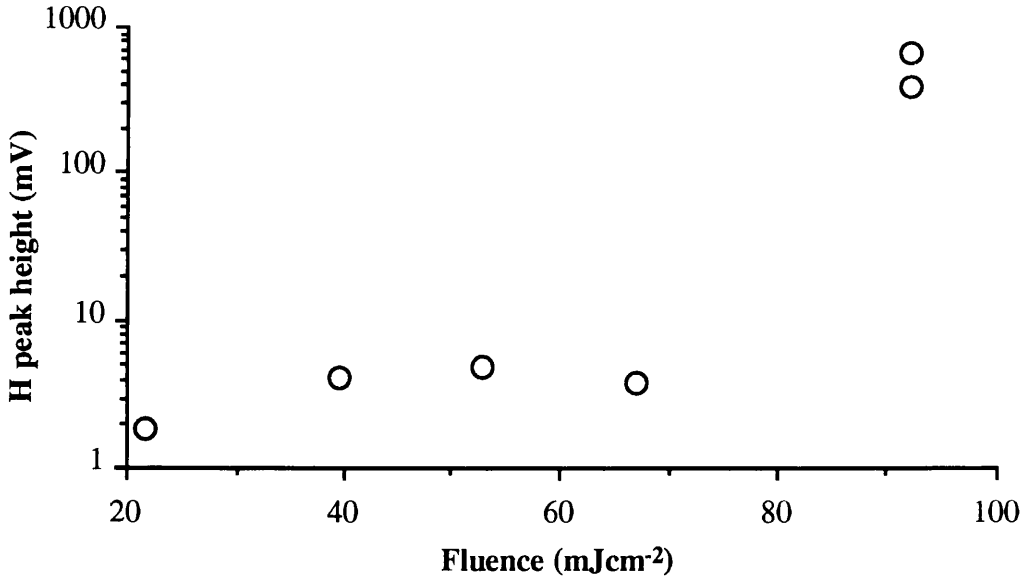

Fig.6.9 Graph showing the variation in maximum hydrogen signal height as a function of the ablation laser fluence (4ns N_2 laser).

The optimum delay times for which the maximum in hydrogen ion signal intensity was obtained are given in table.6.1 below, along with the particle velocity calculated using the PAI laser/sample separation of 300 +/- 40 μm.

Table.6.1

Fluence ($mJcm^{-2}$)	Optimum Delay (ns)	Particle Velocity (ms^{-1})
22	160 +/- 20	1880 +/- 400
39	100 +/- 15	3000 +/- 700
53	80 +/- 15	3750 +/- 1000
67	55 +/- 10	5500 +/- 1400
92	55 +/- 10	5500 +/- 1400

Although similar experiments were not carried out for sinapinic acid (to determine the variation in optimum delay time with ablation fluence), it can be seen from Fig.6.6 and Fig.6.7 that the optimum delay time for the ablation fluence used (67 $mJcm^{-2}$) occurs at approximately the same time as that found in ablation of DHB with the same fluence, and hence the same velocity since the PAI/sample distance was identical in both sets of measurements.

A cursory investigation of the elemental hydrogen in the plume (using the matrix DHB) was carried out using a 300 ps N_2 laser for ablation. Due to the inherent instability of the particular nitrogen laser used (see Chapter 3) it was not possible to obtain quantitative results. However, the behaviour observed was qualitatively similar to that described above for 4 ns N_2 ablation. The optimum delay with the PAI laser 300 μm above the sample, and an ablation laser fluence of 70 $mJcm^{-2}$, was estimated as 70 (+70,-40) ns which gives a particle velocity of approximately 4300 (+5700, -2200) ms^{-1}. Although there is considerable uncertainty as to the exact value of the optimum hydrogen velocity obtained with the 300 ps N_2 laser ablation above the ion production threshold, the results suggest that this velocity is relatively constant within the limited range of variables used (two different matrices and ablation pulselengths).

The experiments reported in this Chapter have demonstrated that neutral hydrogen atoms are present in the MALDI plume with considerably larger velocities than those of the matrix species. It is also clear that the large increase in neutral hydrogen abundance which occurs when the ion production threshold fluence is reached must be linked in some way to the ion production mechanism. Further work is obviously required to clarify some of the issues raised in this Chapter. In would be interesting to study the matrix 9-nitroanthracene which is thought to ionise only via a charge-transfer mechanism having no transferable protons (Juhasz 1993b).

6.4 Resonant Laser Ablation

In addition to the plume investigation work described above, experiments were also carried out on resonant laser ablation (RLA) of matrix materials at 243.13 nm to investigate whether the resultant increase in hydrogen ion production at the ablation site would significantly alter the observed mass spectra. However, it soon became apparent that the laser intensities required to achieve efficient production of hydrogen ions also resulted in large scale fragmentation of matrix parent ions and the loss of analyte ion signals. This can clearly be seen in Fig.6.10 where an abundance of non-specific fragment ions can be seen arriving at flight times between 20 to 60 μs. It has been effectively demonstrated that the ion

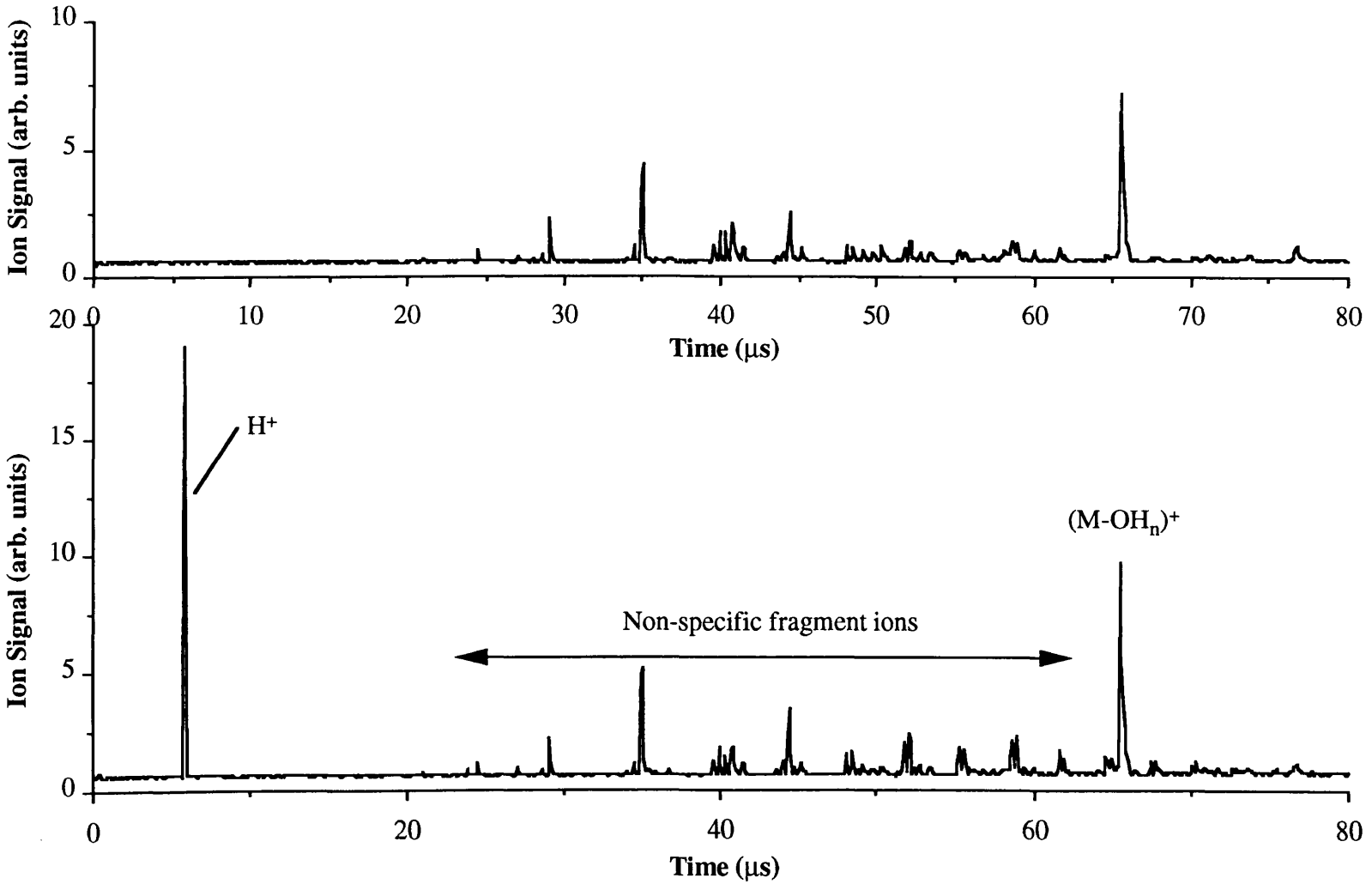

Fig.6.10 Mass spectra obtained following ablation of a single crystal of DHB with ablation laser a) off-resonance at 243.03 nm, and b) on-resonance at 243.13 nm. The ablation laser fluence was approximately 420 $mJcm^{-2}$ for both spectra.

production threshold is dependent to a large extent on the ablation laser fluence (see Chapter 2, section 2.2.2.2 and Chapter 4, section 4.6.1). As a consequence of this, on-resonance (243.13 nm) ablation experiments with picosecond or femtosecond lasers may be more successful in determining whether an increased abundance of hydrogen ions during ablation has any affect on the MALDI process.

Chapter Seven

Photofragmentation Studies

7.1 Photofragmentation using tandem TOF/TOF

One of the aims of the work carried out by the author was to use MALDI as an ion source for photofragmentation studies using tandem time-of-flight mass spectrometry (TOFMS). The structural elucidation and sequencing of peptides and proteins are essential prerequisites to understanding their biological function at a molecular level. One of the main difficulties in using mass spectrometry for this purpose has been that only relatively small fragments of large biomolecules could be introduced intact into a mass spectrometer. With the development of MALDI these problems have been overcome, and it is expected that tandem TOFMS will become increasingly more important in the characterisation of molecular structure, particularly in the analysis of large biomolecules. The initial results of the work carried out by the author in conjunction with another research student are briefly reported in this section.

The reflectron TOF mass spectrometer was modified to allow access for laser light at the turn around point in the reflectron (Chapter 3). Ions produced using MALDI at the ion source region can be selectively fragmented at the turn around point by using a second pulsed UV laser after a delay appropriate for the ion to be investigated. An example fragmentation pattern obtained following 4 ns N_2 ablation from a sample of pure DHB is shown in Fig.7.1. It can be seen that as the photofragmentation laser delay is varied, fragment ions are observed superimposed on top of the original MALDI spectrum, the fragmentation pattern of which is specific to the primary ion investigated ($(M\text{-}OH)^+$, M^+ & $((M\text{-}OH_2)+H)^+$. A detailed description of the equipment and initial results has been published (Jia 1995). After the initial system characteristation had been carried out, laser photofragmentation studies (Jia 1996) were started on the molecular ions of the amino acid derivatives; PTH-tryptophan, PTH-valine, PTH-alanine, cytosine and guanine. Fig.7.2b

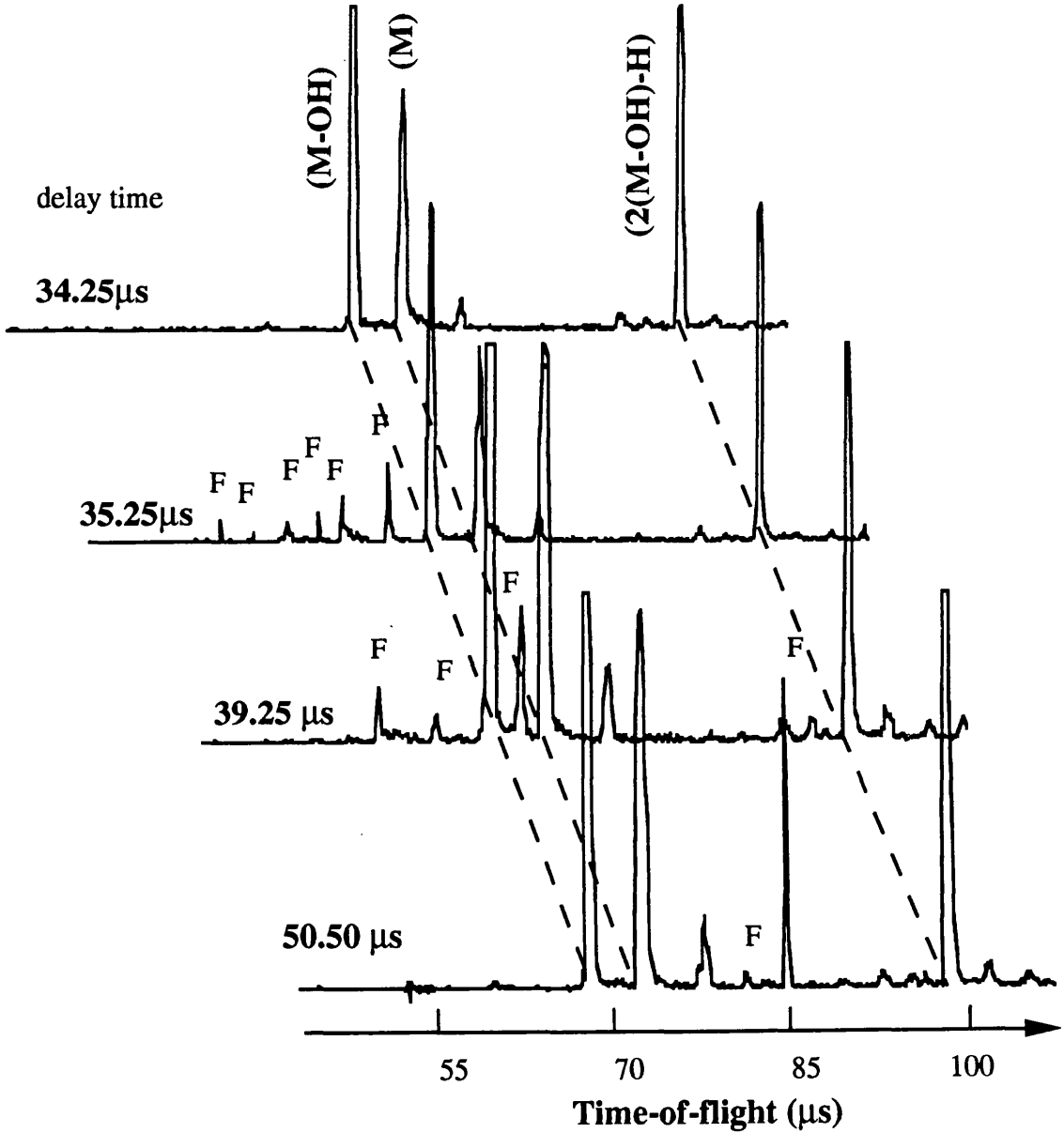

Fig.7.1 The various fragmentation patterns obtained from DHB molecular ions $(M\text{-}OH)^+$, M^+ and $((M\text{-}OH_2)+H)^+$ using a 355 nm laser to fragment. At a delay of 34.25 μs, no photofragmentation ions are present since no molecular ions are at the turn around point at this time. At the delay times of 35.25 μs, 39.25 μs & 50.50 μs the molecular ions $(M\text{-}OH)^+$, M^+ and $((M\text{-}OH_2)+H)^+$ are fragmented respectively. In the spectra above 'F' represents a fragment ion produced by photofragmentation at the turn around point.

shows the photofragmentation pattern observed from the protonated molecular ion of PTH-tryptophan, with the MALDI mass spectrum shown in Fig.7.2a. For the first time photofragmentation mass spectra, from molecular ions of amino acid derivatives initially generated by MALDI, have been succefully recorded using reflectron TOFMS.

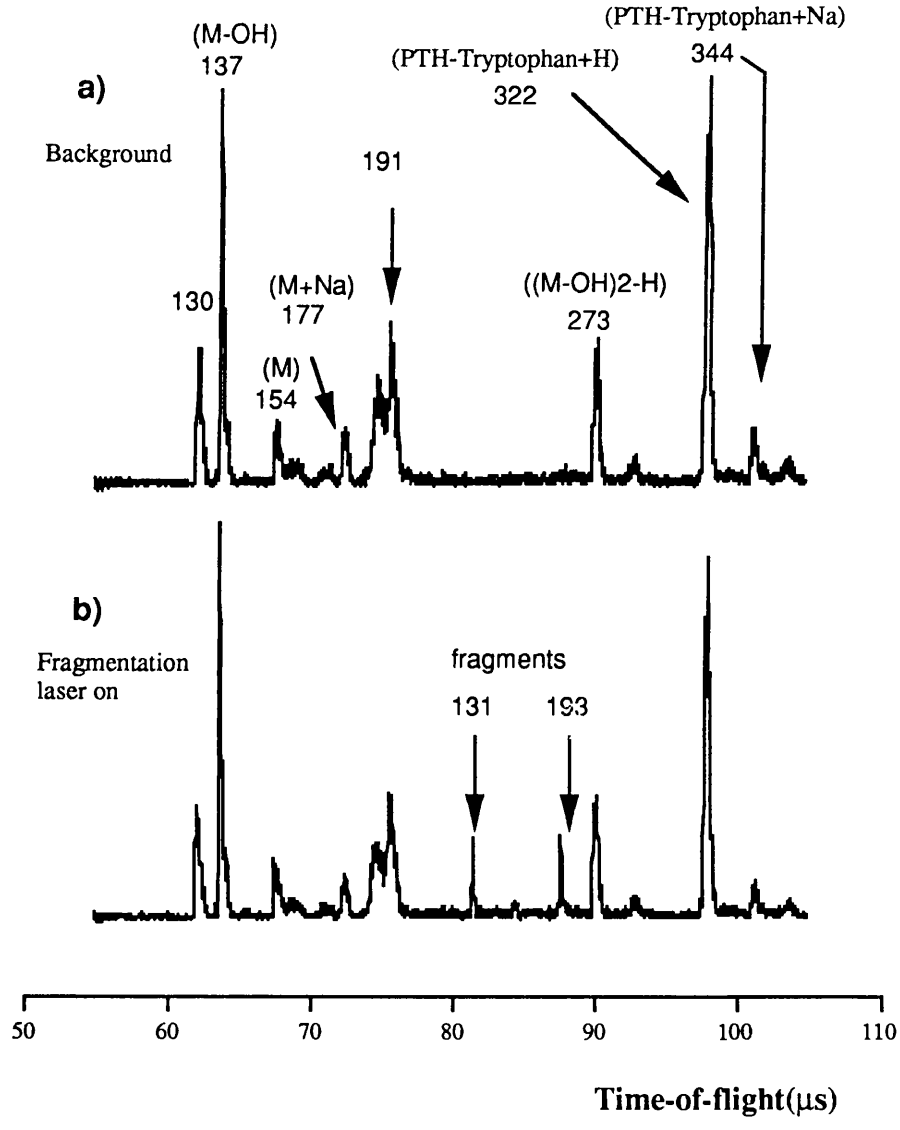

Fig.7.2 a) The MALDI spectrum obtained from a sample of PTH-tryptophan and DHB using a 4 ns N_2 laser with a fluence of 95 $mJcm^{-2}$. b) The photofragmentation spectrum obtained from $(PTH\text{-}tryptophan+H)^+$ using the 266 nm laser to fragment. The ions at *m/z* 130 and 191 in spectrum a) are fragments of PTH-tryptophan from ablation. The ions at *m/z* 131 and 193 in spectrum b) are fragment ions from photofragmentation of $(PTH\text{-}tryptophan+H)^+$.

Chapter Eight

Conclusions and Discussion

In this thesis the experimental results of the author have been modelled using some of the more substantive theoretical models developed to explain MALDI following its discovery in 1988. The findings of the author in relation to these models and results published in the literature are summarised below.

Photomechanical Models

The main photomechanical model used to describe MALDI is the pressure pulse model (Johnson 1991 & 1994). The model predicts the existence of an ablation threshold for the ejected neutral yield, the value of which, amongst other factors, depends on energy transfer rates within the matrix solid. This means that the threshold should be a function of the laser irradiance. However, the experimental evidence to date strongly suggests that the threshold for the production of neutral species occurs at a particular fluence (Table.4.2). Additionally, the experimental data obtained by both the author and Dreisewerd et al (Dreisewerd 1995) for the dependence of the neutral yield on ablation laser fluence could not be fit with any reasonable accuracy to the yield expression derived from the pressure pulse model.

The model also predicts a mass dependent velocity for the ejected neutral analyte species. However, the velocity of ejected analyte ions has been found to have no mass dependence (Beavis 1991), and although this does not necessarily imply that the neutral analyte molecules do not exhibit such a dependence, this is thought unlikely.

In general photomechanical models are based on the generation of large stresses within the matrix lattice following laser pulse absorption producing fractures and mechanical damage in addition to material ablation. However, examination of MALDI sample surfaces using electron microscopy has shown no apparent damage following ablation

with fluences just above $F_{th(ion)}$ (Strupat 1991), approximately 3 times $F_{th(neut)}$.

Photochemical Models

It is quite clear that in the photochemical mechanisms for material ablation proposed to date, processes arising from single photon absorption can be considered essentially negligible for the bulk of the ablation lasers operating in the UV and certainly for all visible and IR lasers. It becomes necessary to invoke two or more photon absorption to avoid immediately dismissing the photochemical model. However, such non-linear absorption has not been found experimentally at the typical fluences used for ablation in MALDI (Taranenko 1995).

Perhaps more conclusive evidence against the photomechanical mechanism is presented by Demirev et al (Demirev 1992) in work with two different pulselength ablation lasers resulting in a factor of approximately 10^4 difference in the sample irradiance. Given that a photochemical ablation model must be driven by non-linear absorption at the ablation wavelengths used, then the ablation threshold must be strongly dependent on the laser irradiance used. However, the onset of neutral ablation was observed at essentially the same sample fluence regardless of the ablation laser pulselength.

In addition, the yield expressions derived from photochemical models fail to accurately model the experimental neutral yield data obtained by both the author and Demirev (Demirev 1992) as earlier found for the photomechanical model.

Photothermal Models

Of the three models investigated the photothermal model provided the best fit to the experimental neutral yield dependence data of both the author and Dreisewerd (Dreisewerd 1995) due to lack of a true threshold in this model. Photothermal models predict that the matrix surface temperature will rise during laser irradiation until some phase transition temperature is reached, followed by a period where the surface

temperature is essentially pegged to this value due to surface cooling by material transport. Values for the sublimation energy (E_{sub}) of the matrix, extracted from the neutral yield curves, were close to both the estimated values of E_{sub} for typical matrix materials, and energy deposited per matrix molecule at the threshold ablation fluence ($F_{th(neut)}$). The surface temperature of the matrix at threshold could also be estimated from the neutral yield curves. However, although the estimates from the authors data were similar to the sublimation temperature (T_{sub}) of the matrix used (DHB), the results of Dreisewerd produced estimates for T_{sub} up to 50 times the expected values, dependent on the laser focusing conditions.

It is apparent from the discussions detailed in this thesis that the current state of knowledge relating to the underlying mechanisms responsible for material ablation in MALDI is still in its infancy. Based on the evidence presented thus far it appears possible that thermal effects may constitute the main component of the ablation mechanism for the typical ablation lasers used in MALDI to date, although further careful investigations are clearly required. It is thought extremely unlikely that a simple, general mechanism will apply to all matrices over all wavelength and pulse duration regimes. This is evident from the discussion above where no one model can account for all the experimental observations, although the photothermal model exhibits the least conflict with the data available to date.

This is further supported by the results of the PAI investigations reported in Chapter 5. The observed velocity distributions can be used to estimate characteristic temperatures (T_c) for the ablation process, which, if it were driven by a purely thermal process would be a good approximation to the sublimation/surface temperature of the matrix. Although the value of T_c determined was always greater than T_{sub}, the value of T_c was significantly greater than T_{sub} for shorter pulselengths, suggesting a non-thermal ablation component with increasing significance at shorter laser pulselengths.

The bulk of experimental data has been obtained with ablation lasers of pulse duration on the order of a few nanoseconds or hundreds of

picoseconds, with one notable exception (Demirev 1992). It is likely that the increasing availability of femtosecond laser systems will provide fertile ground in the ongoing investigations into the mechanisms responsible for material ablation in MALDI. Ideally, these experiments should be carried out with essentially only one variable, the laser irradiance at the sample surface. Variation in factors such as laser wavelength, spot profile, spot area and sample surface conditions should be minimised.

Appendix A

Reflectron TOFMS Resolution Effects

The approach taken in this appendix follows that detailed in a review of reflectron TOF-MS by Mamyrin (Mamyrin 1994). Consider the time of flight of an ion produced in the ion source region of the reflectron time-of-flight mass spectrometer shown in Fig.A.1 (Fig.2.2), and incident upon the ion detector. To simplify the mathematics assume that the ion optics used in the source region are based on the design proposed by Wiley and MacLaren (Wiley and MacLaren 1955). This will produce a first order space focus at some point in the drift region where ions of the same mass, but formed at different positions within the source region, will pass at the same time but with different kinetic energies. This space focus can now act as a source of ion 'packets' with essentially only a kinetic energy distribution.

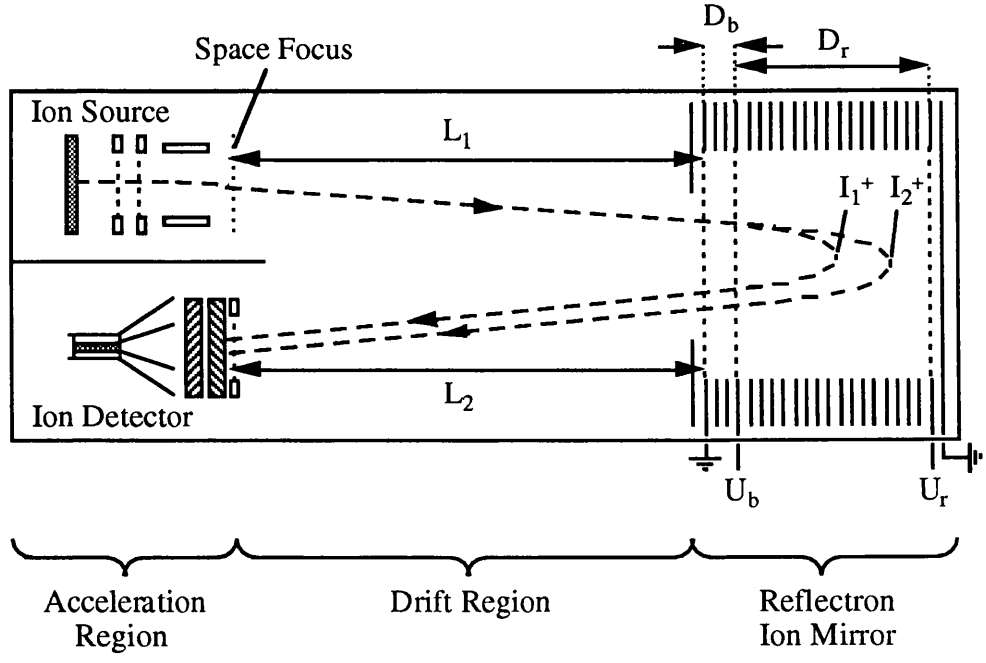

Fig.A.1 Reflectron TOF Mass Spectrometer

The time of flight for an ion travelling from the space focus to the detector, with energy qU and mass m can be separated into three parts and written as

$$t = t_l + t_b + t_r \qquad \text{Eqn.A.1}$$

where t_l, t_b & t_r are the flight times in the field free, retarding and reflecting regions of the spectrometer respectively. Writing the ion energy as $U = kU_0$, where U_0 corresponds to the mean ion energy and k is a variable factor close to unity which represents the initial energy spread (Mamyrin 1994), the times of flight in each region can be written as

$$t_l = L\left[\frac{2qU_0}{m}\right]^{-\frac{1}{2}} k^{-\frac{1}{2}} \text{ with } L = L_1 + L_2 \qquad \text{Eqn.A.1a}$$

$$t_b = 4D_b\left[\frac{2qU_0}{m}\right]^{-\frac{1}{2}} \frac{U_0}{U_b}\left[k^{\frac{1}{2}} - \left[k - \frac{U_b}{U_0}\right]^{\frac{1}{2}}\right] \qquad \text{Eqn.A.1b}$$

$$t_r = 4D_r\left[\frac{2qU_0}{m}\right]^{-\frac{1}{2}} \frac{U_0}{(U_r - U_b)}\left[k - \frac{U_b}{U_0}\right]^{\frac{1}{2}} \qquad \text{Eqn.A.1c}$$

The total time of flight throughout the mass spectrometer can therefore be written as

$$t = L\left[\frac{2qU_0}{m}\right]^{-\frac{1}{2}} F(k) \qquad \text{Eqn.A.2}$$

where the function F(k) is

$$F(k) = k^{-\frac{1}{2}} + A_b\left(k^{\frac{1}{2}} - (k - P)^{\frac{1}{2}}\right) + A_r(k - P)^{\frac{1}{2}} \qquad \text{Eqn.A.3}$$

and

$$A_b = \frac{4D_b}{L}\frac{U_0}{U_b},\ A_r = \frac{4D_r}{L}\frac{U_0}{(U_r - U_b)} \ \&\ P = \frac{U_b}{U_0} \qquad \text{Eqn.A.4}$$

The condition for energy focusing at the detector then corresponds to

$$\frac{\partial F(k)}{\partial k} = 0 \quad \text{for } k = 1 \qquad \text{Eqn.A.5}$$

i.e. a small variation in ion kinetic energy around the mean energy U_0 will make no difference (in the first order) to the time of flight. This condition results in the following condition.

$$A_b + (A_r - A_b)(1 - P)^{-\frac{1}{2}} = 1 \qquad \text{Eqn.A.6}$$

Substituting the dimensions of the Glasgow reflectron and the accelerating and reflecting potentials used by the author (U_0 = 2090 V, U_r = 2130 V, L = 2.49 m, D_b = 0.0243 m & D_r = 0.1385 m) into the above equation, the optimum retarding potential can be calculated to give U_b = 1370 V. This value corresponded with that obtained experimentally.

The mass resolution of the reflectron with respect to an initial kinetic energy distribution can be calculated as follows;

$$R_u = \frac{m}{\Delta m} = \frac{t_0}{2(t_{max} - t_{min})} = \frac{F(k)_{k=1}}{2[F(k)_{k=1} - F(k)_{k=1+\delta}]} \qquad \text{Eqn.A.7}$$

The value of F(k) for k = 1 can be calculated from the system parameters as

$$F(k)_{k=1} = 1 + A_b + (A_r - A_b)(1 - P)^{\frac{1}{2}} = 1.384 \qquad \text{Eqn.A.8}$$

While F(k) for $k = 1 + \delta$ can be expressed as (Eqn.A.9)

$$F(k)_{k=1+\delta} = (1 + \delta)^{-\frac{1}{2}} + A_b\left[(1 + \delta)^{\frac{1}{2}} - ((1 + \delta) - P)^{\frac{1}{2}}\right] + A_r((1 + \delta) - P)^{\frac{1}{2}}$$

From Taylor's theorem

$$(1 + x)^{\alpha} \approx 1 + \alpha x + \frac{\alpha(\alpha - 1)x^2}{2!} \quad \text{for } x << 1 \qquad \text{Eqn.A.10}$$

which allows Eqn.A.7 to be simplified to

$$R_u \approx \frac{4F(k)_{k=1}}{\delta^2}\left[3 - A_b - \frac{(1 - A_b)}{(1 - P)}\right]^{-1} \qquad \text{Eqn.A.11}$$

Substituting for the system parameters and the value of F(k) for k = 1 gives the mass resolution of the reflectron as

$$R_u \approx \frac{26}{\delta^2} \qquad \text{Eqn.A.12}$$

This mass resolution compares very well with the that obtainable (considering only kinetic energy distributions) from a linear TOF system with static extraction fields

$$R_u \approx \frac{1}{\delta} \qquad \text{Eqn.A.13}$$

or that obtainable from a single stage reflectron

$$R_u \approx \frac{4}{\delta^2} \qquad \text{Eqn.A.14}$$

However, the mass resolution given in Eqn.A.12 only reflects the resolution achievable if the initial ion source produced packets of ions with only a kinetic energy distribution. Although the temporal and spatial distribution of the source ion packet is minimised by the design of source optics, second order terms remain. Therefore, the best design of reflectron will still only image the initial flight time distribution at the space focus of the real ion source onto the surface of the ion detector.

Appendix B

Knudsen Layer Formation

An approximate solution to the temporal distribution obtained following the formation of a Knudsen layer is given by (Kelly 1988a),

$$\frac{dn}{n} \propto \frac{1}{t^i} \exp\left[\left(\frac{-m}{2k_B T_K}\right)\left(\frac{z}{t} - u_K\right)^2\right] dz \qquad \text{Eqn.B.1}$$

where T_K is a characteristic temperature of the plume, u_K is the flow velocity and the other parameters are as defined for Eqn.2.28. The simplifying conditions made in transforming from velocity to time (to obtain Eqn.B.1 from Eqn.2.26 & Eqn.2.29) are;

i) The irradiated area and detector volume (laser dimensions) are small compared to the spacing between them.
ii) The desorption time is much smaller than the flight time.
iii) The detector is on axis.
iv) The spatial extent of the Knudsen layer is small compared to the spacing between surface and detector.

It can be shown (Kelly 1988a) that T_K is lower than the characteristic temperature of the ablation process (T_c) by

$$\frac{T_K}{T_c} = \left[\frac{-\left(\frac{\pi\gamma}{2}\right)^{\frac{1}{2}}}{2(j+4)} + \left[1 + \frac{\left(\frac{\pi\gamma}{2}\right)}{4(j+4)^2}\right]^{\frac{1}{2}}\right]^2 \qquad \text{Eqn.B.2}$$

where j is the number of accessible degrees of freedom for the vaporised particle and γ is the heat capacity ratio for a perfect gas.

$$\gamma = \frac{C_p}{C_v} = \frac{(j+5)}{(j+3)} \qquad \text{Eqn.B.3}$$

The flow velocity is approximately equal to the speed of sound in the vapour.

$$u_K = \left[\frac{\gamma\, k_B\, T_K}{m}\right]^{\frac{1}{2}} \qquad \text{Eqn.B.4}$$

The most probable particle energy in the plume $\hat{E}$ can be related to T_K by differentiating Eqn.B.1 and solving for the most probable time $\hat{t}$

$$k_B\, T_K = \frac{\hat{E}}{\eta_K} = \frac{m}{2\,\eta_K}\left[\frac{z}{\hat{t}}\right]^2 \qquad \text{Eqn.B.5}$$

where η_K is given by

$$\eta_K = \frac{\gamma}{8}\left[1 + \left(1 + \frac{16}{\gamma}\right)^{\frac{1}{2}}\right]^2 \qquad \text{Eqn.B.6}$$

The characteristic temperature of the ablation process, T_c, can then be obtained using Eqn.B.2.

$$k_B\, T_c = \frac{\hat{E}}{\eta_c} \qquad \text{Eqn.B.7}$$

where η_c is given by

$$\eta_c = 8\,\frac{\left[-\sqrt{\pi}\,S + \sqrt{4\,(j+4)^2 + \pi\,S^2}\right]^2}{\left[\sqrt{\gamma+16} - \sqrt{\gamma}\right]^2\,[j+4]^2} \qquad \text{Eqn.B.8}$$

with

$$S = \sqrt{\frac{\gamma}{2}} \qquad \text{Eqn.B.9}$$

Bibliography

Albagli D, Dark M, Perelman L T, von Rosenberg C, Itzkan I and Feld M S, (1994)
Photomechanical basis of laser ablation of biological tissue
Optics Lett., 19 pp 1684-1686

Bai J, Liu Y-H, Cain T C and Lubman D M, (1994)
Matrix-assisted laser desorption/ionisation using an active perfluorosulfonated ionomer film substrate
Anal. Chem., 66 pp 3423-3430

Barber M, Bordoli R S, Sedgwick R D and Tyler A N, (1981)
Fast atom bombardment of solids as an ion source in mass spectrometry
Nature, 293 pp 270-275

Beavis R C and Chait B T, (1989a)
Factors affecting the ultraviolet laser desorption of proteins
Rap. Comm. Mass Spectrom., 3 pp 233-237

Beavis R C and Chait B T, (1989b)
Cinnamic acid derivatives as matrices for ultraviolet laser desorption mass spectrometry of proteins
Rap. Comm. Mass Spectrom., 3 pp 432-435

Beavis R C and Chait B T, (1991)
Velocity distributions of intact high mass polypeptide molecule ions produced by matrix assisted laser desorption
Chem. Phys. Lett., 181 pp 479-484

Beavis R C, Chaudhary T and Chait B T, (1992a)
Alpha-cyano-4-hydroxycinnamic acid as a matrix for matrix assisted laser desorption mass spectrometry
Org. Mass Spectrom., 27 pp 156-158

Beavis R C, (1992b)
Matrix-assisted ultraviolet laser desorption: Evolution and principles
Org. Mass Spectrom., 27 pp 653-659

Beavis R C, (1992c)
Phenomenological models for matrix-assisted laser desorption ion yields near the threshold fluence
Organic Mass Spectrom., 27 pp 864-868

Beavis R C and Bridson J N, (1993)
Epitaxial protein inclusion in sinapinic acid crystals
J. Phys. D, 26 pp 442-447

Biemann K and Martin S A, (1987)
Mass spectrometric determination of the amino acid sequence of peptides and proteins
Mass Spectrom. Rev., 6 pp 1-76

Blackledge J A and Alexander A J, (1995)
Polyethylene membrane as a sample support for direct matrix assisted laser desorption/ionisation mass spectrometric analysis of high mass proteins
Anal. Chem., 67 pp 843-848

Bloembergen N, (1993)
Laser-material interactions: Fundamentals and applications
Laser ablation: Mechanisms and applications-II, 1993, AIP conference proceedings 288, pp 3-10.

Borthwick I S, Ledingham K W D, Scott C T J and Singhal R P, (1992)
Laser ablation as a sample atomisation technique for resonant ionisation mass spectrometry
Resonance Ionisation Spectroscopy 1992, Inst. Phys. Conf. Series, 128 pp 279-282

Brannon J H, Lankard J R, Baise A I, Burns F and Kaufman J, (1985)
Excimer laser etching of polyimide
J. Appl. Phys., 58 pp 2036-2043

Burlingame A L, Boyd R K and Gaskell S J, (1996)
Mass spectrometry
Anal. Chem., 68 pp 599R-651R

Chait B T and Kent S B H, (1992)
Weighing naked proteins: Practical, high-accuracy mass measurement of peptides and proteins
Science, 257 pp 1885-1894

Chait B T, Rong Wang, Beavis R C and Kent S B H, (1993)
Protein ladder sequencing
Science, 262 pp 89-92

Chiarelli M P, Sharkey A G Jr and Hercules D M, (1993)
Excited-state proton transfer in laser mass spectrometry
Anal. Chem., 65 pp 307-311

Clark A, Ledingham K W D, Marshall A and Singhal R P, (1992)
Resonant ionisation spectroscopy of carbon atoms following laser-induced fragmentation of nitro-aromatic molecules
Spectrochimica Acta, 47B pp 799-808

Clark A, Kosmidis C, Ledingham K W D, Marshall A, Sander J, Singhal R P and Campbell M, (1993)
Resonant ionisation of oxygen and hydrogen atoms following laser induced photodissociation of nitrobenzene vapour
J. Phys. B, 26 pp L665-L670

Colby S M, King T B and Reilly J P, (1994)
Improving the resolution of matrix-assisted laser desorption/ionisation time-of-flight mass spectrometry by exploiting the correlation between ion position and velocity
Rap. Comm. Mass Spectrom., 8 pp 865-868

Cornett D S, Duncan M A and Amster I J, (1992a)
Matrix-assisted laser desorption at visible wavelengths using a two-component matrix
Org. Mass Spectrom., 27 pp 831-832

Cornish T J and Cotter R J, (1993)
Laser desorption tandem time-of-flight mass spectrometry for fragmentation analysis of biomolecules
Laser ablation: Mechanisms and applications-II, 1993, AIP conference proceedings 288, pp 507-512.

Danis P O and Karr D E, (1993)
A facile sample preparation for the analysis of synthetic organic polymers by matrix-assisted laser desorption/ionisation
Org. Mass Spectrom., 28 pp 923-925

D'Couto G C and Babu S V, (1994)
Heat transfer and material removal in pulsed excimer-laser-induced ablation: Pulsewidth dependence
J. Appl. Phys., 76 pp 3052-3058

Demirev P, Westman A, Reimann C T, Hakansson P, Barofsky D, Sundqvist B U R, Cheng Y D, Seibt W and Siegbahn, (1992)
Matrix-assisted laser desorption with ultra-short laser pulses
Rap. Comm. Mass Spectrom., 6 pp 187-191

Demtroder W, (1982)
Laser Spectroscopy Basic Concepts and Instrumentation
Springer-Verlag, Berlin Heidelberg New York.

Dingus R S and Scammon R J, (1991)
Abaltion of material by front surface spallation
In "Lecture Notes In Physics", Springer Verlag, pp 180-190

Doktycz S J, Savickas P J and Krueger D A, (1991)
Matrix/sample interactions in ultraviolet laser-desorption of proteins
Rap. Comm. Mass Spectrom., 5 pp 145-148

Dominic Chan T W, Colburn A W and Derrick P J, (1991)
Matrix-assisted UV laser desorption. Suppression of the matrix peaks
Org. Mass Spectrom., 26 pp 342-344

Dominic Chan T W, Thomas I, Colburn A W and Derrick P J, (1994)
Initial velocities of positive and negative protein molecule-ions produced in matrix-assisted ultraviolet laser desorption using a liquid matrix
Chem. Phys. Lett., 222 pp 579-585

Doroshenko V M and Cotter R J, (1993)
High-resolution matrix-assisted laser desorption/ionisation mass spectrometry of biomolecules in a quadrupole ion trap
Laser ablation: Mechanisms and applications-II, 1993, AIP conference proceedings 288, pp 513-518.

Dreisewerd K, Schurenberg M, Karas M and Hillenkamp F, (1995)
Influence of the laser intensity and spot size on the desorption of molecules and ions in matrix-assisted laser desorption/ionisation with a uniform beam profile
Int. J. Mass Spectrom. Ion Proc., 141 pp 127-148

Ehring H, Karas M and Hillenkamp F, (1992)
Role of photoionisation and photochemistry in ionisation processes of organic molecules and relevance for matrix-assisted laser desorption ionisation mass spectrometry
Org. Mass Spectrom., 27 pp 472-480

Eisberg R and Resnick R, (1985)
Quantum Physics of Atoms, Molecules, Solids, Nuclei, and Particles
John Wiley & Sons

Ens W, Mao Y, Mayer F and Standing K G, (1991)
Properties of matrix-assisted laser desorption. Measurements with a time-to-digital converter
Rap. Comm. Mass Spectrom., 5 pp 117-123

Fain B and Lin Sheng H, (1989)
Laser-induced explosive desorption
J. Chem. Phys., 91 pp 2726-2734

Favretto D, Seraglia R Traldi P, Curcuruto O and Hamdan M, (1994)
Electrospray vs. matrix-assisted laser desorption/ionisation. 1. Some examples in the protein field
Org. Mass Spectrom., 29 pp 526-532

Fenn J B, Mann M, Meng C K, Wong S F and Whitehouse C M, (1989)
Electrospray ionisation for mass spectrometry of large biomolecules
Science, 246 pp 64-71

Fitzgerald M C, Parr G R and Smith L M, (1993a)
Basic matrices for the matrix-assisted laser desorption/ionisation mass spectrometry of proteins and oligonucleotides
Anal. Chem., 65 pp 3204-3211

Fitzgerald M C, Zhu L and Smith L M, (1993b)
The analysis of mock DNA sequencing reactions using matrix-assisted laser desorption/ionisation mass spectrometry
Rap. Comm. Mass Spectrom., 7 pp 895-897

Fitzgerald M E, (1996)
Photonics speeds up DNA research
Photonics Spectra, April pp 70-77

Fountain S T, Lee Heewon and Lubman D M, (1994)
Ion fragmentation activated by matrix-assisted laser desorption/ionisation in an ion-trap/reflectron time-of-flight device
Rap. Comm. Mass Spectrom., 8 pp 407-416

Garrison B J, (1985)
Laser ablation of organic polymers: Microscopic models for photochemical and thermal processes
J. Appl. Phys., 57 pp 2909-2914

George M, Wellemans J M Y, Cerny R L, Gross M L, Li K and Cavalieri E L, (1994)
Matrix design for matrix-assisted laser-desorption ionisation - sensitive determination of PAH-DNA adducts
J. Am. Soc. Mass Spectrom., 5 pp 1021-1025

Gimon M E, Preston L M, Solouki T, White M A and Russell D H, (1992)
Are proton transfer reactions of excited states involved in UV laser desorption ionisation?
Org. Mass Spectrom., 27 pp 827-8308

Grundwürmer J M, Bönisch M, Kinsel G R, Grotemeyer J and Schlag E W, (1994)
High-resolution mass spectrometry in a linear time-of-flight mass spectrometer
Int. J. Mass Spectrom. Ion Proc., 131 pp 139-148

Gusev A I, Wilkinson W R, Proctor A and Hercules D M, (1995)
Improvement of signal reproducibility and matrix/comatrix effects in MALDI analysis
Anal. Chem., 67 pp 1034-1041

Harvey D J, Rudd P M, Bateman R H, Bordoli R S, Howes K, Hoyes J B and Vickers R G(1994)
Examination of complex oligosaccharides by matrix-assisted laser desorption ionisation mass-spectrometry on time-of-flight and magnetic-sector instruments
Org. Mass Spectrom., 29 pp 753-766

Hedin A, Westman A, Hakansson P and Sundqvist Bo U R, (1991)
Laser desorption mass spectrometry - Some technical and mechanistic aspects
In "Methods and Mechanisms for Producing Ions from Large Molecules", Ed. Standing K G and Ens W, Plenum Press, New York, pp 211-219

Hillenkamp F, Karas M, Holtkamp D and Klusener P, (1986)
Energy deposition in ultraviolet laser desorption mass spectrometry of biomolecules
Int. J. Mass Spectrom. Ion Proc., 69 pp 265-276

Hillenkamp F, Karas M, Beavis R C and Chait B T, (1991)
Matrix-assisted laser desorption/ionisation mass spectrometry of biopolymers
Anal. Chem., 63 pp 1193A-1203A

Hurst G S and Payne M G, (1988)
Principles and applications of resonance ionisation spectroscopy
IOP Publishing Ltd, Bristol

Huth-Fehre T and Becker C H, (1991)
Energetics of gramicidin S after UV laser deporption from a ferulic acid matrix
Rap. Comm. Mass Spectrom., 5 pp378-382

Ingendoh A, Karas M, Hillenkamp F and Giessmann U, (1994)
Factors affecting the resolution in matrix-assisted laser desorption-ionisation mass spectrometry
Int. J. Mass Spectrom. Ion Proc., 131 pp 345-354

Jellinek H H G and Srinivasan R, (1984)
Theory of etching of polymers by far-ultraviolet, high-intensity pulsed laser and long-term irradiation
J. Phys. Chem., 88 pp 3048-3051

Jespersen S, Niessen W M A, Tjaden U R, van der Greef J, Litborn E, Lindberg U and Roeraade J, (1994)
Attomole detection of proteins by matrix-assisted laser desorption/ionisation mass spectrometry with the use of picolitre vials
Rap. Comm. Mass Spectrom., 8 pp 581-584

Jia W J, Ledingham K W D, Scott C T J, Kosmidis C and Singhal R P, (1995)
A tandem reflectron time-of-flight mass spectrometer for the investigation of laser photofragmentation of molecular ions
Rap. Comm. Mass Spectrom., 9 pp 761-766

Jia W J, Ledingham K W D, Scott C T J, Kosmidis C and Singhal R P, (1996)
Photofragmentation studies of biomolecular ions of amino acids using a tandem reflectron time-of-flight mass spectrometer
Rap. Comm. Mass Spectrom., 10 pp 1597-1604

Johnson R E, Sundquist B U R, Hedin A and Fenyo D, (1989)
Sputtering by fast ions based on a sum of impulses
Phys. Rev. B, 40 pp 49-53

Johnson R E and Sundqvist B U R, (1991)
Laser-pulse ejection of organic molecules from a matrix: Lessons from fast-ion-induced ejection
Rap. Comm. Mass Spectrom., 5 pp 574-578

Johnson R E, (1993)
Mechanisms for the desorption of large organic molecules
Int. J Mass Spectrom. Ion Proc., 126 pp 17-24

Johnson R E, (1994)
Models for matrix-assisted desorption by a laser-pulse
Int. J. Mass Spectrom. Ion Proc., 139 pp 25-38

Jonscher K, Currie G, McCormack A L and Yates J R, (1993)
Matrix-assisted laser desorption of peptides and proteins on a quadrupole ion trap mass spectrometer
Rap. Comm. Mass Spectrom., 7 pp 20-26

Juhasz P, Costello C E and Biemann K, (1993a)
Matrix-assisted laser desorption ionisation mass spectrometry with 2-(4-hydroxyphenylazo)benzoic acid matrix
J. Am. Soc. Mass Spectrom., 4 pp 399-409

Juhasz P and Costello C E, (1993b)
Generation of large radical ions from oligometallocenes by matrix assisted laser desorption ionisation
Rap. Comm. Mass Spectrom., 7 pp 343-351

Karas M, Bachmann D and Hillenkamp F, (1985)
Influence of the wavelength in high-irradiance ultraviolet laser desorption mass spectrometry of organic molecules
Anal. Chem., 57 pp 2935-2939

Karas M and Hillenkamp F, (1988)
Laser desorption ionisation of proteins with molecular masses exceeding 10000 daltons
Anal. Chem., 60 pp 2301-2303

Karas M, Bahr U, Ingendoh A, Nordhoff E, Stahl B, Strupat K and Hillenkamp F, (1990)
Principles and applications of matrix-assisted UV-laser desorption/ionisation mass spectrometry
Analytica Chimica Acta, 241 pp 175-185

Karas M, Bahr U and Giebmann U, (1991)
Matrix-assisted laser desorption ionisation mass spectrometry
Mass Spectrom. Rev., 10 pp 335-357

Karas M, Ehring H, Nordhoff E, Stahl B, Strupat K, Hillenkamp F, Grehl M and Krebs B, (1993)
Matrix-assisted laser desorption/ionisation mass spectrometry with additives to 2,5-dihydroxybenzoic acid
Org. Mass Spectrom., 28 pp 1476-1481

Kaufmann R, Spengler B and Lutzenkirchen F, (1993)
Mass spectrometric sequencing of linear peptides by product-ion analysis in a reflectron time-of-flight mass spectrometer using matrix-assisted laser desorption ionisation
Rap. Comm. Mass Spectrom., 7 pp 902-910

Kaufmann R, Kirsch D and Spengler B, (1994)
Sequencing of peptides in a time-of-flight mass spectrometer: evaluation of postsource decay following matrix-assisted laser desorption ionisation (MALDI)
Int. J. Mass Spectrom. Ion Proc., 131 pp 355-385

Kaufmann R, (1995)
Matrix-assisted laser desorption ionisation (MALDI) mass spectrometry: a novel analytical tool in molecular biology and biotechnology
J. Biotechnology, 41 pp 155-175

Kelly R and Dreyfus R W, (1988a)
On the effect of knudsen-layer formation on studies of vaporisation, sputtering, and desorption
Surface Sci., 198 pp 263-276

Kelly R and Dreyfus R W, (1988b)
Reconsidering the mechanisms of laser sputtering with knudsen layer formation taken into account
Nuc. Instr. Meth. Phys. Res. B, 32 pp 341-348

Kelly R, (1990)
On the dual role of the knudsen laser and unsteady, adiabatic expansion in pulse sputtering phenomena
J. Chem. Phys., 92 pp 5047-5056

Kittel C and Kroemer H, (1980)
Thermal Physics
W H Freeeman and Co, San Francisco

Kools J C S, Baller T S, De Zwart S T and Dieleman J, (1992)
Gas flow dynamics in laser ablation deposition
J. Appl. Phys., 71 pp 4547-4556

Kools J C S and Dieleman J, (1993)
Angle-resolved time-of-flight studies on ground-state neutrals formed by near-threshold excimer laser ablation of copper
J. Appl. Phys., 74 pp 4163-4167

Kuang Jen Wu, Steding A and Becker C H, (1993)
Matrix-assisted laser desorption time-of-flight mass spectrometry of oligonucleotides using 3-hydroxypicolinic acid as an ultraviolet-sensitive matrix
Rap. Comm. Mass Spectrom., 7 pp 142-146

Kuper S and Stuke M, (1987)
Femtosecond uv excimer laser ablation
Appl. Phys. B, 44 pp 199-204

Lax M, (1977)
Temperature rise induced by a laser beam
J. Appl. Phys., 48 pp 3919-3924

Lazare S and Granier V, (1989)
Ultraviolet laser photoablation of polymers: A review and recent results
Laser Chem., 10 pp 25-40

Lazneva E F, (1991)
Laser induced desorption
Rad. Eff., 115 pp 257-284

Lecchi P, Le H M T and Pannell L K, (1995)
6-aza-a-thiothymine - a matrix for MALDI spectra of oligonucleotides
Nuc. Acids Res., 23 pp 1276-1277

Lee H W and Lubman D M, (1995)
Sequence-specific fragmentation generated by matrix-assisted laser desorption/ionisation in a quadrupole ion trap/reflectron time-of flight device
Anal. Chem., 67 pp 1400-1408

Levis R J, (1994)
Laser desorption and ejection of biomolecules from the condensed phase into the gas phase
Annu. Rev. Phys. Chem., 45 pp 483-518

Liao P-C and Allison J, (1995)
Ionisation processes in matrix-assisted laser desorption/ionisation mass spectrometry: Matrix dependent formation of $[M+H]^+$ vs $[M+Na]^+$ ions of small peptides and some mechanistic comments
J. Mass Spectrom., 30 pp 408-423

Loza P, Kouznetsov D and Roberto Ortego, (1994)
Temperature distribution in a uniform medium heated by linear absorption of a gaussian light beam
Appl. Optics, 33 pp 3831-3836

Lu Y F, Loh T E, Teo B S and Low T S, (1994)
Effect of polarisation on laser-induced surface-temperature rise
Appl. Phys. A, 58 pp 423-429

Luk'yanchuk B, Bityurin N, Anisimov S and Bauerle D, (1993)
The role of excited species in UV-laser materials ablation
Appl. Phys. A, 57 pp 367-374

MacFarlane R D and Torgerson D F, (1976)
Californium-252 plasma desorption mass spectroscopy
Science, 191 pp 920-925

Mamyrin B A, Karataev V I, Shmikk D V and Zagulin V A, (1973)
The mass-reflectron, a new nonmagnetic time-of-flight mass spectrometer with high resolution
Sov. Phys. JETP, 37 pp 45-48

Mamyrin B A, (1994)
Laser assisted reflectron time-of-flight mass spectrometry
Int. J. Mass Spectrom. Ion Proc., 131 pp 1-19

Mann M and Talbo G, (1996)
Developments in matrix-assisted laser desorption/ionisation peptide mass spectrometry
Curr. Op. Biotech., 7 pp 11-19

McCombes P T, Borthwick I S, Jennings R, Ledingham K W D and Singhal R P, (1991)
Resonance ionisation mass-spectrometry applied to the trace analysis of gold
Inst. Phys. Conf. Series, 113 pp 163-168

McIver R T Jr, Li Yunzhi and Hunter R L, (1994)
Matrix-assisted laser desorption/ionisation with an external ion source fourier-transform mass spectrometer
Rap. Comm. Mass Spectrom., 8 pp 237-241

Medina N, Huth-Fehre T Westman A and Sundqvist B U R, (1994)
Matrix-assisted laser desorption: Dependence of the threshold fluence on analyte concentration
Org. Mass Spectrom., 29 pp 207-209

Metzger J O, Woisch R, Tuszynski W and Angermann R, (1994)
New-type of matrix for matrix-assisted laser-desorption mass spectrometry of polysaccharides and proteins
Fres. J. Anal. Chem., 349 pp 473-474

Mock K K, Sutton C W and Cottrell J S, (1992)
Sample immobilisation protocols for matrix-assisted laser-desorption mass spectrometry
Rap. Comm. Mass Spectrom., 6 pp 233-238

Montaudo G, Montaudo M S, Puglisi C and Samperi F, (1994)
2-(4-Hydroxyphenylazo)-benzoic acid: A solid matrix for matrix-assisted laser desorption/ionisation of polystyrene
Rap. Comm. Mass Spectrom., 8 pp 1011-1015

Murray K K and Russell D H, (1993)
Liquid sample introduction for matrix-assisted laser desorption ionisation
Anal. Chem., 65 pp 2534-2537

NoorBatcha I and Lucchese R R, (1987)
Monte carlo simulations of gas-phase collisions in rapid desorption of molecules from surfaces
J. Chem. Phys., 86 pp 5816-5824

Oraevsky A A, Esenaliev R O and Letokhov V S, (1991)
Pulsed laser ablation of biological tissue: Review of the mechanisms
In "Lecture Notes in Physics", Ed. Miller J C and Haglund Jr R F, Laser Ablation, Mechanisms and Applications, Proceedings Oak Ridge, Springer Verlag

Overberg A, Karas M, Bahr U, Kaufmann R and Hillenkamp F, (1990)
Matrix-assisted infrared-laser (2.94 μm) desorption/ionisation mass spectrometry of large biomolecules
Rap. Comm. Mass Spectrom., 4 pp 293-296

Pappin D J C, Hojrup P and Bleasby A J, (1993)
Rapid identification of proteins by peptide-mass fingerprinting
Curr. Biology, 3 pp 327-332

Patterson S D and Katta V, (1994)
Prompt fragmentation of disulfide-linked peptides during matrix-assisted laser desorption ionisation mass spectrometry
Anal. Chem., 66 pp 3727-3732

Perera I K, Kantartzoglou S and Dyer P E, (1994)
Coumarin laser dyes as matrices for matrix assisted UV laser desorption/ionisation mass spectrometry
Int. J. Mass Spectrom. Ion Proc., 137 pp 151-171

Perera I K, Perkins J and Kantartzoglou S, (1995)
Spin-coated samples for high resolution matrix-assisted laser desorption/ionisation time-of-flight mass spectrometry of large proteins
Rap. Comm. Mass Spectrom., 9 pp 180-187

Philippoz J-M, Zenobi R and Zare R N, (1989)
Pulsed heating of surfaces: Comparison between numerical simulation, analytical models, and experiments
Chem. Phys. Lett., 158 pp 12-17

Quist A P, Huth-Fehre T and Sundqvist Bo U R, (1994)
Total yield measurements in matrix-assisted laser desorption using a quartz crystal microbalance
Rap. Comm. Mass Spectrom., 8 pp 149-154

Ready J F, (1971)
Effects of High Power Laser Radiation
Academic Press, New York

Riahi K, Bolbach G, Brunot A, Breton F, Spiro M and Blais J-C, (1994)
Influence of laser focusing in matrix-assisted laser *desorption/ionisation*
Rap. Comm. Mass Spectrom., 8 pp 242-247

Roepstorff P and Fohlman J, (1984)
Proposal for a common nomenclature for sequence ions in mass spectra of peptides
Biomedical Mass Spectrom., 11 pp 601

Scott C T J, Kosmidis C, Jia W J, Ledingham K W D and Singhal R P, (1994)
Formation of atomic hydrogen in matrix-assisted laser desorption ionisation
Rap. Comm. Mass Spectrom., 8 pp 829-832

Solouki T, Gillig K J and Russell D H, (1994)
Mass measurement accuracy of matrix-assisted laser desorbed biomolecules: A fourier-transform ion cyclotron resonance mass spectrometry study
Rap. Comm. Mass Spectrom., 8 pp 26-31

Spengler B, Kirsch D and Kaufmann R, (1991)
Metastable decay of peptides and proteins in matrix-assisted laser desorption mass spectrometry
Rap. Comm. Mass Spectrom., 5 pp 198-202

Spengler B, Kirsch D and Kaufmann R, (1992)
Fundamental aspects of postsource decay in matrix-assisted laser desorption mass spectrometry. 1. Residual gas effects
J. Phys. Chem., 96 pp 9678-9684

Srinivasan R and Braren B, (1989)
Ultraviolet laser ablation of organic polymers
Chem. Rev., 89 pp 1303-1316

Strobel F H, Solouki T, White M A and Russell D H, (1991)
Detection of femtomole and sub-femtomole levels of peptides by tandem magnetic sector/reflectron time-of-flight mass spectrometry and matrix-assisted laser desorption ionisation
J. Am. Soc. Mass Spectrom., 2 pp 91-94

Strupat K, Karas M and Hillenkamp, (1991)
2,5-Dihydroxybenzoic acid: a new matrix for laser desorption ionisation mass spectrometry
Int. J. Mass Spectrom. Ion Proc., 111 pp 89-102

Stryer L, (1988)
Biochemistry
Third edition, W H Freeman and Co, New York

Stults J T, (1995)
Matrix-assisted laser desorption/ionisation mass spectrometry (MALDI-MS)
Curr. Op. Struct. Biology, 5 pp 691-698

Sundqvist Bo U R, Hakansson P, Hedin A, Fenyo D, Brinkmalm G, Roepstorff P and Johnson R E, (1991)
Plasma desorption mass spectrometry - Achievements and frontiers
In "Methods and Mechanisms for Producing Ions from Large Molecules", Ed. Standing K G and Ens W, Plenum Press, New York, pp 7-17

Sutcliffe E and Srinivasan R, (1986)
Dynamics of UV laser ablation of organic polymer surfaces
J. Appl. Phys., 60 pp 3315-3322

Tanaka K, Waki H, Ido Y, Akita S and Yoshida Y, (1988)
Rap. Comm. Mass Spectrom., 2 pp151

Tang K, Allman S L, Jones R B and Chen C H, (1992)
Comparison of rhodamine dyes as matrices for matrix-assisted laser desorption/ionisation mass spectrometry
Org. Mass Spectrom., 27 pp 1389-1392

Tang K, Taranenko N I, Allman S L, Chen C H, Chang L Y and Jacobson K B, (1994)
Picolinic-acid as a matrix for laser mass-spectrometry of nucleic-acids and proteins
Rap. Comm. Mass Spectrom., 8 pp 673-677

Taranenko N I, Tang K, Allman S L, Ch'ang L Y and Chen C H, (1994)
3-aminopicolinic acid as a matrix for laser desorption mass spectrometry of biopolymers
Rap. Comm. Mass Spectrom., 8 pp 1001-1006

Taranenko N I, Golovlev V V, Puretzky A A, Allman S L and Chen C H, (1995)
Direct monitoring of laser absorption of MALDI matrices by fast piezoelectric transducer
Chem. Phys. Lett., 234 pp 165-171

Towrie M, Drysdale S L T, Jennings R, Land A P, Ledingham K W D, McCombes P T, Singhal R P and Smyth M H C, (1990)
Trace analysis using a commercial resonant ionisation mass spectrometer
Int. J. Mass Spectrom. Ion Proc., 96 pp 309-320

Vertes A and Levine R D, (1990a)
Sublimation versus fragmentation in matrix-assisted laser desorption
Chem. Phys. Lett., 171 pp 284-290

Vertes A, Gijbels R and Levine R D, (1990b)
Homogeneous bottleneck model of matrix-assisted ultraviolet laser desorption of large molecules
Rap. Comm. Mass Spectrom., 4 pp 228-233

Vertes A and Gijbels R, (1991)
Restricted energy transfer in laser desorption of high molecular weight biomolecules
Scann. Micr., 5 pp 317-328

Vertes A, Irinyi G and Gijbels R, (1993a)
Hydrodynamic model of matrix-assisted laser desorption mass spectrometry
Anal. Chem.,65 pp 2389-2393

Vertes A, (1993b)
Methods utilising low and medium laser irradiance
In "Laser Ionisation Mass Analysis", Ed. Vertes A, Gijbels R and Adams F, Chem. Analysis Series, 124 pp 127-175

Vestal M L, Juhasz P and Martin S A, (1995)
Delayed extraction matrix-assisted laser desorption time-of-flight mass spectrometry
Rap. Comm. Mass Spectrom., 9 pp 1044-1050

von Allmen M, (1987)
Laser-beam interactions with materials - Physical principles and application
Springer Series in Materials Science 2, Springer Verlag, Berlin Heidelberg

Vorm O, Roepstorff P and Mann M, (1994a)
Improved resolution and very high sensitivity in MALDI TOF of matrix surfaces made by fast evaporation
Anal. Chem., 66 pp 3281-3287

Vorm O and Mann M, (1994b)
Improved mass accuracy in matrix-assisted laser desorption/ionisation time-of-flight mass spectrometry of peptides
J. Am. Soc. Mass Spectrom., 5 pp 955-958

Wang B H, Dreisewerd K, Bahr U, Karas M and Hillenkamp F, (1993)
Gas-phase cationisation and protonation of neutrals generated by matrix-assisted laser desorption
J. Am. Soc. Mass Spectrom., 4 pp 393-398

Wang L, Borthwick I S, Jennings R, McCombes P T, Ledingham K W D, Singhal R P and McLean C J, (1991)
Observations and analysis of resonant laser ablation of GaAs
Appl. Phys., B53 pp 34-38

Werlen R C, (1994)
Effect of resolution on the shape of mass spectra of proteins: Some theoretical considerations
Rap. Comm. Mass Spectrom., 8 pp 976-980

Westman A, Demirev P, Huth-Fehre T, Bielawski J and Sundqvist Bo U R, (1994a)
Sample exposure effects in matrix-assisted laser desorption ionisation mass spectrometry of large biomolecules
Int. J. Mass Spectrom. Ion Proc., 130 pp 107-115

Westman A, Huth-Fehre T, Demirev P, Bielawski J, Medina N and Sundqvist Bo U R, (1994b)
Matrix-assisted laser desorption/ionisation: Dependence of the ion yield on the laser beam incidence angle
Rap. Comm. Mass Spectrom., 8 pp 388-393

Westman A, Huth-Fehre T, Demirev P and Sundqvist B U R, (1995)
Sample morphology effects in matrix-assisted laser desorption/ionisation mass spectrometry of proteins
J. Mass Spectrom., 30 pp 206-211

Williams P and Nelson R W, (1991)
On the mechanism of volatilisation of large biomolecules by pulsed laser ablation of frozen aqueous solutions
In "Methods and Mechanisms for Producing Ions from Large Molecules", Ed. Standing K G and Ens W, Plenum Press, New York, pp 265-273

Wiley W C and McLaren I H, (1955)
Time-of-flight mass spectrometry with improved resolution
Rev. Sci. Instr., 26 pp 1150-1157

Xiang F and Beavis R C, (1993)
Growing protein-doped sinapinic acid crystals for laser desorption: an alternative preparation method for difficult samples
Org. Mass Spectrom., 28 pp 1424-1429

Xiang F and Beavis R C, (1994)
A method to increase contaminant tolerance in protein matrix-assisted laser desorption/ionisation by the fabrication of thin protein-doped polycrystalline films
Rap. Comm. Mass Spectrom., 8 pp 199-204

Yau P Y, Dominic Chan T-W, Cullis P G, Colburn A W and Derrick P J, (1993)
Threshold fluences for production of positive and negative ions in matrix-assisted laser desorption/ionisation using liquid and solid matrices
Chem. Phys. Lett., 202 pp 93-100

Zare R N and Levine R D, (1987)
Mechanism for bond-selective processes in laser desorption
Chem. Phys. Lett., 136 pp 593-599

Zhao S, Somayajula K V, Sharkey A G and Hercules D M, (1991)
Novel method fo matrix-assisted laser mass spectrometry of proteins
Anal. Chem., 63 pp 450-453

Zhou J, Ens W, Standing K G and Verentchikov A, (1992)
Kinetic energy measurements of molecular ions ejected into an electric field by matrix-assisted laser desorption
Rap. Comm. Mass Spectrom., 6 pp 671-678

Zhu Y F, Lee K L, Tang K, Allman S L, Taranenko N I and Chen C H, (1995)
Revisit of MALDI for small proteins
Rap. Comm. Mass Spectrom., 9 pp 1315-1320

Zimmermann F M and Ho W, (1994)
Velocity distributions of photochemically desorbed molecules
J. Chem. Phys., 100 pp 7700-7706